https://doi.org/10.15388/vu.thesis.71
https://orcid.org/0000-0001-6640-9464

VILNIUS UNIVERSITY

Evaldas
BALČIŪNAS

# Development of Bioactive Scaffolds for Tissue Engineering Applications

**DOCTORAL DISSERTATION**

Natural sciences,
Biochemistry (N 004)

VILNIUS 2020

This dissertation was prepared between 2014 and 2018 while studying at Vilnius University Life Sciences Center. The dissertation is defended on an external basis.

The research was supported by the European Commission via the Marie Skłodowska-Curie research fellowship programme AngioMatTrain (grant agreement 317304), INFOBALT Lithuania, the World Federation of Scientists, Lancaster University via Early Career Small Grants programme and the Research Council of Lithuania (grant agreement SEN-13/2015 as well as via scholarships for academic accomplishments).

Academic consultants: **Dr. Daiva Baltriukienė** (Vilnius University, Natural Sciences, Biochemistry - N 004) and **Dr. John George Hardy** (University of York, Natural Sciences, Chemistry - N 003).

Dissertation Defence Panel:
Chairman – **Prof. Dr. Gintaras Valinčius** (Vilnius University, Natural Sciences, Biochemistry - N 004).
Members:
**Dr. Aušra Imbrasaitė** (Vilnius University, Natural Sciences, Biochemistry - N 004),
**Prof. Dr. Rūta Navakauskienė** (Vilnius University, Natural Sciences, Biochemistry - N 004),
**Assoc. Prof. Dr. Jolita Ostrauskaitė** (Kaunas University of Technology, Natural Sciences, Chemistry - N 003),
**Prof. Dr. Vytautė Starkuvienė-Erfle** (Heidelberg University, Natural Sciences, Biochemistry - N 004).

The dissertation shall be defended at a public meeting of the Dissertation Defence Panel at 13:00 on the 11th of September 2020 in Room 101 of the Life Sciences Center at Vilnius University. Address: Saulėtekio ave. 7, Vilnius, Lithuania.

Tel. +37067872091; e-mail: ev.balciunas@gmail.com

The text of this dissertation can be accessed at the library of Vilnius University as well as on the web: www.vu.lt/lt/naujienos/ivykiu-kalendorius

https://doi.org/10.15388/vu.thesis.71
https://orcid.org/0000-0001-6640-9464

VILNIAUS UNIVERSITETAS

Evaldas
BALČIŪNAS

# Bioaktyvaus karkaso kūrimas audinių inžinerijai

**DAKTARO DISERTACIJA**

Gamtos mokslai,
Biochemija (N 004)

VILNIUS 2020

Disertacija rengta 2014 – 2018 metais studijuojant doktorantūroje Vilniaus universiteto Gyvybės mokslų centre. Disertacija ginama eksternu.

Mokslinius tyrimus rėmė Europos komisija per Marie Skłodowska-Curie tyrimų programą AngioMatTrain (sutarties numeris 317304), INFOBALT Lietuva, Pasaulio mokslininkų federacija, Lankasterio universitetas ir Lietuvos mokslo taryba (sutarties numeris SEN-13/2015 ir stipendijomis už akademinius pasiekimus).

Moksliniai konsultantai: **dr. Daiva Baltriukienė** (Vilniaus universitetas, gamtos mokslai, biochemija - N 004) ir **dr. John George Hardy** (Jorko universitetas, gamtos mokslai, chemija - N 003).

Gynimo taryba:
Pirmininkas – **prof. dr. Gintaras Valinčius** (Vilniaus universitetas, gamtos mokslai, biochemija - N 004).
Nariai:
**dr. Aušra Imbrasaitė** (Vilniaus universitetas, gamtos mokslai, biochemija - N 004),
**prof. dr. Rūta Navakauskienė** (Vilniaus universitetas, gamtos mokslai, biochemija - N 004),
**assoc. prof. dr. Jolita Ostrauskaitė** (Kauno technologijos universitetas, gamtos mokslai, chemija - N 003),
**prof. dr. Vytautė Starkuvienė-Erfle** (Heidelbergo universitetas, gamtos mokslai, biochemija - N 004).

Disertacija ginama viešame Gynimo tarybos posėdyje 2020 m. rugsėjo mėn. 11 d. 13 val. Vilniaus universiteto Gyvybės mokslų centro 101 auditorijoje. Adresas: Saulėtekio al. 7, Vilnius, Lietuva.

Tel. +37067872091; el. paštas: ev.balciunas@gmail.com

Disertaciją galima peržiūrėti Vilniaus universiteto bibliotekoje ir VU interneto svetainėje adresu: www.vu.lt/lt/naujienos/ivykiu-kalendorius

# TABLE OF CONTENTS

# ABBREVIATIONS

3D – 3-dimensional
AA – acrylic acid
AIP – aluminium isopropoxide
AO – acridine orange
APTES – (3-aminopropyl)triethoxysilane
AzA – azealic acid
BIS – 4,4'-bis(diethylamino)benzophenone
BM – bone marrow
BMA – buthyl methacrylate
CAD – computer-aided design
DEG – diethylene glycol
DLW – direct laser writing
DNA – deoxyribonucleic acid
EB – ethidium bromide
ECM – extracellular matrix
EDTA – ethylenediaminetetraacetic acid
EDX – energy-dispersive X-ray spectroscopy
ESCs – embryonic stem cells
FAK – focal adhesion kinase
FBS – fetal bovine serum
GMA – glicidyl methacrylate
HEMA – hydroxyethylmethacrylate
IMDM – Iscove's modified Dulbecco's medium
LED – light-emitting diode
MAA – methacrylic acid
MAPTHS – methacryloxypropyltrihydroxysilane
MAPTMS – methacryloxypropyltriethoxysilane
MSCs – mesenchymal stem cells
MTT – 3-(4,5-dimethylthiazol-2-yl)-2,5-diphenyltetrazolium bromide
NA – numerical aperture
NIH/3T3 – mouse embryo fibroblast cell line
PBS – phosphate buffered saline
PCL – polycaprolactone
PDMS – polydimethylsiloxane
PEG-DA – polyethylene glycol diacrylate
PI – photoinitiator
PI3K – phosphatidylinositol 3-kinase
PGA – polyglycolic acid
PLA – polylactic acid
PLGA – poly(lactic-co-glycolic) acid
RGD – arginine-glycine-aspartate tripeptide
RNA – ribonucleic acid
SEM – scanning electron microscopy
TE – tissue engineering
TGF-β – transforming growth factor β
UV – ultraviolet
VEGF – vascular endothelial growth factor
VOTIP – vanadium triisopropoxide oxide
VP – vinylpyrrolidone
ZPO – zirconium (IV) propoxide

# INTRODUCTION

Tissue engineering (TE) is an interdisciplinary field, where biologists, chemists, engineers and clinicians combine their expertise to solve the problems of modern day transplantation by constructing individual patient-tailored tissues and organs. This is possible due to advances in material science, 3D printing and cell biology, where biocompatible tissue-like structures are being fabricated and populated with the patient's own cells to be later used for tissue replacement.

Different types of tissues require different strategies. First, a biocompatible 3D structure has to be created that would have the right biochemical cues for cells to attach and proliferate. Multiple other aspects of TE scaffolds have to be considered, but the major challenge is in creating structures as reminiscent of native ECM as possible. To this end, various natural tissue decellularisation strategies have been considered. However, the approach is intrinsically flawed due to limitations in donor organ availability. Therefore, an alternative approach was chosen in this work – artificial material-based scaffolds with bioactive cues for cellular guidance.

For hard tissue engineering, an approach based on hybrid organometallic polymers and direct laser writing was chosen, since these technologies allow for 3D structure fabrication down to micron-level precision. In addition to fabrication possibilities, the material compositions can be tuned to ensure their biocompatibility and can potentially be further modified to include additional bioactive molecules for cellular guidance. The choice of scaffold physicochemical properties ranging from elasticity and hydrophilicity to nano-topography and chemical integrity all play a role in cellular responses and their ability to form desired tissues for subsequent medical use. Therefore, the engineering approach has to be precise and reproducible. This would be difficult to achieve using any other fabrication methods.

For soft tissue engineering, a set of approaches based on PDMS was chosen. The decision was made based on the highly desirable properties of PDMS – elasticity, strength and ease of fabrication. The material, however, is known to be hydrophobic and that would pose significant challenges in a TE setting. Therefore, PDMS-based block copolymers were chosen as a scaffolding material in this case. Such chemical constructs not only have hydrogel properties, but can be designed to biodegrade over time and be replaced by newly formed ECM. To foster cellular attachment and further proliferation processes, a biodecoration approach was used where bioactive

cues were tethered to the surfaces. Finally, bulk material mechanical properties were shown to be modifiable via reinforcement using silk. All of these technologies can be integrated together to yield scaffolds that would recreate the cellular surroundings not only from a mechanical and physicochemical standpoint, but also from a biochemical one.

The aim of this work was to identify material candidates that would be best suited for tissue engineering applications in terms of their *in vitro* biocompatibility and cellular function support and to investigate their bioactive properties.

## TASKS

1. Develop and characterise the physicochemical properties of a novel hybrid organometallic polymer containing aluminium.
2. Investigate the 3D structuring capacity of the novel material using direct laser writing.
3. Investigate the biocompatibility of different organometallic polymers *in vitro*.
4. Select the most promising material candidates for tissue engineering and investigate how they affect cellular adhesion.
5. Assess how collagen production is influenced by hybrid organometallic polymer surface chemistry.
6. Perform biocompatibility screening of several groups of novel PDMS block copolymers.
7. Investigate how biodecoration affects the surface biocompatibility of PDMS.
8. Assess how PDMS mechanical properties are affected by silk reinforcement.

## NOVELTY

When engineering artificial tissues, certain parameters of the scaffolds have to be precisely tuned in order to foster the desired cellular responses and tissue maturation. These properties differ significantly from tissue to tissue and thus, materials and techniques with certain advantages have to be chosen. The next two paragraphs describe the strategies and novelties employed in this study.

**Hard tissue**. To engineer a scaffold for hard tissue, materials and fabrication techniques have to be chosen that would allow for precise 3D niche fabrication that would induce cellular differentiation towards osteogenic or chondrogenic lineages. This is important, because the extracellular surroundings and the spatial distribution of focal adhesions play significant roles in the resulting types of tissues.

Direct laser writing is one of the most promising strategies for such applications. Using this 3D printing technique, structures can be fabricated from a multitude of different materials with micro- to nano- architectures precisely in accordance with CAD models, not to mention a range of possible physicochemical properties.

Scaffolds have to be biocompatible, support cellular adhesion and extracellular matrix protein secretion, adsorption as well as metabolite transport to and from the cells. The engineering of an artificial tissue will likely require the integration of several materials with different properties. Although currently reported materials used for direct laser writing are appealing, a study directly comparing their influences on cellular processes was needed. In addition to published formulations of hybrid materials containing V, Ti and Zr, a new polymer containing Al was developed and investigated in this study. This class of materials was chosen due to its high structuring capacity and demonstrated biocompatibility. A thorough review of the literature did not reveal any such comparisons in terms of essential cellular responses of the abovementioned materials in terms of cellular adhesion, viability, proliferation or collagen secretion. These processes are essential to evaluate if a TE strategy based on these materials is to be envisaged.

The results show that of all the tested materials, Al, Ti and Zr were the most promising in terms of their cellular adhesion, proliferation and viability support. Al was shown to induce significantly higher levels of collagen secretion as compared to Zr surfaces. V was found to be cytotoxic due to low polymer integrity and diffusion of toxic compounds. The novel Al containing polymer displayed surprisingly high quality structure fabrication capacity.

**Soft tissue**. For soft tissue engineering, materials have to be selected so that they correspond to the mechanical properties of the surrounding tissues. In addition to that, the material has to be supportive of biochemical cues that are relevant to cells.

A great material in terms of its structure fabrication, mechanical property and biocompatibility aspects is PDMS. It’s used for a variety of bio-applications ranging from microfluidics to lenses. However, it still has some

drawbacks. For example, this material is hydrophobic and prone to breakage upon surgical suturing. In addition to that, its mechanical properties are limited to a relatively narrow range. Some attempts have focused on solving these issues by creating block copolymers or composites. However, a thorough screening study had to be performed to find the best constituent combinations for block copolymer synthesis and biodecoration to support the highest levels of cellular viability and attachment. In addition to screening a range of materials and biodecoration techniques, we also investigated for the first time how the mechanical properties of PDMS change with reinforcement using silk.

Our findings include some block copolymer compositions that provide higher levels of cellular viability support as compared to pure PDMS. In addition to that, the benefits of various types of biodecoration were quantified in terms of cellular adhesion support. Finally, it was shown that reinforcement using silk can be used to attenuate the elastic modulus of PDMS.

# 1. LITERATURE OVERVIEW

## 1.1 Introduction to Tissue Engineering

A lack of donor tissues and organs that could be used for transplantation are among the greatest challenges facing modern medicine. According to the World Health Organisation, ischaemic heart disease and stroke are the leading causes of death worldwide [1]. They are followed by chronic obstructive pulmonary disease, infectious disease, dementias, cancer, diabetes and road injury. Many of these problems are associated with long-term tissue and organ dysfunction. Today, end-stage organ failure is treated by allogeneic transplantation, which is hindered by donor shortage and the need for lifelong immunosuppression for the recipient. This is by far not an optimal solution and many patients would benefit greatly from advances in tissue engineering (TE).

The field of TE was created with a report by Vacanti *et al.* in 1988 of an idea and a prototype of bioresorbable artificial polymers that could be used as cell delivery carriers for transplantation [2]. This early approach caught on quickly and was investigated by multiple other groups focused on creating technologies for a variety of tissues, like endothelial [3], hepatic [4] and osteochondral [5]. After an overview of the research state and a market analysis for tissue engineered products by Langer *et al.* in 1993 [6], tissue engineering became a widespread research area with ever increasing commercial opportunities. The process of TE is depicted in Figure 1. It starts with a biopsy from a patient, whereupon the cells are expanded *in vitro* and later seeded on 3D scaffolds that can be biodecorated with molecules that induce specific cellular functions. This kind of structure could later be implanted back to the patient, where it would replace a damaged part of the body. The field has seen immense progress lately as reviewed in multiple papers [7], [8].

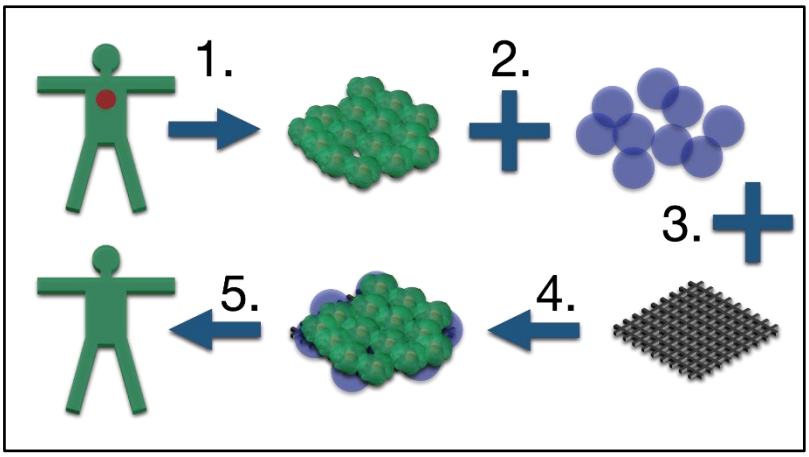


Figure 1. The principle of tissue engineering. First, cells are collected from a patient (1). They are cultured and expanded *in vitro* and subsequently seeded on 3D-printed scaffolds (3) with bioactive cues (2). The cells react to bioactive molecules in their surroundings, undergoing proliferation and differentiation towards a mature tissue (4). Finally, the construct is used to replace the damaged part of the patient's body (5).

Examples of TE progress include bladders, which are relatively simple organs in the sense that they do not require intricate vasculature and consist of only a couple of cell types. Atala *et al.* have pioneered bladder tissue engineering and successfully transplanted such artificial constructs to patients [9]. The group's approach was based on culturing urothelial and muscle cells on bladder-shaped collagen or collagen-PGA composite scaffolds.

Progress in bone tissue engineering has been extensively reviewed in the literature [10], [11]. A wide range of materials are being used as scaffolds - from biopolymers, like silk fibroin [12], chitosan [13] or alginate [14] to synthetic compounds, like polydopamine-coated PLA [15] or ceramics of calcium phosphate [16]. TE is a platform technology and this work investigates strategies for any type of soft and hard tissue engineering applications. Some examples of TE products and their applications are described more thoroughly in the next couple of paragraphs.

**Skin** is one of the largest organs in the human body. It provides protection to the internal organs, senses the surroundings and acts as a homeostasis controller. The skin is composed of several layers, each with their own function and cell types. The most important classification of these layers is (from the outermost to the innermost): epidermis, basement membrane, dermis and subcutaneous tissue or hypodermis. Damage and loss of skin is

usually attributed to various burns with many people being afflicted each year. However, there are some congenital disorders of the skin, the treatment of which could potentially save affected newborns from morbidity and in many cases, death. The progress of skin tissue engineering has been extensively reviewed in the literature [17], [18]. Some of the latest examples of this include a successful transplantation of a TE graft to a third degree burn wound. This work, performed by Ho *et al.* [19] used commercially available ActivSkin® graft patches containing allogeneic epidermal and fibroblast cells layered in a collagen matrix to coat spots of the damaged skin and showed significant healing during a 76 day follow-up. Another example by Yu *et al.* demonstrated that bioglass can be used to stimulate fibroblast sheets to produce more growth factors *in vivo* and thus, improve artificial skin graft integration with the surrounding tissue [20].

The **trachea** is a tube connecting the larynx to the bronchi. It is composed of cartilaginous tissue and its main function is to supply the lungs with air. Tracheal trauma or disease can cause significant health threats and strategies to overcome such problems by growing artificial replacement tracheas are being developed [21]. To date, several attempts have focused on employing such a strategy, but one of the most recent and exciting ones includes a scaffold-free approach, where 3D bioprinted chondrocyte and mesenchymal stem cell-based spheroids are matured in a bioreactor and then transplanted [22].

Other applications of TE include **organ-on-a-chip** and **body-on-a-chip** devices for drug screening. The idea behind organ-on-a-chip and body-on-a-chip devices is that compartments containing different cell types could be joined together using microfluidic technologies. Such artificially segregated colonies of cells could represent different tissues comprising organs or even whole human bodies and the microfluidics would ensure the transport of metabolites and signalling molecules between them – just like in a living organism. Such systems could be used to investigate the activity, efficacy and toxicity of materials, especially drugs prior to transitioning to expensive and morbidity-associated animal testing. These ideas have been reviewed thoroughly [23], [24]. For example, Esch *et al.* have developed a modular body-on-a-chip platform that could be used to imitate a variety of tissue types and tested it using the co-culture of gastrointestinal tract epithelium and 3D primary liver tissue [25]. They found that cells remain viable even after 14 days of culture and measured the rate of urea and albumin synthesis throughout the experiment, which indicated a high metabolic activity.

Another application of TE is **artificial meat** – it's the idea that edible scaffolds can be cultured with animal-derived cells *in vitro* for use as meat replacements. At this point, the idea is being actively pursued not only by research teams, but also commercial companies, like Memphis Meats® in the US. Recent progress has been reviewed by Gaydhane *et al.* [26].

The key ingredients for TE are:

1. a scaffold that provides structure and substrate for tissue development,
2. a source of cells to facilitate required tissue formation and
3. biological cues to promote integration and differentiation of cells within the scaffold [27].

## 1.2 Bioactive Scaffolds – the Structural Basis

Tissue engineering scaffolds serve as a base for further cell culture. Depending on the tissue being constructed, TE scaffolds have to correspond to the properties of native tissues in terms of their physical, chemical and biological properties. The most important physical properties include compressive and tensile moduli and nano- to micro- architecture. In terms of chemistry, the materials have to have good hydrophilicity and no toxic decomposition products. Biological requirements include controlled biodegradability, cellular adhesion motifs, induction of proliferation and differentiation towards desired cellular lineages as well as low cytotoxicity. All these aspects of TE scaffolds have been reviewed in the literature [28], [29] and are more thoroughly discussed later in this chapter.

Materials for TE applications need to conform to these requirements and be structurable by various techniques in order to yield scaffolds with desired micro- to macro- architectures. According to Billiet *et al.* [30], the main functions of scaffolds are:

1. to define the space that moulds the regenerating tissue,
2. to provide a temporary substitution for tissue functions and
3. to act as a guide for tissue ingrowth.

**Porosity and pore size**. It has been widely shown that the behaviour of cells is not only influenced by the surface chemical properties of the materials being used as scaffolds, but also by the elasticity and micro- to nano-architecture of the structures. This influences the 3D positioning of the focal adhesions and thus plays a key role in cytoskeletal organisation. This in turn

is responsible for downstream protein activation and corresponding gene expression. Another important aspect of porosity is the exchange of nutrients and waste with the surroundings. Porosity, pore size and their effects on TE constructs have been thoroughly reviewed by Loh *et al.* [21].

A study by Rnjak-Kovacina *et al.* assessed how different porosities and pore sizes of electrospun synthetic human elastin scaffolds influenced the attachment, proliferation and spreading of primary dermal fibroblasts [31]. They found that both scaffolds with porosities of around 15 % and 35 % supported cellular attachment, spreading and proliferation, but only the 35 % porosity scaffolds supported cellular migration and integration into the scaffold.

Another study by McMillan *et al.* used dermal fibroblasts to investigate how the parameters of porous poly (ε-caprolactone) films with pore sizes from 3 to 20 μm affect cellular properties [32]. They discovered that 3-5 μm pores induced the highest levels of adhesion and survival, while preventing migration into the pores.

A study by Gomes *et al.* [33] investigated how the porosity of starch-based fibre mesh scaffolds influences the proliferation and osteogenic differentiation of bone marrow stromal cells. They investigated scaffolds with 50 % and 75 % porosities and discovered that cells cultured on the 75 % porosity scaffolds had significantly higher rates of proliferation and calcium deposition, enhancing the differentiation towards osteoblastic lineage.

**Surface topography**. Pores and surface irregularities that are significantly smaller than cells all contribute to the distribution of cellular anchorage sites known as focal adhesions. Multiple studies demonstrate the link between surface topography and cellular properties. For example, Teo *et al.* demonstrated that human mesenchymal stem cells (MSCs) grown on PDMS nanogratings had elongated along the surface patterns and were more prone to neuronal differentiation as compared to flat surfaces [34]. The underlying cause was linked to patterned focal adhesion layout and increased phosphorylation of focal adhesion kinase (FAK).

Another study by Yang *et al.* demonstrated that the surface topography of hydroxyapatite could be tuned in such a way so as to promote osteogenic differentiation of human bone marrow mesenchymal stem cells [35].

**Mechanical properties**. It is equally important to choose mechanical properties that resemble those of the native tissue as closely as possible, because any mismatch can cause scarring and deformation of the surrounding structures. Strategies to overcome these issues are being created like in the

work of Varnosfederani *et al.*, where they have developed a system for mimicking the natural stress-strain behaviour of tissues in synthetic elastomers [36]. Pan *et al.* investigated how gelatin/alginate scaffold mechanical properties and swelling depend on curing conditions [37]. They found that although the porosity and swelling were not affected by the curing conditions, the pore diameter distributions of dried scaffolds were affected significantly as were water absorption rates and elastic moduli. Mechanical properties play a significant role in cellular behaviour and differentiation as well. For example, MSCs were shown to become neuron-like, myocyte-like and osteoblast-like when cultured on surfaces with 0.1, 11 and 34 kPa elasticity, respectively [38].

In another study, bone marrow mesenchymal stem cell differentiation in the presence of TGF-β was guided by changing the substrate stiffness [39]. When grown on a stiff matrix (15 kPa), the cells tended to differentiate towards a smooth muscle lineage, while on a soft matrix (1 kPa), the cells differentiated into chondrogenic and adipogenic lineages.

**Surface hydrophilicity/hydrophobicity**. *In vivo,* all cells are surrounded by an aqueous media. All extracellular matrix proteins the cells interact with are hydrophilic and so should artificial tissues be. The effects of surface contact angle on material biocompatibility have been reviewed by Menzies *et al.* [40]. They have examined the literature about the properties of TE substrates, blood-contacting devices, dental impressions and lenses (both regular and hydrogel-based). They found that highly hydrophobic surfaces were not biocompatible. However, overly hydrophilic surfaces tend to reduce the number of cell-cell interactions, which are essential for TE and are thus not desirable either.

Surface water contact angle is closely related not only to the surface chemistry, but its topographical features as well. For example, Lu *et al.* have demonstrated that micro-patterns on PDMS surfaces can significantly affect the hydrophilicity and biofouling of the surfaces [41].

**Biodegradability**. If a biodegradable scaffolding material is chosen for TE, its decomposition products should ideally be non-toxic and easy to metabolise further. The selection of biodegradable polymers has been reviewed extensively [42], [43]. A relatively recent review by Amani *et al.* [44] describes the use of 3D graphene foams as tissue engineering scaffolds. The material was shown to be biocompatible, supporting cellular attachment, proliferation and differentiation with no toxic biodegradation products. A study by Pavia *et al.* investigated polylactic acid (PLA) as a scaffolding

material for vascular grafts with one of the aspects being biodegradability [45]. They discovered that the products of biodegradation are biocompatible and that the scaffolds were suitable for TE applications.

### 1.2.1 Materials for Hard Tissue Scaffold Fabrication

The choice of materials for TE ranges from inorganic materials like hydroxyapatite for bone tissue engineering [46] to recombinant extracellular matrix proteins, for example elastin-like recombinamers [47] or various synthetic polymers [48]. It all depends on the specific needs of that particular type of scaffold being developed. To achieve this goal with maximum precision, new materials with improved mechanical, structural and biological functionalities and parameters over their predecessors are constantly being developed.

An ideal biomaterial for engineering bone-like hard tissue should be biocompatible, bioactive, and osteoconductive. Numerous natural and synthetic polymers such as calcium phosphates, calcium carbonate, and bioactive glasses have been used to fabricate scaffolds. Recent outstanding approaches are reviewed next.

**Hybrid organometallic polymers**. These are highly promising due to their versatility of applications, properties and microstructurability. These materials are composed of metal alkoxides and acrylates with silicon oxide. In most cases, the hybrid materials are rendered photosensitive by adding photoinitiators (PIs) with high two-photon absorption cross-sections – either commercially available ones, like Irgacure 2959, Irgacure 369 and Michler's ketone or custom-synthesised ones [49]–[52]. To date, organometallic polymers containing germanium [53], titanium [54], vanadium [55] and zirconium [56] have been used for direct laser writing (DLW).

Ge containing hybrids have been used to fabricate photonic structures and microoptical elements such as photonic crystals, prisms and spatial polarisation plates on either flat substrates or fibre tips [57].

Ti containing hybrids are less commonly used in DLW as compared to Zr containing hybrids. Three-dimensional photonic crystal structures have been fabricated using this material [54]. It has also been used in tissue engineering applications, demonstrating good *in vitro* biocompatibility [58]. NIH/3T3 fibroblasts were used in this study and during follow-ups after 1-7 days, the majority of seeded cells remained viable as demonstrated by acridine orange/ethidium bromide staining. It was also shown that different material

component proportions can result in different cell densities during one week of culture. In this study, cells tended to attach to the 3D microstructures and populated the laser-fabricated scaffolds.

Zr containing hybrid materials have been used in the production of various 3D structures – from microoptical elements [59], photonic crystals [60], mechanical metamaterials [61] to scaffolds for tissue engineering applications [62], [63]. 3D scaffolds fabricated out of the Zr containing material have been shown to improve the proliferative potential, clonogenic capacity and differentiation potential of human MSCs [64]. The post-fabrication shrinkage of this material can be easily tuned by changing the laser irradiation [65]. Use of the polymer poly(2-(dimethylamino)ethyl methacrylate) (poly-DMAEMA) can be used to further tune the mechanical properties of this material [66]. Out of all hybrid organometallic polymers, the Zr containing hybrid has been the most thoroughly investigated in terms of its TE applications. Psycharakis *et al.* [58] have investigated the biocompatibility of this material *in vitro*, comparing it to another, Ti containing hybrid material in terms of NIH/3T3 fibroblast viability and proliferation. They found that cells readily proliferate and integrate into such scaffolds. These results inspired further research into the material *in vivo*, where small pieces of the polymers were subcutaneously implanted into laboratory rats. After 3 weeks, histological examinations of the surrounding tissues were performed and revealed the *in vivo* biocompatibility of the Zr containing hybrid material to be comparable to that of surgical sutures [63].

V containing hybrids are interesting materials in the sense that they do not require a photoinitiator to be polymerised. Pentavalent vanadium in VOTIP (vanadium triisopropoxide oxide) absorbs light and generates radicals, which induces a polymerisation reaction, and following the reaction, vanadium is reduced to a tetravalent form. Photonic crystal structures have been fabricated out of this material [55]. To date, this material has not been used in TE applications. It could be assumed that the V containing hybrid material would be more biocompatible than its counterparts containing Ti or Zr, since it does not include toxic photoinitiators. On the other hand, vanadium and its compounds are known to be toxic [67]. Part of this work was aimed at investigating the *in vitro* cytotoxicity of the V containing hybrid material.

**Polymeric acids**. Polylactic acid (PLA), polyglycolic acid (PGA) and poly(lactic-co-glycolic) acid (PLGA) are synthetic biodegradable polymers, widely used in TE and drug delivery systems. These materials are highly biocompatible and easy to structure using 3D printing techniques.

For example, Meng *et al.* have integrated PLGA together with gelatin to construct nanofibrous scaffolds using electrospinning [68]. The resulting high porosity scaffolds allowed for osteoblasts to attach along the direction of electrospun fibres and demonstrated good *in vitro* biocompatibility. PLGA has even been approved for use in humans by the US Food and Drug Administration [69].

**Hydroxyapatites**. These are a class of bone-like materials composed of calcium phosphate. These materials have been extensively used in bone tissue engineering. Hydroxyapatites are known to integrate well into bone and to its surrounding tissues like skin, muscle and gums [70]. Kim *et al.* have conducted a study on PLGA scaffolds doped with hydroxyapatite [71] via gas foaming and particulate leaching. Upon culturing osteoblasts on these surfaces, the team discovered that the hydroxyapatite-exposed surfaces stimulated cellular proliferation and osteogenic differentiation.

### 1.2.2 Materials for Soft Tissue Scaffold Fabrication

Soft tissues have a range of properties and functions in the body. A scaffolding material used for soft TE has to correspond to the mechanical properties of the surrounding tissues ideally, since a stiffer material would start damaging the surrounding tissue, resulting in scarring. Additional requirements include good metabolite permeability and hydrogel-like properties. Some potential materials for soft TE are reviewed next.

**Polydimethylsiloxane** (PDMS) is a highly promising material for soft tissue engineering applications because of its elasticity, good gas ($CO_2$ and $O_2$) and small molecule permeability as well as durability. PDMS is a clear, rubber-like material that is widely used as a lithographic mask in PDMS soft lithography or microfluidics [72]. However, PDMS has some intrinsic drawbacks, like hydrophobicity. Although this makes applications of PDMS, like oil spill collection possible [73], it is not great for cell adhesion, because cells prefer hydrophilic environments. Siddique *et al.* have demonstrated that under shear flow conditions, the adhesion of cells to PDMS is short-lived and could be significantly improved by grafting collagen to the surface of PDMS via APTES [74] - this was demonstrated under varying shear flow conditions after 24 and 48 hours. This can be attributed to a high surface contact angle and this aspect can be further altered by using chemical immersion or oxygen plasma treatment [75].

PDMS also has a high thermal stability with very low deformation due to temperature fluctuations - a property that can be exploited for structure fabrication. Another useful attribute of PDMS is its light permeability down to 300 nm, enabling light to be used as a source of power for polymerisation. PDMS is isotropic and homogenous, easily copolymerisable with other chemical moieties (for example, poly(ε-caprolactone) [76]) to yield block copolymers with new and exciting properties.

Apart from a high water contact angle, its other limitations include relatively poor surgical suture support and a lack of biodegradability.

**Silk**. Structurally, silks are a class of proteinaceous materials produced by a variety of species for task-specific applications. The domesticated silk worm *Bombyx mori* produces fibres for coccoons (to protect it during its transformation from a silkworm to a moth) and these fibres are biphasic, composed of a 2 fibre core coated by a layer of sericin. Naturally spun silk fibroin fibres are water-insoluble due to their beta sheet contents (formed by repeating units of $(Gly\text{-}Ser\text{-}Gly\text{-}Ala\text{-}Gly\text{-}Ala)_n$) that act as crosslinkers within the fibres [77]. Large quantities of silk from *Bombyx mori* silkworms are produced across the world for the textiles industry, and there is increasing interest in silks produced by spiders (e.g. *Nephila clavipes*) and other species owing to their interesting mechanical properties and that they can in principle be processed into a range of biomaterial forms using various techniques. Interestingly, the natural fibroins produced by wild *Antheraea pernyi* silkworms contains the cell adhesive RGD motif in its backbone [78], and this motif can be engineered into recombinant silks and have even been produced in *Escherichia coli* [79]. Silk is also being widely investigated as a material for drug delivery systems or as a coating material for stents [80].

**Hyaluronic acid** is a naturally occurring glycosamynoglycan, found abundantly in the human body. It's a highly versatile material, the physical properties and degradation rate of which can be tuned by changing its molecular weight, crosslinking density or mixing it with other polymers. Hyaluronic acid is naturally degraded by hyaluronidase, but its degradability rate can be attenuated by grafting amino acids to its backbone [81].

**Elastin-like recombinamers** are a class of synthetic biopolymers that contain elastin-like features. This class of materials is obtained by means of genetically engineering and culturing microorganisms. Putzu *et al.* have employed this technique to create elastin-like recombinamers containing cellular adhesion sequences (REDV and RGD) [82]. They used this material to create scaffolds using electrospinning and subsequently demonstrated the

biocompatibility and adhesion support of such constructs using human umbilical vein endothelial cells.

### 1.2.3 Biodecoration of Scaffold Surfaces

Biodecoration is the process of adding bioactive cues to the bulk or the surface of polymer scaffolds in order to imbue them with extra functionality. Extracellular matrix (ECM) proteins, growth factors, carbohydrates and other bioactive molecules can be either covalently linked or non-covalently bound to the scaffold structures.

**Collagen** is one of the most abundant proteins in the body, responsible for around a third of the entire protein content. It is one of the most important structural components of the ECM in both soft and hard tissues, providing not only mechanical strength, but also anchorage sites for cells, like the RGD tripeptide sequences. Structurally, collagen is formed from three intertwining helices. To date, 28 different types of collagen have been discovered, with types I, II, III and V being the most abundant in human tissues, both soft and hard [83]. Collagen can be used to coat various biomedical devices and TE constructs, thus improving their biocompatibility and rate of integration with the surrounding tissues. For example, Ma *et al.* have constructed PLA scaffolds and covalently grafted collagen to their surfaces and basic fibroblast growth factor (bFGF). This resulted in significantly better chondrocyte spreading and growth [84].

Another study by Lee *et al.* investigated how type I collagen coating affects cellular adhesion onto microporous biphasic calcium phosphate scaffolds and found the coating to not only improve surface wettability, but also to improve osteoblast interaction with the surfaces via integrins, resulting in higher spreading, proliferation and differentiation [85].

Almeida *et al.* [86] studied how shape-memory alginate scaffolds can be functionalised with either type I or type II collagen for cartilage tissue engineering and found that biodecoration with collagen improved stem cell recruitment into the scaffold as well as facilitated a more consistent cartilage tissue deposition. Type II collagen incorporation led to a higher cellular proliferation of adult human stem cells with higher tissue-specific molecule deposition and better mechanical properties of the resulting tissue graft.

**RGD tripeptide** is an adhesion motif, found in many ECM proteins. It can be added to scaffold surfaces in order to promote integrin-mediated cell

adhesion. Burdick *et al.* found that binding RGD peptides to PEG hydrogels improved osteoblast attachment and number as well as spreading area [87].

Zisch *et al.* have constructed synthetic PEG-based hydrogel matrices, covalently modified with RGD, matrix metalloproteinase substrate peptides and VEGF [88]. Such constructs not only improved endothelial cell survival and migration within the structures *in vitro*, but were also completely biodegraded and remodelled into native tissue with vascularisation.

**Carbohydrates**. Another interesting way to coat TE scaffolds is using carbohydrates. Their abundance within tissues makes them a safe choice for not only providing a more hydrophilic surrounding for the cells, but also in improving specific adhesion. Progress in polysaccharide-based nanocomposite development and use as biomaterials has been reviewed by Zheng *et al.* [89]. Examples of carbohydrate application in TE include the work by Russo *et al.*, who have demonstrated that by covalently glycosylating hydroxyapatite, an improved surface to lectin interaction can be achieved [90].

A study by Zhou *et al.* [91] demonstrated that it is possible to incorporate cellulose nanocrystals into maleic anhydride grafted PLA, resulting in improved mechanical properties of the scaffolds as well as a slower biodegradation rate *in vitro*. This type of scaffolds showed good biocompatibility with human adipose-derived stem cells *in vitro*.

### 1.2.4 Scaffold Fabrication Techniques

Scaffolds for tissue engineering can be fabricated using a variety of techniques and the choice depends on the tissue being constructed, required structure size and precision as well as the material of choice. This section reviews the most promising fabrication techniques employed in the field of TE.

**Allogeneic tissue decellularisation** is an attractive strategy for tissue engineering as it does not require the complexity of the ECM to be constructed *de novo* - most ECM components remain intact after decellularisation. For this reason, some TE strategies based on decellularised tissues as scaffolds are currently in preclinical trials [92], [93]. Tissue decellularisation is usually a combination of physical, chemical and enzymatic techniques. Physical methods include pressure, stretching, ultrasound and cycles of freezing and drying. Chemical methods include using detergents, solutions of salt, acids or bases in order to lyse the cells and remove them from the ECM [30]. Enzymatic methods include the use of trypsin, endonucleases, exonucleases

and other enzymes which degrade cellular macromolecules [94]. The choice of decellularisation technique influences the composition of the resulting ECM structure and remaining components. When decellularising xenogeneic tissues, most of the antigens present in that tissue are removed as well. ECM proteins are highly conservative among species and do not invoke an immune response upon transplantation [95].

Most of mammalian tissues have been successfully decellularised for use as TE scaffolds: heart valves [96], blood vessels [97], skin [98], neural tissue [99], skeletal muscle [100], tendons [101], ligaments [102], small intestine [103], urinary bladders [104] and liver [105].

Nevertheless, decellularized tissues and organs used as scaffolds have multiple drawbacks that limit their use on a large scale. These have been mentioned in multiple reviews concerning the pros and cons of using decellularized tissue matrices for tissue engineering [106]. Even though the probability of an immune response is low, a major setback in using artificial tissue scaffolds is donor organ shortage and the time it takes for full decellularisation and recellularization of such scaffolds. Poor mechanical strength is often mentioned as a significant disadvantage of recellularised tissues as well [107].

**Direct laser writing** (DLW) is a 3D printing technique based on multiphoton absorption with unprecedented precision and reproducibility. The technique opens possibilities to tailor scaffolds for tissue engineering [108], photonics elements [109], microfluidics [110] and other structures directly from CAD software. It differs from stereolithography in the sense that instead of single photon absorption, a UV-sensitive material is illuminated by visible light that is two or three times the wavelength of the material absorption peak. Due to a high spatial and temporal concentration of photons, a photosensitive material absorbs the lower energy photons as if they were a single higher energy (UV) photon.

Most often, high repetition rate (kHz to MHz), ultra-short pulsed lasers (fs to ns) are used for this purpose. The laser beam is guided through an objective lens to a drop of a photosensitive material. Polymerisation takes place only in the focal point of the laser beam because multiphoton absorption requires a certain threshold concentration of photons to take place. Upon illumination, photosensitive molecules present in the material absorb light becoming radicals. These radicals join molecules with double bonds or other moieties prone to polymerisation. This process becomes a chain reaction until two radicals join and terminate the reaction. In order to increase the spatial

resolution of the resulting structures, the chain reaction could be attenuated by introducing polymerisation inhibitors to the material.

By moving the sample relatively to the focal point, a 3D structure is polymerised. Unexposed parts of the material are washed out using a solvent and the free-standing structure is revealed. DLW systems are commercially available by companies like Nanoscribe® in Germany and Femtika® in Lithuania. Resolutions down to 100 nm are achievable using this technique and a great variety of materials can be used. However, the approach is relatively expensive and is limited to cm- scale object fabrication. A schematic illustration of the DLW fabrication process is given in Figure 2.

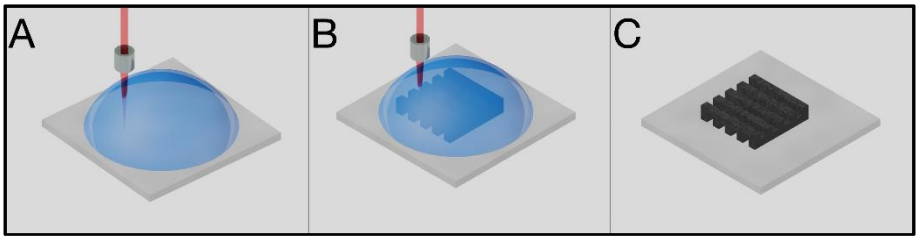


Figure 2. A – a femtosecond laser beam is focused in the material and scanned in 3D according to a CAD file. B – once the fabrication process is complete, a 3D structure surrounded by uncrosslinked monomers is acquired. The sample is then immersed in a solvent to wash out unexposed parts of the material. D – a free-standing 3D structure according to the CAD model.

**Fused deposition modelling** is a 3D printing technique that works by melting a polymer thread and extruding it through a nozzle, where upon extrusion, the polymer is solidified due to lower temperature at the nozzle tip. By moving the nozzle in 3D, a CAD model is materialised. Such systems are fully automated. A variety of commercially available 3D printers are available based on this technique and the market for such devices is rapidly growing. Ultimaker®, MakerBot®, Monoprice®, Airwolf 3D® are just several examples of companies that manufacture such printers. One of the more outstanding projects – RepRap is based on the idea that an open source 3D printer could be used to print most of the parts required to make an identical copy of the machine. Most of these 3D printers are limited in the choice of material – PLA, acrylonitrile butadiene styrene (ABS) or chlorinated polyethylene (CPE). The resolution of such devices is low, usually around 50 μm.

**Soft lithography** is a 2D structure replication technique. A surface pattern fabricated using techniques, like DLW or electron beam lithography is coated

by a thermo-sensitive elastomer PDMS. It is then heated, whereupon a thermo-initiated polymerisation takes place and PDMS solidifies. The resulting mask is peeled off of the original pattern and used to make replicas in photosensitive materials, like PEG-DA or OrmoComp [111]. Upon coating with a thin layer of gold, the PDMS masks can be used to make replicas in PDMS itself. The process is depicted in Figure 3. This technique allows features down to 50 nm to be reproduced. A single PDMS mask can be used multiple times [112].

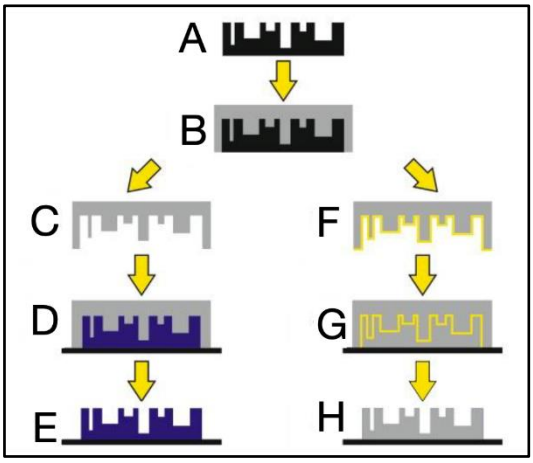


Figure 3. Polymer scaffold replication using PDMS soft lithography. A – the primary structure to be replicated. B – a PDMS mask of A is made by pouring and degassing PDMS, then subsequently heating the sample at 100 °C for 1 hour. C – the PDMS mask of A is peeled off. D – the mask can be used for replica moulding in another material by UV crosslinking. E – a copy of the primary structure. F – the mask, obtained in step B, can be covered by a thin layer of gold. G – the gold-coated mask can be used for replica moulding in PDMS, obtained by heating to 100 °C for 1 hour. H – a copy of the primary structure A in PDMS.

**Stereolithography** is a 3D printing method based on the polymerisation of a photosensitive material using UV light. A liquid or gel-like material is deposited layer-by-layer and each layer is illuminated by UV through a photolithographic mask or by laser scanning. The process is fully software-automated and 3D CAD models are used as input sources. Compared to other 3D printing techniques like fused deposition modelling, stereolithography provides a wider range of materials that can be structured as well as a better spatial resolution. Stereolithographic printers are generally more expensive than fused deposition ones. Formlabs®, Autodesk® and Materialise® are some examples of companies that manufacture such printers.

**Electrospinning** is a simple technique that extrudes a charged polymer nanowire towards a grounded collector (either a flat surface or a spinning

mandrel). The technique is highly versatile, due to the wide selection of processable materials and tuneable parameters as reviewed by Pham *et al.* [113]. Although the thickness of the polymer nanowires and the resulting structure porosity can be finely tuned, the technique is somewhat limited in structure production – the nano- and micro- architecture is difficult to tailor in 3D (although it is possible to make aligned fibres using a rotating sample collector).

**Freeze-drying** is based on sublimation. A porous water containing structure is frozen and then placed in a chamber that is kept below melting temperature with low pressure or vacuum. Alternatively, water can be replaced by liquid $CO_2$ under high pressure and low temperature and then depressurised to evaporate the liquid $CO_2$. This technique is particularly promising when working with biopolymer samples. For example, Tangsadthakun *et al.* have fabricated and investigated collagen or chitosan scaffolds fabricated using this technique, demonstrating a positive *in vitro* cell culture response [114]. However, as was the case with electrospinning, structures fabricated using this technique have chaotic micro- morphologies.

**Gas Foaming** is another TE scaffold fabrication technique, where gas-producing substances are used as porogens – mixed within a scaffolding material and then released to yield porous structures. Structures resulting from gas foaming are chaotic, but their parameters can be tuned to yield varying degrees of porosity, pore size and pore interconnectivity. A great application of this technique was demonstrated by Poursamar *et al.* [115], where microporous gelatin scaffolds were fabricated for skin TE applications.

**Phase inversion and phase separation** are yet another approach to scaffold formation. Here, a polymer dissolved in a solvent is poured into a desired shape and then placed in a nonsolvent, which is miscible with the solvent and thus, replaces it. The presence of the nonsolvent causes the polymer to crosslink, resulting in a porous structure. Ma and McHugh have used this approach to create membrane-based drug delivery systems based on cellulose acetate [116].

**Porogen or particulate leaching** is another way of producing porous materials. This approach is based on an analogous principle to that of gas foaming, but instead of gas, particles are used as porogens. For example, Liang *et al.* have used quasi-spherical salt particles as porogens to create PLGA scaffolds that support osteogenic lineage differentiation of mesenchymal stem cells (MSCs) [117].

**Self-assembly** is a technique where specific building block-like macromolecules such as peptides or proteins, crosslink in a predictable and chemically predefined way to form supramolecular structures. This approach was reviewed by Loo *et al.* [118]. An example of self-assembled structures used for TE applications was described by Nagahama *et al.* [119], where cholesterol-substituted PEG-PLA copolymers were investigated as potentially injectable scaffolds. An *in vitro* investigation showed that the self-assembled structures had favourable micron-scale porosities for cell integration and that L929 fibroblasts used as a model system tended to infiltrate into the 3D hydrogel-like material pores and proliferate well.

**Thermally-induced phase separation** is a technique widely used for the production of microporous membranes. Here, a polymer is dissolved in a solvent at an elevated temperature to keep the mixture homogenous. Then, the temperature is gradually reduced to achieve phase separation. This is possible due to the fact that solvent efficiency decreases with decreasing temperature. The polymer-solvent mixture separates to yield a polymer-rich and a polymer-lean phase. After rinsing out the solvent, a microporous structure is obtained [120].

## 1.3 Cells in Tissue Engineering

The interaction between scaffold materials and cells must promote cellular adhesion and maturation towards a desired tissue type. The cells should be able to migrate from the implanted tissue construct and integrate with the surrounding tissues as should the cells surrounding the implanted scaffold be able to integrate with the new structure. A variety of cell types can be used in TE and in a clinical setting, their choice should depend on the number of required cells, time available for tissue construction and most importantly, tissue type and complexity. Every tissue in the human body is composed of several types of specialised and support cells, a network of blood vessels, ECM and other components. In order to create a natural tissue substitute *in vitro*, as many of these components have to be reconstructed as possible.

One of the most important criteria in choosing a cell source is its immunocompatibility with patient tissues, the ease of harvesting and cultivation of cells under *in vitro* conditions, and their sensitivity to biochemical and biomechanical cues. One of the most promising sources of cells which meet these criteria are autologous stem cells, harvested from adult organisms. Their advantages include a relatively high proliferation rate,

differentiation capacity towards several lineages and a lower probability of tumour formation as compared to embryonic stem cells. In addition, when using autologous cells, the probability of an immune response is minimised, so immunosuppression after transplantation is not required. The risk of infections, cancer and other complications, associated with immunosuppression, is also reduced in such case.

A very important property of non-terminally differentiated cells is their ability to renew. After tissue damage or its component cell death, primary cells not only rebuild the damaged part by differentiating, but also divide, thus replenishing the number of primary cells used up for differentiation. To explain this process, two mechanisms have been proposed - cells either divide asymmetrically, giving rise to one differentiated and one stem cell, or symmetrically, when some cells differentiate towards a tissue lineage and others divide to form more undifferentiated cells.

Examples of autologous cell therapy already in the clinic include skin transplants [121], autologous stem cell therapy for peripheral artery disease [122], blood vessel grafting in obstructive coronary disease [123] and bone marrow transplantation in acute conditions, like multiple myeoloma [124], or chronic conditions, like chronic myocardial infarction [125], osteoarthritis [126] and multiple sclerosis [127]. Unfortunately, some organs, like pancreas, heart or lungs are difficult to extract cells from due to high donor site morbidity.

### 1.3.1 Cell Sources

This section describes the types of cells that can be used for TE applications and discuss their properties, advantages and disadvantages.

**Embryonic stem cells (ESCs)** are multipotent cells, capable of maturation into all three germ layer tissues. These cells are extracted from fertilised egg cells or early blastocyst inner cell mass *in vitro*. A characteristic of ESCs is their unlimited proliferative potential, they do not possess any epigenetic modifications. The main drawbacks to using this cell source are ethical concerns and the possibility of teratoma formation [128], [129]. ESC markers have been reviewed in the literature [130] and include stage-specific embryonic antigen molecules (SSEA-1, -3 and -4), which are associated with carbohydrates, CD324 (E-cadherin), CD90 (Thy-1), CD117 (c-KIT, SCFR), CD326, CD9 (MRP1, TM4SF, DRAP-27, p24), CD29 (β1 integrin), CD24 (HAS), CD59 (Protectin), CD133, CD31 (PECAM), CD49f (Integrin α

6/CD29), TRA-1-60, TRA-1-81, Frizzled5, Stem cell factor (SCF or c-Kit ligand) and Cripto (TDGF-1).

**Foetal stem cells** are highly proliferative and capable of multi-lineage differentiation. Reports have shown the applications of such cells for neuronal [131] and bone [132] tissue construction. However, this cell source, as well as ESCs, is ethically and legally debated.

**Amniotic fluid stem cells** are already widely used in many pre-clinical TE trials – urology [133], bone reconstruction [134], [135], airways [136], attempts are being made to go into clinical trials [137]. Judging from the multipotency of these cells, it is possible that with improving isolation and expansion techniques, the rates of amniotic fluid stem cell use in regenerative medicine will increase in the coming years. Common markers for these cells have been reviewed in the literature [138] and include CD117 (c-Kit), CD29, CD44, CD73, CD90, CD105 and SSEA-4. They have been shown to be negative for CD34, CD45 and CD133.

**Induced pluripotent stem cells (iPSCs)** do not have the issues associated with ESCs – an allogeneic source is not needed, so their use is not hindered by ethical or legal concerns. In several instances, patient-specific iPSCs have already been obtained [139]. iPSCs can be expanded to large numbers *in vitro*, which is important if a large-scale TE product is to be constructed. iPSCs can be differentiated into various types of tissues *in vitro*, used for creating chimeric animals or transplanted into damaged tissues with the aim of reconstructing them. The major cons to iPSC use are epigenetic DNA modifications which can change their responses to extracellular factors [140] as well as probability of teratoma formation and formation of mutations during reprogramming [141].

**Adult stem cells** can be extracted from any tissue after birth (including bone marrow, blood and the umbilical cord). They differ from ESCs in their proliferation and differentiation potentials. For purposes of regenerative medicine, these cells are usually extracted during a biopsy of bone marrow (BM) [142], peripheral blood [143], liver [144], skeletal muscle [145], heart [146] or fat tissue [147].

**Umbilical cord blood stem cells** were introduced as an alternative to BM stem cells. Although they are more difficult to extract than BM cells and are present in lower numbers, their potential in TE applications is great. Umbilical cord cells are capable of differentiating towards chondrogenic, osteogenic, adipogenic, myogenic, neuronal, pancreatic and hepatic lineages [148]. They

are basically mesenchymal stem cells, but deserve a separate mention due to their widespread use.

For example, Schmidt *et al.* have used umbilical cord blood derived endothelial progenitor cells to create an artificial blood vessel based on a PGA scaffold [149]. They found that the cells tended to attach and exhibit an endothelial phenotype, including specific endothelial markers, like CD31 and von Willebradt factor.

Another study by Gang *et al.* investigated the possibility of umbilical cord blood cell differentiation towards myogenic lineage and found that such an approach is promising for muscle regeneration and tissue engineering applications [150].

**Mesencymal stem cells** are multipotent cells, capable of differentiating towards multiple lineages – osteogenic, chondrogenic, myogenic and adipogenic. They can be isolated from aforementioned tissues as well as bone marrow in relatively high quantitates and have good proliferative capacity *in vitro*. Multiple studies have used this cell source for tissue engineering approaches.

For example, Wen *et al.* investigated three potential MSCs sources in terms of their potential for bone tissue engineering – bone marrow stromal cells, human adipose tissue-derived mesenchymal stem cells and umbilical cord-derived mesenchymal stem cells [151]. They found that the umbilical cord-derived and adipose-derived stem cells were the most suitable for bone tissue engineering even though the highest activity of alkaline phosphatase was observed in bone marrow stromal cells. This was because the umbilical cord and adipose-derived cells showed higher levels of osteopontin and collagen type I expression.

Another study by Chang *et al.* demonstrated that synovium-derived MSCs can be successfully used for engineering of cartilage [152], when the cells were cultured on acellular cartilage matrix powder scaffolds.

**Fibroblasts** are connective tissue cells, found in many different types of tissues. These cells have a mesenchymal origin and have a characteristic spindle-shape *in vitro*. They are surface-adherent and their growth is contact-inhibited. Fibroblast cell lines, like the mouse embryo 3T3 line from the National Institutes of Health are a gold standard when assessing the cytocompatibility of various substances *in vitro*. For instance, Vaz *et al.* used a coculture of NIH/3T3 fibroblasts to test the biocompatibility of electro-spun PLA/PCL-based scaffolds for vascular tissue engineering [153]. They found that the investigated scaffolds were suitable for cellular attachment and

proliferation. Although fibroblasts are considered to be terminally differentiated cells and used mostly for biocompatibility studies, they can still be used for TE applications – for example, Tang et. al. compared fetal and adult fibroblasts in terms of their abilities to induce tendon tissue regeneration and general applicability in tendon tissue engineering [154]. They found that using a scaffold-free TE approach, fetal fibroblasts had more potential for tendon repair as demonstrated by a higher level of tendon-related gene expression. Fetal fibroblasts also tended to recruit fibroblast-like cells from the surrounding tissues and reduce the infiltration of inflammatory cells to the site of injury.

In addition to their potential as TE components, fibroblasts have the capacity to change towards an osteogenic-like phenotype upon treatment with dexamethasone and 1,25-dihydroxyvitamin d3 [155]. Fibroblasts can also be transdifferentiated towards multiple other types of cells using specific transcription and growth factors – for example, cardiomyocytes [156], skeletal muscle [157] and endothelial cells [158].

### 1.3.2 Cellular Processes and Regulation

Each cell is composed of hundreds of thousands of different components – phospholipids, proteins, carbohydrates, nucleic acids and metabolites, all of which interact in highly coordinated processes, some of which are described in this section and are essential to consider when designing artificial tissues.

**Integrin-mediated cell adhesion**. Cellular adhesion is a process in which a cell attaches to and interacts with its environment. Adhesion can be mediated by a variety of transmembrane receptors – some of which are responsible for interactions with ECM proteins, while others – with neighbouring cells. Integrin-mediated cell adhesion is responsible for linking ECM proteins like collagen, fibronectin, laminin and vitronectin to the cytoskeleton [12].

Integrin-mediated cell adhesion starts when the extracellular parts of integrin receptors recognise specific ECM binding sites, then dimerise and autophosphorylate on the intracellular parts and this changes their affinity for an array of different intracellular proteins that together form focal adhesions – structures that are responsible for linking the ECM to the cytoskeleton. One of the central proteins in this process is focal adhesion kinase (FAK), which activates phosphatidylinositol 3-kinase (PI3K). Its downstream effector is Akt – a signalling molecule, whose activation results in cellular survival under

stressful conditions, proliferation, differentiation and cell cycle activation [159], [160]. A simple schematic of the process is given in Figure 4.

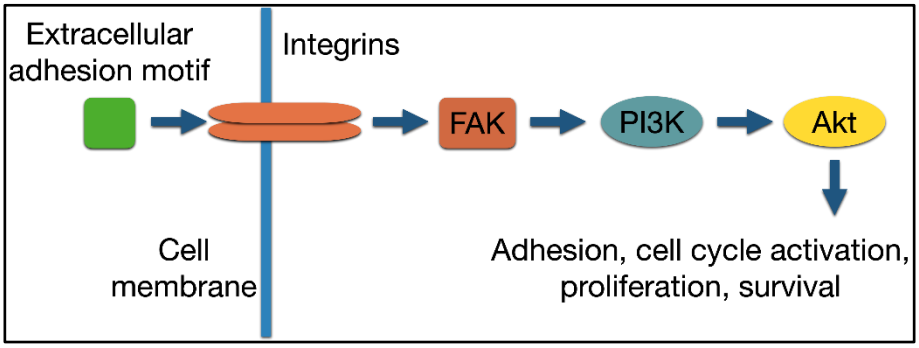


Figure 4. Integrin-mediated cell adhesion. An extracellular adhesion ligand is bound by integrins, which dimerise, autophosphorylate and then activate FAK. This in turn phosphorylates PI3K, which leads to the activation of Akt and subsequently – cellular survival, proliferation, differentiation and cell cycle activation.

FAK (also referred to as PTK2) is a 125 kDa protein that is one of the main players in cellular adhesion. It was shown that by blocking FAK, it was possible to reduce metastasis in cancer by impeding cellular migration [161].

PI3K is a family of kinases that is responsible for the phosphorylation of membrane-bound molecules phosphatidylinositol (3,4)-bisphosphates and phosphatidylinositol (3,4,5)-triphosphates. PI3K is also responsible for activating Akt.

The real process of cell adhesion is much more complex with each of the molecules that take part in this pathway also being responsible for the effects on multiple other molecules and pathways. For example, the PI3K/Akt pathway also takes part in the process of glucose homeostasis [162].

Focal adhesions are highly complex structures, comprising over 50 different components, like the proteins talin, α-actinin, filamin, vinculin and tensin. Their main function is linking the ECM to the cytoskeleton. However, once a focal adhesion is formed, it responds not only to the changes in ECM, but also to cell surfaces, physiological and mechanical stresses. Changes in the cellular environment sensed by focal adhesions can result in either cell growth or death, motility, reorganisation of the cytoskeleton and a change in gene expression.

**Cell proliferation** is a process, during which cells perform all their functions - digest food, synthesise various molecules, interact with their surroundings, multiply, etc. The process has been extensively reviewed in

literature [163]. A new cell that has just been produced after a division is considered to be in G1 (growth) phase. During this time, the majority of cellular proteins, RNA, membrane components and other molecules are being synthesised. At the end of G1 phase, a certain point is reached, after which, cells become independent of growth factors. After this phase comes the S phase, otherwise known as the stage of DNA synthesis. Next comes the G2 phase, during which protein and other essential cellular molecule production intensifies. After interphase (the time, when a cell continues to grow and perform its metabolic functions) starts mitosis, during which the cellular nucleus and the entire cell divide. If, for some reason, the cell cycle stops, the cells go into a quiescent (G0) phase and their proliferative activity is considered to be paused.

Different surfaces cause varying rates of proliferation, so when constructing artificial tissues, materials have to be selected so as to provide the cells with optimal sets of proliferation-modulating cues. Most often, for *in vitro* cell culture, either glass or polystyrene surfaces are used. However, their properties are greatly different from native extracellular environment, which is composed of ECM proteins (collagen, fibronectin, laminin, etc.) as well as containing growth factors and other structural and biochemical components.

Scientific literature on how different surfaces influence cellular proliferation is abundant. For example, chitosan and collagen based scaffolds for skin reconstruction have been used to culture human skin fibroblasts and were shown to support high proliferative activity. After a month-long implantation under the skin of a rat, the scaffolds were extensively infiltrated by cells from the surrounding tissues [164].

Chang *et al.* have constructed PEG-DA (polyethylene glycol diacrylate) – laponite (a commercially available silicate) nanoparticle scaffolds. Human MSCs, grown on such surfaces, exhibited stronger adhesion than pure PEG-DA, but their proliferative activity was independent of laponite nanoparticle concentration in the scaffolds [165].

**Synthesis of ECM**. During proliferation, various types of cells secrete ECM proteins - collagen, fibronectin, elastin, laminin and a selection of proteoglycans. These molecules take part in strengthening and modelling the extracellular environment, which in turn influences cellular behaviour. The role and functions of the ECM have been extensively reviewed in the literature [166]. Collagen is perhaps the most important component of the ECM, providing not only appropriate adhesion motifs, like RGD, but also constituting almost 25 % of the total dry weight of a human body. Multiple

reviews and books have focused on the process of collagen biosynthesis and secretion [167]–[169].

The process starts with the transcription of collagen-encoding genes in the nucleus. The mRNA is then transported outside of the nucleus where it is translated to prepro-α-chain containing a signal peptide at the end. The signal peptide is used to transport the prepro-α-chain to the rough endoplasmic reticulum, where the signal peptide is cleaved off and the prepro-α-chain is hydroxylated and glycosylated. The resulting pro-collagen is transported outside of the rough endoplasmic reticulum to the cytoplasm, where collagen sequences bind together via disulfide bonds and are then cleaved via peptidase to yield tripeptide fragments that are joined together by lysyloxidase. The process is depicted in Figure 5.

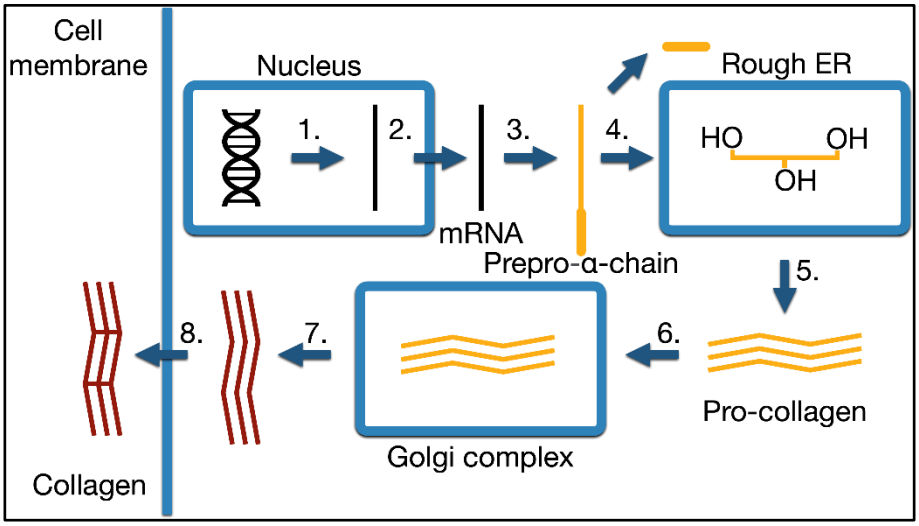


Figure 5. Secretion of collagen. The process starts with the transcription of collagen-encoding genes to mRNA (1) and its transport outside of the nucleus (2). Next, mRNA is translated to prepro-α-chain with a signal peptide (3). The signal peptide is then cleaved prior to translocation of the prepro-α-chain to the rough endoplasmic reticulum (4). In the rough ER, the chain is hydroxylated and returned to the cytoplasm, where triplicates form pro-collagen (5). The pro-collagen is transported to the Golgi complex, where glycosylation takes place (6). Afterwards, the glycosylated tri-helix is transported out of the cell (7, 8), where peptide tri-helixes are connected together by lysyloxidase enzyme (8) to yield the final form of collagen.

### 1.3.3 Cell Death

Cell death is an essential process in tissue development and homeostasis. Faults in controlled cell death result in various diseases, such as neurodegeneration, developmental disorders and cancers. There are many different ways in which cells can die, but the most notable ones are apoptosis and necrosis that are reviewed in this chapter. Other types of cell death include but are not limited to the ones described in the next couple of paragraphs. All these processes differ in their controllability, molecules and signalling pathways involved and resulting structures as well as their effects on the surrounding cells and tissues.

During **necroptosis,** a cell dies in a controlled, but caspase-independent way. It is especially known as a viral defence mechanism that still works in the presence of caspase inhibitors [170].

**Ferroptosis** is another type of programmed cell death that involves iron and the accumulation of lipid peroxides [171].

**Pyroptosis** is a type of cell death that is associated with caspase-1 activity. During pyroptosis, an immune response is triggered via release of cytokines [172].

**Parthanatos** is associated with the accumulation of poly(ADP-ribose), which causes apoptosis-inducing factor to be translocated to the nucleus and thus induce fragmentation of DNA and cell death [173].

**Autophagy** is a form of partial cellular recycling [174], where intracellular components are being collected into vesicles that merge with lysosomes, whereupon the vesicle components are being digested and released back into the cytosol. However, this is not a proper type of cell death, since partial autophagy can take place as well, without destroying the cell.

**Apoptosis** is a controlled process in which a cell that is no longer functioning properly or has received a death signal, undergoes compartmentalisation and lyses its internal structures. There are two types of apoptosis activation pathways - intrinsic and extrinsic. One of the characteristics specific to this type of cell death is the activation of caspases - a class of proteases that mediate the entire process from initiation to execution. Apoptosis consists of three main steps: initiation, execution and phagocytosis. The entire process is nicely reviewed in [175].

Caspases are present in the cytoplasm in the form of zymogens. Upon activation by either extrinsic or intrinsic signalling, the zymogens are cleaved to yield active forms of caspase enzymes. The main caspases, taking part in

the initiation of apoptosis are caspase-8 and 9, while effector caspases are denoted 3 and 7. These proteins digest cellular components, including cytoskeletal and nuclear proteins. In addition, caspases activate DNAses, which digest DNA. During apoptosis, phosphatidylserine, which is translocated to the outside of the cell, takes part in signalling macrophages to engulf and destroy them. During apoptosis, the cells tend to shrink and split into smaller vesicles that are easier for macrophages to destroy.

Stage 1. Initiation. The intrinsic apoptosis pathway is initiated in most cases by irreparable damage to the DNA. This activates the protein ATM, which in turn activates the tumour suppression protein p53. p53, among other proteins, activates BAX, which in its active form acts to make pores in the membranes of mitochondria. Following this, mitochondrial intermembrane components, like $Ca^{2+}$ and cytochrome C start leaking out into the cytosol. In the cytosol, cytochrome C binds to APAF, thus integrating with the inactive form of procaspase-9. During his process, a part of the pro-caspase zymogen is removed and caspase-9 becomes active, which then goes on to activate additional caspases and destroy cellular proteins. This chain reaction of more caspase activation is referred to as the caspase cascade. The process is depicted in Figure 6.

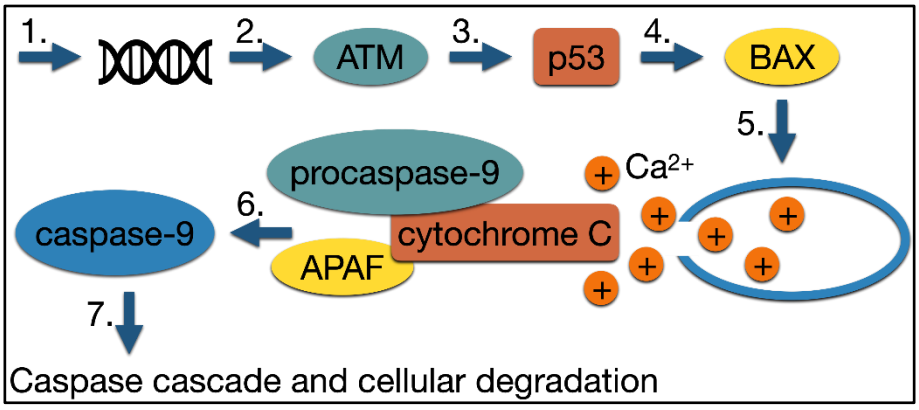


Figure 6. The process of apoptosis initiation via the intrinsic pathway. After irreparable DNA damage (1), ATM protein is activated (2), which in turn activates p53 kinase (3). p53 activates BAX (4), which acts to create pores in mitochondrial membranes (5). This leads to the release of $Ca^{2+}$ ions and cytochrome C to the cytoplasm. APAF joins cytochrome C and procaspase-9 (6), which results in active caspase-9 formation. It starts a chain reaction of caspase production, referred to as a caspase cascade after which the caspases begin cellular component degradation (7).

The extrinsic pathway starts upon the activation of transmembrane receptors, like (TNFR), upon binding TNFα. Then, the intracellular domain of TNFR, referred to as the death domain, is activated as well. As a result, various cytosolic proteins bind to the death domain and become activated as well. One of the first proteins to do this is TRADD (TNF receptor-associated protein with death domain). Next, FADD (Fas-associated protein with death domain) binds to the conglomerate and activates procaspase-8, which autocatalyses its cleavage to an active caspase-8, which then goes on to activate the caspase cascade and digest cellular components. The process is illustrated in Figure 7.

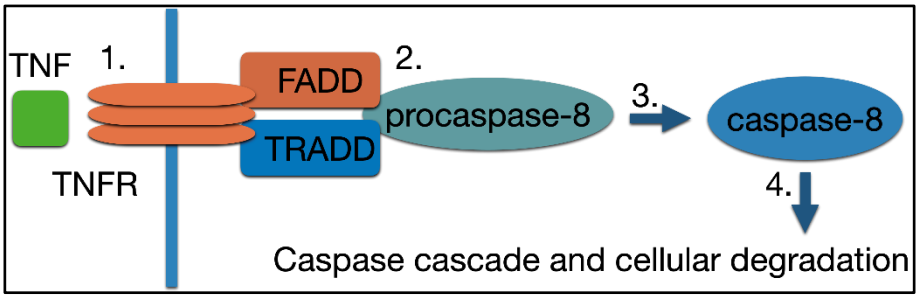


Figure 7. The process of apoptosis initiation via the extrinsic pathway. Activation starts with the activation of TNFR by TNFα (1). This invokes the assembly of TRADD, FADD and procaspase-8 (2), which results in the formation of active caspase-8 (3) that proceeds with initiating the caspase cascade and cellular component digestion (4).

Stage 2. Execution. In cells, DNAses are complexed with inhibitors. However, caspase-3 breaks this complex to free the DNAses, which go on to degrade DNA into around 180 bp strands. Histones play a protective role in this process, hindering the DNAses from cutting DNA into smaller fragments. Caspase-3 also cleaves other proteins, including those of the cytoskeleton. The digested cellular components are then assembled by other proteins into vesicles, which detach from the cell and into the surrounding tissues. The process taking place in execution is depicted in Figure 8.

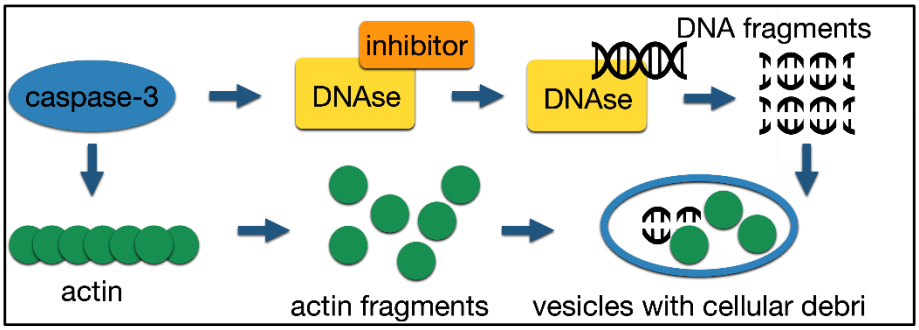


Figure 8. The process of apoptosis execution. First, caspase-3 removes the inhibitor from DNAse. Then, DNAse cuts DNA into around 180 bp strands. Histones protect the strands from further degradation. Caspase-3 also acts on other proteins, like those of the ECM. Finally, cellular debris are packaged into vesicles which leave the cell, where they are engulfed and broken down further by macrophages.

Stage 3. Phagocytosis. Macrophages then engulf the vesicles, where they merge with lysosomes. There, the components are metabolised even further, to their constituents.

**Necrosis**. If a cell is physically damaged or stressed by chemical or electrical stimuli, it swells and bursts uncontrollably - this process is called necrosis. This process is usually detrimental to the surrounding tissues and the organism itself. Upon necrosis, no specific signals are being transduced to macrophages, causing the cellular debris to accumulate in the damaged area. This leads to damage to the surrounding tissues and an inflammatory response. The process has been thoroughly reviewed by Ouyang [174] together with other types of cell death. Unlike other types of cell death, necrosis is energy-independent. The process is depicted in Figure 9.

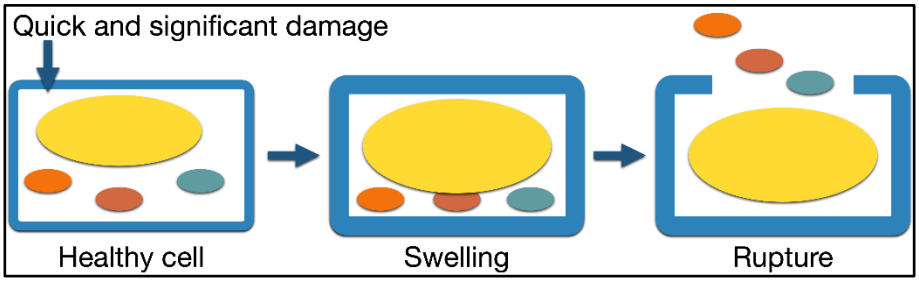


Figure 9. When a healthy cell experiences quick and significant damage and is unable to proceed with apoptosis, it starts to swell and eventually ruptures, releasing its organelles and other components into the surrounding tissue. This causes inflamation and further damage.

# 2. MATERIALS AND METHODS

## 2.1 Scaffold Material Preparation

### 2.1.1 Hybrid Organometallic Polymers

A list of materials used in preparing hybrid organometallic polymers is given in Table 1.

Table 1. A list of materials used to prepare the hybrid organometallic polymers. NA stands for not applicable.

| Name | Full name | Purity | Supplier |
|---|---|---|---|
| AIP | aluminium (III) isopropoxide | ≥99 % | Sigma-Aldrich |
| BIS | 4,4'-bis(diethylamino)benzophenone | ≥99 % | Sigma-Aldrich |
| HCl | hydrochloric acid | 37 % | Sigma-Aldrich |
| MAA | methacrylic acid | 99 % | Sigma-Aldrich |
| MAPTHS | 3-(trihydroxisilyl)propyl methacrylate | - | Sigma-Aldrich |
| MAPTMS | 3-(trimethoxysilyl)propyl methacrylate | 98 % | Sigma-Aldrich |
| TIPO | titanium (IV) isopropoxide | 97 % | Sigma-Aldrich |
| Toluene | toluene | ACS ISO | Sigma-Aldrich |
| VOTIP | vanadium (V) triisopropoxide oxide | - | Sigma-Aldrich |
| ZPO | zirconium (IV) propoxide | 70 % | Sigma-Aldrich |

**Al Hybrid**. MAPTMS was hydrolysed to MAPTHS using 0.1 M HCl by stirring for 15 min. In parallel, AIP was dissolved in toluene in an ultrasonic bath for 30 min. MAA was then added to the MAPTHS solution at a 1:1 molar ratio to that of AIP. The two solutions - MAA:MAPTHS and AIP:toluene were mixed together at 1:1:4 AIP:MAA:MAPTHS molar ratio and stirred for 15 min. BIS was used as a photoinitiator (1 % by weight to the sum of AIP, MAA and MAPTHS) and stirred for 15 min. The procedure has been published in Polymer International [176].

**Ti Hybrid**. The Ti containing hybrid material was prepared according to published data [54]. Briefly, MAPTHS was mixed with MAA and TIPO was slowly added to the mixture to a resulting solution with molar ratios between TIPO:MAA:MAPTHS corresponding to 1:1:4. BIS was used as a photoinitiator (1 % by weight to the sum of TIPO, MAA and MAPTHS) and stirred for 15 min. Finally, the material was filtered using a 0.22 μm pore syringe filter.

**V Hybrid**. The preparation of the V containing hybrid material was performed according to published data [55]. Briefly, MAPTMS was hydrolysed to MAPTHS using 0.1 M HCl. Then, VOTIP was added to the MAPTHS at a 1:1 molar ratio. Finally, the material was filtered using a 0.22 μm pore syringe filter.

**Zr Hybrid**. The preparation of the Zr containing hybrid was performed according to published data [56]. Briefly, MAPTMS was hydrolysed to MAPTHS using 0.1 M HCl. In parallel, zirconium propoxide (ZPO) was added to MAA at a 1:1 molar ratio. The two solutions – MAPTHS and MAA:ZPO were mixed together at a 1:1:4 ZPO:MAA:MAPTHS molar ratio. BIS was used as a photoinitiator (1 % by weight to the sum of ZPO, MAA and MAPTHS). The material was filtered using a 0.22 μm syringe filter.

### 2.1.2 Polydimethylsiloxane and Its Composites

A list of materials used in preparing PDMS samples and composites is given in Table 2.

Table 2. A list of materials used to prepare the PDMS samples and composites.

| Name | Full name | Purity | Supplier |
|---|---|---|---|
| Acetic acid | acetic acid | - | Appli-Chem |
| DMSO | dimethyl sulfoxide | - | Sigma-Aldrich |
| Ethanol | ethanol | 70 % | Vilniaus degtinė |
| FBS | fetal bovine serum | - | Gibco |
| HEMA | 2-hydroxyethyl methacrylate | - | Sigma-Aldrich |
| IMDM | Iscove‘s modified Dulbecco‘s medium | - | Gibco |
| $Na_2CO_3$ | sodium carbonate | - | Sigma-Aldrich |
| PBS | phosphate buffered saline | - | Gibco |
| PDMS | polydimethyl siloxane and thermoinitiator kit (Sylgard 184) | - | Dow Corning |
| PVA | polyvinyl alcohol | - | Sigma-Aldrich |

| | | | |
|---|---|---|---|
| RGD tripeptide | arginine-glycine-asparagine tripeptide | - | Sigma-Aldrich |
| Silk | *Bombyx mori* silk | - | Amazon |
| Sulfo-SANPAH | sulfosuccinimidyl 6-(4'-azido-2'-nitrophenylamino)hexanoate | - | Thermo Scientific |

**Pure PDMS**. For pure PDMS sample preparation, PDMS was mixed together with its proprietary thermoinitiator at a 10:1 w/w ratio. The components were thoroughly stirred, degassed and either spin-coated on glass slides or moulded into shapes. Finally, they were heated for 1 hour at 100 °C in order to crosslink the components.

**PDMS Biodecoration**. First, PDMS films were immersed in 70 % ethanol for 24 hours, then washed in PBS and dried under UV light for 1 hour. The surfaces were modified in five different ways:

1. By immersion in IMDM growth medium with 10 % FBS.
2. By immersion in 100 % FBS.
3. By immersion in a solution of collagen.
4. By immersion in a solution of laminin.
5. By covalently linking RGD tripeptides via a photocrosslinker.

Reference PDMS samples were incubated in PBS. In case of IMDM, 100 % FBS and PBS, the PDMS samples were treated with 1 mL of corresponding liquid and incubated for 24 hours at 4 °C. A solution of 0.1 % collagen was prepared in 0.1 M acetic acid and diluted 10 times in deionised water prior to applying 1 mL of 0.01 % solution to the samples and incubating for 24 hours at 4 °C. RGD tripeptide was covalently bound to the samples via sulfo-SANPAH. The sulfo-SANPAH photocrosslinker (100 μg/mL in DMSO) was applied to the surfaces and treated with UV light for 1 hour. The photoactive part is activated via UV and binds to PDMS. After removing the photocrosslinker solution, samples were washed in PBS and then a solution of RGD tripeptides was applied to the surface and incubated for 24 hours at room temperature. During this time, links between the RGD tripeptides and the free side of the photocrosslinker molecule are formed.

**PDMS block copolymers**. PDMS block copolymers were synthesised at Vilnius University Faculty of Chemistry and Geosciences. Four types of PDMS block copolymers were investigated:

A – α,ω-diepoxy-PDMS block copolymers with AA, BMA, HEMA and VP, using glycerol and photoinitiator for crosslinking. Varying compound proportions are summarised in Table 3.

Table 3. Varying proportions of the constituents used for the α,ω-diepoxy-PDMS-AA-BMA-HEMA-VP block copolymer crosslinking.

| Name | BMA, % | GMA, % | Glycerol, % | PI, % |
|---|---|---|---|---|
| A1 | 6.4 | 2.56 | 10 | 2 |
| A2 | 6.4 | 2.44 | 10 | 2 |
| A3 | 8.0 | 2.19 | 10 | 2 |
| A4 | 6.4 | 2.56 | 10 | 2 |

B – α,ω-diepoxy-PDMS block copolymers with BMA, HEMA, VP at varying molar ratios, using photoinitiator for crosslinking. Varying constituent proportions are summarised in Table 4.

Table 4. Varying proportions of the constituents used for the α,ω-diepoxy-PDMS-BMA-HEMA-VP block copolymer crosslinking.

| Name | BMA, molar ratio | HEMA, molar ratio | VP, molar ratio | α,ω-diepoxy-PDMS, molar ratio | PI, % |
|---|---|---|---|---|---|
| B1 | 0.4 | 0.2 | 1 | 0.2 | 2 |
| B2 | 0.4 | 0.2 | 1 | 0.2 | 2 |
| B3 | 0.4 | 0.3 | 1 | 0.3 | 2 |
| B4 | 0.4 | 0.3 | 1 | 0.15 | 2 |

C – dihydroxy-PDMS block copolymers with AzA, DEG and MAA, using photoinitiator for crosslinking. The constituent proportions were the same in all cases, but the crosslinking conditions were different and are summarised in Table 5.

Table 5. Varying proportions of the constituents used for the dihydroxy-PDMS-AzA-DEG-MAA block copolymer crosslinking.

| Name | GMA, % | BMA, % | PI, % |
|---|---|---|---|
| C1 | 164 | 62.1 | 5 |
| C2 | 82 | 45.1 | 5 |
| C3 | 20 | 16.7 | 3 |
| C4 | 40 | - | 3 |

D – α,ω-diepoxy-PDMS block copolymers with GMA and PVA, using photoinitiator for crosslinking. The constituent proportions were the same in all cases, but the crosslinking conditions were different and are summariesed in Table 6.

Table 6. Varying proportions of the constituents used for the α,ω-diepoxy-PDMS-GMA-PVA block copolymer crosslinking.

| Name | BMA, % | GMA, % | Glycerol, % | PI, % |
|---|---|---|---|---|
| D1 | 13.7 | - | 7.8 | 3 |
| D2 | 7.3 | - | 8.4 | 3 |

**Silk-reinforced PDMS**. The silk preparation procedure was adapted from a protocol developed by Prof. Kaplan‘s group [177]. *Bombyx mori* silkworm cocoons were cut using scissors and subsequently boiled for 1 h in a 0.02 M solution of $Na_2CO_3$, while gently stirring. Cocoon leftovers were removed from the solution and the remaining silk was washed three times with deionised water for 1 h each time. The silk fibres were pressed to remove excess water and left overnight to dry. PDMS was thoroughly mixed with proprietary thermoinitiator at a 10:1 mass to mass ratio. Silk was subsequently added to the mixture at 1 %, 5 % or 10 % mass ratio. Pure PDMS-thermoinitiator mixture was used as control. The mixtures were poured into wells of 24-well polystyrene tissue culture plates (cylinders with diameters of 15.6 mm, heights of 17.8 mm and volumes of approximately 3.4 mL) and left in a refrigerator (4 °C) for 1 hour for the air bubbles to evaporate. The plate with PDMS-silk mixtures was then heated for 1 h at 100 °C. Finally, the polystyrene plate was broken to remove the samples.

## 2.2 Scaffold and Surface Fabrication

Materials used for sample preparation are summarised in Table 7.

Table 7. A list of materials used for sample preparation.

| Name | Full name | Purity | Supplier |
|---|---|---|---|
| Acetic acid | acetic acid | 99 % | Sigma-Aldrich |
| Borosilicate glass | borosilicate glass | NA | Thermo Scientific |
| Ethanol | ethanol | 96 % | Vilniaus degtinė |
| MAPTMS | 3-(trimethoxysilyl)propyl methacrylate | 98 % | Sigma-Aldrich |

### 2.2.1 Polymer Films

**Glass Slide Silanisation**. The glass slides used for sample preparation were silanised according to a protocol adopted from Käpylä et al [178]. Circular 12 mm diameter borosilicate glass coverslips were washed in ethanol

for at least 1 hour in an ultrasonic bath. Ethanol was removed and a new portion of 30 mL ethanol with 0.5 mL of MAPTMS and 0.5 mL of acetic acid were added together with 2 mL of deionised water and placed in an ultrasonic bath for 1 hour. Finally, the glass slides were once more washed in ethanol in an ultrasonic bath. The glass slides were subsequently air-dried at room temperature.

**Spin-Coating**. Around 70 μL droplets of materials were spin-coated on silanised circular 12 mm diameter borosilicate glass slides for 30 s at 3000 RPM. Samples with hybrid organometallic polymers would then be carefully collected and placed in a dark fume hood for at least 24 hours in order for the solvents to evaporate. Samples with photoinitiators would then be photocrosslinking under UV, while pure PDMS-thermoinitiator mixture would be crosslinked at 100 °C for 1 hour.

**UV Treatment**. Spin-coated polymers were crosslinked using a Sylvania 15W UV-C bactericidal lamp at a distance of 20 cm, correspnding to around 1.8 mW/cm$^2$ irradiance for at least 5 hours. The samples were subsequently placed upside down to sterilise the bottoms for at least 1 hour and then transferred to 24 well tissue culture plates to be UV-treated for 1 more hour.

**Sample Sterilisation and Washing**. The samples were finally washed three times with sterile PBS - twice for an hour and once overnight. Subsequently, they were washed with IMDM, supplemented with FBS and antibiotics for one hour.

### 2.2.2 Polymer Extracts

Two polymer extract preparation approaches were used:

1. Polymer films that were prepared as discussed previously were incubated in PBS on a plate shaker at 40 RPM for 24 hours at room temperature. The PBS containing spin-coated polymer extracts were subsequently aspirated to new tissue culture plate wells and heated for 5 hours at 80 °C until the water had evaporated.

2. An alternative method was to place spin-coated and UV-polymerised samples in IMDM, supplemented with FBS and antibiotics and incubate them for 24 hours on a plate shaker at 40 RPM and then to apply these extracts in cell medium to monolayers of cells.

### 2.2.3 3D Structures

For structure fabrication, samples were prepared by drop casting a small volume of the material on a glass slide and leaving the samples overnight in a fume hood in order for the solvents to evaporate. Samples were shielded from ambient light during all steps prior to polymerisation in order to avoid unintentional photoactivation. After polymerisation, the samples were washed in either 4-methyl-2-pentanone (Ti, V and Zr-based hybrid) or toluene (Al-based hybrid) for 15 min, then rinsed with isopropanol and air-dried. Two direct laser writing systems were used in the experiments.

**Nanoscribe**. A commercially available Nanoscribe Photonic Professional GT (Nanoscribe GmbH, Germany) system was used at the Department of Chemistry at Lancaster University. The system is based on a Topica FemtoFiber Pro 100 fs pulsed 780 nm wavelength laser with a maximum power of 50 mW. A 63X 1.4 NA oil immersion Zeiss objective lens was used for fabrication. Structures were imported or programmed in DeScribe scripting software for controlling the fabrication process.

**Ti:Sapphire**. The direct laser writing system used in this study has been described previously [179]. It is based at the Foundation for Research and Technology – Hellas, Institute for Electronic Structure and Laser (FORTH-IESL) in Heraklion, Greece. Briefly, a Ti:Sapphire laser (Femtolasers Fusion) was used as a light source, operating at 780 nm central wavelength with 20 fs pulse duration and a 75 MHz repetition rate. The average laser power was set between 10 – 100 mW using an attenuator (Altechna). The sample was positioned on piezo-electric stages and the laser beam was guided using a galvanometric mirror scanner (Scanlabs Hurryscan II) through a 40X 0.95 NA (Zeiss, Plan-Apochromat) or an oil immersion 100X 1.4 NA (Zeiss, Plan-Apochromat) objective lens. The process of fabrication was controlled by SAMLight (SCAPS) software. Writing speeds between 0.1 and 1 mm/s were found to be suitable for this purpose. A simple schematic representation of the system is given in Figure 10.

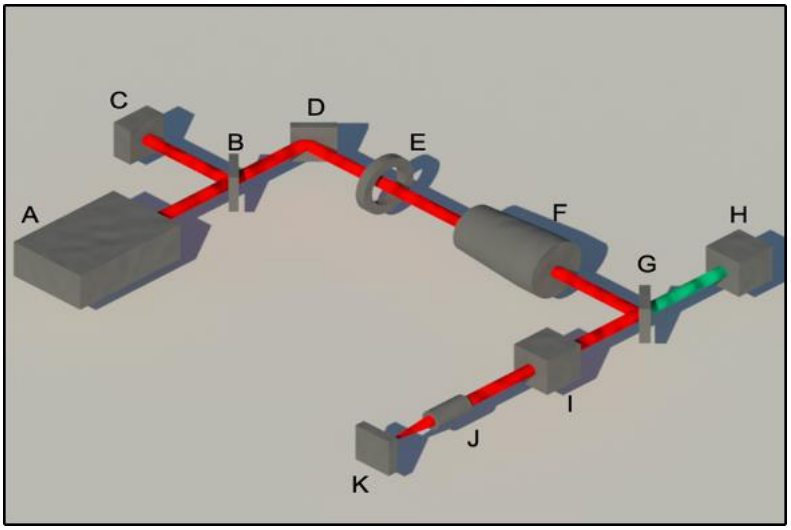

Figure 10. A schematic representation of the system used at FORTH-IESL. A – the laser, B – beam splitter, C – spectrum analyser, D – mirror, E – attenuator, F – telescope, G – dichroic mirror, H – CCD camera for real time observation of the fabrication process, I – galvanometric scanner, J – objective lens, K – sample stage with LED illumination for the CCD camera.

## 2.3 Characterisation of Scaffolds and Surfaces

### 2.3.1 Surface Contact Angle Measurements

2 µL droplets of deionised water were carefully pipetted on the polymer films. Pictures were taken using a Krüss EasyDrop contact angle measurement system and analysed using proprietary software. Sample chamber temperature was kept constant at 21 °C using a LabTech H50-500 water cooler. A total of 5 measurements per material were performed. Results are presented as mean ± standard deviation.

### 2.3.2 Assesment of Collagen Adsorption

A protocol for assessing the concentration of collagen was adapted from Tullberg-Reinert and Jundt [180] with slight modifications. First, a solution of collagen type I (1 mg/mL in 0.1 N acetic acid) was added to the sample and incubated for 1 hour at 37 °C. Then, the collagen solution was gently replaced with fixating Bouin's solution (15 mL saturated aqueous picric acid with 5 mL 35 % formaldehyde and 1 mL glacial acetic acid), incubated for 1 hour and then washed using PBS. The samples were then transferred to new wells with

a solution of Sirius Red (1 mg/mL in picric acid) for 1 h under mild rocking conditions (30 RPM). Afterwards, the samples were washed with 0.01 N hydrochloric acid to remove unbound dye. The dye was then dissolved in 0.2-0.3 mL of 0.1 N sodium hydroxide by shaking at room temperature for 30 min. Optical density of the solution was measured using Varioskan Flash microplate reader (Thermo Fisher Scientific) at 550 nm. For reference, a calibration curve was prepared by using known concentrations of collagen type I. The method is relatively specific to collagen type I and III. Glass was used as control. 3 independent experiments were carried out, results are presented as averages ± standard deviations.

### 2.3.3 Scanning Electron Microscopy

The samples were sputter coated with a 10 nm layer of gold using a Quorum Q150RES sputter coater (Quorum Technologies Ltd). Then, they were observed using one of two SEMs:

1. JEOL JSM−6390LV operating at 15 kV at FORTH-IESL (Heraklion, Crete, Greece).
2. JEOL JSM 7800F operating at 10-15 kV at the Department of Chemistry at Lancaster University (Lancaster, United Kingdom).

### 2.3.4 Energy-Dispersive X-Ray Analysis

The samples were sputter-coated with a layer of gold (60 s, 20 mA, $8x10^{-2}$ mBar, 5 nm) using a Quorum Q150RES sputter coater (Quorum Technologies Ltd) and then investigated using a field-emission SEM JEOL JSM-7800F with an EDX system (X-Max50, Oxford Instruments) at 10 mm working distance and 10 kV voltage mounted on a brass JEOL holder with 25 mm Carbon tabs (G3348N, Agar Scientific) at the Department of Chemistry at Lancaster University (Lancaster, United Kingdom). 3 measurements were performed per sample and average results are presented.

### 2.3.5 Inductively Coupled Plasma Optical Emission Spectroscopy

These experiments were performed by collaborators at Kratos Analytical Ltd in Manchester, United Kingdom. Measurements were performed using an Agilent 5100 VDV ICP-OES in axial mode. The sample introduction system consisted of a glass concentric neb- uliser, a glass cyclonic double pass spray chamber, and a demountable dual view quartz 1.8 mm torch. The solid

samples were dissolved directly from the well-plate locations in dilute nitric acid (2 % w/V) with several washings and made up to the final volume (10 mL) with diluted nitric acid (2 % w/V). Calibration curves of target elements Al, Ti, V, Zr, Na, and P were prepared between 1 - 100 ppm using single element standards (Sigma-Aldrich, Trace- CERT, 2 % $HNO_3$), with the exception of P (Alfa Aesar, SpecPure, 5 % HNO3). All blanks were prepared from the original stock of dilute nitric acid (2 % w/V) used to prepare standards and samples. All blanks, standards, and samples were prepared with yttrium internal standard (1 ppm, Sigma-Aldrich, TraceCERT, 2 % $HNO_3$)

### 2.3.6 Compression Tests

The compression tests were performed by collaborators at Vilnius Gediminas Technical University Faculty of Mechanics using a Mecmesin MultiTest 2,5-i micro-compression machine (Mecmesin Ltd in Slinford, UK) in a Mecmesin AFG25 load cell with controlled load of measured accuracy ± 0.01 mm and compression force in the range between 2 - 2500 N with an accuracy of ± 0.1 %. After placing the sample in the instrument, cyclic compression tests were performed. Displacement – load curves were registered automatically up to a maximum displacement of 4 mm for each sample. Compression speed was set to 0.167 mm/s. All measurements were performed at room temperature.

To calculate the elastic moduli of the samples, the applied force (N) was divided by surface area ($m^2$) and then divided by sample compression ratio.

## 2.4 Cell Isolation, Characterisation and Culture

All materials used for cell isolation, characterisation and culture are summarised in Table 8. Three types of cells were used in these experiments in total:

1. Rat muscle stem cells.
2. Rabbit muscle stem cells.
3. NIH/3T3 mouse embryo fibroblasts.

Table 8. Materials used in cell isolation, characterisation and culture.

| Name | Full name | Supplier |
|---|---|---|
| Anti-CD34 mAb | - | Abcam |
| Anti-CD45 mAb | - | Abcam |
| Anti-c-kit mAb | - | Thermo Fisher Scientific |
| Anti-MYF5 mAb | - | Thermo Fisher Scientific |
| BSA | bovine serum albumin | Sigma-Aldrich |
| Collagenase | - | Sigma-Aldrich |
| Cy3-conjugated secondary antibodies | - | Merck |
| DMSO | dimethyl sulfoxide | Sigma-Aldrich |
| EDTA-trypsin | ethylenediaminetetraacetic acid-trypsin | Gibco |
| FBS | fetal bovine serum | Gibco |
| Hyaluronidase | - | Sigma-Aldrich |
| IMDM | Iscove‘s modified Dulbecco‘s medium | Gibco |
| PFA | paraformaldehyde | Sigma-Aldrich |
| PBS | phosphate buffered saline | Gibco |
| Pen-strep | penicillin-streptomycin | Gibco |
| MTT | 3-(4,5-dimethylthiazol-2-yl)-2,5-diphenyltetrazolium bromide | Merck |
| Triton X-100 | - | Sigma-Aldrich |

All types of cells were grown in IMDM medium, supplemented with 10 % FBS and antibiotics - 100 U/mL penicillin and 100 µg/mL streptomycin in polystyrene flasks. Every three to four days, the cells were subcultured by aspirating the medium, washing the cell monolayer with PBS, dissociating with EDTA-trypsin and subsequently resuspending in fresh medium. The flasks were kept in an incubator under controlled conditions – a 37 °C temperature and a 5 % level of $CO_2$.

For backup, the cells were cryopreserved in liquid nitrogen in IMDM, supplemented with 30 % FBS, antibiotics and 10 % DMSO.

### 2.4.1 NIH/3T3 Fibroblasts

The NIH/3T3 fibroblasts were obtained from ATCC. The vial was thawed as per supplier’s instructions and then seeded in tissue culture flasks in IMDM, supplemented with FBS and antibiotics. Once the cells had formed a monolayer, they were passaged several times, then collected and frozen at -80 °C until further use.

### 2.4.2 Rat Muscle Stem Cells

A Wistar rat was euthanised and a small piece of skeletal muscle tissue was removed. The experiments were approved by License of Animal Research Ethics Committee (Lithuania) No. G2-39, 03/08/2016. Large blood vessels were separated, then skeletal muscle tissue was minced and incubated in a solution of EDTA-trypsin with collagenase and hyaluronidase (0.5 % and 0.3 %, respectively) for 30 min at 37 °C under mild shaking conditions. The resulting cell suspension was centrifuged, mixed with growth medium and seeded to tissue culture plates. The growth medium was replaced every 3-4 days and after 5 passages the cells were cloned by serial dilution. A highly proliferative colony forming unit was selected as a cell source, multiplied *in vitro* and banked in liquid nitrogen for further use. The cells were cultured in IMDM, supplemented with 10 % foetal bovine serum and penicillin-streptomycin (100 U/mL and 100 μg/mL). They were subcultured every 3-4 days, by detaching with EDTA-trypsin and resuspending in fresh medium. The cells were grown in an incubator (Thermo Fisher Scientific) at 37 °C with 5 % $CO_2$.

For characterisation purposes, these cells were grown in 30 mm diameter Petri dishes with glass slides on the bottom, then fixed with 4 % paraformaldehyde for 15 min. The cells were subsequently washed with PBS and incubated with 0.2 % Triton X-100 in PBS for 15 min to permeabilise the membranes. After blocking with 1 % BSA in PBS, the cells were incubated with primary antibodies against CD34, CD45, MYF5 and c-kit overnight according to manufacturer's instructions at 4 °C. The samples were then rinsed with 1 % BSA in PBS and incubated with Cy3-conjugated secondary antibodies. Analysis was performed using an Olympus IX71 (Olympus, Tokyo, Japan) fluorescence microscope.

### 2.4.3 Rabbit Muscle Stem Cells

A full anesthesia of a laboratory rabbit was performed using ketamine (30-50 μg/kg) and diazepam (5 μg/kg). A 0.5 $cm^3$ piece of muscle tissue from left thigh area was surgically removed and mechanically minced. It was then treated enzymatically using collagenase (1 mg/mL) and hyaluronidase (0.3 mg/mL) in 0.125 % trypsin and 0.1 % EDTA for 15 min at 37 °C. The resulting suspension was then diluted in growth medium with serum and centrifuged for 1-2 min at 100 G. The suspension was then diluted in full

growth medium and planted in polystyrene dishes. They were initially passaged every 1-2 weeks until a fully confluent monolayer was achieved and after that, the cells were subcultured every 3-4 days. The cell line has been described in the literature previously by Kalvelytė *et al.* [181] and D. Baltriukienė [182].

## 2.5 Assessment of Biocompatibility

### 2.5.1 Fluorescence and Light Microscopy

For light microscopy imaging, the samples were seeded and cultured with cells, then visualised using a NIKON Eclipse TS 100 microscope with a Lumenera Infinity 2C CCD camera.

For fluorescence imaging, the cells were stained using AO/EB mixture prior to visualisation. AO/EB staining is a fluorescece microscopy technique used to distinguish between viable and non-viable (apoptotic and necrotic) cells. The cellular membrane is permeable to AO, which interacts with DNA, staining it green. AO also binds RNA and single-stranded DNA, staining those orange, while EB only permeates the membranes of non-viable cells, binding to DNA and staining the nucleus red. This allows for a distinction between live non-apoptotic cells (green chromatin), live apoptotic (condensed or fragmented green chromatin), dead apoptotic (condensed or fragmented orange chromatin) and necrotic (red chromatin) cells as described by Mercille *et al.* [183].

A mixture of AO (100 µg/mL) and EB (100 µg/mL) was applied to the cells grown on the samples – 5 µL per 1 mL of growth medium. After 10-20 minutes, the medium was gently aspirated and replaced with warm PBS. The cells were observed using an Olympus fluorescence microscope.

### 2.5.2 Flow Cytometry

Cells were cultured on the test surfaces for 24, 48, 72 and 96 hours. The growth medium with any unattached cells was collected and the monolayer cells were treated with EDTA-trypsin and then collected as well. All of them were subsequently stained using AO/EB as in the case of fluorescence microscopy. The cells were analysed using a BD FACSCanto™ II (BD Biosciences) flow cytometer, registering 10 000 events per sample and time point. Green fluorescence of acridine orange was detected using FITC channel

and red fluoresce of ethidium bromide was detected using PE channel. 3 independent experiments were performed with 3 repetitions per material within each experiment. The cells were split into four categories based on their fluorescence profile.

### 2.5.3 MTT Assay

The MTT proliferation assay is based on mitochondrial oxidoreductase enzyme activity. Water-soluble MTT (3-(4,5-dimethylthiazol-2-yl)-2,5-diphenyltetrazolium bromide) is reduced to water-insoluble purple formazan, which can be colorimetrically detected upon dissolution in an organic solvent, like ethanol.

**For cells grown on polymer surfaces**. The growth medium was gently aspirated from cultured cells and replaced with a solution of MTT (0.2 mg/mL in PBS). After incubating at 37 °C for 1 hour, the MTT solution was removed and the formazan crystals were dissolved in 96 % ethanol. The absorbance of this solution was then measured at 570 nm using a Varioskan Flash (Thermo Fisher Scientific) plate reader. The absorption is proportional to the number of viable cells and their metabolic rate.

**Assessment of polymer extract toxicity**. Polymer samples were spin-coated and polymerised under UV. The samples were then incubated in a full cell growth medium (containing serum and antibiotics) for 24 hours at room temperature. The media containing spin-coated polymer extracts were subsequently aspirated and used on NIH/3T3 fibroblasts grown in a monolayer for 24 hours. They were cultured for another 24 hours with normal medium as a reference at 37 °C with 5 % $CO_2$ atmosphere. An MTT assay was then performed on the cells grown in extract containing media.

### 2.5.4 Adhesion Strength

Rat muscle stem cells were seeded at a density of 100 000 cells/mL/sample in 24 well tissue culture plates and cultured for either 4 or 24 hours at 37 °C with 5 % $CO_2$. At those time points, samples were transferred to new tissue culture plates and half of the plates were shaken at 500 RPM for 5 minutes using a plate shaker (Thermomixer Comfort, Eppendorf). The reference samples were incubated in an incubator at 37 °C. The number of cells remaining adhered to the surface was measured by replacing the growth medium with 0.1 % crystal violet solution in 20 % ethanol for 30 min and then

comparing it to analogously dyed, unshaken cell monolayers by measuring the crystal violet absorption using a Varioskan Flash plate reader (Thermo Fisher Scientific). 3 independent experiments were performed with 3 repetitions per material within each experiment.

### 2.5.5 Signalling Molecule Expression and Phosphorylation

Rat muscle stem cells were seeded on the samples at a density of 100 000 cells/mL/sample and cultured for either 4 or 24 hours. At these time points, the samples were transferred to new tissue culture plates and gently washed with PBS. The PBS was then replaced with a lysis buffer consisting of 8 M urea, 2 M thiourea and 50 mM DTT. Cells were collected from 5 samples for each time point by pipetting 5-10 times. The lysates were then centrifuged for 10 minutes at 20000 G at room temperature. The supernatants of each vial were then transferred to new vials and frozen at -20 °C until further use. 3 independent experiments were carried out.

Protein concentrations were normalised by running an SDS-PAGE gel, staining with Coomassie brilliant blue, taking images using a transilluminator (UVP) and analysis with ImageJ software. After diluting the highest concentration samples using lysis buffer, the concentration-equalised samples were subjected to gel electrophoresis at 200 V for 45 min using a BioRad electrophoresis apparatus. The proteins were then transferred to a PVDF membrane at 25 V, 300 mA.

The membranes were subsequently treated with primary antibodies against p-Akt (Ser473), p-Akt (Thr308), Akt (Molecular Probes), FAK (BD Biosciences) and tubulin overnight according to manufacturer's instructions at 4 °C. Next day, the membranes were washed three times using a wash buffer and incubated with secondary antibodies: fluorescently-labelled anti-tubulin, HRP-conjugated goat anti-mouse (Invitrogen) and HRP-conjugated anti-rabbit (Invitrogen) according to manufacturer's instructions for 1 hour. Finally, the membranes were washed again three times using wash buffer. Tubulin was detected using a fluorescence measuring device. HRP-conjugated antibodies were treated with enhanced chemiluminescence (ECL) reagent, which upon catalysis by HRP yields chemiluminescence, which was detected using a transilluminator (UVP). Membrane image analysis was performed using ImageJ software.

### 2.5.6 Collagen Synthesis Assay

The method for collagen synthesis assessment was analogous to that of collagen adsorption. Rat muscle stem cells were seeded on the test surfaces at a density of 20 000 cells/mL/sample in 24 well tissue culture plates. After 1, 7 and 14 days of incubation, the samples were fixed using Bouin's solution, then dyed using a Solution of Sirius Red and subsequently washed with a solution of HCl. Finally, the dye was dissolved in a solution of NaOH and measured spectrophotometrically against pure NaOH and the amount of collagen was determined from the calibration curve. 3 independent experiments were performed with 3 replicates per material within each experiment.

## 2.6 Statistical Analysis

Statistical analysis was performed using RStudio and plotted using the ggplot2 package. The data is presented as either mean ± standard error or standard deviation. Statistical significance was assessed using one-way ANOVA and Tukey's HSD post-hoc test. Differences between groups were considered to be significant if $p < 0.05$ (*), $p < 0.01$ (**) and $p < 0.001$ (***).

# 3. RESULTS AND DISCUSSION

Tissue engineering is a highly interdisciplinary field aiming at creating artificial tissue and organ substitutes. There are multiple approaches being developed to achieve this goal, but the overarching challenge is the same - how to construct an extracellular environment that fosters cellular integration, maturation and functional reconstitution of a damaged part of the body.

This work investigates strategies for the development of two different types of tissues:

1. Hard tissue. A hybrid organometallic polymer-based approach for hard tissue engineering, where strictly defined 3D cellular niches can be created using direct laser writing.
2. Soft tissue. A PDMS-based approach of delivering cells, where the properties of PDMS are tuned in a way so as to match the mechanical and chemical properties of soft tissues as well as to support biochemical cues that are attractive for stem cells.

## 3.1 Hard Tissue Engineering

For hard tissue engineering, it is important to have a rigid structure with predefined micro-architectural cues, since these affect cellular properties like adhesion, proliferation and differentiation. In addition to that, the scaffold has to support the mechanical loads on that particular tissue. This can only be ensured by employing biocompatible materials that can be precisely microstructured and tuned. Such materials are in high demand and are constantly being developed and improved. The development of such materials goes hand in hand with their fabrication techniques. The end result of this endeavor will be a combination of optimal biomaterials, techniques and fabrication parameters.

### 3.1.1 Synthesis of Hybrid Organometallic Polymers

For hard tissue such as bone and cartilage engineering, scaffolding materials that are stiff and rigid have to be chosen. This is not only needed to support the mechanical properties of the tissue itself, but also to attenuate the differentiation of cells as exemplified in multiple studies [184]–[186]. Hard tissue micro-architectures have to be precisely tuned, so the materials have to

be precisely controllable as well. There are hundreds, or perhaps even thousands of different TE materials described in the literature and choosing the right one will not only depend on the tissue being constructed and the cells that are being used, but also on the technique that is going to be used for scaffold fabrication.

A class of materials called hybrid organometallic polymers were chosen due to a previously demonstrated biocompatibility *in vitro* and *in vivo* [62], [63] as well as their excellent 3D structuring capabilities [56]. Since several hybrid organometallic materials have been used for direct laser writing before – like those containing Zr [56], V [55], Ge [53] and Ti [54], one of the challenges in this work was to investigate if a new material containing Al could be developed. First, hybrid organometallic materials containing Ti, V and Zr were synthesized according to published formulations [54]–[56]. The preparation procedure for the Al containing hybrid was analogous to those for Ti and Zr with an extra step to dissolve aluminium isopropoxide in toluene for improved miscibility with other components – methacrylic acid and MAPTHS. The Al containing material is a clear liquid with a yellow shade due to the presence of BIS. After evaporation of the solvent, the material transitions to a viscous gel-like state. Gelation reduces structural distortions that would arise during fabrication in a liquid due to vibrations, diffusion and stage movement in some laser two-photon polymerisation systems. Since the samples used in this work were of miniscule dimensions, it was important to assure good quality substrates for the samples.

To achieve this goal, borosilicate glass slides were used as a base for polymer linking and the glass slides were chemically modified to improve polymer – glass linking. By crosslinking the Si-OH groups to the glass, double bonds of the MAPTHS would be exposed to the surface, allowing for covalent bonding to the polymer materials. To test, whether the silanization procedure was successful, contact angles were measured for ethanol-washed glass slides and MAPTMS-treated glass slides. The results are presented in Figure 11. Successful silanization of the borosilicate glass slides was proven – the contact angle had significantly increased upon treatment with MAPTMS - from around 39 for ethanol-washed and air dried reference slides up to around 53 for MAPTMS-treated, ethanol-washed and air-dried samples. The next step would be to assess the water contact angles of the synthesized materials.

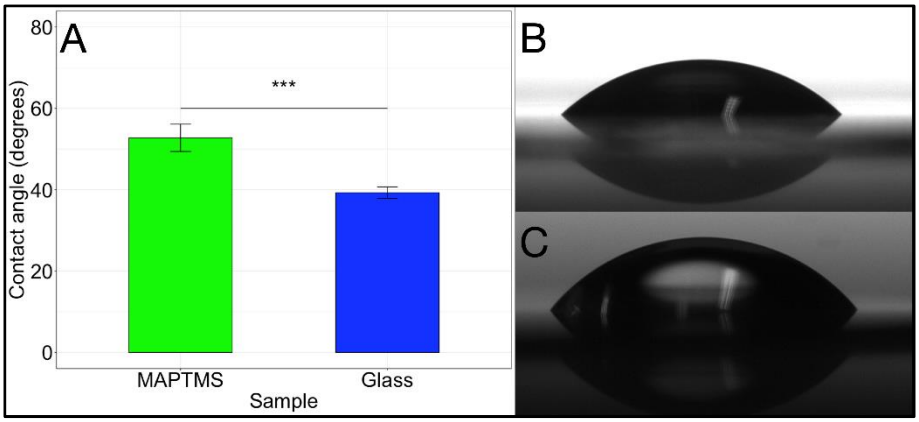

Figure 11. A – water contact angles of reference and MAPTMS-treated borosilicate glass slides. B – a water droplet on a reference, ethanol-washed glass slide. C – a water droplet on MAPTMS-treated glass surface. The results are presented as averages ± standard deviation with n = 5. *** - p <0.001.

### 3.1.2 Material Characterisation

**Surface water contact angle**. When testing material biocompatibility *in vitro*, one of the first processes to take place is serum protein adsorption to the cell culture surface. Motifs of the protein that have surface-corresponding hydrophilicity and charge form non-covalent bonds with the culture surface. Cell suspensions usually contain trace amounts of ECM proteins, which also bind to the surface. Parts of these proteins are subsequently recognized by cellular adhesion proteins and activate intracellular signaling pathways that influence adhesion, proliferation, differentiation and other processes. Surface contact angle is one of the most important determinants for protein-surface interaction, since it is a direct indicator of how hydrophilic or hydrophobic a material is. This is why we first investigated the water contact angles of different hybrid organometallic polymers. The results are presented in Figure 12.

Contact angle measurements were performed on spin-coated glass slides. All materials coated the glass slides evenly and adhered strongly enough for contact angles to be measured. Results show that the hybrid organic- inorganic materials had significantly higher contact angles (***, $p < 0.001$) than those of glass slides. The Al and Zr hybrid materials had contact angles of around 72 and 71 degrees, respectively. The Ti hybrid material was more hydrophobic, with a contact angle of around 90 degrees. The V hybrid material had the highest contact angle of around 102 degrees.

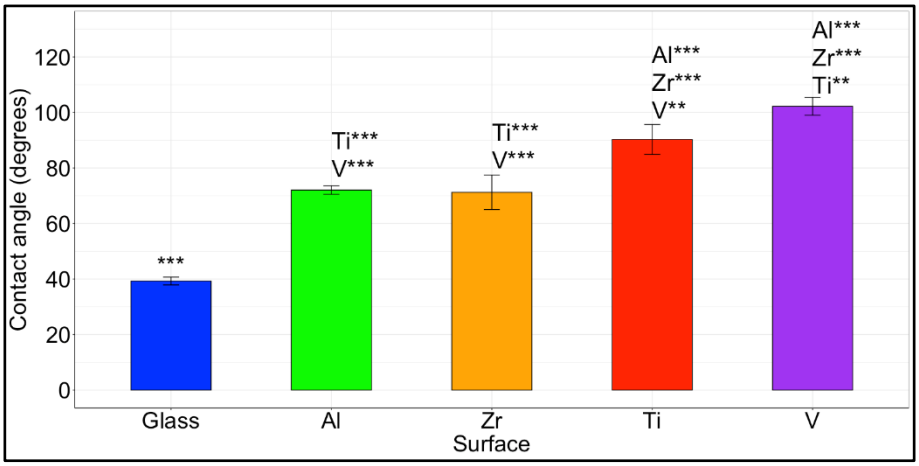


Figure 12. Hybrid organometallic polymer water contact angles. The results are presented as averages ± standard deviations with n = 5. Al, Ti, V and Zr correspond to Al, Ti, V and Zr hybrid materials, glass was used as a control. * – $p < 0.05$, ** – $p < 0.01$, *** – $p < 0.001$.

Since all living organisms are mostly comprised of water, an ideal TE material candidate should be hydrophilic. However, during cell culture, proteins adsorb to the surface and change its properties significantly. Attempting to measure biomolecule-adsorbed sample surface water contact angles would be a complex endeavour due to diffusion. Therefore, in addition to contact angle measurements, assays that look into both the adsorption of biomolecules and cellular responses should be employed.

For biomolecules to adsorb properly, a contact angle of around 70 degrees was shown to be optimal by Bumgardner *et al.* [187]. This study used chitosan-coated titanium samples to assess the adsorption of albumin, fibronectin and associated cellular attachment. It demonstrated that chitosan-coating significantly increased not only the contact angle of the surface from around 32 to around 76 degrees, but also corresponding abovementioned biomolecule adsorption and subsequent cellular adhesion and proliferation.

**Assessment of polymer chemical integrity**. The next step was to investigate the chemical integrities and constitutions of the polymers. The reason for this is that after 3D structure fabrication using direct laser writing, there is a step aimed at washing out uncrosslinked monomers. The rationale behind this next experiment was to assess if metal ions or metal-containing compounds get washed out of the polymer network during this process. So, an EDX analysis was performed on crosslinked films of the hybrid materials containing Al, Ti, V and Zr.

The analysis was performed on drop-cast films and confirmed the presence of metals in the organometallic materials and the results are depicted in Figure 13. The films were relatively thick (on the order of hundreds of microns), so the X-ray signals were most likely being generated by the materials. The same type of glass slides on which the materials were drop-cast were used as references. The Al hybrid showed a peak at around 1.5 keV that had around 2 times greater X-ray photon count than that measured in glass, indicating the presence of Al (characteristic Kα = 1.486 keV). In the case of V hybrid, a peak at around 5 keV indicates the presence of V (characteristic Kα = 4.949 keV and Lα = 0.511 keV) with X-ray photon count differing around 20 times from that of glass at 4.949 keV. The Lα of V was not visible due to overlap with Kα of O. Significantly larger amounts of Ti were found in Ti hybrid material as compared to control glass slides, with X-ray photon count at Kα = 4.508 keV being around 2.7 times greater than in reference glass. Finally, a peak at 2 keV indicates the presence of Zr (characteristic Lα = 2.042 keV) in the Zr hybrid with X-ray photon counts differing from glass by 10.7 times. The presence of gold due to the coating method was confirmed in all samples at 2.120 keV.

Signals from K and Na were only detectable in the glass, confirming that the resin thickness was high enough for the X-rays to be generated within the resins. In conclusion, the metals remain bound within the materials following development.

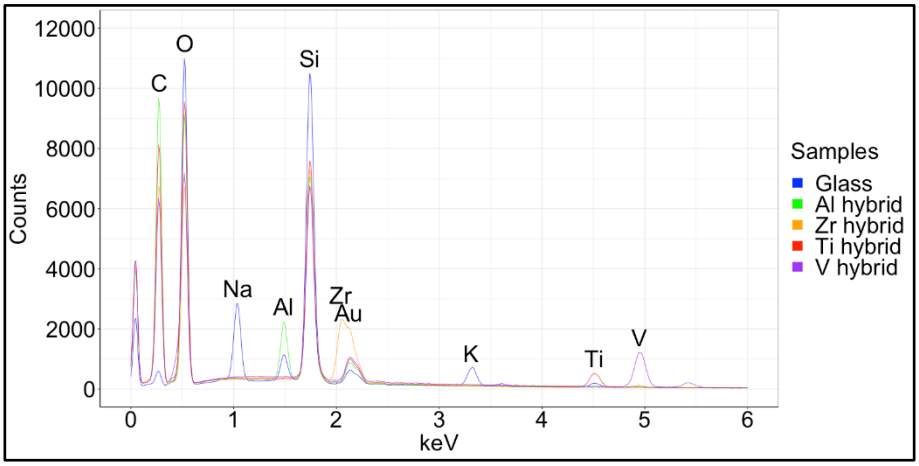


Figure 13. EDX spectra of the different organometallic polymers containing Al, Ti, V and Zr, as well as borosilicate glass slides as reference.

### 3.1.3 Structure Fabrication

The next step in this work was to investigate the structurability of the novel Al containing polymer and to qualitatively compare the structures fabricated with those already of Ge, Ti, V and Zr. Both Ti and Zr hybrid materials have already been used to produce scaffolds for tissue engineering [58], [62].

The Al hybrid material is transparent, while the intrinsic photoinitiator renders it fluorescent upon irradiation with a laser. This makes finding the interface between the material and the glass slide as straightforward as with commercially available photoresists like OrmoComp® or OrmoClear®. We first tested the Al containing hybrid organometallic polymer on both the Nanoscribe® and the custom-built DLW systems in an attempt to fabricate 2D structures. The fabrication procedure was successful, without significant deviations from the CAD models. The results are presented in Figure 14.

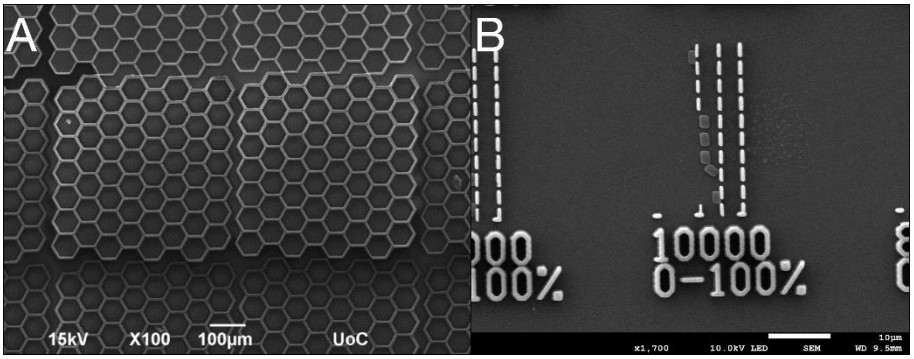


Figure 14. 2D structures fabricated out of the Al containing hybrid material. A – honeycomb patterns fabricated using the custom-built DLW system with a 40X 0.95 NA objective lens. B – calibration lines fabricated using different speeds and different laser powers using the Nanoscribe® system and a 1.4 NA oil immersion lens.

Next, we investigated the surface topography of fabricated structures. Lines with widths of a couple of hundred nanometers were fabricated and observed using SEM (Figure 15A) - the surfaces were observed to be rough and bumpy. For comparison, a droplet of uncrosslinked monomer material was air-dried and observed – a similar, granular texture was observed as can be seen in Figure 15B.

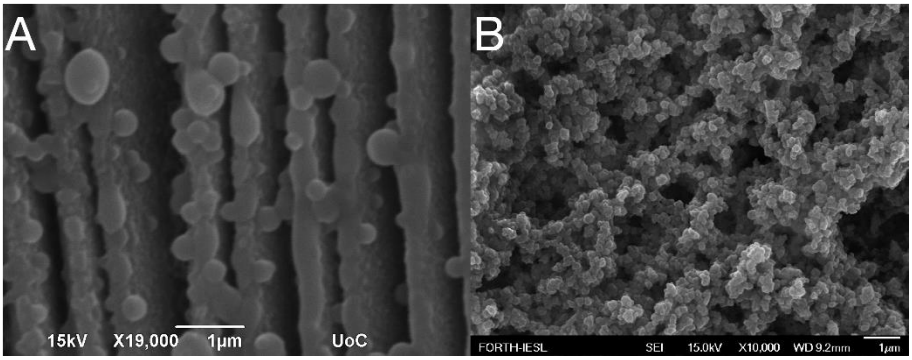

Figure 15. Surface topography of polymerized and unpolymerized Al-based hybrid material. A – lines fabricated using 2 mm/s writing speed and 40X 0.8 NA objective lens. Nanoparticles can be seen on the polymer surface. B – a SEM micrograph of uncrosslinked Al containing hybrid. The material shows a nanoparticle-based surface texture.

Having shown that it is possible to fabricate high quality structures with minimal spatial distortions, we modelled and fabricated suspended lines with varying laser power and scanning speed between bulky support structures to assess maximum resolution of the Al hybrid (Figure 16). Lines that survived the development process, reproducibly reached < 200 nm in width using the 100X 1.4 NA oil immersion lens on the custom-built DLW system and <250 nm using a 63X 1.4 NA oil immersion lens on the Nanoscribe® system.

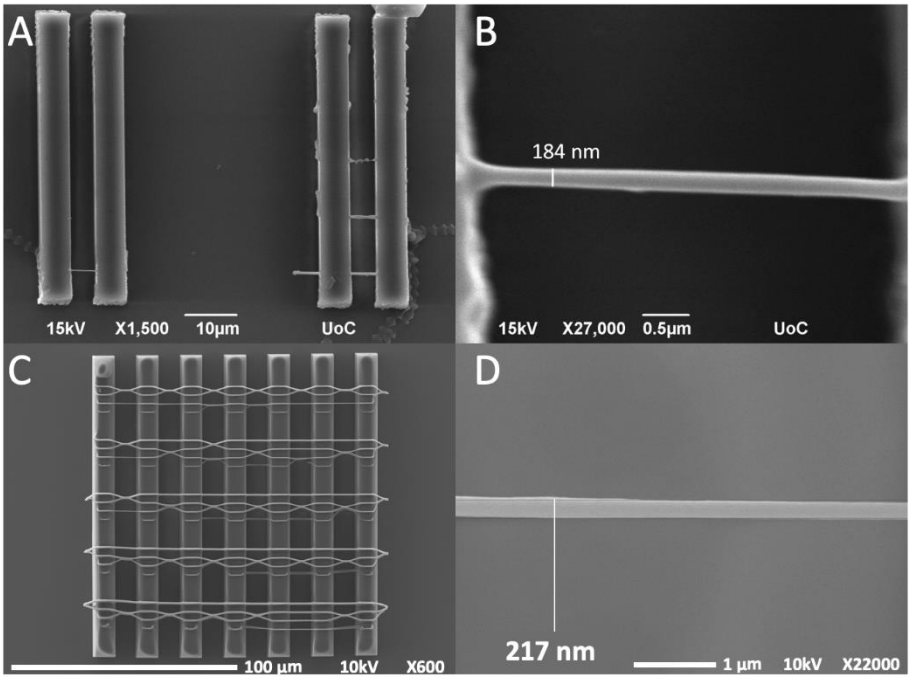


Figure 16. Support structures with suspended lines between them fabricated out of the Al containing hybrid material. A, B – structures fabricated using the custom-built DLW system with a 100X 1.4 NA oil immersion lens at different magnifications. C, D – structures fabricated using the Nanoscribe® system with the 63X 1.4 NA oil immersion lens. Lines with resolutions down to around 200 nm were reproducibly fabricated using both systems.

The result is comparable to resolutions reached using other hybrid organic-inorganic materials via DLW. For example, Sakellari *et al.* have achieved 100 nm resolutions in photonic crystal structures fabricated using this techinqe [188].

Finally, complex 3D structures were fabricated – their SEM images are presented in Figure 17. The structures survived the fabrication and washing processes with minimal shrinkage or deformations. The micro-ship and Lich King statue display detail on par with their CAD models.

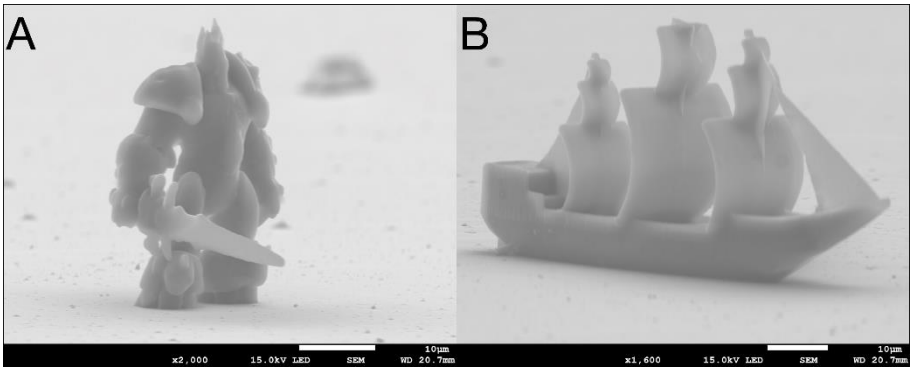

Figure 17. 3D structures fabricated out of the Al containing hybrid material using the Nanoscribe® system and a 63X 1.4 NA oil immersion lens. A – a statue of Lich King was fabricated using 40 % (20 mW) laser power and 10 mm/s scanning speed. B – a micro-ship fabricated using the same parameters. Both scale bars are 10 µm.

All in all, the new Al containing hybrid organometallic polymer demonstrates very good 3D structurability that is comparable to those of Ge, Ti, V and Zr containing polymers. This can be concluded based on extensive literature comparisons. The 3D structuring capacity shows promise for future studies in terms of 3D fabrication, but the question of biocompatibility should be answered first if a tissue engineering strategy based on this new material is to be envisioned.

A successful hard tissue engineering construct will have to incorporate several important parameters – its macro- scale shape will have to match that of the tissue defect to be replaced. In addition to that, the porosity will have to support cellular integration and interconnectivity, so the pore size will have to be on the scale of several to several hundred microns. Both micro- and nano-topographies will have to be tuned in such ways so as to optimise the focal adhesion distribution and thus foster a structure that activates the same signalling pathways inside cells as would natural extracellular surroundings.

### 3.1.4 Protein Adsorption Assay

The biocompatibility study started with an assessment on how extracellular matrix proteins adhere to the different hybdrid organometallic surfaces. Collagen type I was chosen as a model system for this experiment – its adsorption to simple spin-coated samples was assessed due to its abundance in the extracellular matrix. Collagen supports cellular adhesion via RGD sequences, which are specifically recognized by integrins. These interactions ensure strong cellular to ECM binding, so an important factor in designing a TE scaffold is it‘s abbility to support such bioactive molecule adsorption.

Collagen itself has been used as a tissue engineering building block in various studies, like that of Ber *et al.*, where osteoblast growth was guided on 2D surfaces of collagen [189] or work by Ramanathan *et al.*, who have investigated 3D hybrid collagen matrixes as antibacterial dermal substitutes [190]. Collagen and its derivatives are a promising group of materials for soft tissue engineering, while for hard tissue, collagen coating is a highly desirable approach that can be used in conjunction with other materials. Multiple reviews have focused on the use of collagen as a tissue engineering material either in a pure or composite form [191]–[193]. Not only it is supportive of cellular adhesion via integrin activation, but it is also one of the strongest proteins known in nature – a strand with a diameter of 1 mm can hold a weight of around 10 kg [194]. Consequently, the possibility of coating hybrid polymer structures with collagen seems like a promising one and was therefore chosen in this study.

In our experiments, the choice of protein quantification technique was limited by the fact that the presence of photoinitiators within the materials rendered the samples fluorescent. To overcome this issue, a colorimetric assay was employed.

Collagen adsorption was measured on both the hybrid polymers and reference glass slides. We found that even though the largest amount of collagen was found on the Zr surface and the smallest amount – on Al surface, the results in each group were highly disperse with no statistically significant differences between Al and Zr ($p=0.35$), glass and Zr ($p=0.72$) or glass and Al ($p=0.81$). The results are presented in Figure 18.

Figure 18 has been corrected in this electronic version.

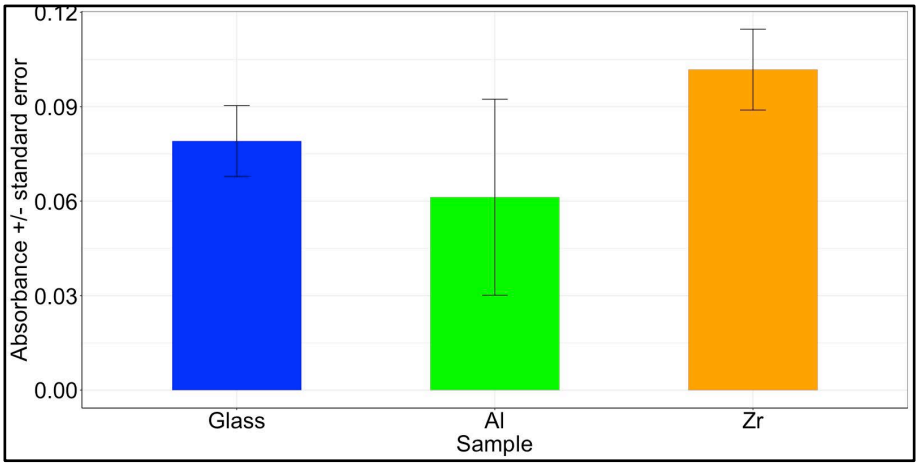


Figure 18. Collagen I adsorption to Al and Zr based hybrid organometallic polymers and glass. The results are presented as average Sirius Red absorbance ± standard error for three independent experiments with n=3 per each experiment (a total of n=9 per material). No statistically significant differences between surfaces were found.

A calibration curve between the total amount of collagen I and Sirius Red absorption was prepared and later used in calculations – it‘s presented in supplementary materials, Figure S1. A highly linear relation was found in the range of 0-100 µg with an $R^2$ value of 0.994. The amounts of collagen adsorbed to the samples was calculated according to the linear model and were found to be 5.59 ± 0.55 µg for Glass, 4.40 ± 1.76 µg for Al and 6.73 ± 0.59 µg for Zr on average per sample.

Previously, we have investigated the contact angles of these materials and found them to be 39 for Glass, 72 for Al and 71 for Zr [176]. The collagen adsorption data does not seem to correlate with the surface contact angles. Even though there is a significant difference between the contact angle of glass to Al or Zr surfaces, the difference in collagen I adsorption could not be distinguished due to a high deviation from the mean. A paper by Ying *et al.* [195] indicates that around a two-fold increase in the adsorption of collagen I to the glass surface is expected with an increase of the surface contact angle from 40 to 70. An analogous result would be expected on other surfaces, since protein adsorption is governed by the same electrostatic and hydrophobic interactions as surface contact angle.

### 3.1.5 Fibroblast Response to Polymer Surfaces

Having established the structurability of the materials as well as their collagen adsorption capacity, we next ventured on to investigate how their surfaces influence cellular viability. For this, we used two cell lines – an embryonic fibroblast cell line (NIH/3T3) and rat muscle stem cells.

We started off with NIH/3T3 fibroblasts, which is a widely used model system for various biocompatibility experiments. For example, Chen *et al.* used this cell line to test the biocompatibility of 3D printed polyurethane/poly (lactic acid)/graphene oxide nanocomposites [196], while Zhang *et al.* have used the same cells to test fluorescent polydopamine organic nanoparticles for imaging [197].

The fibroblasts were seeded on reference glass and Al, Ti, V and Zr containing polymer surfaces and light microscopy images were taken after 96 hours of culture. Healthy fibroblasts tend to be spindle-shaped, while non-viable cells tend to become rounded and detach from the surface. We observed that after 96 hours of culture, spindle-shaped cells can be found on all surfaces except for V hybrids, where the cells tended to become rounded and detach from the surface. Images are presented in Figure 19.

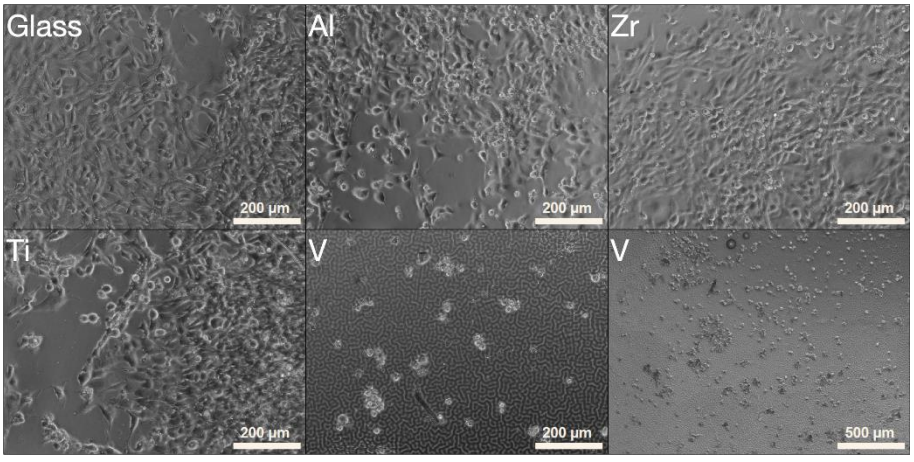


Figure 19. NIH/3T3 fibroblasts grown on organometallic polymer materials and control glass surfaces. Pictures were taken 96 hours after cell seeding using 4X and 10X objective lenses on an inverted light microscope. Cellular morphology is healthy in Glass, Al, Zr and Ti containing polymers. However, none of the cells had attached to the V containing polymers after 96 hours.

To quantify cellular viability, differential staining with AO/EB was applied and the numbers of live, apoptotic and necrotic cells were calculated. Quantitative results confirm that the most cytotoxic surface for cell culture was the V hybrid (Figure 20). The majority of cells had undergone necrosis after 24 hours of culture, while after 96 and 120 there were virtually no living cells remaining on these surfaces. Necrosis was a much more prevalent type of cell death on all of the surfaces as compared to apoptosis. We investigated whether there were any significant differences between the number of live cells on the surfaces. We observed that the number of live cells on all samples (except for the V hybrids) was between 60 and 80 % at all time points (24, 96 and 120 hours).

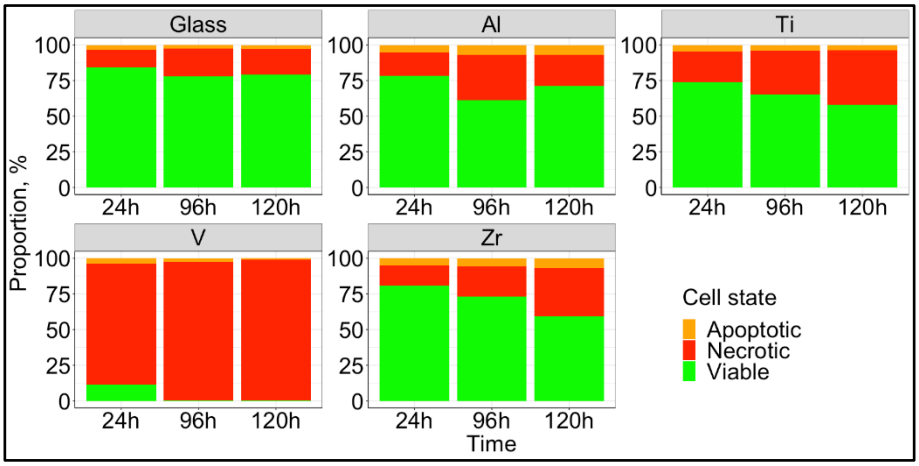


Figure 20. Numbers of live, apoptotic and necrotic NIH/3T3 fibroblast cells on glass, Al, Zr, Ti and V organometallic hybrid materials after 24, 96 and 120 hours of culture determined via acridine orange/ethidium bromide staining. 5 samples per material per time point were used to calculate 100 cells on each. The results are presented as averages. V hybrids were significantly different from all other surfaces with a p value of < 0.001 (***). * - $p < 0.05$, ** - $p < 0.01$, *** - $p < 0.001$.

The V hybrid materials displayed the highest cytotoxicity with the majority of cells dying via necrosis. Statistically significant ($P < 0.001$) differences were found between all samples when compared to the V hybrid material in terms of the number of live and necrotic cells. Our results are in accord with literature as V is known to be toxic both in its elemental and oxide forms [198]. Statistically significant differences are summarised in Table 9. No significant differences between the numbers of apoptotic cells were observed.

Table 9. A summary of statistically significant differences of data in Figure 20. * - p < 0.05, ** - p <0.01, *** - p <0.001.

| Comparison (Surface\|Time) | Live | Necrotic |
|---|---|---|
| Al96-G24 | ** | * |
| Zr120-G24 | *** | ** |
| Ti96-G24 | * | * |
| Ti120-G24 | *** | *** |
| Zr120-G96 | * | - |
| Ti120-G96 | * | * |
| Zr120-Al24 | * | ** |
| Ti120-Al24 | * | - |
| Zr24-Al96 | * | * |
| Zr120-Zr24 | ** | * |
| Ti120-Zr24 | ** | *** |
| G120-Zr120 | * | - |
| G120-Ti120 | ** | * |

NIH/3T3 fibroblasts were cultured for 120 hours on Al, Ti, V and Zr containing polymers and reference glass slides. The metabolic activity data is presented as a ratio of optical density of cells grown on the hybrid materials to that of cells grown on glass (Figure 21). In accordance with light microscopy images and AO/EB staining results, the NIH/3T3 mouse fibroblasts again tended to attach and proliferate on all surfaces except the V hybrid material. The low proliferation rate of cells grown on the V containing surface is consistent with very low viability as shown in the AO/EB assay. Although light microscopy images show comparable numbers of cells on the biocompatible surfaces and comparable numbers of viable cells, the metabolic rates on different materials was substantially different. We observed the highest metabolic activity on the Zr-based hybrid. These findings support the biocompatibility notion of this material together with *in vivo* studies that have previously shown the material to be of comparable biocompatibility to that of a surgical suture composed of glycolide/lactide (Polysorb™ 4-0) [63]. There were no significant differences between the rates of total cellular metabolism on the Al and Ti hybrids. The Zr hybrid was significantly more supportive of cell growth than Al and Ti based hybrids, but all these materials were shown to be promising for TE applications.

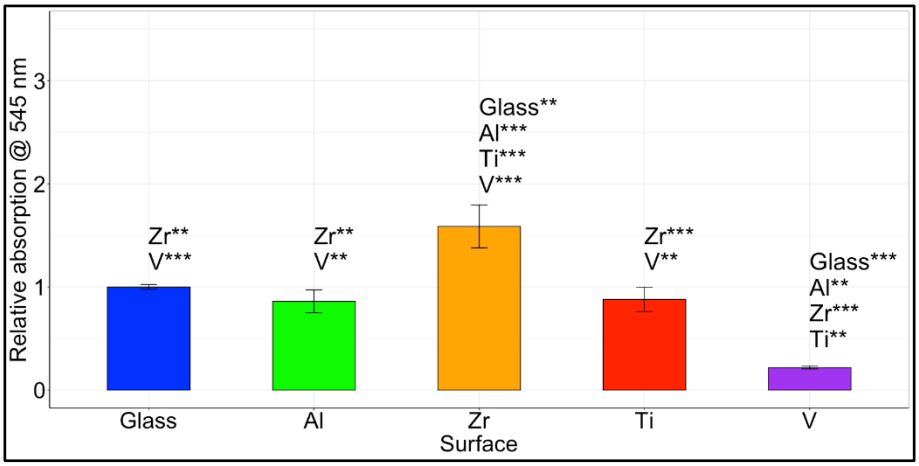


Figure 21. Relative optical density as measured via MTT after 120 hours of NIH/3T3 fibroblast culture. The optical density is directly proportional to the total metabolic activity of cells on each surface. Results are presented as absorption ratio to that of glass ± standard error. ** - $p < 0.01$, *** - $p < 0.001$.

### 3.1.6 Evaluation of Polymer Integrity

We next investigated if the toxicity of V surfaces is due to the surface chemistry and high water contact angle or if it was related to toxic material components being dissolved into the surrounding media. This is important because if the surface is non-biocompatible due to a high contact angle, the issue could be easily solved by biodecoration using more hydrophilic materials, like proteins or adhesion sequences. However, if decomposition products are causing the cytotoxicity, this will cause the surrounding cells and tissues to die upon implantation and will eventually cause inflammation and scarring.

Although aluminium, vanadium and titanium ions are known to be toxic *in vitro* and *in vivo* [199], they are bound in oxide and other compound forms when in hybrid organometallic polymers. However, even trace amounts of these metals can accumulate within cells and cause undesired long-term effects. Therefore, it was important to evaluate their chemical integrities.

Rhoads *et al.* have demonstrated that when present in culture, vanadium oxides are not toxic to human cells, but were highly toxic when in the form of nanotubes [200]. The shape of the nanotubes was found to have an impact on the level of toxicity, suggesting that the mechanism of cell damage is associated with either adhesion molecule inhibition or damage to the plasma membrane. This could imply that nanostructures are being formed during the

DLW process that damage cells due to their sharp nano-structure that pierces cellular membranes, inducing the observed necrosis. However, the formation of V nano-crystals was not within the scope of this study and would have to be investigated using transmission electron microscopy separately.

Another study by Sabbioni *et al.* investigated how BALB/3T3 cells are affected by vanadium (IV) and vanadium (V) [201]. Having treated cells in culture with doses ranging from $10^{-5}$ to $5x10^{-8}$ M, they found that concentrations of ammonium or sodium metavanadate above a $10^{-5}$ M exposure were highly cytotoxic with < 3 % the initial cellular viability, while that of vanadyl sulphate were reduced to only <17 % at the same concentration. Vanadium leaching from the polymers was assessed using the following experiment.

First, polymer extracts in full growth medium were prepared and applied to monolayers of cultured cells. The results are presented in Figure 22. Cells grown in control medium were shown to have a comparable, but slightly lower rate of metabolism as compared to Al, Zr and Ti polymer extracts. Interestingly, there was even a significant difference between Al and control extracts with $p < 0.05$. However, as predicted, the V cell group were not metabolically active, indicating that the V containing material tended to leach toxic components into the medium.

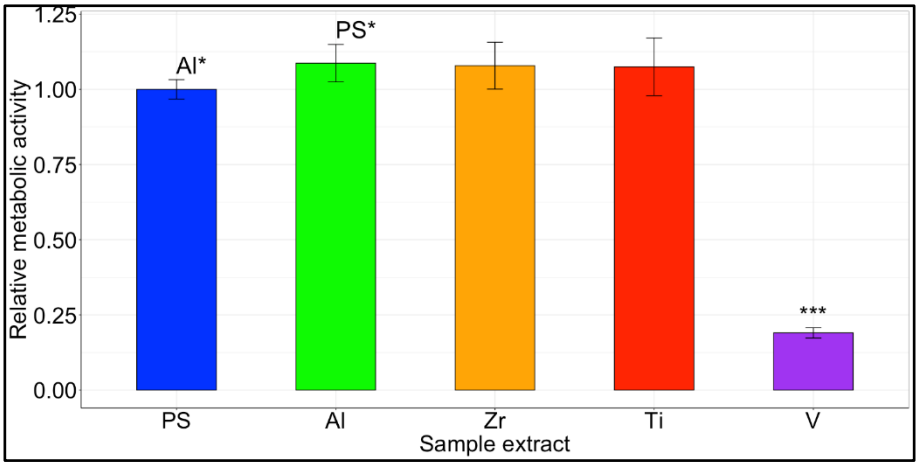


Figure 22. NIH/3T3 fibroblasts cultured in media containing the polymer extracts. Results are presented as absorption ratio to that of glass ± standard deviation. Al and control surfaces had a significant difference with * - $p < 0.05$, while V was significantly different from all other surfaces with *** - $p < 0.001$. PS – polystyrene.

The potential cytotoxicity of other metal containing polymers did not manifest itself during this experiment, suggesting that the levels of metal ions and compounds that were released into the medium were too low to have an effect. However, aluminium ions are known to have pro-oxidant and genotoxic properties [202], therefore their release to the surrounding tissue should be kept to a minimum.

To investigate whether the V containing polymer is releasing parts of it to the media, an ICP-OES experiment was performed. This demonstrated that the Al, Ti and Zr containing polymers had basically no metal leeching. V, on the other hand, had shown substantial leeching from the polymer with 35000 parts per million of PBS salt crystals being vanadium ions. The results are presented in Figure 23.

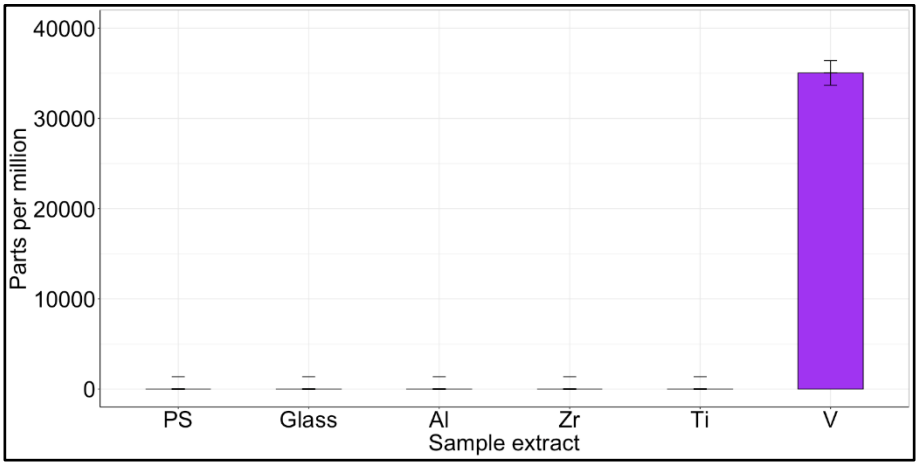


Figure 23. ICP-OES data of extracts from polystyrene (PS), glass, Al, Zr, Ti and V.

Results show a very high level of particles getting washed out of the surface, suggesting a low chemical integrity of the polymer. This would result in significant V accumulation within cellular cytosol, oxidating and modifying cellular components of cytosol and some organelles – mitochondria, lysosomes, and microsomes [201].

### 3.1.7 Assessment of Biocompatibility Using Muscle Stem Cells

A rat muscle cell line was used to model a situation that would be as close as possible to a clinical one. Using primary muscle-derived stem cells seems like a promising approach due to the abundance of donor tissue sites, rel-

atively mild donor site morbidity and high proliferative capacity as well as multipotency of the cells. Our isolated rat muscle-derived progenitor cells were positive for CD34, MYF5 and c-kit and negative for CD45 – see Figure 24. CD34 is a cell surface phosphoglycoprotein that is involved in adhesion with other cells. Although mostly found in hematopoietic stem cells, the presence of CD34 in parenchymal cells is asociated with progenitor or stem cell-like properties [203]. Myf5 is a myogenic factor found in cells of myogenic origin [204]. The presence of this factor shows that the cells were indeed of muscular nature. c-kit (also known as CD117) is another hematopoietic and multipotent progenitor-specific marker. It is a tyrosine kinase, responsible for survival, proliferation and differentiation signalling [205]. CD45 is a receptor tyrosine phosphatase, responsible mostly for cytokine receptor, like JAK kinases, signal attenuation and is most commonly found in terminally differentiated cells of hematopoietic or mesenchymal origin. Results suggest that the investigated cells are not terminally differentiated [206], [207] and that they could be considered as being stem cells.

A great example by Nieponice *et al.* demonstrates how rat muscle-derived stem cells could be used together with elastomeric scaffold-building materials in constructing vascular grafts [208]. The study successfully showed that the cells tended to home to the lumen of the vascular grafts and started to express α-actin, calponin as well as secrete collagen. Endothelial differentiation was supported because of the presence of von Willebrand factor.

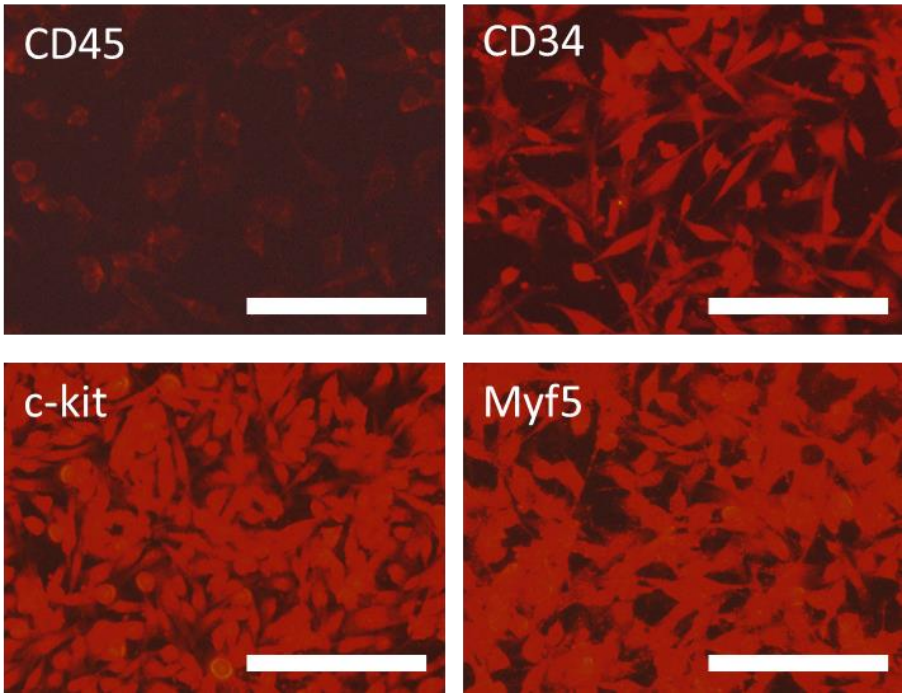

Figure 24. Characterization of rat skeletal muscle-derived cells. Fluorescence microscopy images of cells immunostained for CD45, CD34, c-kit and MYF5. The scale bars correspond to 100 μm.

In this part of the investigation, only three surfaces were used – glass, Al and Zr. Since V was shown to be toxic and while Ti and Zr were comparable, Zr was chosen due to its wider use in DLW applications and a higher number of reports.

First, light microscopy images were taken at different time points. No significant differences were observed neither in daily culture check-ups nor in the images taken of those cells as seen in Figure 25. Rat muscle stem cells had healthy spindle-shaped morphologies and stopped dividing after having reached confluency.

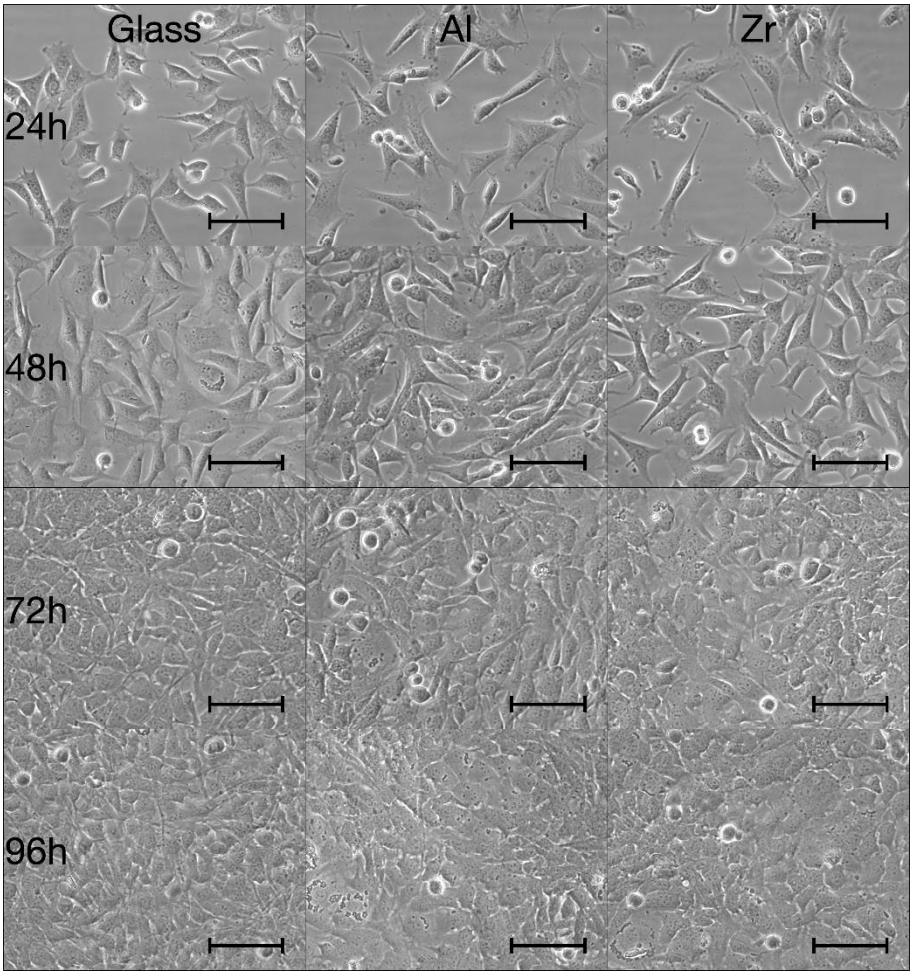

Figure 25. Representative images of cells grown on glass (first column), Al (second column) and Zr (third column) surfaces after 24 (first row), 48 (second row), 72 (third row) and 96 (fourth row) hours. 20X magnification. The scalebars correspond to 100 μm.

The next step of this experiment was aimed at finding the ratios between the numbers of viable, apoptotic and necrotic cells at different time points and on different surfaces. Flow cytometry data shows that no statistically significant differences between the numbers of cells in each category can be observed, since the majority of cells at each time point was viable – see flow cytometry data in Figure 26.

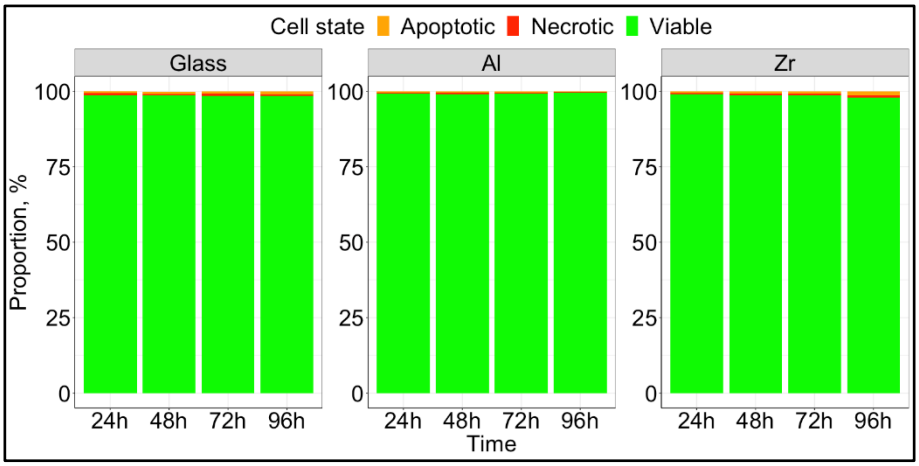


Figure 26. Flow cytometry data on cellular viability on Glass, Al and Zr surfaces after 24, 48, 72 and 96 hours. The results are presented as average absorbance derived from 3 independent experiments with n=3 per experiment. No statistically significant differences were found between the surfaces.

The results are in accord with the data on NIH/3T3 cells as presented previously in Figure 20. Similar levels of NIH/3T3 fibroblast viability were observed on Ti and Zr based hybrid materials by Psycharakis *et al.* [58]. The results obtained with both cell types are highly promising for the future applications of both Al and Zr based hybrid materials.

Having shown that cells form confluent monolayers and are viable on most of the materials, the next step in assessing polymer biocompatibility was to measure their metabolic activity. For this purpose, an MTT assay was performed. This assay provides a direct link between optical density and the total metabolic activity of cells. It is important to know if cellular metabolism rates are different among the various surfaces, since significant deviations could potentially yield new properties of the cell population on that particular surface. Increased rates of metabolism could be associated with malignant formations and dysregulation of the cell cycle, while down-regulated rates of metabolism could indicate low cellular viability or transfer into a more quiescent state via differentiation or other mechanisms.

The total metabolic activity as assessed using MTT revealed that the metabolic rate of cells grown on glass was significantly higher than on the hybrid organometallic polymers after 72 and 96 hours of culture ($p < 0.001$) and significantly higher than on the Al based hybrid just after 48 hours ($p < 0.05$). These results are presented in Figure 27.

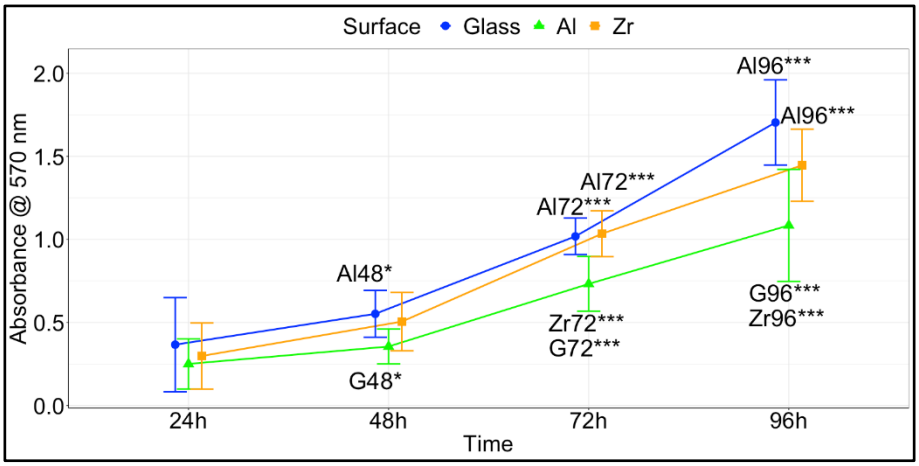


Figure 27. Cell proliferation as measured by MTT. The results are presented as average ± standard deviation. A total of 9 measurements were performed per material per time point (3 independent experiments with 3 repetitions in each).

The results obtained in this experiment show promise in using both the Al and Zr hybrid polymers in tissue engineering applications with primary stem cell sources. Both the materials supported cell growth, even though the total rate of metabolism was lower than on reference glass surfaces.

### 3.1.8 Assessment of Adhesion Strength

Once the cells are seeded on the investigated surfaces *in vitro*, they adhere to the surface-bound proteins via integrins, attach to one another via cadherins and also interact non-specifically. Depending on the interplay between these processes, different levels of adhesion strength are reached. To assess the strength of adhesion, an experiment was devised involving intense shaking of cell-bound surfaces. Cellular viability, proliferation and adhesion are highly intertwined processes. Seeing that the viability does not change significantly with surface and that the rate of cellular metabolism grown on the Al hybrid is lower than on the Zr surface, we next assessed if the reduced metabolic activity was associated with weaker adhesion. Rat muscle stem cells were seeded on the samples and then shaken vigorously at two time points. The number of remaining cells was counted and calculated against the number of cells on reference surfaces without shaking. The results are presented in Figure 28. There was a clear trend that showed a decrease in the number of adhered cells after 24 hours, suggesting that the initial stage of attachment after 4 hours was stronger. Even though there were substantial differences between the

number of adhered cells after 24 hours, the differences were not significant. However, in spite of a lack of statistical significance, the number of cells that remained attached to the Al surface was the lowest and thus in accord with the proliferation data that showed the lowest rate of MTT metabolism on the Al containing hybrid. This leads to the conclusion that Al is less supportive of cell adhesion. The reason for that could potentially be the lowest adsorption of collagen to the Al surface, as presented back in Figure 18.

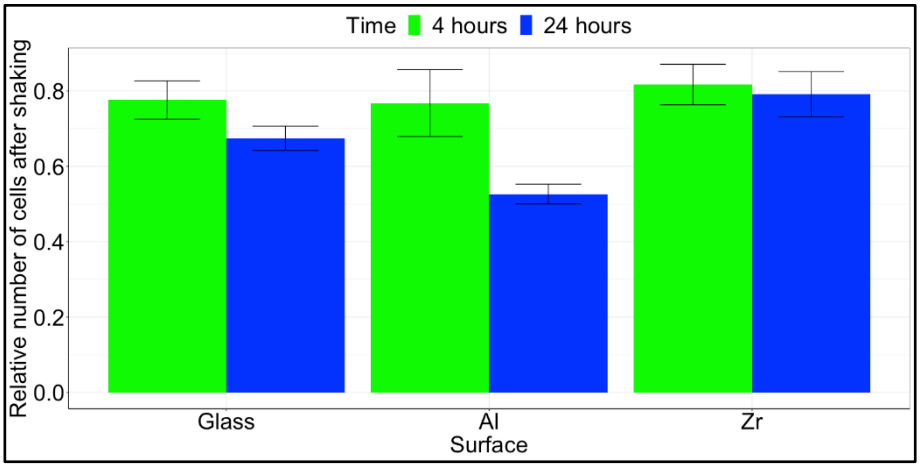


Figure 28. The results are presented as a ratio between the average number of cells after shaking to that of cells before shaking after 4 and 24 hours of culture ± standard deviation. A total of 9 measurements per material were performed (3 independent experiments with 3 replicates in each). No statistically significant differences were observed between the different time points on each surface.

To further investigate this difference, an experiment was devised to assess the expression of adhesion-associated proteins.

### 3.1.9 Adhesion-Associated Protein Expression

When integrin-mediated cell adhesion takes place, a cascade of biochemical reactions is activated that delivers a signal about cellular attachment to the cell nucleus, which in turn activates the transcription and translation of certain proteins that are required for these processes. The cascade is activated when cell surface integrins dimerise and bind to a specific adhesion sequence in the ECM [209]. Upon dimerization, integrins autophosphorylate and then multiple other adhesion-associated proteins are being recruited to the site, like FAK (focal adhesion kinase), which is one of

the first proteins to join the newly forming focal adhesion. Upon formation of a focal adhesion, multiple pathways can be activated, one of which is the Akt pathway. It is responsible for transferring a survival and proliferation signal to the nucleus via the mTOR pathway [210]. Akt can be activated by either phosphorylation on Ser473 or Thr308 – this depends on the phosphorylating protein. In the case of integrin-mediated adhesion, PI3K is being activated and thus, only Ser473 is phosphorylated [211]. Phosphorylation on the Thr308 occurs from mTORC2 [212], which is associated with cellular metabolism and cytoskeletal reorganisation.

To assess the expression and activation of adhesion-associated FAK pathway proteins, a Western blot analysis was performed on cells grown on the investigated glass, Al and Zr surfaces. The results of the Western blot analysis are presented in Figure 29. Even though no statistically significant results were observed on the investigated surfaces, a tendency for reduced phosphorylation of Akt kinase can be seen in most of the cases when comparing 4 and 24 hours. This is to be expected as the role of adhesion-associated Akt kinase is mostly pronounced during the initial cell-to-surface and cell-cell interactions that take place upon cell seeding.

Figure 29 has been corrected in this electronic version.

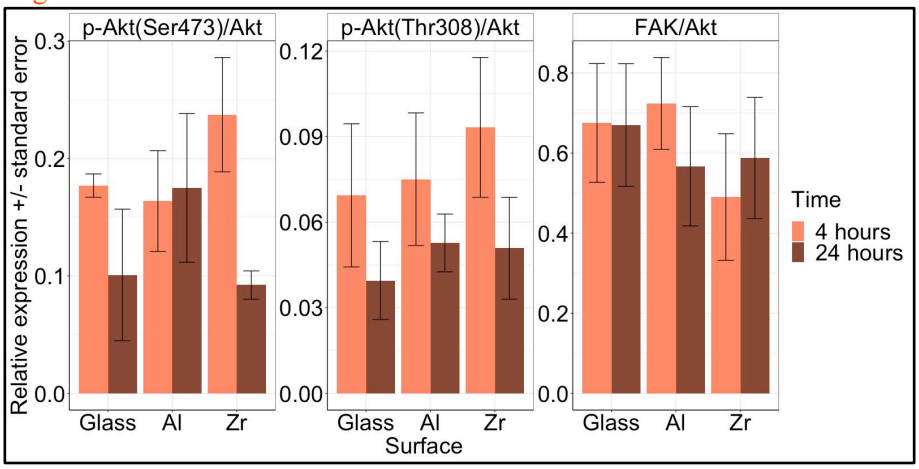


Figure 29. Western blot data, showing the expression of FAK and the expression and activation of Akt kinase after 4 and 24 hours of culture on glass, Al and Zr surfaces. The amount of p-Akt (Ser 473), p-Akt (Thr308), Akt and FAK were observed. The results are presented as relative expression. Three independent experiments were performed. No statistically significant differences were observed.

The ratio between FAK and Akt kinases was mostly unchanged between time points and only slightly and insignificantly lower on Zr surfaces. This is

to be expected as the ratio between the amount of total FAK and Akt kinases should remain unchanged unless there are significant changes in the numbers of focal adhesions that are being formed. On the glass surface, the cells tended to attach stronger during the initial 4 hours – this is in accord with a higher level of Akt kinase activation in this time point. After 24 hours the drop in the number of adhered cells and p-Akt (both Ser473 and Thr308) could be observed, though insignificant.

On the Al surface, the situation is similar in terms of p-Akt (Thr308), where the amount of phosphorylated Akt drops after 24 hours suggesting decreased cytoskeletal remodelling-associated signalling. However, this was not observed in the p-Akt (Ser473) test. The level of FAK appeared to decrease as well, suggesting that the number of focal adhesions had been reduced.

The highest drop in terms of level of phosphorylation was observed on the Zr surface. From 4 to 24 hours, the level of p-Akt (Ser473) dropped with a $p=0.25$ and the level of p-Akt (Thr308) dropped with a $p=0.67$. A slight, but insignificant increase was observed in the level of total FAK. Even though the changes in phosphorylation of Akt on Zr surfaces was the highest, the change in observed cell detachment was lowest in this case.

Even though some tendencies in cell attachment and adhesion-associated protein expression can be seen, a more thorough investigation is needed if these processes are to be linked with statistical confidence.

Strong cellular adhesion is an essential prerequisite for successful tissue engineering techniques as discussed in a review by Lee *et al.* [213]. Whenever adhesion-associated signalling is insufficient, anchorage-dependent cells undergo anoikis. Therefore, a longer-term *in vitro* study should be performed additionally in order to evaluate how the adhesion-associated protein expression and activation changes over time and whether that impacts cellular adhesion, viability and metabolism in a significant way.

### 3.1.10 Evaluation of Collagen Synthesis

Finally, we wanted to investigate whether the surface had any effect on the synthesis of collagen type I. Rat muscle stem cells were grown on the hybrid polymer surfaces for 1, 7 or 14 days and the amounts of collagen secreted at these time points was registered.

Even though the adsorption was weakest to the Al-based hybrid and so was the cellular adhesion and proliferation, the synthesis of collagen in cells grown on the Al hybrid was the highest. The results are presented in Figure 30. The

difference is already visible after one week, but the difference only becomes significant after 2 weeks. This is to be expected as the process of extracellular matrix remodelling takes a substantial amount of time. Other statistically significant differences were observed between Al surfaces after 1 day, 1 week and 2 weeks with $p < 0.001$ between all periods. As well as Zr surfaces after 1 day and 1 week with a $p < 0.05$.

The results are highly promising for tissue engineering applications, because they show a significant increase in the amount of collagen produced in cells grown on the Al containing hybrid surfaces.

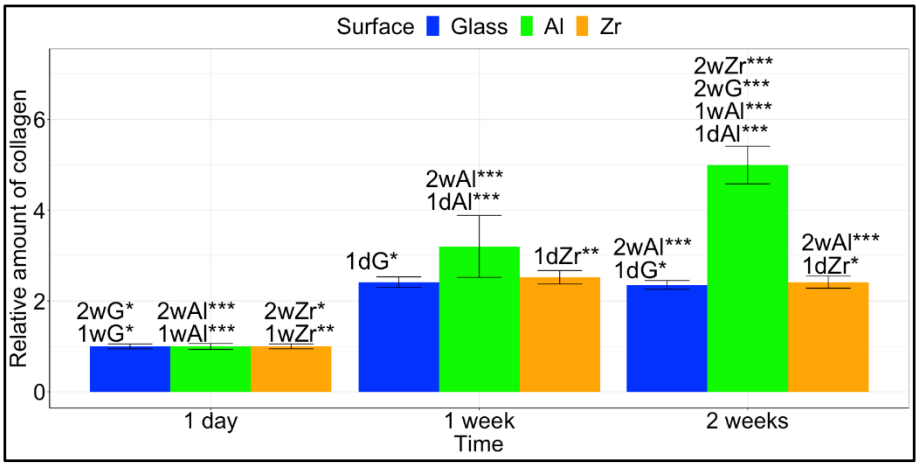


Figure 30. Collagen synthesis. Relative amount of collagen produced by cells grown on the different surfaces after 1 day (1d), 1 week (1w) and 2 weeks (2w). * - $p < 0.05$, ** - $p < 0.01$, *** - $p < 0.001$.

The growth media used in our study contained 10 % foetal bovine serum, which is mostly composed of non-adhesion proteins. The cells were shown to secrete collagen and were likely secreting other ECM proteins. It is highly likely that the cells bind to integrin-activating sequences in ECM proteins that are found in trace amounts in the medium during subculture (secreted by the cells). As demonstrated by Koblinski *et al.* [214], non-adhesion proteins like bovine serum albumin (present in the foetal bovine serum), significantly increase integrin binding to small amounts of ECM proteins. This is further supported by the results in Figure 29 that indicate adhesion-associated molecules Akt and FAK are more highly activated (though insignificantly) in the initial stages of cell attachment to the surfaces.

## 3.2 Soft Tissue Engineering

### 3.2.1 PDMS Biodecoration Influence on Biocompatibility

Biodecoration is a process in which the surface of a material is treated with an additional layer of biofuncional substances. This can be a range from simple biomolecules like peptides, oligonucleotides or polysaccharides to proteins, antibodies and complex extracellular matrix-mimicking assemblages. Biodecoration can be achieved using different techniques – by covalently crosslinking biomaterials to the surface, by linking non-covalently via adsorption and by mixing into the bulk of the material so that parts of the biomolecules are exposed to the surfaces and are accessible by cellular receptors. These approaches have been widely reviewed in the literature [215], [216].

Biodecoration can also be applied to nanoparticles, where additional features imbued by the biomolecules would allow the nanoparticles to be transported directly to the target cell types [217]. A great example of this was demonstrated by Min *et al.*, where PEG-Pt-prodrug coated gold nanorods were designed to have improved tumour cell targeting properties [218]. Such constructs can be used for cancer treatment by heating the nanoparticle-accumulated cells with subsequent infra-red radiation.

Multiple examples of the applicability of this process in TE can be found in literature. Ma *et al.*, for example, have developed PLA scaffolds with covalently immobilized collagen and coated them with basic fibroblast growth factor [84]. This resulted in significantly improved chondrocyte spreading, distribution and growth.

PDMS is known to be bicompatible both *in vivo* and *in vitro*, but is also known to be hydrophobic [219], [220]. In order to improve cellular adhesion and growth, PDMS surfaces were biodecorated using a selection of materials – collagen, laminin and RGD sequences. Reference PDMS surfaces were incubated in FBS, growth medium or PBS. Figure 31 depicts rabbit muscle stem cells grown on these differently modified surfaces.

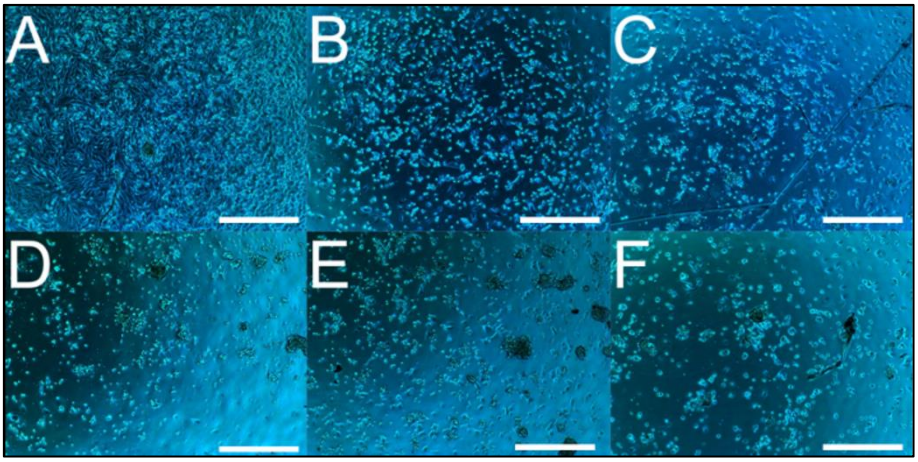


Figure 31. Qualitative assessment of rabbit muscle stem cell growth on differently biodecorated PDMS. Surface treatments: A – collagen, B – RGD tripeptide, C – reference incubated in PBS, D – laminin, E – reference incubated in FBS, F – reference incubated in IMDM supplemented with 10 % FBS and antibiotics. Scale bars correspond to 400 μm.

The images were obtained using fluorescence microscopy and indicate representative cellular morphologies on each surface. The rabbit muscle stem cells tended to form a full monolayer after 48 hours when grown on collagen-coated samples. This was to be expected, since collagen provides an environment that is most reminiscent of the native extracellular matrix.

RGD-functionalised surfaces were less supportive of cell growth, but still significantly better than control. This was in accord with expectation as well, since when crosslinking to the surface, only a fraction of the RGD sequences would take up the optimal conformation [221] that is required for integrin activation and FAK-mediated cell adhesion.

All other surfaces supported comparable levels of cell attachment. Interestingly enough, laminin treatment did not show a significant improvement in cellular adhesion. Laminin is a high molecular weight glycoprotein of the ECM with a specific crux-like conformation. It‘s actively involved in cellular adhesion, migration and differentiation [222]. However, its effects are mostly due to the laminin‘s role in structural maintenance of other proteins in the ECM. Laminin doesn‘t have RGD sequences and this could explain a significantly lower level of cell adhesion. Another explanation could be a lower level of laminin to PDMS adsorption and a conformation that is unfavorable for cell binding. Only certain types of cells have strong laminin interactions – mostly those residing on basement membranes [223]. This is

not to say that laminin can not be used for TE applications – for example, Junka *et al.* used laminin to coat PCL-chitosan nanofibrous matrices, which resulted in a significant improvement in Schwann cell adhesion and proliferation [224].

A further investigation was carried out to assess the rate of cellular metabolism on each surface using MTT. The results of this following experiment are presented in Figure 32.

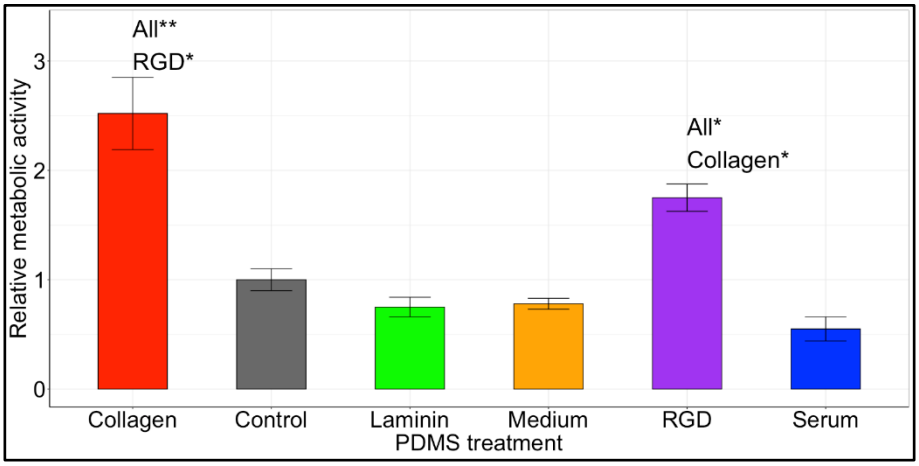


Figure 32. The effects of PDMS surface biodecoration on rabbit muscle stem cell division intensity after 48 hours. This graph presents relative cellular metabolism on differently treated surfaces. Results are presented in comparison to control (PBS-incubated) PDMS surfaces.

The results are in accord with the previous experiment. Cells were significantly more metabolically active on collagen-treated samples than they were on the majority of other surfaces ($p<0.01$). RGD-functionalized surfaces supported a lower cellular metabolic activity than collagen-treated ones ($p<0.05$), but still higher than all other surfaces ($p<0.05$).

### 3.2.2 Investigation of PDMS Block Copolymers

Although PDMS has desirable mechanical and physical properties as well as good structure fabrication potential, its support of cellular adhesion and integration could be improved. One of the ways to do this would be through creating block copolymers with other compounds. Many such composites have been reported. For example, back in the 1999, Sugiyama and colleagues have developed PDMS copolymers with poly(2-methacryloxy)ethyl

phosphorylcholine segments and have shown that they not only had hydrogel properties, but also improved blood protein to surface adsorption [225].

Kai *et al.* have developed poly(ε-PCL)-PDMS copolymers and molded them into fibers with shape memory for bone tissue engineering [76]. To achieve this, an electrospinning technique was used. Changing the proportions between the PCL and PDMS, they were able to fabricate fibers with varying diameters, thermal behaviours and mechanical properties. The fabricated scaffolds were able to recover their shape up to 7 times after mechanical stretching and subsequent heating. In addition to that, the composites showed great biocompatibility with human fetal osteoblasts and some of the combinations improved their osteogenic differentiation.

PDMS-based block copolymers investigated in this work showed varying degrees of swelling in aqueous media, where some materials would expand up to five times their initial volume upon immersion in water. The observed hydrogel properties might prove useful in loading scaffolds with drugs or other bioactive molecules. So first, contact angles of these materials were measured. Results are presented in Figure 33.

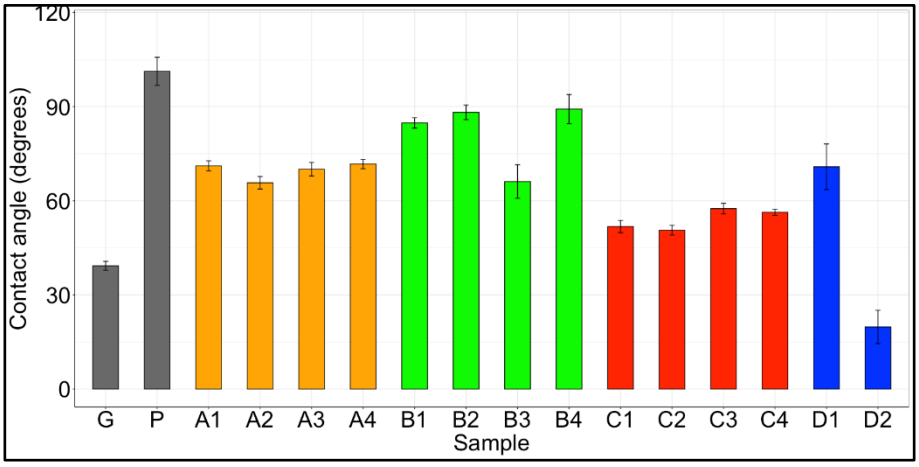


Figure 33. Contact angles of PDMS block copolymers. The results are presented as averages ± standard deviation with n = 5. G – glass, P – PDMS.

Pure PDMS had the highest contact angle of all samples, which surpassed 100 degrees. Copolymers in the A group had comparable contact angles of around 70 degrees. B3 had the lowest contact angle in the entire group, just above 60 degrees, while the others were around 85 degrees. The C group had an overall lowest result with the average contact angle reaching around 50.

The D group was highly discrepant with D2 polymer having the lowest contact angle of about 20 degrees and D1 with around 70.

However, material contact angles don't always correlate with biocompatibility. For example, Seo *et al.* have modified PDMS surfaces using ABA type block copolymers with phospholipid moieties [226]. Resulting polymers had significantly lower contact angles than pure PDMS. Interestingly, the exposed phospholipid groups reduced protein binding to the surface, thus significantly reducing cellular adhesion. This shows that the contact angle is not the only determinant in protein adsorption or cellular adhesion. Therefore, we next investigated the polymer extract cytotoxicity using rat myogenic stem cells. The results are presented in Figure 34.

| Polymer extract | A1 | A2 | A3 | A4 | B1 | B2 | B3 | B4 | C1 | C2 | C3 | C4 | D1 | D2 |
|---|---|---|---|---|---|---|---|---|---|---|---|---|---|---|
| vs PDMS at 24h | + | ± | + | + | + | + | ± | ± | + | - | ± | ± | ± | ± |
| vs PDMS at 48h | - | - | - | - | - | - | + | + | - | ± | - | - | ± | ± |

Figure 34. Polymer extract toxicity *in vitro*. Rat myogenic stem cells were treated with growth media containing extracts from different polymers and then their proliferation activity was measured and compared to reference media incubated with PDMS. Results represent the following: „+" – better than PDMS, „±" – comparable to PDMS and „-" – worse than PDMS.

Some of the investigated material extracts slightly improved cellular proliferation, some have worsened it and part of the materials did not have a significant impact. These results would suggest that some materials release compounds that are toxic to cells, while others release compounds that improve cellular proliferation. Interestingly, the compounds that tended to have a positive effect after 24 hours, had negative effects after 48 hours.

As expected, both the chemical structure and polymerisation conditions had a strong influence on cellular metabolism. Some of the copolymers show promise for use in tissue engineering applications.

Having determined the metabolic activity of cells grown on different PDMS block copolymers, we next wanted to figure out if the differences were cell viability-associated. To that end, they were stained using a mixture of AO and EB after 24 hours of culture. The results are presented as a ratio of fluorescence to reference polystyrene-cultured cells. Results are presented in Figure 35.

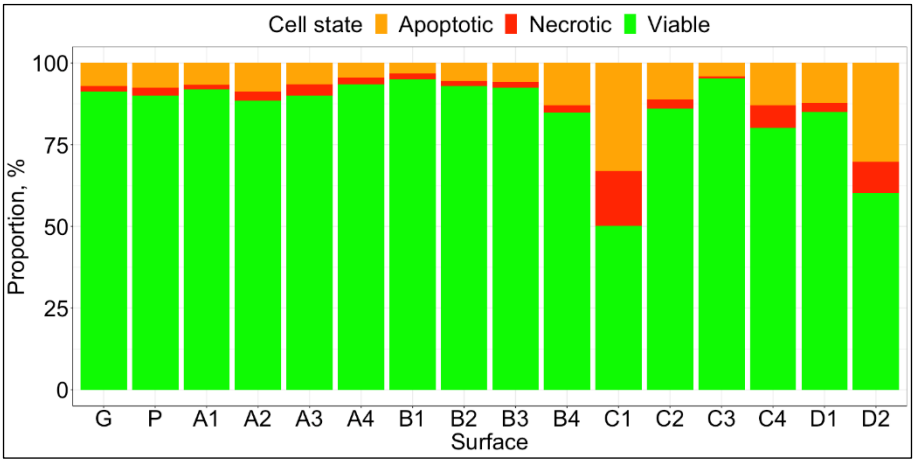


Figure 35. Rat myogenic stem cell fluorescence profiles after 24 hours of culture and AO/EB staining. The results are presented as a ratio to reference polystyrene-cultured cells. G – glass, P – PDMS.

In most cases, the number of viable cells was higher on the block copolymers than on PDMS. B1 and C3 supported the highest levels of cellular viability after 24 hours, reaching around 90 %. C1 and D2 had the lowest levels of viability with around 50-60 % of cells dying during the first 24 hours.

### 3.2.3 Mechanical Properties of Silk-Reinforced PDMS

We observed that the silk-reinforced PDMS samples had some air bubbles formed within the bulks of the fabricated cylinders. This might have influenced the mechanical properties of the samples. A degassing step in a vacuum chamber could improve this aspect of the samples in the future. The silk was observed to have dispersed throughout the samples in an inhomogenous fashion – see Figure 36.

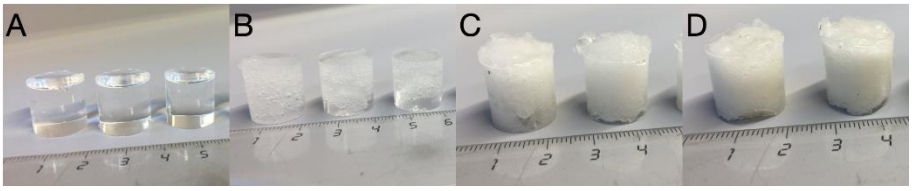


Figure 36. PDMS samples with varying silk content. A – Reference PDMS, B – PDMS with 1 % silk, C – PDMS with 5 % silk, D – PDMS with 10 % silk.

A series of compression tests were performed in order to evaluate how the different composites would react.

First, displacement-load curves were acquired for pure PDMS to assess the reproducibility of mechanical properties between samples. The results are presented in Figure 37. The displacement-load curves were obtained for 5 samples, and subsequently averaged. Hysteresis was observed in the first loading and unloading paths of the stress-strain curves. The results are presented as a scatter plot within the limits of accuracy and their values represent nonlinear elastic behaviour observed during the experiment. The loading at maximum (4 mm) displacement was found to be 145 N (average value of 5 experiments). The results are characterised by a relatively low scattering of 3.45 %. Sample to sample variability was observed to be minimal.

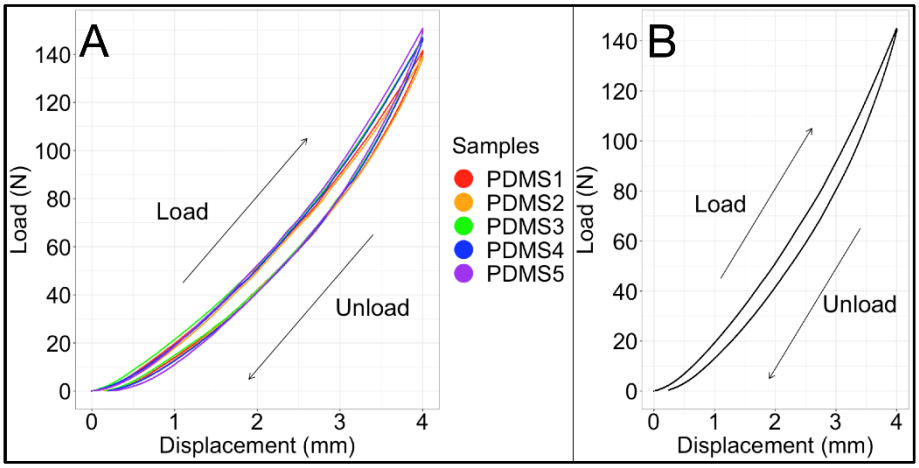


Figure 37. Displacement-load curves of PDMS without silk. The loading and unloading stages of the experiment are indicated in the graphs by arrows. A – the results of 5 independent tests on 5 samples. B – the average displacement-load curve for all 5 experiments.

Next, silk-reinforced samples were tested in the same manner and their stress-strain diagrams were obtained by processing measured load-displacement curves. Calculated stress-strain curves of all the tested materials are shown in Figure 38.

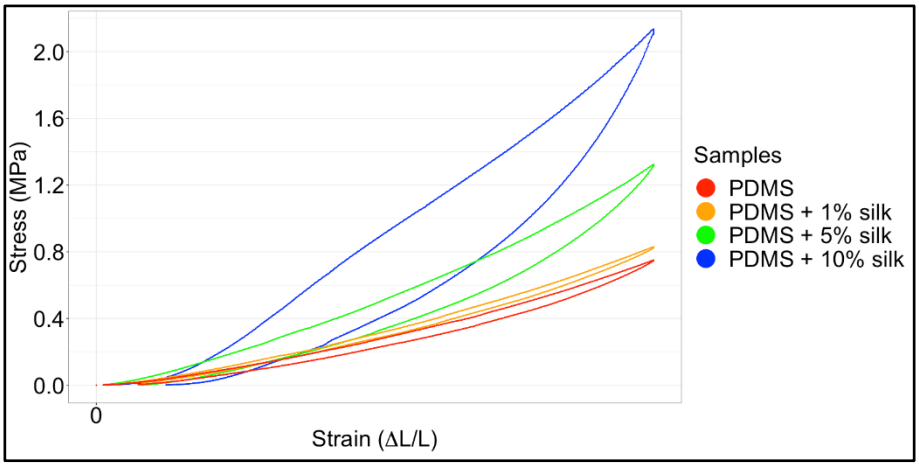


Figure 38. Stress-strain curves of silk-reinforced PDMS samples. The results are presented as average curves of 5 tests per material.

Results show the PDMS samples were the softest with only 752 kPa needed to achieve maximum strain of 0.27 (corresponding to 4 mm sample displacement), corresponding to an elastic modulus of 2.79 MPa. With increasing silk concentration from 1 % to 5 % and 10 %, the maximum stresses (and corresponding elastic moduli) increased to 820 kPa (3.04 MPa), 1324 kPa (4.90 MPa) and 2144 kPa (7.94 MPa), respectively. This means that with increasing silk content, a higher level of force is needed in order to achieve the same displacement. These results are contrary to our initial prediction that the air bubbles formed within the bulks of the cylinder samples would have reduced the rigidity of the samples. The relationship between silk content and elastic modulus is depicted in Figure 39.

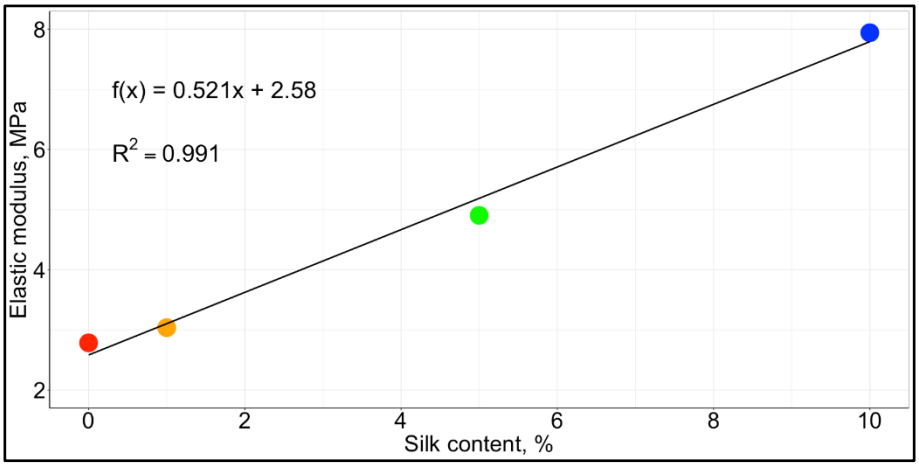

Figure 39. The relationship between silk content and elastic modulus of silk-reinforced PDMS.

Silk reinforcement could potentially be useful not only in attenuating the mechanical properties of the samples, but also in altering the surface properties to accomodate better cellular adhesion and proliferation. For example, Lawrence *et al.* have used silk-based materials to construct corneal scaffolds using human and rabbit corneal fibroblasts [227]. They found that the cellular cytoskeletons tended to align along the silk fiber orientation, implying favorable interactions. The cells remained viable over a period of 10 days.

# CONCLUSIONS

1. A novel hybrid organometallic polymer containing aluminium has been synthesised and characterised in terms of its physicochemical properties. Its water contact angle was found to be around 72 degrees with no significant differences in collagen adsorption when compared to glass or Zr containing hybrid surfaces. The material was shown to retain aluminium within its chemical framework after polymerisation and did not tend to break down significantly in aqueous surroundings.

2. High precision structures were reproducibly fabricated out of the novel Al containing hybrid polymer with resolutions down to 200 nm using direct laser writing. Complex 3D structures with overhanging motifs successfully survived the fabrication and development processes and were well in accord with their CAD models.

3. Al, Ti and Zr containing hybrid polymers are biocompatible *in vitro* with NIH/3T3 fibroblasts and rat myogenic stem cells.

4. Al and Zr containing hybrid polymers showed comparable support of cellular adhesion of rat myogenic stem cells to that of glass.

5. Al containing hybrid polymer was shown to induce the highest level of collagen secretion in rat myogenic stem cells as compared to glass or Zr containing hybrid polymer surfaces.

6. Some novel PDMS block copolymers with BMA-HEMA-VP, AzA-DEG-MAA and GMA-PVA are biocompatible hydrogels *in vitro* when assessing the proliferation of rat myogenic stem cells.

7. PDMS biodecoration using collagen and RGD significantly improves rabbit muscle stem cell adhesion.

8. Incorporating silk into PDMS samples significantly affects its elastic modulus. With increasing silk content, the elastic modulus increases.

# REFERENCES


[1] World Health Organization, "The top 10 causes of death," 2018. https://www.who.int/news-room/fact-sheets/detail/the-top-10-causes-of-death.

[2] J. P. Vacanti *et al.*, "Selective cell transplantation using bioabsorbable artificial polymers as matrices," *J. Pediatr. Surg.*, vol. 23, no. 1, pp. 3–9, 1988.

[3] J. A. Hubbell *et al.*, "Endothelial cell-selective materials for tissue engineering in the vascular graft via a new receptor," *Bio/Technology*, vol. 9, no. 6, pp. 568–572, 1991.

[4] M. L. Yarmush *et al.*, "Hepatic Tissue Engineering: Development of Critical Technologies," *Ann. N. Y. Acad. Sci.*, vol. 665, no. 1, pp. 238–252, 1992.

[5] V. C. Mow *et al.*, "Experimental studies on repair of large osteochondral defects at a high weight bearing area of the knee joint: A tissue engineering study," *J. Biomech. Eng.*, vol. 113, no. 2, pp. 198–207, 1991.

[6] R. Langer *et al.*, "Tissue engineering," *Science*, vol. 260, no. 5110, pp. 920–926, 1993.

[7] A. Shafiee *et al.*, "Tissue Engineering: Toward a New Era of Medicine," *Annu. Rev. Med.*, vol. 68, no. 1, pp. 29–40, 2017.

[8] G. Kaushik *et al.*, "Concise Review: Organ Engineering: Design, Technology, and Integration," *Stem Cells*, vol. 35, no. 1. pp. 51–60, 2017.

[9] A. Atala *et al.*, "Tissue-engineered autologous bladders for patients needing cystoplasty," *Lancet*, vol. 367, pp. 1241–1246, 2006.

[10] J. O. Hollinger *et al.*, "Bone tissue engineering," *Bone Tissue Eng.*, vol. 1, no. 3, pp. 1–337, 2004.

[11] I. Sakellari *et al.*, "Diffusion-assisted high-resolution direct femtosecond laser writing," *ACS Nano*, vol. 6, no. 3, pp. 2302–2311, 2012.

[12] J. Melke *et al.*, "Silk fibroin as biomaterial for bone tissue engineering," *Acta Biomaterialia*, vol. 31, no. 4. pp. 1–16, 2016.

[13] R. Logithkumar *et al.*, "A review of chitosan and its derivatives in bone tissue engineering," *Carbohydrate Polymers*, vol. 151. pp. 172–188, 2016.

[14] J. Venkatesan *et al.*, "Alginate composites for bone tissue engineering: A review," *International Journal of Biological Macromolecules*, vol. 72. pp. 269–281, 2015.

[15] C. T. Kao *et al.*, "Poly(dopamine) coating of 3D printed poly(lactic acid) scaffolds for bone tissue engineering," *Mater. Sci. Eng. C*, vol. 56, pp. 165–173, 2015.

[16] R. Trombetta *et al.*, "3D Printing of Calcium Phosphate Ceramics for Bone Tissue Engineering and Drug Delivery," *Ann. Biomed. Eng.*, vol. 45, no. 1, pp. 23–44, 2017.

[17] N. Bhardwaj *et al.*, "Tissue Engineered Skin and Wound Healing: Current Strategies and Future Directions," *Curr. Pharm. Des.*, vol. 23, no. 24, pp. 3455–3482, 2017.

[18] M. Tenenhaus *et al.*, "Current concepts in tissue engineering: Skin and wound," *Plast. Reconstr. Surg.*, vol. 138, no. 3, pp. 42S-50S, 2016.

[19] J. K. Ho *et al.*, "Successful Application of Tissue Engineering Skin to Third Degree Burn Wound on Lateral Thorax: A Case Study," *Biomed. J. Sci. Tech. Res.*, vol. 16, no. 3, pp. 12122–12125, 2019.

[20] H. Yu *et al.*, "Bioglass Activated Skin Tissue Engineering Constructs for Wound Healing," *ACS Appl. Mater. Interfaces*, vol. 8, no. 1, pp. 703–715, 2016.

[21] Q. L. Loh *et al.*, "Three-dimensional scaffolds for tissue engineering applications: Role of porosity and pore size," *Tissue Engineering - Part B: Reviews*, vol. 19, no. 6. pp. 485–502, 2013.

[22] D. Taniguchi *et al.*, "Scaffold-free trachea regeneration by tissue engineering with bio-3D printing," *Interact. Cardiovasc. Thorac. Surg.*, vol. 26, no. 5, pp. 745–752, 2018.

[23] B. Zhang *et al.*, "Advances in organ-on-a-chip engineering," *Nature Reviews Materials*, vol. 3, no. 8. pp. 257–278, 2018.

[24] A. Skardal *et al.*, "Organoid-on-a-chip and body-on-a-chip systems for drug screening and disease modeling," *Drug Discovery Today*, vol. 21, no. 9. pp. 1399–1411, 2016.

[25] M. B. Esch *et al.*, "Modular, pumpless body-on-a-chip platform for the co-culture of GI tract epithelium and 3D primary liver tissue," *Lab Chip*, vol. 16, no. 14, pp. 2719–2729, 2016.
[26] M. K. Gaydhane *et al.*, "Cultured meat: state of the art and future," *Biomanufacturing Rev.*, vol. 3, no. 1, pp. 1–10, 2018.
[27] C. M. Murphy *et al.*, "Cell-scaffold interactions in the bone tissue engineering triad," *European Cells and Materials*, vol. 26. pp. 120–132, 2013.
[28] A. Eltom *et al.*, "Scaffold Techniques and Designs in Tissue Engineering Functions and Purposes: A Review," *Advances in Materials Science and Engineering*, vol. 2019. pp. 1–13, 2019.
[29] R. N. Babita Mahanta, "An Overview of Various Biomimetic Scaffolds: Challenges and Applications in Tissue Engineering," *J. Tissue Sci. Eng.*, vol. 5, no. 2, p. 1000137, 2014.
[30] T. Billiet *et al.*, "A review of trends and limitations in hydrogel-rapid prototyping for tissue engineering," *Biomaterials*, vol. 33, no. 26. pp. 6020–6041, 2012.
[31] J. Rnjak-Kovacina *et al.*, "Tailoring the porosity and pore size of electrospun synthetic human elastin scaffolds for dermal tissue engineering," *Biomaterials*, vol. 32, no. 28, pp. 6729–6736, 2011.
[32] J. R. McMillan *et al.*, "Small-diameter porous poly (ε-caprolactone) films enhance adhesion and growth of human cultured epidermal keratinocyte and dermal fibroblast cells," *Tissue Eng.*, vol. 13, no. 4, pp. 789–798, 2007.
[33] M. E. Gomes *et al.*, "Influence of the porosity of starch-based fiber mesh scaffolds on the proliferation and osteogenic differentiation of bone marrow stromal cells cultured in a flow perfusion bioreactor," *Tissue Eng.*, vol. 12, no. 4, pp. 801–809, 2006.
[34] B. K. K. Teo *et al.*, "Nanotopography modulates mechanotransduction of stem cells and induces differentiation through focal adhesion kinase," *ACS Nano*, vol. 7, no. 6, pp. 4785–4798, 2013.
[35] W. Yang *et al.*, "Surface topography of hydroxyapatite promotes osteogenic differentiation of human bone marrow mesenchymal stem cells," *Mater. Sci. Eng. C*, vol. 60, pp. 45–53, 2016.
[36] M. Vatankhah-Varnosfaderani *et al.*, "Mimicking biological stress–strain behaviour with synthetic elastomers," *Nature*, vol. 549, no. 7673, pp. 497–501, 2017.
[37] T. Pan *et al.*, "3D Bioplotting of Gelatin/Alginate Scaffolds for Tissue Engineering: Influence of Crosslinking Degree and Pore Architecture on Physicochemical Properties," *J. Mater. Sci. Technol.*, vol. 32, no. 9, pp. 889–900, 2016.
[38] G. C. Reilly *et al.*, "Intrinsic extracellular matrix properties regulate stem cell differentiation," *J. Biomech.*, vol. 43, no. 1, pp. 55–62, 2010.
[39] J. S. Park *et al.*, "The effect of matrix stiffness on the differentiation of mesenchymal stem cells in response to TGF-β," *Biomaterials*, vol. 32, no. 16, pp. 3921–3930, 2011.
[40] K. L. Menzies *et al.*, "The impact of contact angle on the biocompatibility of biomaterials," *Optometry and Vision Science*, vol. 87, no. 6. pp. 387–399, 2010.
[41] N. Lu *et al.*, "Fabrication of PDMS surfaces with micro patterns and the effect of pattern sizes on bacteria adhesion," *Food Control*, vol. 68, pp. 344–351, 2016.
[42] B. Guo *et al.*, "Synthetic biodegradable functional polymers for tissue engineering: A brief review," *Sci. China Chem.*, vol. 57, no. 4, pp. 490–500, 2014.
[43] I. Armentano *et al.*, "Biodegradable polymer matrix nanocomposites for tissue engineering: A review," *Polym. Degrad. Stab.*, vol. 95, no. 11, pp. 2126–2146, 2010.
[44] H. Amani *et al.*, "Three-Dimensional Graphene Foams: Synthesis, Properties, Biocompatibility, Biodegradability, and Applications in Tissue Engineering," *ACS Biomaterials Science and Engineering*, vol. 5, no. 1. pp. 193–214, 2018.
[45] F. C. Pavia *et al.*, "Tuning of biodegradation rate of plla scaffolds via blending with PLA," *Int. J. Mater. Form.*, vol. 2, no. SUPPL. 1, pp. 713–716, 2009.
[46] S. Deville *et al.*, "Freeze casting of hydroxyapatite scaffolds for bone tissue

engineering," *Biomaterials*, vol. 27, no. 32, pp. 5480–5489, 2006.
[47] J. C. Rodrguez-Cabello *et al.*, "Emerging applications of multifunctional elastin-like recombinamers," *Nanomedicine*, vol. 6, no. 1. pp. 111–122, 2011.
[48] P. A. Gunatillake *et al.*, "Biodegradable synthetic polymers for tissue engineering," *European Cells and Materials*, vol. 5. pp. 1–16, 2003.
[49] R. Nazir *et al.*, "π-expanded α,β-unsaturated ketones: Synthesis, optical properties, and two-photon-induced polymerization," *ChemPhysChem*, vol. 16, no. 3, pp. 682–690, 2015.
[50] R. Nazir *et al.*, "Donor-acceptor type thioxanthones: Synthesis, optical properties, and two-photon induced polymerization," *Macromolecules*, vol. 48, no. 8, pp. 2466–2472, 2015.
[51] R. Nazir *et al.*, "π-Expanded 1,3-diketones-synthesis, optical properties and application in two-photon polymerization," *J. Mater. Chem. C*, vol. 4, no. 1, pp. 167–177, 2015.
[52] R. Nazir *et al.*, "Push-pull acylo-phosphine oxides for two-photon-induced polymerization," *Macromolecules*, vol. 46, no. 18, pp. 7239–7244, 2013.
[53] M. Malinauskas *et al.*, "3D microoptical elements formed in a photostructurable germanium silicate by direct laser writing," *Opt. Lasers Eng.*, vol. 50, no. 12, pp. 1785–1788, 2012.
[54] I. Sakellari *et al.*, "Two-photon polymerization of titanium containing sol-gel composites for three-dimensional structure fabrication," *Appl. Phys. A Mater. Sci. Process.*, vol. 100, no. 2, pp. 359–364, 2010.
[55] E. Kabouraki *et al.*, "Redox multiphoton polymerization for 3D nanofabrication," *Nano Lett.*, vol. 13, no. 8, pp. 3831–3835, 2013.
[56] A. Ovsianikov *et al.*, "Ultra-low shrinkage hybrid photosensitive material for two-photon polymerization microfabrication," *ACS Nano*, vol. 2, no. 11, pp. 2257–2262, 2008.
[57] M. Malinauskas *et al.*, "Direct laser writing of microoptical structures using a Ge containing hybrid material," *Metamaterials*, vol. 5, no. 2–3, pp. 135–140, 2011.
[58] S. Psycharakis *et al.*, "Tailor-made three-dimensional hybrid scaffolds for cell cultures," *Biomed. Mater.*, vol. 6, no. 4, p. 45008, 2011.
[59] R. Guo *et al.*, "Micro lens fabrication by means of femtosecond two photon photopolymerization," *Opt. Express*, vol. 14, no. 2, p. 810, 2006.
[60] N. Vasilantonakis *et al.*, "Three-dimensional metallic photonic crystals with optical bandgaps," *Adv. Mater.*, vol. 24, no. 8, pp. 1101–1105, 2012.
[61] B. T *et al.*, "Tailored 3D mechanical metamaterials made by dip-in direct-laser-writing optical lithography," *Adv. Mater.*, vol. 24, no. 20, pp. 2710–2714, 2012.
[62] J. Mačiulaitis *et al.*, "Preclinical study of SZ2080 material 3D microstructured scaffolds for cartilage tissue engineering made by femtosecond direct laser writing lithography," *Biofabrication*, vol. 7, no. 1, p. 15015, 2015.
[63] M. Malinauskas *et al.*, "In vitro and in vivo biocompatibility study on laser 3D microstructurable polymers," *Appl. Phys. A Mater. Sci. Process.*, vol. 108, no. 3, pp. 751–759, 2012.
[64] M. M. Nava *et al.*, "Synthetic niche substrates engineered via two-photon laser polymerization for the expansion of human mesenchymal stromal cells," *J. Tissue Eng. Regen. Med.*, vol. 11, no. 10, pp. 2836–2845, 2017.
[65] A. Ovsianikov *et al.*, "Shrinkage of microstructures produced by two-photon polymerization of Zr-based hybrid photosensitive materials," *Opt. Express*, vol. 17, no. 4, p. 2143, 2009.
[66] K. Terzaki *et al.*, "Pre-osteoblastic cell response on three-dimensional, organic-inorganic hybrid material scaffolds for bone tissue engineering," *J. Biomed. Mater. Res. - Part A*, vol. 101 A, no. 8, pp. 2283–2294, 2013.
[67] B. V Venkataraman *et al.*, "Vanadium toxicity," *Asian J. Exp. Sci.*, vol. 19, no. 2, pp.

127–134, 2005.
[68] Z. X. Meng *et al.*, “Electrospinning of PLGA/gelatin randomly-oriented and aligned nanofibers as potential scaffold in tissue engineering,” *Mater. Sci. Eng. C*, vol. 30, no. 8, pp. 1204–1210, 2010.
[69] P. Gentile *et al.*, “An overview of poly(lactic-co-glycolic) Acid (PLGA)-based biomaterials for bone tissue engineering,” *International Journal of Molecular Sciences*, vol. 15, no. 3. pp. 3640–3659, 2014.
[70] H. Zhou *et al.*, “Nanoscale hydroxyapatite particles for bone tissue engineering,” *Acta Biomaterialia*, vol. 7, no. 7. pp. 2769–2781, 2011.
[71] S. S. Kim *et al.*, “Poly(lactide-co-glycolide)/hydroxyapatite composite scaffolds for bone tissue engineering,” *Biomaterials*, vol. 27, no. 8, pp. 1399–1409, 2006.
[72] L. K. Fiddes *et al.*, “A circular cross-section PDMS microfluidics system for replication of cardiovascular flow conditions,” *Biomaterials*, vol. 31, no. 13, pp. 3459–3464, 2010.
[73] S. J. Choi *et al.*, “A polydimethylsiloxane (PDMS) sponge for the selective absorption of oil from water,” *ACS Appl. Mater. Interfaces*, vol. 3, no. 12, pp. 4552–4556, 2011.
[74] A. Siddique *et al.*, “Improved cell adhesion under shear stress in PDMS microfluidic devices,” *Colloids Surfaces B Biointerfaces*, vol. 150, pp. 456–464, 2017.
[75] A. Mata *et al.*, “Characterization of polydimethylsiloxane (PDMS) properties for biomedical micro/nanosystems.,” *Biomed. Microdevices*, vol. 7, no. 4, pp. 281–293, 2005.
[76] D. Kai *et al.*, “Elastic poly(ε-caprolactone)-polydimethylsiloxane copolymer fibers with shape memory effect for bone tissue engineering,” *Biomed. Mater.*, vol. 11, no. 1, p. 15007, 2016.
[77] D. Saravanan, “Spider silk - Structure, properties and spinning,” *J. Text. Apparel, Technol. Manag.*, vol. 5, no. 1, pp. 1–20, 2006.
[78] A. Varone *et al.*, “The potential of Antheraea pernyi silk for spinal cord repair,” *Sci. Rep.*, 2017.
[79] E. Bini *et al.*, “RGD-functionalized bioengineered spider dragline silk biomaterial,” *Biomacromolecules*, vol. 7, no. 11, pp. 3139–3145, 2006.
[80] X. Wang *et al.*, “Controlled release from multilayer silk biomaterial coatings to modulate vascular cell responses,” *Biomaterials*, vol. 29, no. 7, pp. 894–903, 2008.
[81] M. N. Collins *et al.*, “Hyaluronic acid based scaffolds for tissue engineering - A review,” *Carbohydrate Polymers*, vol. 92, no. 2. pp. 1262–1279, 2013.
[82] M. Putzu *et al.*, “Elastin-like-recombinamers multilayered nanofibrous scaffolds for cardiovascular applications,” *Biofabrication*, vol. 8, no. 4, p. 45009, 2016.
[83] L. Cen *et al.*, “Collagen tissue engineering: Development of novel biomaterials and applications,” *Pediatric Research*, vol. 63, no. 5. pp. 492–496, 2008.
[84] Z. Ma *et al.*, “Cartilage tissue engineering PLLA scaffold with surface immobilized collagen and basic fibroblast growth factor,” *Biomaterials*, vol. 26, no. 11, pp. 1253–1259, 2005.
[85] M. H. Lee *et al.*, “Combined effect of a microporous layer and type I collagen coating on a biphasic calcium phosphate scaffold for bone tissue engineering,” *Materials (Basel).*, vol. 8, no. 3, pp. 1150–1161, 2015.
[86] H. V. Almeida *et al.*, “Anisotropic Shape-Memory Alginate Scaffolds Functionalized with Either Type I or Type II Collagen for Cartilage Tissue Engineering,” *Tissue Eng. Part A*, vol. 23, no. 1–2, pp. 55–68, 2017.
[87] J. A. Burdick *et al.*, “Photoencapsulation of osteoblasts in injectable RGD-modified PEG hydrogels for bone tissue engineering,” *Biomaterials*, vol. 23, no. 22, pp. 4315–4323, 2002.
[88] A. H. Zisch *et al.*, “Cell-demanded release of VEGF from synthetic, biointeractive cell-ingrowth matrices for vascularized tissue growth,” *FASEB J.*, vol. 17, no. 15, pp. 2260–2262, 2003.

[89] Y. Zheng *et al.*, "Polysaccharide-based nanocomposites and their applications," *Carbohydr. Res.*, vol. 405, pp. 23–32, 2015.
[90] L. Russo *et al.*, "Sugar-decorated hydroxyapatite: An inorganic material bioactivated with carbohydrates," *Carbohydr. Res.*, vol. 346, no. 12, pp. 1564–1568, 2011.
[91] C. Zhou *et al.*, "Electrospun bio-nanocomposite scaffolds for bone tissue engineering by cellulose nanocrystals reinforcing maleic anhydride grafted PLA," *ACS Appl. Mater. Interfaces*, vol. 5, no. 9, pp. 3847–3854, 2013.
[92] S. F. Badylak *et al.*, "Whole-Organ Tissue Engineering: Decellularization and Recellularization of Three-Dimensional Matrix Scaffolds," *Annu. Rev. Biomed. Eng.*, vol. 13, no. 1, pp. 27–53, 2011.
[93] A. Lichtenberg *et al.*, "Preclinical testing of tissue-engineered heart valves re-endothelialized under simulated physiological conditions," *Circulation*, vol. 114, no. SUPPL. 1, pp. 559–565, 2006.
[94] P. M. Crapo *et al.*, "An overview of tissue and whole organ decellularization processes," *Biomaterials*, vol. 32, no. 12. pp. 3233–3243, 2011.
[95] Y. C. Choi *et al.*, "Decellularized extracellular matrix derived from porcine adipose tissue as a xenogeneic biomaterial for tissue engineering," *Tissue Eng. - Part C Methods*, vol. 18, no. 11, pp. 866–876, 2012.
[96] J. Zhou *et al.*, "Impact of heart valve decellularization on 3-D ultrastructure, immunogenicity and thrombogenicity," *Biomaterials*, vol. 31, no. 9, pp. 2549–2554, 2010.
[97] C. Quint *et al.*, "Decellularized tissue-engineered blood vessel as an arterial conduit," *Proc. Natl. Acad. Sci. U. S. A.*, vol. 108, no. 22, pp. 9214–9219, 2011.
[98] Z. Wu *et al.*, "Use of decellularized scaffolds combined with hyaluronic acid and basic fibroblast growth factor for skin tissue engineering," *Tissue Eng. - Part A*, vol. 21, no. 1–2, pp. 390–402, 2015.
[99] J. De Waele *et al.*, "3D culture of murine neural stem cells on decellularized mouse brain sections," *Biomaterials*, vol. 41, pp. 122–131, 2015.
[100] J. Zhang *et al.*, "Perfusion-decellularized skeletal muscle as a three-dimensional scaffold with a vascular network template," *Biomaterials*, vol. 89, pp. 114–126, 2016.
[101] Z. Yin *et al.*, "The effect of decellularized matrices on human tendon stem/progenitor cell differentiation and tendon repair," *Acta Biomater.*, vol. 9, no. 12, pp. 9317–9329, 2013.
[102] D. W. Youngstrom *et al.*, "Functional Characterization of Detergent-Decellularized Equine Tendon Extracellular Matrix for Tissue Engineering Applications," *PLoS One*, vol. 8, no. 5, pp. 1–9, 2013.
[103] G. Totonelli *et al.*, "A rat decellularized small bowel scaffold that preserves villus-crypt architecture for intestinal regeneration," *Biomaterials*, vol. 33, no. 12, pp. 3401–3410, 2012.
[104] B. Yang *et al.*, "Development of a porcine bladder acellular matrix with well-preserved extracellular bioactive factors for tissue engineering," *Tissue Eng. - Part C Methods*, vol. 16, no. 5, pp. 1201–1211, 2010.
[105] N. Shirakigawa *et al.*, "Decellularized liver as a practical scaffold with a vascular network template for liver tissue engineering," *J. Biosci. Bioeng.*, vol. 114, no. 5, pp. 546–551, 2012.
[106] H. H. Elmashhady *et al.*, "Decellularized extracellular matrices for tissue engineering applications," *Electrospinning*, vol. 1, no. 1, pp. 1–15, 2017.
[107] F. Blaudez *et al.*, "An overview of decellularisation techniques of native tissues and tissue engineered products for bone, ligament and tendon regeneration," *Methods*, vol. 171. pp. 28–40, 2020.
[108] A. Ovsianikov *et al.*, "Engineering 3D cell-culture matrices: Multiphoton processing technologies for biological and tissue engineering applications," *Expert Review of Medical Devices*, vol. 9, no. 6. pp. 613–633, 2012.

[109] J. Scrimgeour *et al.*, "Three-dimensional optical lithography for photonic microstructures," *Adv. Mater.*, vol. 18, no. 12, pp. 1557–1560, 2006.
[110] G. Kumi *et al.*, "High-speed multiphoton absorption polymerization: Fabrication of microfluidic channels with arbitrary cross-sections and high aspect ratios," *Lab Chip*, vol. 10, no. 8, pp. 1057–1060, 2010.
[111] E. Balciunas *et al.*, "Lithographic microfabrication of biocompatible polymers for tissue engineering and lab-on-a-chip applications," *Biophotonics Photonic Solut. Better Heal. Care III*, vol. 8427, p. 84271X, 2012.
[112] Y. Xia *et al.*, "Soft lithography," *Annu. Rev. Mater. Sci.*, vol. 28, no. 1, pp. 153–184, 1998.
[113] Q. P. Pham *et al.*, "Electrospinning of polymeric nanofibers for tissue engineering applications: A review," *Tissue Engineering*, vol. 12, no. 5. pp. 1197–1211, 2006.
[114] C. Tangsadthakun *et al.*, "Properties of Collagen/Chitosan Scaffolds for Skin Tissue Engineering," *J. Met. Mater. Miner.*, vol. 16, no. 1, pp. 37–44, 2017.
[115] S. A. Poursamar *et al.*, "Potential application of gelatin scaffolds prepared through in situ gas foaming in skin tissue engineering," *Int. J. Polym. Mater. Polym. Biomater.*, vol. 65, no. 6, pp. 315–322, 2016.
[116] A. Xiang *et al.*, "The interplay of phase inversion, polymer membrane formation, and drug release in a membrane-based delivery system," *J. Memb. Sci.*, vol. 358, no. 1–2, pp. 85–92, 2010.
[117] X. Liang *et al.*, "Design and preparation of quasi-spherical salt particles as water-soluble porogens to fabricate hydrophobic porous scaffolds for tissue engineering and tissue regeneration," *Mater. Chem. Front.*, vol. 2, no. 8, pp. 1539–1553, 2018.
[118] Y. Loo *et al.*, "Self-Assembled Proteins and Peptides as Scaffolds for Tissue Regeneration," *Adv. Healthc. Mater.*, vol. 4, no. 16, pp. 2557–2586, 2015.
[119] K. Nagahama *et al.*, "Temperature-induced hydrogels through self-assembly of cholesterol- substituted star PEG-b-PLLA copolymers: An injectable scaffold for tissue engineering," *Adv. Funct. Mater.*, vol. 18, no. 8, pp. 1220–1231, 2008.
[120] J. S. Lee *et al.*, "Thermally induced phase separation in poly(lactic acid)/dialkyl phthalate systems," *J. Appl. Polym. Sci.*, vol. 88, no. 9, pp. 2224–2232, 2003.
[121] C. W. Patterson *et al.*, "Regeneration and expansion of autologous full-thickness skin through a self-propagating autologous skin graft technology," *Clin. Case Reports*, vol. 7, no. 12, pp. 2449–2455, 2019.
[122] G. P. Fadini *et al.*, "Autologous stem cell therapy for peripheral arterial disease. Meta-analysis and systematic review of the literature," *Atherosclerosis*, vol. 209, no. 1. pp. 10–17, 2010.
[123] S. Hu *et al.*, "Isolated coronary artery bypass graft combined with bone marrow mononuclear cells delivered through a graft vessel for patients with previous myocardial infarction and chronic heart failure: A single-center, randomized, double-blind, placebo-controlled cl," *J. Am. Coll. Cardiol.*, vol. 57, no. 24, pp. 2409–2415, 2011.
[124] M. Korthals *et al.*, "The Level of Minimal Residual Disease in the Bone Marrow of Patients with Multiple Myeloma before High-Dose Therapy and Autologous Blood Stem CellTransplantation Is an Independent PredictiveParameter," *Biol. Blood Marrow Transplant.*, vol. 18, no. 3, pp. 423–431, 2012.
[125] L. M. De La Fuente *et al.*, "Transendocardial autologous bone marrow in myocardial infarction induced heart failure, two-year follow-up in an open-label phase I safety study (the TABMMI study)," *EuroIntervention*, vol. 7, no. 7, pp. 805–812, 2011.
[126] L. Orozco *et al.*, "Treatment of knee osteoarthritis with autologous mesenchymal stem cells: A pilot study," *Transplantation*, vol. 95, no. 12, pp. 1535–1541, 2013.
[127] M. Radaelli *et al.*, "Autologous bone marrow transplantation for the treatment of multiple sclerosis," *Curr. Neurol. Neurosci. Rep.*, vol. 14, no. 9, p. 478, 2014.
[128] E. Minami *et al.*, "Response to 'Comment on "Transplantation of undifferentiated

murine embryonic stem cells in the heart: teratoma formation and immune response,"" *FASEB J.*, vol. 21, no. 7, pp. 1291–1291, 2007.
[129] J. G. Lees *et al.*, "Transplantation of 3D scaffolds seeded with human embryonic stem cells: Biological features of surrogate tissue and teratoma-forming potential," *Regen. Med.*, vol. 2, no. 3, pp. 289–300, 2007.
[130] W. Zhao *et al.*, "Embryonic stem cell markers," *Molecules*, vol. 17, no. 6. pp. 6196–6236, 2012.
[131] Y. Zhang *et al.*, "Plasticity of marrow mesenchymal stem cells from human first-trimester fetus: From single-cell clone to neuronal differentiation," *Cell. Reprogram.*, vol. 13, no. 1, pp. 57–64, 2011.
[132] Z. Y. Zhang *et al.*, "A comparison of bioreactors for culture of fetal mesenchymal stem cells for bone tissue engineering," *Biomaterials*, vol. 31, no. 33, pp. 8684–8695, 2010.
[133] T. Aboushwareb *et al.*, "Stem cells in urology," *Nature Clinical Practice Urology*, vol. 5, no. 11. pp. 621–631, 2008.
[134] J. Antonucci *et al.*, "Human amniotic fluid stem cells culture onto titanium screws: A new perspective for bone engineering," *J. Biol. Regul. Homeost. Agents*, vol. 23, no. 4, pp. 277–279, 2009.
[135] A. Peister *et al.*, "Amniotic fluid stem cells produce robust mineral deposits on biodegradable scaffolds," *Tissue Eng. - Part A*, vol. 15, no. 10, pp. 3129–3138, 2009.
[136] G. M. Roomans, "Tissue engineering and the use of stem/progenitor cells for airway epithelium repair.," *European cells & materials*, vol. 19. pp. 284–299, 2010.
[137] M. Cananzi *et al.*, "Stem Cells Derived from Amniotic Fluid," *Essentials Stem Cell Biol. Third Ed.*, vol. 18, pp. 141–156, 2014.
[138] R. B. Jaffe, "Isolation of amniotic stem cell lines with potential for therapy: Commentary," *Obstetrical and Gynecological Survey*, vol. 62, no. 5. pp. 316–317, 2007.
[139] C. J. Lengner, "IPS cell technology in regenerative medicine," *Ann. N. Y. Acad. Sci.*, vol. 1192, pp. 38–44, 2010.
[140] N. Maherali *et al.*, "Directly Reprogrammed Fibroblasts Show Global Epigenetic Remodeling and Widespread Tissue Contribution," *Cell Stem Cell*, vol. 1, no. 1, pp. 55–70, 2007.
[141] J. Bilic *et al.*, "Concise review: Induced pluripotent stem cells versus embryonic stem cells: Close enough or yet too far apart?," *Stem Cells*, vol. 30, no. 1. pp. 33–41, 2012.
[142] C. D *et al.*, "Therapeutic potential of adult bone marrow-derived mesenchymal stem cells in diseases of the skeleton," *J. Cell. Biochem.*, vol. 111, no. 2, pp. 249–257, 2010.
[143] J. Rehman *et al.*, "Peripheral blood 'endothelial progenitor cells' are derived from monocyte/macrophages and secrete angiogenic growth factors," *Circulation*, vol. 107, no. 8, pp. 1164–1169, 2003.
[144] M. R. Alison, "Liver stem cells: Implications for hepatocarcinogenesis," *Stem Cell Rev.*, vol. 1, no. 3, pp. 253–260, 2005.
[145] Y. Li *et al.*, "Isolating stem cells from soft musculoskeletal tissues," *J. Vis. Exp.*, vol. 41, no. 41, pp. 1–3, 2010.
[146] M. S. Parmacek, "Cardiac stem cells and progenitors: developmental biology and therapeutic challenges.," *Transactions of the American Clinical and Climatological Association*, vol. 117. pp. 239–255, 2006.
[147] K. Jezierska-Woźniak *et al.*, "[Use of adipose tissue as a source of mesenchymal stem cells].," *Postepy Hig. Med. Dosw. (Online)*, vol. 64, pp. 326–32, 2010.
[148] L. Wang *et al.*, "Musculoskeletal tissue engineering with human umbilical cord mesenchymal stromal cells," *Regenerative Medicine*, vol. 6, no. 1. pp. 95–109, 2011.
[149] D. Schmidt *et al.*, "Umbilical cord blood derived endothelial progenitor cells for tissue engineering of vascular grafts," *Ann. Thorac. Surg.*, vol. 78, no. 6, pp. 2094–2098, 2004.
[150] E. J. Gang, "Skeletal Myogenic Differentiation of Mesenchymal Stem Cells Isolated

from Human Umbilical Cord Blood," *Stem Cells*, vol. 22, no. 4, pp. 617–624, 2004.
[151] Z.-Y. Zhang *et al.*, "Superior Osteogenic Capacity for Bone Tissue Engineering of Fetal Compared with Perinatal and Adult Mesenchymal Stem Cells," *Stem Cells*, vol. 27, no. 1, pp. 126–137, 2009.
[152] C. H. Chang *et al.*, "Human acellular cartilage matrix powders as a biological scaffold for cartilage tissue engineering with synovium-derived mesenchymal stem cells," *J. Biomed. Mater. Res. - Part A*, vol. 102, no. 7, pp. 2248–2257, 2014.
[153] S. R. Bhattarai *et al.*, "Design of scaffolds using multi-layering electrospinning technique for blood vessel tissue engineering," *Proc. - Int. Fiber Conf. 2006 Extrem. Aesthetic Text. IFC 2006*, vol. 1, no. 5, pp. 511–512, 2006.
[154] Q. M. Tang *et al.*, "Fetal and adult fibroblasts display intrinsic differences in tendon tissue engineering and regeneration," *Sci. Rep.*, vol. 4, no. 5515, pp. 1–12, 2014.
[155] C. Shui *et al.*, "Mouse embryo-derived NIH3T3 fibroblasts adopt an osteoblast-like phenotype when treated with 1α,25-dihydroxyvitamin D3 and dexamethasone in vitro," *J. Cell. Physiol.*, vol. 193, no. 2, pp. 164–172, 2002.
[156] K. Klose *et al.*, "Turning fibroblasts into cardiomyocytes: Technological review of cardiac transdifferentiation strategies," *FASEB Journal*, vol. 33, no. 1. pp. 49–70, 2019.
[157] S. M. Boularaoui *et al.*, "Efficient transdifferentiation of human dermal fibroblasts into skeletal muscle," *J. Tissue Eng. Regen. Med.*, vol. 12, no. 2, pp. 918–936, 2018.
[158] N. Sayed *et al.*, "Transdifferentiation of human fibroblasts to endothelial cells role of innate immunity," *Circulation*, vol. 131, no. 3, pp. 300–309, 2015.
[159] J. Xiong *et al.*, "Integrin signaling in control of tumor growth and progression," *International Journal of Biochemistry and Cell Biology*, vol. 45, no. 5. pp. 1012–1015, 2013.
[160] F. M. Watt, "Role of integrins in regulating epidermal adhesion, growth and differentiation," *EMBO Journal*, vol. 21, no. 15. pp. 3919–3926, 2002.
[161] K. T. Chan *et al.*, "Fak alters invadopodia and focal adhesion composition and dynamics to regulate breast cancer invasion," *J. Cell Biol.*, vol. 185, no. 2, pp. 357–370, 2009.
[162] S. M. Schultze *et al.*, "PI3K/AKT, MAPK and AMPK signalling: Protein kinases in glucose homeostasis," *Expert Reviews in Molecular Medicine*, vol. 14, no. E1. pp. 1–21, 2012.
[163] P. Nurse, "A long twentieth century of the cell cycle and beyond," *Cell*, vol. 100, no. 1. pp. 71–78, 2000.
[164] L. Ma *et al.*, "Collagen/chitosan porous scaffolds with improved biostability for skin tissue engineering," *Biomaterials*, vol. 24, no. 26, pp. 4833–4841, 2003.
[165] C. W. Chang *et al.*, "PEG/clay nanocomposite hydrogel: A mechanically robust tissue engineering scaffold," *Soft Matter*, vol. 6, no. 20, pp. 5157–5164, 2010.
[166] J. K. Mouw *et al.*, "Extracellular matrix assembly: A multiscale deconstruction," *Nature Reviews Molecular Cell Biology*, vol. 15, no. 12. pp. 771–785, 2014.
[167] V. Malhotra *et al.*, "The Pathway of Collagen Secretion," *Annu. Rev. Cell Dev. Biol.*, vol. 31, no. 1, pp. 109–124, 2015.
[168] E. G. Canty *et al.*, "Collagen fibril biosynthesis in tendon: A review and recent insights," *Comp. Biochem. Physiol. - A Mol. Integr. Physiol.*, vol. 133, no. 4, pp. 979–985, 2002.
[169] T. Koide *et al.*, "Collagen biosynthesis," *Top. Curr. Chem.*, vol. 247, pp. 85–114, 2005.
[170] L. A *et al.*, "Necroptosis," *N. Engl. J. Med.*, vol. 370, no. 5, pp. 455–465, 2014.
[171] Y. Xie *et al.*, "Ferroptosis: Process and function," *Cell Death and Differentiation*, vol. 23, no. 3. pp. 369–379, 2016.
[172] T. Bergsbaken *et al.*, "Pyroptosis: Host cell death and inflammation," *Nature Reviews Microbiology*, vol. 7, no. 2. pp. 99–109, 2009.

[173] K. K. David *et al.*, “Parthanatos, A messenger of death,” *Front. Biosci.*, vol. 14, no. 3, pp. 1116–1128, 2009.
[174] L. Ouyang *et al.*, “Programmed cell death pathways in cancer: A review of apoptosis, autophagy and programmed necrosis,” *Cell Prolif.*, vol. 45, no. 6, pp. 487–498, 2012.
[175] A. Ashkenazi *et al.*, “Regulated Cell Death: Signaling and Mechanisms,” *Annu. Rev. Cell Dev. Biol.*, vol. 30, no. 1, pp. 337–356, 2014.
[176] E. Balčiūnas *et al.*, “3D printing hybrid organometallic polymer-based biomaterials via laser two-photon polymerization,” *Polym. Int.*, vol. 68, no. 11, pp. 1928–1940, 2019.
[177] D. N. Rockwood *et al.*, “Materials fabrication from Bombyx mori silk fibroin,” *Nat. Protoc.*, vol. 6, no. 10, pp. 1612–1631, 2011.
[178] E. Käpylä *et al.*, “Ormocomp-Modified glass increases collagen binding and promotes the adherence and maturation of human embryonic stem cell-derived retinal pigment epithelial cells,” *Langmuir*, vol. 30, no. 48, pp. 14555–14565, 2014.
[179] F. Claeyssens *et al.*, “Three-dimensional biodegradable structures fabricated by two-photon polymerization,” *Langmuir*, vol. 25, no. 5, pp. 3219–3223, 2009.
[180] H. Tullberg-Reinert *et al.*, “In situ measurement of collagen synthesis by human bone cells with a Sirius Red-based colorimetric microassay: Effects of transforming growth factor β2 and ascorbic acid 2-phosphate,” *Histochem. Cell Biol.*, vol. 112, no. 4, pp. 271–276, 1999.
[181] A. Kalvelyte *et al.*, “Long-term muscle-derived cell culture: Multipotency and susceptibility to cell death stimuli,” *Cell Biol. Int.*, vol. 37, pp. 292–304, 2013.
[182] D. Baltriukienė, “Signalinių molekulių ir kelių, apsprendžiančių miogeninių ląstelių išgyvenimą po kardiotoksinių poveikių, identifikavimas,” *PhD thesis*, pp. 1–133, 2009.
[183] S. Mercille *et al.*, “Induction of apoptosis in nutrient-deprived cultures of hybridoma and myeloma cells,” *Biotechnol. Bioeng.*, vol. 44, no. 9, pp. 1140–1154, 1994.
[184] C. M. Murphy *et al.*, “Mesenchymal stem cell fate is regulated by the composition and mechanical properties of collagen-glycosaminoglycan scaffolds,” *J. Mech. Behav. Biomed. Mater.*, vol. 11, pp. 53–62, 2012.
[185] S. Bai *et al.*, “Silk scaffolds with tunable mechanical capability for cell differentiation,” *Acta Biomater.*, vol. 20, pp. 22–31, 2015.
[186] J. Nam *et al.*, “Modulation of embryonic mesenchymal progenitor cell differentiation via control over pure mechanical modulus in electrospun nanofibers,” *Acta Biomater.*, vol. 7, no. 4, pp. 1516–1524, 2011.
[187] J. D. Bumgardner *et al.*, “Contact angle, protein adsorption and osteoblast precursor cell attachment to chitosan coatings bonded to titanium,” *J. Biomater. Sci. Polym. Ed.*, vol. 14, no. 12, pp. 1401–1409, 2003.
[188] S. I *et al.*, “Diffusion-assisted high-resolution direct femtosecond laser wrtiting,” *ACS Nano*, vol. 6, no. 3, pp. 2302–2311, 2012.
[189] S. Ber *et al.*, “Bone tissue engineering on patterned collagen films: An in vitro study,” *Biomaterials*, vol. 26, no. 14, pp. 1977–1986, 2005.
[190] G. Ramanathan *et al.*, “Design and characterization of 3D hybrid collagen matrixes as a dermal substitute in skin tissue engineering,” *Mater. Sci. Eng. C*, vol. 72, pp. 359–370, 2017.
[191] E. E. Antoine *et al.*, “Review of collagen i hydrogels for bioengineered tissue microenvironments: Characterization of mechanics, structure, and transport,” *Tissue Engineering - Part B: Reviews*, vol. 20, no. 6. pp. 683–696, 2014.
[192] B. Sarker *et al.*, “Combining collagen and bioactive glasses for bone tissue engineering: A review,” *Advanced Healthcare Materials*, vol. 4, no. 2. pp. 176–194, 2015.
[193] C. Dong *et al.*, “Application of collagen scaffold in tissue engineering: Recent advances and new perspectives,” *Polymers*, vol. 8, no. 2. p. 42, 2016.

[194] C. Ford, “Principles of Medical Biochemistry (3rd edn),” *Ann. Clin. Biochem. Int. J. Lab. Med.*, vol. 49, no. 6, pp. 613–613, 2012.
[195] P. Ying *et al.*, “Competitive adsorption of collagen and bovine serum albumin - Effect of the surface wettability,” *Colloids Surfaces B Biointerfaces*, vol. 33, no. 3–4, pp. 259–263, 2004.
[196] Q. Chen *et al.*, “3D printing biocompatible polyurethane/poly(lactic acid)/graphene oxide nanocomposites: Anisotropic properties,” *ACS Appl. Mater. Interfaces*, vol. 9, no. 4, pp. 4015–4023, 2017.
[197] X. Zhang *et al.*, “Biocompatible polydopamine fluorescent organic nanoparticles: Facile preparation and cell imaging,” *Nanoscale*, vol. 4, no. 18, pp. 5581–5584, 2012.
[198] E. Eisenbarth *et al.*, “Biocompatibility of β-stabilizing elements of titanium alloys,” *Biomaterials*, vol. 25, no. 26, pp. 5705–5713, 2004.
[199] V. Sansone *et al.*, “The effects on bone cells of metal ions released from orthopaedic implants. A review,” *Clinical Cases in Mineral and Bone Metabolism*, vol. 10, no. 1. pp. 34–40, 2013.
[200] L. S. Rhoads *et al.*, “Cytotoxicity of nanostructured vanadium oxide on human cells in vitro,” *Toxicol. Vitr.*, vol. 24, no. 1, pp. 292–296, 2010.
[201] E. Sabbioni *et al.*, “Cellular retention, cytotoxicity and morphological transformation by vanadium(IV) and vanadium(V) in BALB/3T3 cell lines,” *Carcinogenesis*, vol. 12, no. 1, pp. 47–52, 1991.
[202] C. Exley, “The toxicity of aluminium in humans,” *Morphologie*, vol. 100, no. 329, pp. 51–55, 2016.
[203] L. E. Sidney *et al.*, “Concise review: Evidence for CD34 as a common marker for diverse progenitors,” *Stem Cells*, vol. 32, no. 6, pp. 1380–1389, 2014.
[204] L. A. Sabourin *et al.*, “The molecular regulation of myogenesis,” *Clin. Genet.*, vol. 57, no. 1, pp. 16–25, 2000.
[205] R. Roskoski, “Structure and regulation of Kit protein-tyrosine kinase - The stem cell factor receptor,” *Biochem. Biophys. Res. Commun.*, vol. 338, no. 3, pp. 1307–1315, 2005.
[206] F. J. Lv *et al.*, “Concise review: The surface markers and identity of human mesenchymal stem cells,” *Stem Cells*, vol. 32, pp. 1408–1419, 2014.
[207] A. Rheinländer *et al.*, “CD45 in human physiology and clinical medicine,” *Immunol. Lett.*, vol. 196, pp. 22–32, 2018.
[208] A. Nieponice *et al.*, “In Vivo assessment of a tissue-engineered vascular graft combining a biodegradable elastomeric scaffold and muscle-derived stem cells in a rat model,” *Tissue Eng. - Part A*, vol. 16, no. 4, pp. 1215–1223, 2010.
[209] P. J. Reddig *et al.*, “Clinging to life: Cell to matrix adhesion and cell survival,” *Cancer and Metastasis Reviews*, vol. 24, no. 3. pp. 425–439, 2005.
[210] D. Y. Lee *et al.*, “Oscillatory flow-induced proliferation of osteoblast-like cells is mediated by αvβ3 and β1 integrins through synergistic interactions of focal adhesion kinase and Shc with phosphatidylinositol 3-kinase and the Akt/mTOR/p70S6K pathway,” *J. Biol. Chem.*, vol. 285, no. 1, pp. 30–42, 2010.
[211] M. Martini *et al.*, “PI3K/AKT signaling pathway and cancer: An updated review,” *Annals of Medicine*, vol. 46, no. 6. pp. 372–383, 2014.
[212] S. F. Moore *et al.*, “Erratum: mTORC2 protein-mediated protein kinase B (Akt) serine 473 phosphorylation is not required for Akt1 activity in human platelets,” *J. Biol. Chem.*, vol. 286, no. 35, p. 31062, 2011.
[213] S. Lee *et al.*, “Cell adhesion and long-term survival of transplanted mesenchymal stem cells: A prerequisite for cell therapy,” *Oxidative Medicine and Cellular Longevity*, vol. 2015, no. 632902. pp. 1–9, 2015.
[214] J. E. Koblinski *et al.*, “Matrix cell adhesion activation by non-adhesion proteins,” *J. Cell Sci.*, vol. 118, no. 13, pp. 2965–2974, 2005.
[215] Z. Ma *et al.*, “Surface modification and property analysis of biomedical polymers used

for tissue engineering," *Colloids and Surfaces B: Biointerfaces*, vol. 60, no. 2. pp. 137–157, 2007.
[216] D. Katti *et al.*, "Improved Biomaterials for Tissue Engineering Applications: Surface Modification of Polymers," *Curr. Top. Med. Chem.*, vol. 8, no. 4, pp. 341–353, 2008.
[217] I. Capek, "Smart Biodecorated hybrid Nanoparticles," *Curr. Bionanotechnol.*, vol. 1, no. 1, pp. 60–78, 2015.
[218] Y. Min *et al.*, "Gold nanorods for platinum based prodrug delivery," *Chem. Commun.*, vol. 46, no. 44, pp. 8424–8426, 2010.
[219] D. S. Lee *et al.*, "Biocompatibility of a pdms-coated micro-device: Bladder volume monitoring sensor," *Chinese J. Polym. Sci.*, vol. 30, pp. 242–249, 2012.
[220] A. Mata *et al.*, "Characterization of polydimethylsiloxane (PDMS) properties for biomedical micro/nanosystems.," *Biomed. Microdevices*, vol. 7, no. 4, pp. 281–293, 2005.
[221] S. E. Ochsenhirt *et al.*, "Effect of RGD secondary structure and the synergy site PHSRN on cell adhesion, spreading and specific integrin engagement," *Biomaterials*, vol. 27, no. 20, pp. 3863–3874, 2006.
[222] S. N. Dixit *et al.*, "Isolation and characterization of pepsin solubilized basement membrane collagens (type IV) from human placenta, bovine kidney cortices, and bovine lens capsule," *Immunochem. Extracell. Matrix Vol. 1 Methods*, pp. 61–74, 2018.
[223] M. Aumailley, "The laminin family," *Cell Adhesion and Migration*, vol. 7, no. 1. pp. 48–55, 2013.
[224] R. Junka *et al.*, "Laminin functionalized biomimetic nanofibers for nerve tissue engineering," *J. Biomater. Tissue Eng.*, vol. 3, no. 4, pp. 494–502, 2013.
[225] K. Sugiyama *et al.*, "Biocompatible block copolymers composed of polydimethylsiloxane and poly[(2-methacryloyloxy)ethyl phosphorylcholine] segments," *Polym. J.*, vol. 31, no. 10, pp. 883–886, 1999.
[226] J. H. Seo *et al.*, "Surface tethering of phosphorylcholine groups onto poly(dimethylsiloxane) through swelling-deswelling methods with phospholipids moiety containing ABA-type block copolymers," *Biomaterials*, vol. 29, no. 10, pp. 1367–1376, 2008.
[227] B. D. Lawrence *et al.*, "Silk film biomaterials for cornea tissue engineering," *Biomaterials*, vol. 30, no. 7, pp. 1299–1308, 2009.

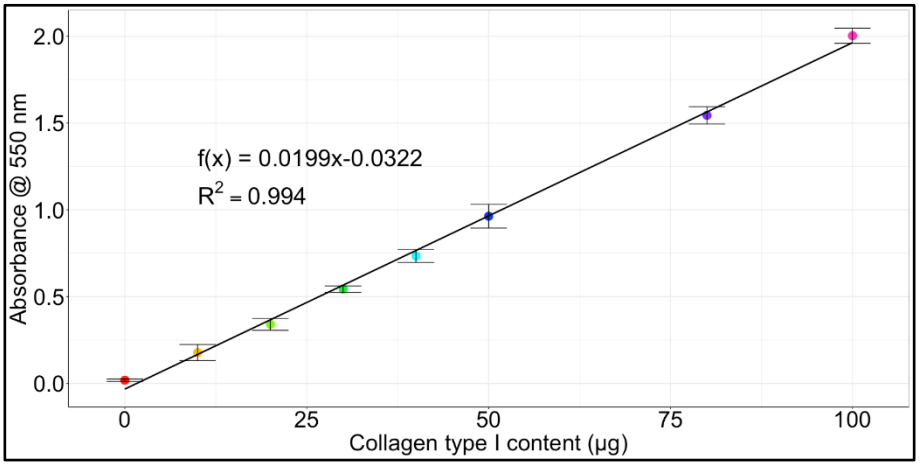


Figure S1. Calibration curve used to determine the amount of collagen I adsorbed to a surface.

# ABOUT THE AUTHOR

**Work Experience**

2018/11 – Present. Molecular Solutions Specialist at Roche, Vilnius (Lithuania).

2015/7 – 2019/7. Junior Researcher at the Institute of Biochemistry, Life Sciences Centre, Vilnius University, Vilnius (Lithuania).

2016/7 – 2016/9. Visiting Researcher at the Department of Chemistry, Lancaster University, Lancaster (United Kingdom).

2013/10 – 2015/6. Early Stage Marie Skłodowska-Curie Researcher at the Institute of Electronic Structure and Laser, Foundation for Research and Technology – Hellas, Heraklion (Greece).

2012/9 – 2013/9. Engineer at the Department of Chemistry and Bioengineering, Vilnius Gediminas Technical University, Vilnius (Lithuania).

2012/5 – 2013/9. Engineer at the Department of Quantum Electronics and Laser Research Centre, Faculty of Physics, Vilnius University, Vilnius (Lithuania).

2010/9 – 2012/5. Intern at the Institute of Biochemistry, Vilnius University, Vilnius (Lithuania).

2010/9 – 2012/4. Laboratory Assistant at the Department of Quantum Electronics and Laser Research Centre, Faculty of Physics, Vilnius University, Vilnius (Lithuania).

2009/9 – 2010/11. Laboratory Assistant at the Department of Chemistry and Bioengineering, Vilnius Gediminas Technical University, Vilnius (Lithuania).

**Education and Training**

Certified to work with laboratory animals according to Article 23 of the Directive 2010/63/EU.

2014. MSc in Molecular Biology at Vilnius University.

2012. BSc in Bioengineering at Vilnius Gediminas Technical University.

2008. Simonas Daukantas Secondary School.

**Participation in Summerschools**

2015/3/23 – 27. Tissue Engineering and Regenerative Medicine II. National University of Ireland, Galway (Ireland).

2014/10/21 – 24. Tissue Engineering and Regenerative Medicine I. University of Valladolid, Valladolid (Spain).

2014/5/13 – 16. Nature-Inspired Nanomaterials: Synthesis, Characterisation and Applications for Ischemic Conditions. Foundation for Research and Technology - Hellas, Heraklion (Greece).

2013/9/30 – 10/3. Photonics Meets Biology. Foundation for Research and Technology - Hellas, Hersonissos (Greece).

**Languages**

Lithuanian – native.

English – fluent.

German – conversational.

Russian – basic communication.

Greek – basic understanding.

**Digital Competences**

LaTeX – experienced user.

Intermediate R statistical programming language skills – the graphs and statistics in this thesis were done using RStudio.

Experienced AutoCAD user – some of the images in this thesis were rendered using it.

Advanced Microsoft Office user.

**Honours and Awards**

The 2019 paper, entitled “3D Printing Hybrid Organometallic Polymer-based Biomaterials Via Laser Two-photon Polymerization”, published in Polymer International was named the top downloaded paper in 2018 – 2019.

2nd place in best student-led research paper contest at the Rapid Design, Prototyping and Manufacturing 2017 conference in Newcastle, UK.

3rd place in best student presentation contest at the Rapid Design, Prototyping and Manufacturing 2017 conference in Newcastle, UK.

Research scholarship from the World Federation of Scientists, 2017.

INFOBALT scholarship for the best interdisciplinary student research project, 2017.

Promotional scholarship for doctoral candidates, awarded by the Research Council of Lithuania, 2016.

Promotional scholarship for doctoral candidates, awarded by the Research Council of Lithuania, 2015.

Marie Skłodowska-Curie fellowship under AngioMatTrain project, grant agreement 317304 in 2013-2015.

3rd place in best student poster presentation competition at the 15th International Symposium on Laser Precision Microfabrication 2014.

Award for the best student research paper, entitled "Biocompatibility testing of laser microstructured polymers for tissue engineering applications", awarded by the Lithuanian National Academy of Sciences in 2011.

**Participation in Projects**

2015/9 – 2018/12. Soft tissue engineering: from cell to artificial tissue (ReSoft). Funded by the Lithuanian Research Council, project No. SEN-13/2015, project coordinator – Dr. Daiva Baltriukienė.

2013/9 – 2015/6. Development of Biomaterial-Based Delivery Systems for Ischaemic Conditions: An Integrated Pan-European Approach. Funded by the European Commission, project No. 317304, project coordinator – Prof. Abhay Pandit.

2012/12 – 2013/9. Biocatalysts, recombinant proteins and cell technologies. Funded by the European Social Fund Agency, project No. VP1-3.1-ŠMM-08-K-01-001, project coordinator – Prof. Juozas Kulys.

# SANTRAUKA

## Įvadas

Audinių inžinerija – tai tarpdisciplininė sritis, kurioje biologai, chemikai, inžinieriai ir gydytojai apjungia savo žinias, siekdami išspręsti šiuolaikinės transplantologijos problemas – sukonstruoti individualiems pacientams pritaikytus dirbtinius audinius ir organus. Tuo tikslu, siekiama pagaminti biosuderinamas audinių struktūras, kurios vėliau apauginamos paties paciento ląstelėmis ir naudojamos kaip pažeisto audinio pakaitalas.

Skirtingų rūšių audiniams reikalingos skirtingos konstravimo strategijos. Pirmiausia, reikia pagaminti 3D struktūras, turinčias reikiamus biocheminius žymenis ir gebančias užtikrinti ląstelių integraciją, proliferaciją, diferenciaciją. Čia susiduriama su pagrindiniu iššūkiu – poreikiu sukurti struktūras kiek įmanoma panašesnes į natyvų ekstraląstelinį matriksą. Vienas galimų sprendimo būdų galėtų būti natūralių audinių nuląstelinimo metodikos panaudojimas. Deja, šiuo atveju susiduriama su ribotais donorinių organų ištekliais. Alternatyvus kelias – karaksų gamyba panadujant sintetines medžiagas. Šie karkasai gali būti padengiami (biodekoruojami) įvairiomis bioaktyviomis mokelulėmis siekiant pagerinti jų sąveiką su ląstelėmis.

Šiame darbe kieto audinio konstravimui pasirinkome hibridinius organinius-neorganinius polimerus, kurie gali būti apdirbami pasitelkiant tiesioginį lazerinį rašymą. Ši technologija leidžia formuoti 3D darinius mikronų tikslumu, užtikrina didelį formuojamos struktūros vidinį tikslumą ir atkartojamumą. Be to, tokie hibridiniai polimerai gali būti modifikuojami, siekiant maksimaliai pagerinti jų biosuderinamumą. Ląstelių atsakui ir gebėjimui formuoti norimus audinius implantacijai įtaką turi įvairūs veiksniai – fizikocheminės medžiagos savybės (elastingumas ir hidrofiliškumas), paviršiaus nanotopografija, cheminis integralumas.

Minkšto audinio konstravimui buvo pasirinkta keletas su PDMS susijusių sprendimų. Šio polimero pasirinkimą lėmė keletas patrauklių jo savybių – elastingumas, tvirtumas ir nesudėtingas formavimas. Tačiau tai yra hidrofobinė medžiaga, o tai kelia nemažai iššūkių audinių inžinerijos taikymuose. Todėl tyrimuose buvo pasirinkti PDMS blokiniai kopolimerai. Šie cheminiai konstruktai ne tik turi hidrogeliams būdingas savybes, bet taip pat gali būti sukuriami taip, kad laikui bėgant organizme suirtų ir būtų pakeičiami ląstelių naujai suformuotu ekstraląsteliniu matriksu. Hidrofobinis paviršius nėra patrauklus ląstelių adhezijai, todėl, siekdami paskatinti ląstelių

prikibimą ir kitas ląstelių savybes, pasitelkėme biodekoravimo strategiją, kai bioaktyvios molekulės prikabinamos prie tirtų paviršių. Galiausiai vertinome, kaip medžiagos mechaninės savybės gali būti keičiamos sutvirtinant polimerą šilku. Visos šios technologijos gali būti integruojamos kartu, konstruojant karkasus, kurie ne tik atkurtų ląstelių mechaninę ar fizikocheminę aplinką, bet taip pat ir pagerintų biochemines savybes.

Šio darbo tikslas buvo nustatyti *in vitro* biosuderinamumas bei ląstelių funkcijas palaikančias medžiagas, tinkamas audinių inžinerijos taikymams ir ištirti jų bioaktyvumą.

Užduotys

1. Sukurti naują hibridinį organinį-neorganinį polimerą, savo sudėtyje turintį aliuminio, ir charakterizuoti jo fizikochemines savybes.
2. Pasitelkiant tiesioginį lazerinį rašymą, įvertinti naujosios medžiagos panaudojimo galimybes trimačių darinių konstravimui.
3. Ištirti skirtingų organinių-neorganinių polimerų biosuderinamumą *in vitro*.
4. Parinkti audinių inžinerijos taikymams geriausiai tinkančias medžaigas ir įvertinti jų poveikį ląstelių adhezijai.
5. Įvertinti hibridinių organinių-neorganinių polimerų paviršiaus cheminių savybių poveikį kolageno gamybai ląstelėse.
6. Atlikti naujų PDMS blokinių kopolimerų biosuderinamumo vertinimą.
7. Ištirti kaip paviršiaus biodekoravimas veikia PDMS biosuderinamumą.
8. Įvertinti kaip šilkas keičia PDMS mechaniness savybes.

Naujumas

Kuriant dirbtinius audinius, siekiant gauti norimą ląstelių atsaką ir audinio brendimą, būtina preciziškai kontroliuoti karkasų parametrus. Tačiau kiekvieno audinio savybės yra skirtingos, todėl svarbu tikslingai pasirinkti medžiagas ir gamybos technologiją.

**Kietas audinys**. Kuriant kietą audinį, reikia pasirinkti tokias medžiagas ir gamybos technologijas, kurios leistų preciziškai formuoti 3D nišas ląstelėms, indukuotų diferenciaciją osteogenine ar chondrogenine linkmėmis, nes ekstraląstelinė aplinka ir erdvinis fokalinių adhezijų išsidėstymas užtikrina tinkamą audinio vystymąsi.

Tai pasiekti leidžia tiesioginio lazerinio rašymo technologija, kuria galima formuoti skirtingus 3D darinius su mikro- ir nano- architektūromis,

panaudojant platų spektrą medžiagų. Be to, modifikuojant šių medžiagų sudėtis, galima keisti jų fizikochemines savybes.

Gauti karkasai turi būti biosuderinami, palaikyti ląstelių adheziją ir ekstraląstelinio matrikso baltymų sekreciją, adsorbciją ir metabolitų pernašą į ląstelę ir iš jos. Literatūroje aprašyta daugybė medžiagų, kurios tinkamos tiesioginiam lazeriniam rašymui, tačiau žinių, kaip jos veikia ląstelių savybes, nepakanka. Šiame darbe, be jau žinomų hibridinių polimerų, savo sudėtyje turinčių V, Ti ir Zr, buvo sukurtas ir ištirtas naujas polimeras su Al. Ši medžiagų klasė pasižymi puikiomis struktūrizavimo galimybėmis ir biosuderinamumu. Atlikus išsamią literatūros apžvalgą, neaptikta tiesioginių šių medžiagų palyginimų, vertinant ląstelių adheziją, gyvybingumą, proliferaciją ir kolageno sekreciją. O norint toliau tirti šių hibridinių polimerų tinkamumą audinių inžinerijos tikslams, būtina suprasti šiuos procesus.

Mūsų gauti rezultatai parodė, kad iš visų tirtų medžiagų, Al, Ti ir Zr turintys hibirdiniai polimerai geriausiai veikė ląstelių adheziją, proliferaciją ir gyvybingumą. Nustatyta, kad Al turintis polimeras reikšmingai pagerina kolageno sekreciją, lyginant su Zr turinčiu polimeru. Tačiau V turintis polimeras pasižymėjo toksiškumu. To priežastis – mažas cheminis integralumas ir toksiškų komponentų difuzija. Nustatėme, kad naujasis, Al turintis hibridinis polimeras yra tinkamas konstruojant itin aukštos raiškos trimačius darinius.

**Minkštas audinys**. Minkšto, kaip ir kieto audinio inžinerijai turi būti parenkamos tokios medžiagos, kad jų mechaninės savybės kiek įmanoma tiksliau atitiktų aplinkinių audinių savybes, o naudojamos medžiagos turi užtikrinti biocheminius signalus, svarbius auginamoms ląstelėms.

PDMS – puiki medžiaga minkštųjų audinių konstravimui, nes yra nesudėtingai formuojama, pasižymi tinkamomis mechaninėmis savybėmis ir biosuderinamumu. Ši medžiaga plačiai naudojama įvairiems tikslams – nuo mikrofluidikos iki lęšių gamybos. Tačiau ji turi ir trūkumų. PDMS yra hidrofobiškas ir linkęs plyšti, todėl sudėtinga implantuoti. Mechaninės PDMS savybės varijuoja sąlyginai siaurame diapazone. Siekiant sumažinti neigiamas PDMS savybes, kuriami blokiniai kopolimerai arba kompozitai. Tačiau siekiant parinkti perspektyviausias blokinių kopolimerų komponentų kombinacijas bei biodekoravimo strategijas, reikia atlikti išsamius tyrimus įvertinant šių modifikacijų poveikį ląstelių adhezijai ir kitoms savybėms. Darbo metu atradome keletą blokinių kopolimerų, pasižyminčių geru, aukštesniu nei gryno PDMS, biosuderinamumu. Nustatėme, kad parinkus tinkamą biodekoravimo strategiją, galima pagerinti PDMS ir ląstelių sąveiką.

Be to, šiame darbe pirmą kartą įvertinome kaip PDMS mechaninės savybės keičiasi sutvirtinus polimerą šilku ir nustatėme, kad tai yra tinkama strategija moduliuoti tamprumo modulį.

# 1. MEDŽIAGOS IR METODAI

## 1.1 Hibridiniai organiniai-neorganiniai polimerai

Sąrašas medžiagų, kurios buvo naudojamos ruošiant hibridinius organininus-neorganinius polimerus pateiktas 1 lentelėje.

1 lentelė. Medžiagos, naudotos hibridinių organinių-neorganininių polimerų ruošimui.

| Pavadinimas | Pilnas pavadinimas | Grynumas | Tiekėjas |
|---|---|---|---|
| AIP | aliuminio (III) izopropoksidas | ≥99 % | *Sigma-Aldrich* |
| BIS | 4,4'-bis(dietilamino)-benzofenonas | ≥99 % | *Sigma-Aldrich* |
| HCl | druskos rūgštis | 37 % | *Sigma-Aldrich* |
| MAA | metakrilo rūgštis | 99 % | *Sigma-Aldrich* |
| MAPTHS | 3-(trihidroxisilil)propil-metakrilatas | - | *Sigma-Aldrich* |
| MAPTMS | 3-(trimetoksilil)propil-metakrilatas | 98 % | *Sigma-Aldrich* |
| TIPO | titano (IV) izopropoksidas | 97 % | *Sigma-Aldrich* |
| Toluenas | toluenas | ACS ISO | *Sigma-Aldrich* |
| VOTIP | vanadžio (V) triizopropoksido oksidas | - | *Sigma-Aldrich* |
| ZPO | cirkonio (IV) propoksidas | 70 % | *Sigma-Aldrich* |

**Al hibridas**. MAPTMS buvo hidrolizuojamas iki MAPTHS, maišant su 0.1 M HCl. Lygiagrečiai, AIP buvo tirpinamas toluene, ultragarsinėje vonelėje. Į MAPTHS tirpalą buvo pridedama MAA (1:1 moliniu santykiu su AIP). Tuomet, du tirpalai - MAA:MAPTHS ir AIP:toluenas buvo maišomi kartu, 1:1:4 moliniu santykiu tarp AIP:MAA:MAPTHS. BIS buvo įmaišomas kaip fotoiniciatorius (1 % pagal AIP, MAA ir MAPTHS masę). Procedūra detaliai aprašyta publikacijoje Polymer International žurnale [176].

**Ti hibridas**. Hibridinis polimeras su Ti buvo ruošiamas pagal publikaciją [54]. Trumpai, MAPTHS buvo maišomas su MAA, o tuomet lėtai, maišant pridedamas TIPO. Komponentų molinė proporcija tarp TIPO:MAA:MAPTHS buvo 1:1:4. BIS buvo pridedamas kaip fotoiniciatorius (1 % pagal TIPO, MAA ir MAPTHS suminę masę). Gautas mišinys buvo filtruojamas per švirkštinį filtrą.

**V hibridas**. Hibridinio polimero su V paruošimo procedūra buvo analogiška publikuotiems duomenims [55]. Trumpai, MAPTMS buvo hidrolizuojamas iki MAPTHS su 0.1 M HCl. Tuomet, VOTIP buvo dedamas

į MAPTHS iki 1:1 molinio santykio. Galiausiai mišinys buvo filtruojamas per švirkštinį filtrą.

**Zr hibridas**. Hibridinio polimero su Zr paruošimo procedūra buvo analogiška publikacijoje aprašytai [56]. Trumpai, MAPTMS buvo hidrolizuojamas iki MAPTHS naudojant 0.1 M HCl. Lygiagrečiai, cirkonio propoksidas (ZPO) buvo maišomas su MAA 1:1 moliniu santykiu. Du gauti mišiniai buvo maišomi iki 1:1:4 ZPO:MAA:MAPTHS molinio santykio. BIS buvo naudojamas kaip fotoiniciatorius (1 % pagal ZPO, MAA ir MAPTHS masę). Galiausiai mišinys buvo filtruojamas per švirkštinį filtrą.

## 1.2 Polidimetilsiloksanas ir jo kompozitai

Sąrašas medžiagų, naudotų ruošiant PDMS mėginius ir kompozitus, pateiktas 2 lentelėje.

2 lentelė. Medžiagos, naudotos PDMS mėginių ir jų kompozitų paruošimui.

| Pavadinimas | Pilnas pavadinimas | Grynumas | Tiekėjas |
|---|---|---|---|
| Acto rūgštis | acto rūgštis | - | *Appli-Chem* |
| DMSO | dimetilsulfoksidas | - | *Sigma-Aldrich* |
| Etanolis | etanolis | 70 % | *Vilniaus degtinė* |
| FBS | fetalinis veršelio serumas | - | *Gibco* |
| HEMA | 2-hidroksietilmetakrilatas | - | *Sigma-Aldrich* |
| IMDM | Iskovo modifikuota Dulbeko terpė | - | *Gibco* |
| $Na_2CO_3$ | natrio karbonatas | - | *Sigma-Aldrich* |
| PBS | fosfatinis druskos buferis | - | *Gibco* |
| PDMS | polidimetil siloksano ir termoiniciatoriaus mišinys (Sylgard 184) | - | *Dow Corning* |
| PVA | poli(vinilo alkoholis) | - | *Sigma-Aldrich* |
| RGD tripeptidas | arginino-glicino-asparagino tripeptidas | - | *Sigma-Aldrich* |
| Silk | *Bombyx mori* šilkas | - | *Amazon* |
| Sulfo-SANPAH | sulfosukcinimidil-6-(4'-azido-2'-nitrofenilamino)heksanoatas | - | *Thermo Scientific* |

**Grynas PDMS**. Gryno PDMS mėginių ruošimui, PDMS buvo maišomas su atitinkamu termoiniciatoriumi santykiu 10:1 pagal masę. Komponentai

buvo kruopščiai išmaišomi, nuorinami ir dengiami išsukant ant stiklelių arba liejami į formas. Galiausiai, mišinys buvo kaitinamas 100 °C temperatūroje, kad komponentai susipolimerizuotų.

**PDMS biodekoravimas**. Pirmiausia, PDMS plėvelės buvo pamerkiamos į 70 % etanolį 24 valandoms, tuomet plaunamos PBS ir džiovinamos po UV. Paviršiai buvo midifikuojami penkiais skirtingais būdais:

1. Pamerkiant į IMDM augimo terpę su 10 % FBS.
2. Pamerkiant į 100 % FBS.
3. Pamerkiant į kolageno tirpalą.
4. Pamerkiant į laminino tirpalą.
5. Kovalentiniais ryšiais prijungiant RGD tripeptidus, naudojant fotosusiuvimo agentus.

Kontrolei buvo naudojamos PDMS plėvelės, inkubuotos PBS. IMDM, 100 % FBS ir PBS atvejais, PDMS mėginiai buvo inkubuojami 1 mL atitinkamo tirpalo 24 valandas, 4 °C temperatūroje. 0.1 % kolageno tirpalas buvo ruošiamas 0.1 M acto rūgštyje ir prieš naudojant 10 kartų skiedžiamas dejonizuotu vandeniu. 1 mL 0.01 % koncentracijos tirpalo buvo užpilamas ant mėginių ir inkubuojama 24 valandas 4 °C temperatūroje. RGD tripeptidas buvo kovalentiniais ryšiais prijungiamas prie mėginių per sulfo-SANPAH. Sulfo-SANPAH fotosusiuvimo agentas (100 μg/mL, ištirpintas DMSO) buvo užpilamas ant paviršių ir 1 valandą veikiamas UV. Tokiu būdu, aktyvuojama fotoaktyvi fotosusiuvimo agento dalis, kuri prisijungia prie PDMS. Nusiurbus fotosusiuvimo agento tirpalą, mėginiai buvo praplaunami PBS ir tuomet ant jų buvo užpilamas RGD tripeptidų tirpalas, kuris buvo 24 valandas inkubuojamas kambario temperatūroje. Per šį laiką susiformuoja ryšiai tarp RGD tripeptido molekulių ir laisvųjų fotosusiuvimo agento molekulių dalių.

**PDMS blokiniai kopolimerai**. PDMS blokiniai kopolimerai buvo sintetinami Vilniaus universiteto Chemijos ir geomokslų fakultete. Tirti keturi PDMS blokinių kopolimerų tipai:

A – α,ω-diepoksi-PDMS blokiniai kopolimerai su AA, BMA, HEMA ir VP, makromolekulių susiuvimui naudojant glicerolį ir fotoiniciatorių. Komponentų proporcijos pateiktos 3 lentelėje.

3 lentelė. Skirtingų komponentų, sudarančių α,ω-diepoxy-PDMS-AA-BMA-HEMA-VP blokinius kopolimerus, komponentų proporcijos makromolekulių susiuvimo metu.

| Pavadinimas | BMA, % | GMA, % | Glicerolis, % | PI, % |
|---|---|---|---|---|
| A1 | 6.4 | 2.56 | 10 | 2 |
| A2 | 6.4 | 2.44 | 10 | 2 |
| A3 | 8.0 | 2.19 | 10 | 2 |
| A4 | 6.4 | 2.56 | 10 | 2 |

B – α,ω-diepoksi-PDMS blokiniai kopolimerai su BMA, HEMA, VP, esant skirtingiems moliniams santykiams. Makromolekulių susiuvimui naudotas fotoiniciatorius, o sudėtinių komponentų proporcijos pateikiamos 4 lentelėje.

4 lentelė. α,ω-diepoksi-PDMS-BMA-HEMA-VP blokinių kopolimerų sudėtinės dalys.

| Pavadinimas | BMA, molinis santykis | HEMA, molinis santykis | VP, molinis santykis | α,ω-diepoksi-PDMS, molinis santykis | PI, % |
|---|---|---|---|---|---|
| B1 | 0.4 | 0.2 | 1 | 0.2 | 2 |
| B2 | 0.4 | 0.2 | 1 | 0.2 | 2 |
| B3 | 0.4 | 0.3 | 1 | 0.3 | 2 |
| B4 | 0.4 | 0.3 | 1 | 0.15 | 2 |

C – dihidroksi-PDMS blokiniai kopolimerai su AzA, DEG ir M, makromolekulių susiuvimui naudojant fotoiniciatorių. Sudėtinių dalių proporcijos visais atvejais buvo vienodos, skyrėsi tik makromolekulių susiuvimo sąlygos, kurios yra apibendrintos 5 lentelėje.

5 lentelė. Dihidroksi-PDMS-AzA-DEG-MAA blokinių kopolimerų makromolekulių susiuvimo sąlygos.

| Pavadinimas | GMA, % | BMA, % | PI, % |
|---|---|---|---|
| C1 | 164 | 62.1 | 5 |
| C2 | 82 | 45.1 | 5 |
| C3 | 20 | 16.7 | 3 |
| C4 | 40 | - | 3 |

D – α,ω-diepoksi-PDMS blokiniai kopolimerai su GMA ir PVA, makromolekulių susiuvimui naudojant fotoiniciatorių. Komponentų proporcijos visais atvejais buvo vienodos, skyrėsi tik makromolekulių susiuvimo sąlygos, kurios apibendrintos 6 lentelėje.

6 lentelė. α,ω-diepoksi-PDMS-GMA-PVA blokinių kopolimerų makromolekulių susiuvimo sąlygų apibendrinimas.

| Pavadinimas | BMA, % | GMA, % | Glicerolis, % | PI, % |
|---|---|---|---|---|
| D1 | 13.7 | - | 7.8 | 3 |
| D2 | 7.3 | - | 8.4 | 3 |

**Šilku sutvirtintas PDMS**. Šilko paruošimo procedūra buvo adaptuota pagal Prof. Kaplan grupės publikuotą procedūrą [177]. Šilkverpių *Bombyx mori* kokonai buvo sukarpomi žirklėmis ir verdami 0.02 M $Na_2CO_3$ tirpale, švelniai maišant. Kokonų likučiai buvo išrenkami ir likęs šilkas buvo tris kartus plaunamas dejonizuotu vandeniu. Iš šilko siūlų tuomet buvo išspaudžiamas vanduo ir paliekama per naktį išdžiūti. PDMS buvo kruopščiai išmaišomas su atitinkamu termoiniciatoriumi 10:1 masių santykiu. Tuomet į mišinį buvo dedamas šilkas – 1 %, 5 % arba 10 % pagal masę. Grynas PDMS-termoiniciatoriaus mišinys buvo naudojamas kaip kontrolė. Mišiniai buvo supilami į 24 šulinėlių polistireno plokštelių šulinėlius ir valandai įkeliami į šaldytuvą (4 °C), kad pasišalintų oro burbuliukai. Plokštelės su PDMS-šilko mišiniais tuomet buvo kaitinamos 100 °C temperatūroje. Galiausiai, polistireno plokštelės buvo sulaužomos ir mėginiai išimami.

## 1.3 Karkasų ir paviršių gamyba

Medžiagos, naudotos mėginių paruošimui, apibendrintos 7 lentelėje.

7 lentelė. Medžiagų, naudotų mėginių paruošimui, sąrašas.

| Pavadinimas | Pilnas pavadinimas | Grynumas | Tiekėjas |
|---|---|---|---|
| Acto rūgštis | acto rūgštis | 99 % | *Sigma-Aldrich* |
| Borosilikatinis stiklas | borosilikatinis stiklas | NA | *Thermo Scientific* |
| Etanolis | etanolis | 96 % | *Vilniaus degtinė* |
| MAPTMS | 3-(trimetoksisilil)propil-metakrilatas | 98 % | *Sigma-Aldrich* |

### 1.3.1 Polimerų plėvelės

**Stikliukų silanizavimas**. Stikliukai, naudoti mėginių paruošimui, buvo silanizuojami pagal Käpylä su kolegomis aprašytą protokolą [178]. Apvalūs 12 mm skersmens borosilikatiniai dengiamieji stikliukai buvo plaunami ultragarsinėje vonelėje etanolyje bent 1 valandą. Vėliau etanolis buvo

nupilamas ir nauja 30 mL etanolio porcija su 0.5 mL MAPTMS, 0.5 mL acto rūgšties ir 2 mL dejonizuoto vandens buvo užpilama ant stikliukų, o vėliau viskas perkeliama į ultragarsinę vonelę dar 1 valandai. Tuomet, stikliukai buvo dar kartą plaunami etanoliu ultragarsinėje vonelėje. Galiausiai, stikliukai buvo džiovinami kambario temperatūros ore.

**Dengimas išsukant**. Maždaug 70 µL tūrio medžiagų lašeliai buvo išsukami ant silanizuotų 12 mm skersmens borosilikatinių stiklelių 30 s, 3000 aps./min. greičiu. Mėginiai, dengti hibridiniais organiniais-neorganiniais polimerais tuomet buvo kruopščiai perkeliami į tamsią traukos spintą ir paliekami bent 24 valandoms, kad išgaruotų tirpikliai. Mėginiai su fotoiniciatoriais tuomet buvo fotopolimerizuojami naudojant UV, o gryni PDMS-termoiniciatoriaus mėginiai buvo 1 valandą polimerizuojami 100 °C temperatūroje.

**Poveikis UV**. Ant stikliukų išsuktos hibridinės organinės-neorganinės medžiagos buvo polimerizuojamos, o PDMS blokiniai kopolimerai – tinklinami, naudojant *Sylvania 15W UV-C* baktericidinę lempą, esant 20 cm atstumui, kas atitinka maždaug 1.8 mW/cm$^2$ apšvitą, bent 5 valandas. Mėginiai vėliau buvo apverčiami, kad išsterilinti jų apačias, švitinant UV bent 1 valandą, tuomet perkeliami į 24 šulinėlių plokšteles ir dar kartą 1 valandą švitinami.

**Mėginių sterilinimas ir plovimas**. Mėginiai galiausiai buvo tris kartus mirkomi steriliame PBS 12 šulinėlių plokštelėse – užpilant po 5 mL ir inkubuojant valandą, vėliau pakeičiant PBS nauju, inkubuojant dar valandą ir trečią kartą pakeičiant PBS nauju, inkubuojant pernakt. Vėliau, mėginiai buvo valandą mirkomi IMDM terpėje, papildyta FBS ir antibiotikais.

### 1.3.2 Polimerų ekstraktai

Naudoti du polimerų ekstraktų paruošimo būdai:

1. Polimerinės plėvelės buvo paruošiamos kaip aprašyta anksčiau ir 24 valandas inkubuojamos PBS ant plokštelių purtyklės 40 aps./min. greičiu kambario temperatūroje. Tuomet, PBS su polimerų ekstraktais buvo nusiurbiami į naujas ląstelių auginimo plokšteles ir kaitinama 5 valandas 80 °C temperatūroje, kad išgaruotų vanduo.

2. Alternatyvus polimerinių ekstraktų paruošimo būdas buvo perkelti polimerais dengtus stikliukus į IMDM terpę, papildytą FBS ir antibiotikais ir 24 valandas inkubuoti ant plokštelių purtyklės 40 aps./min. greičiu, panaudojant gautus polimerų ekstraktus terpėje ląstelių auginimui.

### 1.3.3 3D struktūrų gavimas

Struktūrų gamybai, mėginiai buvo ruošiami užlašinant nedidelį lašelį tiriamos medžiagos ant silanizuoto stikliuko ir paliekant per naktį traukos spintoje, kad išgaruotų tirpiklis. Mėginiai buvo saugomi nuo aplinkinės šviesos, kad išvengti nepageidaujamos fotoaktyvacijos. Po polimerizacijos lazeriu, mėginiai buvo plaunami 4-metil-2-pentanonu (Ti, V ir Zr atvejais) arba toluenu (Al atveju) 15 min, vėliau dar praskalaujant izopropanoliu ir išdžiovinant ore. Šiame darbe naudotos dvi tiesioginio lazerinio rašymo sistemos.

**Nanoscribe**. Komerciškai prieinama sistema *Nanoscribe Photonic Professional GT* (*Nanoscribe GmbH*, Vokietija) buvo naudojama Chemijos padalinyje Lankasterio universitete. Sistema paremta *Topica FemtoFiber Pro* 100 fs impulsų 780 nm bangos ilgio lazeriu su maksimalia 50 mW galia. Darbui su šia sistema naudotas 63X 1.4 NA imersinis objektyvas. Gaminamų darinių struktūros buvo importuojamos iš .STL failų arba programuojamos *DeScribe* programoje, kuri kontroliavo ir visą darinių formavimo procedūrą.

**Ti:safyras**. Ši tiesioginio lazerinio rašymo sistema buvo aprašyta literatūroje [179]. Ji įrengta *Foundation for Research and Technology - Hellas, Institute for Electronic Structure and Laser* (*FORTH-IESL*) Heraklione, Graikijoje. Trumpai, Ti:Safyro lazeris (*Femtolasers Fusion*) buvo naudojamas kaip šviesos šaltinis, veikiantis prie 780 nm centrinio bangos ilgio, su 20 fs impulsų trukme, esant 75 MHz dažniui. Vidutinė lazerio galia buvo nustatya tarp 10-100 mW, naudojant ateniuatorių (*Altechna*). Mėginys buvo pozicionuojamas ant piezoelektrinių stalų, o lazerio pluoštas į mėginį atvedamas galvanometrinių skanavimo veidrodžių pagalba (*Scanlabs Hurryscan II*) per 40X 0.95 NA (*Zeiss, Plan-Apochromat*) arba imersinį 100X 1.4 NA (*Zeiss, Plan-Apochromat*) objektyvą. Visas rašymo procesas buvo kontroliuojamas *SAMLight* (*SCAPS*) programine įranga. Rašymo greičiai tarp 0.1 ir 1 mm/s buvo tinkami šiam procesui. Supaprastinta sistemos schema pateikta 1 paveiksle.

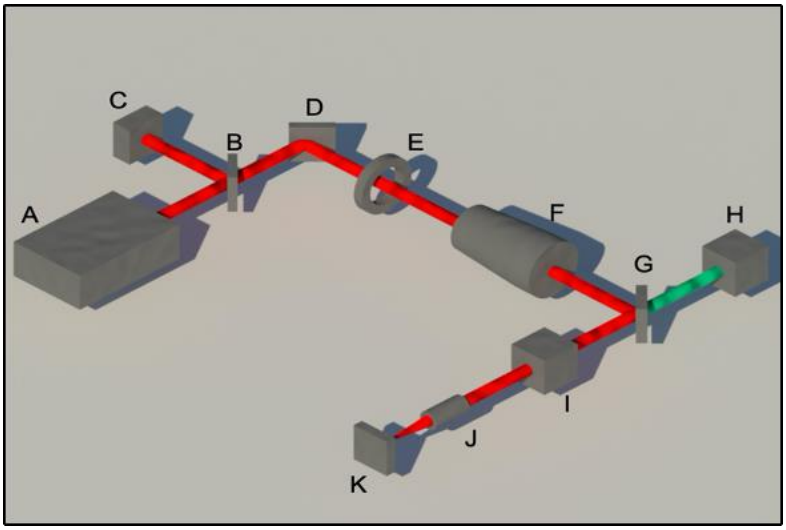

1 paveikslas. Tiesioginio lazerinio rašymo sistemos, naudotos FORTH-IESL, schema. A – lazeris, B – spindulio skirstytuvas, C – spektro analizatorius, D – veidrodis, E – ateniuatorius, F – teleskopas, G – dichroinis veidrodis, H – CCD kamera, skirta gamybos proceso stebėjimui realiu laiku, I – galvanometrinis skaneris, J – objektyvas, K – piezoelektrinis mėginio pozicionavimo stalas su LED apšvietimu CCD kamerai.

## 1.4 Mėginių charakterizavimas

### 1.4.1 Kontaktinio kampo matavimai

2 µL dejonizuoto vandens lašiukai buvo atsargiai užlašinami ant polimerinių plėvelių ir fotografuojami naudojant *Krüss EasyDrop* kontaktinio kampo matavimo sistemą bei analizuojami atitinkamo gamintojo programine įranga. Mėginių celėje buvo palaikoma pastovi 21 °C temperatūra, naudojant *LabTech H50-500* vandens vėsintuvą. Iš viso buvo atliekami 5 matavimai per mėginį. Rezultatai pateikiami kaip vidurkis ± standartinis nuokrypis.

### 1.4.2 Kolageno adsorbcijos vertinimas

Protokolas kolageno koncentracijos nustatymui buvo adaptuotas pagal Tullberg-Reinert ir Jundt [180]. Pirmiausia, ant mėginių buvo pilamas I tipo kolageno tirpalas (1 mg/mL 0.1 N acto rūgštyje) ir inkubuojama 1 valandą 37 °C temperatūroje. Tuomet kolageno tirpalas buvo atsargiai nusiurbiamas ir pakeičiamas Bouin'o tirpalu (15 mL prisotintos pikrino rūgšties su 5 mL 35 % formaldehido ir 1 mL ledinės acto rūgšties), 1 valandą inkubuojamas ir praplaunamas PBS. Tuomet mėginiai buvo perkeliami į naujus šulinėlius su

Sirius Red dažu (1 mg/mL pikrino rūgštyje) ir švelniai vartant (30 aps./min.) inkubuojami 1 val. Po to, mėginiai buvo praplaunami 0.01 N druskos rūgšties tirpalu, siekiant nuplauti nesurištą dažą. Likęs nespecifiškai prisijungęs dažas buvo 30 min. tirpinamas 0.2-0.3 mL 0.1 N natrio hidroksido tirpale ant purtyklės kambario temperatūroje. Tirpalo optinis tankis buvo matuojamas naudojant *Varioskan Flash* (*Thermo Fisher Scientific*) spektrofotometrą prie 550 nm. Atskaitai buvo naudojama kalibracinė kreivė, paruošta naudojant žinomos koncentracijos I tipo kolageno tirpalus. Metodas sąlyginai specifinis I ir III tipo kolagenams. Stiklas buvo naudojamas kaip kontrolė. Atlikti 3 nepriklausomi eksperimentai, kurių rezultatai pateikiami kaip vidurkis ± standartinis nuokrypis.

### 1.4.3 Skenuojanti elektronų mikroskopija

Mėginiai buvo dengiami 10 nm aukso sluoksniu, naudojant *Quorum Q150RES* mėginių dengimo įrenginį (*Quorum Technologies Ltd*). Mėginiai buvo apžiūrimi vienu iš dviejų SEM:

1. *JEOL JSM−6390LV* veikiančiu prie 15 kV įtampos, FORTH-IESL (Heraklione, Graikijoje).
2. *JEOL JSM 7800F* veikiančiu prie 10-15 kV įtampos, Chemijos padalinyje Lankasterio universitete (Lankasteryje, Jungtinėje Karalystėje).

### 1.4.4 Energijos sklaidos Rentgeno spindulių analizė

Mėginiai buvo dengiami aukso sluoksniu (60 s, 20 mA, $8x10^{-2}$ mBar, ~ 5 nm) naudojant *Quorum Q150RES* mėginių dengimo įrenginį (*Quorum Technologies Ltd*) ir vaizdinami lauko emisijos *SEM JEOL JSM-7800F* su EDX sistema (*X-Max50, Oxford Instruments*) esant 10 mm darbiniam atstumui ir 10 kV įtampai ant žalvarinio *JEOL* laikiklio, pritvirtinus 25 mm anglies plėvelėmis (G3348N, *Agar Scientific*) Chemijos padalinyje Lankasterio universitete (Lankasteryje, Jungtinėje Karalystėje). Kiekvienas mėginys buvo matuojamas 3 kartus, rezultatai pateikiami kaip vidurkis.

### 1.4.5 Su indukcija susietos optinės spinduliuotės spektroskopija

Šie tyrimai buvo atliekami *Kratos Analytical Ltd* (Mančesteryje, Jungtinėje Karalystėje). Matavimai buvo atliekami naudojant *Agilent 5100*

*VDV ICP-OES* ašiniame režime. Mėginiai buvo ištirpinami silpnoje azoto rūgštyje (2 % masės/tūrio santykiu) su keliais perplovimo žingsniais ir sudarė galutinį 10 mL mėginio tūrį. Taikininių elementų (Al, Ti, V, Zr, Na ir P) kalibracinės kreivės buvo paruoštos tarp 1 - 100 milijoninių dalių naudojant pavienių elementų standartus (*Sigma-Aldrich*, TraceCERT, 2 % $HNO_3$), išskyrus P (*Alfa Aesar*, SpecPure, 5 % $HNO_3$). Visi tušti mėginiai buvo paruošti naudojant originalią 2 % azoto rūgštį, kuri buvo naudojama ir standartų bei mėginių paruošimui. Tušti mėginiai, standartai ir tiriamieji mėginiai buvo ruošimi su itrio vidiniu standartu (1 milijoninė dalis, *Sigma-Aldrich*, TraceCert, 2 % $HNO_3$).

### 1.4.6 Suspaudimo testai

Suspaudimo testai buvo atliekami Vilniaus Gedimino technikos Universiteto Mechanikos fakultete, naudojant *Mecmesin MultiTest 2,5-i* mikro-suspaudimų prietaisą (*Mecmesin Ltd* iš Slinfordo Jungtinėje Karalystėje), *Mecmesin AFG25* kameroje su kontroliuojamu poslinkiu, kurio matavimo tikslumas ± 0.01 mm, o suspaudimo jėga 2-2500 N ± 0.1 %. Patalpinus mėginį į instrumentą, buvo atlikti cikliniai suspaudimo testai. Deformacijos-apkrovos kreivės buvo registruojamos automatiškai iki maksimalaus 4 mm kiekvieno mėginio suspaudimo. Suspaudimo greitis buvo nustatytas 0.167 mm/s. Visi matavimai buvo atliekami kambario temperatūroje.

Tamprumo modulis buvo apskaičiuojamas mėginį veikiančią jėgą (N) padalinus iš paviršiaus ploto ($m^2$) ir padalinus iš deformacijos pokyčio.

## 1.5 Ląstelių išskyrimas, charakterizavimas ir kultivavimas

Visos medžiagos, kurios buvo naudojamos ląstelių išskyrimui, charakterizacijai ir kultivavimui yra surašytos 8 lentelėje. Šiame darbe buvo naudojamos trys ląstelių rūšys:

1. Žiurkės raumens kamieninės ląstelės.
2. Triušio raumens kamieninės ląstelės.
3. NIH/3T3 pelės embriono fibroblastai.

8 lentelė. Medžiagos, naudotos ląstelių išskyrimui, charakterizavimui ir kultivavimui.

| Pavadinimas | Pilnas pavadinimas | Tiekėjas |
|---|---|---|
| Anti-CD34 mAb | - | *Abcam* |
| Anti-CD45 mAb | - | *Abcam* |
| Anti-c-kit mAb | - | *Thermo Fisher Scientific* |
| Anti-MYF5 mAb | - | *Thermo Fisher Scientific* |
| BSA | jaučio serumo albumias | *Sigma-Aldrich* |
| Kolagenazė | - | *Sigma-Aldrich* |
| Cy3-konjuguoti antriniai antikūnai | - | *Merck* |
| DMSO | dimetilsulfoksidas | *Sigma-Aldrich* |
| EDTA-tripsinas | etilendiamino tetraacto rūgšties ir tripsino mišinys | *Gibco* |
| FBS | fetalinis veršelio serumas | *Gibco* |
| Hialuronidazė | - | *Sigma-Aldrich* |
| IMDM | Iskovo modifikuota Dulbeko terpė | *Gibco* |
| PFA | paraformaldehidas | *Sigma-Aldrich* |
| PBS | fosfatinis buferinis tirpalas | *Gibco* |
| Pen-strep | penicilino-streptomicino mišinys | *Gibco* |
| MTT | 3-(4,5-dimetiltiazol-2-il)-2,5-difeniltetrazolio bromidas | *Merck* |
| Triton X-100 | - | *Sigma-Aldrich* |

Visos ląstelės buvo auginamos IMDM terpėje, praturtintoje 10 % FBS ir antibiotikais – 100 U/mL penicilino ir 100 µg/mL streptomicino polistireno induose. Kas tris-keturias dienas, ląstelės buvo persėjamos nusiurbiant augimo terpę, praplaunant monosluoksnį PBS ir disocijuojant EDTA-tripsinu, o vėliau resuspenduojant ir išsėjant naujoje terpėje. Ląstelės buvo auginamos termostate, 37 °C temperatūroje su 5 % $CO_2$.

Dalis ląstelių buvo saugoma atsargai, užšaldant skystame azote IMDM terpėje su 30 % FBS, antibiotikais ir 10 % DMSO.

### 1.5.1 NIH/3T3 fibroblastai

NIH/3T3 fibroblastai buvo įsigyti iš ATCC. Mėgintuvėlis buvo atitirpinamas pagal gamintojo pateiktas instrukcijas, tuomet ląstelės išsėjomos į flakonėlius IMDM terpėje, praturtintoje FBS ir antibiotikais. Ląstelėms suformavus monosluoksnį, jos buvo kelis kartus persėjamos, tada surenkamos

ir užšaldomos -80 °C temperatūroje iki vėlesnio panaudojimo eksperimentuose.

### 1.5.2 Žiurkės raumens kamieninės ląstelės

Wistar žiurkė buvo eutanazuojama ir gabalėlis griaučių raumens buvo chirurgiškai išimamas. Tyrimai buvo patvirtinti Valstybinės maisto ir veterinarijos tarnybos (leidimo nr. G2-39, 03/08/2016). Didžiosios kraujagyslės buvo atskiriamos, tuomet griaučių raumens audinys buvo susmulkinamas ir 30 min. inkubuojamas švelniai vartant 37 °C temperatūroje EDTA-tripsino mišinyje su kolagenaze ir hialuronidaze (atitinkamai 0.5 % ir 0.3 %). Gauta ląstelių suspensija buvo centrifuguojama, sumaišoma su augimo terpe ir išsėjama į ląstelių kultūrai skirtus indus. Augimo terpė buvo keičiama kas 3-4 dienas, o po 5 pasažų ląstelės buvo klonuojamos serijinio praskiedimo metodu. Gauta aukšto proliferacinio aktyvumo kolonija buvo naudojama kaip ląstelių šaltinis – padauginta *in vitro* ir saugoma skystame azote tolesniam naudojimui. Ląstelės buvo auginamos IMDM terpėje su 10 % fetalinio veršelio serumo ir penicilinu-streptomicinu (100 U/mL ir 100 µg/mL). Jos buvo persėjamos kas 3-4 dienas, disocijuojant su EDTA-tripsinu ir resuspenduojant šviežioje augimo terpėje. Ląstelės buvo auginamos inkubatoriuje (*Thermo Fisher Scientific*) 37 °C temperatūroje su 5 % $CO_2$.

Ląstelės, skirtos charakterizavimui, buvo auginamos 30 mm skersmens Petri lėkštelėse su dengiamaisiais stikliukais, vėliau fiksuojamos 4 % paraformaldehidu 15 min. Ląstelės vėliau buvo plaunamos PBS ir inkubuojamos su 0.2 % Triton X-100 tirpalu PBS 15 min, siekiant permeabilizuoti ląstelių membranas. Užblokavus 1 % BSA tirpalu PBS, ląstelės buvo inkubuojamos su pirminiais antikūnais prieš CD34, CD45, MYF5 ir c-kit pernakt pagal gamintojo instrukcijas 4 °C temperatūroje. Mėginiai vėliau buvo skalaujami 1 % BSA tirpalu PBS ir inkubuojami su antriniais Cy3-konjuguotais antikūnais. Analizė buvo atliekama su Olympus IX71 fluorescenciniu mikroskopu.

### 1.5.3 Triušio raumens kamieninės ląstelės

Laboratoriniam triušiui buvo sukeliama pilna nejautra, naudojant ketaminą (30-50 µg/kg) ir diazepamą (5 µg/kg). 0.5 $cm^3$ dydžio raumens gabalėlis buvo chirurgiškai paimamas iš kairės šlaunies ir mechaniškai susmulkinamas. Vėliau jis buvo fermentiškai veikiamas kolagenazės (1 mg/mL) ir

hialuronidazės (0.3 mg/mL) tirpalu 0.125 % tripsino ir 0.1 % EDTA tirpale 15 min., esant 37 °C temperatūrai. Gauta suspensija buvo skiedžiama augimo terpe su serumu ir centrifuguojama 1-2 min prie 100 G. Gauta suspensija vėl buvo skiedžiama augimo terpe su priedais ir išsėjama į polistireno ląstelių auginimo indus. Iš pradžių, ląstelės buvo persėjamos kas 1-2 savaites iki kol buvo pasiektas pilnas monosluoksnis, o po to – kas 3-4 dienas.

### 1.6 Biosuderinamumo vertinimas

#### 1.6.1 Fluorescencinė ir šviesos mikroskopija

Mėginiai buvo apsėjami ląstelėmis, kurios buvo auginamos ir vizualizuojamos *NIKON Eclipse TS 100* mikroskopu su *Lumenera Infinity* 2C CCD kamera. Fluorescencinėms nuotraukoms, ląstelės prieš vaizdinimą buvo dažomos AO/EB dažų mišiniu arba DAPI.

Dažymas AO/EB yra fluorescencijos mikroskopijos metodika, skirta atskirti gyvas nuo negyvų (apoptozinių ir nekrozinių) ląstelių. Ląstelių membrana yra laidi AO, kuris sąveikauja su DNR, nudažydamas žaliai. AO taip pat rišasi prie RNR ir viengrandės DNR, nudažydamas jas oranžine spalva. Tuo tarpu EB patenka tik į negyvas ląsteles, kurių membraninis integralumas pažeistas, ir susirišdamas su DNR, nudažo branduolį raudonai. Ši metodika leidžia atskirti gyvas neapoptozines (žalias chromatinas), gyvas apoptozines (kondensuotas arba fragmentuotas žalias chromatinas), negyvas apoptozines (kondensuotas ar fragmentuotas oranžinis chromatinas) ir nekrozines (raudonas chromatinas) ląsteles kaip aprašyta literatūroje [183].

AO (100 µg/mL) ir EB (100 µg/mL) mišinys buvo užpilamas ant ląstelių, augintų ant tiriamųjų mėginių – 5 µL mišinio į 1 mL augimo terpės. Po 10-20 minučių, terpė buvo švelniai nusiurbiama ir pakeičiama šiltu PBS. Ląstelės buvo stebimos *Olympus* fluorescenciniu mikroskopu.

#### 1.6.2 Tėkmės citometrija

Ląstelės buvo auginamos ant tiriamųjų paviršių 24, 48, 72 ir 96 valandas. Šiais laiko intervalais buvo surenkama augimo terpė su neprilipusiomis ląstelėmis, o likęs monosluoksnis buvo veikiamas EDTA-tripsinu ir taip pat surenkamas. Visos surinktos ląstelės buvo dažomos AO/EB mišiniu kaip ir ruošiant fluorescencinei mikroskopijai. Ląstelės buvo analizuojamos *BD FACSCanto™ II* (*BD Biosciences*) tėkmės citometru, registruojant 10 000

įvykių kiekviename mėginyje. Žalia AO fluorescencija buvo detektuojama FITC kanale, o raudona etidžio bromido fluorescencija buvo detektuojama PE kanale. Buvo atlikti 3 nepriklausomi eksperimentai po 3 pakartojimus kiekvienos medžiagos atveju, kiekvienam laiko taškui. Ląstelės buvo padalintos į keturias kategorijas pagal jų fluorescencijos profilius.

### 1.6.3 MTT tyrimas

MTT proliferacijos tyrimas paremtas mitochondrijų fermento oksidoreduktazės veikimu. Vandenyje tirpus MTT (3-(4,5-dimetiltiazol-2-il)-2,5-difeniltetrazolio bromidas) redukuojamas iki vandenyje netirpaus violetinio formazano, kuris gali būti tirpinamas organiniuose tirpikliuose, kaip pvz. etanolis ir aptinkamas kolorimetriškai.

**Ląstelėms, augančioms ant paviršių**. Augimo terpė buvo švelniai nusiurbiama nuo ląstelių ir pakeičiama MTT tirpalu (0.2 mg/mL PBS). Po inkubacijos 37 °C temperatūroje 1 valandą, MTT tirpalas buvo nusiurbiamas, o susidarę formazano kristalai tirpinami 96 % etanolyje. Tirpalo sugertis buvo matuojama 570 nm bangos ilgyje, naudojant *Varioskan Flash* (*Thermo Fisher Scientific*) plokštelių skaitytuvą. Sugertis proporcinga gyvų ląstelių skaičiui ir jų metaboliniam aktyvumui.

**Polimerų ekstraktų toksiškumo vertinimas**. Polimerų mėginiai buvo gauti išsukant ant stikliukų ir polimerizuojant UV. Vėliau, mėginiai buvo inkubuojami pilnoje augimo terpėje su serumu ir antibiotikais) 24 valandas kambario temperatūroje. Terpė su polimerų ekstraktais vėliau buvo nusiurbiama ir užpilama ant monosluoksnyje augančių NIH/3T3 fibroblastų. Po 24 valandų auginimo 37 °C temperatūroje su 5 % $CO_2$, buvo atliekamas MTT testas. Atskaitai naudotos ląstelės, inkubuotos terpėje, kuri nebuvo sąveikavusi su polimerais.

## 1.7 Adhezijos stiprumas

Žiurkės raumenų kamieninės ląstelės buvo išsėjamos 100 000 ląstelių/mL/mėginį tankiu į 24 šulinėlių plokšteles ir auginamos 4 arba 24 valandas 37 °C temperatūroje su 5 % $CO_2$. Šiais laiko intervalais, mėginiai buvo perkeliami į naujas plokšteles ir pusė plokštelių buvo purtomos 500 aps./min. intensyvumu 5 minutes, naudojant *Thermomix Comfort* (*Eppendorf*) purtyklę. Palyginimui naudoti mėginiai buvo nepurtomi ir atitinkamą laiką inkubuojami termostate 37 °C temperatūroje. Likusių ant paviršiaus ląstelių

skaičius buvo vertinamas pakeičiant augimo terpę su nusiplovusiomis ląstelėmis 0.1 % kristalvioleto tirpalu 20 % etanolyje ir inkubuojant 30 min. Naudojant *Varioskan Flash* (*Thermo Fisher Scientific*) spektrofotometrą, išmatuoti ląstelių kiekiai ant purtytų ir nepurtytų mėginių ir pateikiamas santykis tarp jų. Kiekvienos medžiagos atveju buvo atliekami 3 nepriklausomi tyrimai po 3 pakartojimus.

### 1.8 Signalinių molekulių raiška ir fosforilinimas

Žiurkės raumens kamieninės ląstelės buvo išsėjamos ant tirtų mėginių 100 000 ląstelių/mL/mėginį tankiu ir auginamos 4 arba 24 valandas. Šiais laiko intervalais, mėginiai buvo perkeliami į naujas plokšteles ir švelniai praplaunami PBS. Po to, PBS buvo pakeičiamas lizės buferiu sudarytu iš 8 M karbamido, 2 M tiokarbamido ir 50 mM DTT. Ląstelės buvo surenkamos nuo 5 mėginių kiekvienam laiko intervale pipetuojant 5-10 kartų. Lizatai tada buvo centrifuguojami 10 minučių prie 20000 G kambario temperatūroje. Kiekvieno mėgintuvėlio supernatantas tuomet buvo perkeliamas į naują mėgintuvėlį ir šaldomas -20 °C temperatūroje iki panaudojimo. Buvo atlikti 3 nepriklausomi eksperimentai.

Baltymų koncentracijos buvo normalizuojamos SDS-PAGE gelyje, dažant *Coomasie brilliant blue* dažu ir fotografuojant transiliuminatoriumi (*UVP*), o vėliau analizuojant *ImageJ* programine įranga. Praskiedus didžiausios koncentracijos mėginius lizės buferiu, koncentracijomis suvienodinti mėginiai buvo leidžiami elektroforezės gelyje prie 200 V įtampos 45 min, naudojant *BioRad* elektroforezės įrenginį. Po to, baltymai buvo perkeliami ant PVDF membranos esant 25 V įtampai ir 300 mA srovei.

Sekančiam žingsnyje, membranos su baltymais buvo veikiamos pirminiais antikūnais prieš p-Akt (Ser473), p-Akt (Thr308), Akt (*Molecular Probes*), FAK (*BD Biosciences*) ir tubuliną pernakt pagal gamintojo rekomendacijas 4 °C temperatūroje. Sekančią dieną, membranos buvo tris kartus plaunamos plovimo buferiu ir 1 valandą inkubuojamos su antriniais antikūnais: fluorescencine žyme konjuguotu anti-tubulinu arba HRP-konjuguotais antikūnais prieš kitus pirminius antikūnus. Galiausiai membranos vėl buvo plaunamos plovimo buferiu. Tubulinas buvo aptinkamas matuojant fluorescenciją, tuo tarp HRP-konjuguoti antikūnai buvo veikiami ECL reagentu, kurį katalizuodama HRP generuoja chemiliuminescenciją, aptinkamą transiliuminatoriumi (*UVP*). Membranų vaizdų analizė atlikta naudojant *ImageJ*.

### 1.9 Kolageno sintezės vertinimas

Kolageno sintezės vertinimo metodas buvo analogiškas kolageno adsorbcijos vertinimo metodikai. Žiurkės raumenų kamieninės ląstelės buvo išsėjamos ant tiriamų paviršių 20 000 ląstelių/mL/mėginį tankiu 24 šulinėlių plokštelėse. Po 1, 7 ir 14 inkubacijos dienų, mėginiai buvo fiksuojami Bouin'o tirpalu, tuomet dažomi naudojant *Sirius Red* ir galiausiai plaunami HCl tirpalu. Galiausiai, dažas buvo tirpinamas NaOH tirpalu ir spektrofotometriškai matuojamas prieš gryną NaOH. Kolageno kiekis tuomet buvo nustatomas iš kalibracinės kreivės. Atlikti 3 nepriklausomi eksperimentai po 3 pakartojimus kiekvienai medžiagai kiekvienam laiko taškui.

### 1.10 Statistinė analizė

Statistinė analizė buvo atlikta naudojant *RStudio,* o grafikai nubrėžti naudojant *ggplot2*. Duomenys pateikti kaip kelių matavimų vidurkis ± standartinė paklaida arba standartinis nuokrypis. Statistiškai reikšmingi skirtumai buvo vertinami naudojant vienpusę *ANOVA* ir *Tukey's HSD post-hoc* testą. Skirtumai tarp grupių buvo laikomi reikšmingais, kai $p < 0.05$ (*), $p < 0.01$ (**) ir $p < 0.001$ (***).

# 2. REZULTATAI IR JŲ APTARIMAS

Audinių inžinerija yra tarpdisciplininė sritis, kurios tikslas – sukurti dirbtinių audinių ir organų pakaitus. Pagrindinis iššūkis, su kuriuo susiduriama kuriant dirbtinį audinį yra kaip suformuoti tokią ekstraląstelinę aplinką, kuri užtikrintų ląstelių integraciją, brendimą ir funkcinį pažeistos kūno dalies atstatymą.

Šiame darbe tiriamos strategijos dviejų rūšių audinių konstravimui:

1. Kietieji audiniai. Pasirinkta strategija konstruoti karkasus iš hibridinių organinių-neorganinių polimerų, kadangi pasitelkus tiesioginį lazerinį rašymą iš šių medžiagų galima pagaminti griežtai apibrėžtas trimates nišas ląstelėms.
2. Minkštieji audiniai. Pasirinkta strategija, paremta PDMS – šios medžiagos savybės gali būti modifikuojamos taip, kad atitiktų supančių minkštųjų audinių mechanines ir chemines savybes, taip pat PDMS gali būti papildomas bioaktyviais motyvais, patraukliais ląstelėms.

## 2.1 Kietųjų audinių inžinerija

Kietųjų audinių konstravimui ypatingai svarbu turėti tvirtą struktūrą su iš anksto numatytais mikro-architektūriniais motyvais. Tokia struktūra užtikrina tinkamą ląstelių adheziją, proliferaciją, diferenciaciją ir t. t. Karkaso medžiaga taip pat turi gebėti atlaikyti mechanines konkretaus audinio apkrovas. Siekiant sukonstruoti kieto audinio prototipą, pasitelkta strategija tiesioginio lazerinio rašymo pagrindu. Ji leidžia preciziškai pagaminti ląstelių mikroaplinkas ir yra suderinama su bio-draugiškomis medžiagomis.

### 2.1.1 Hibridinių organinių-neorganinių polimerų sintezė

Kietųjų audinių, kaip kaulas ar kremzlė, kūrimui pasirenkamos medžiagos, kurios būtų nelinkusios deformuotis ir tvirtos. Tai užtikrina ne tik audinio mechaninių savybių palaikymą, bet ir gali reguliuoti ląstelių diferenciaciją [184]–[186]. Kietųjų audinių karkasų mikroarchitektūros turi būti preciziškai formuojamos, todėl svarbu tiksliai kontroliuoti ir pačių medžiagų savybes. Literatūroje aprašoma šimtai ar net tūkstančiai skirtingų šiems tikslams naudojamų medžiagų, o jų pasirinkimas priklauso ne tik nuo konstruojamo audinio ir naudojamų ląstelių, bet ir nuo karkasų gamybai pasirinktos technologijos.

Hibridiniai organiniai-neorganiniai polimerai jau anskčiau buvo pademonstruoti kaip rodantys gerus biosuderinamumo *in vivo* ir *in vitro* rezultatus [62], [63], o taip pat šios medžiagos pasižymi puikiomis struktūrizavimo galimybėmis [56]. Kadangi keletas hibridinių organininų-neorganinių polimerų jau yra naudojami tiesioginiam lazeriniam rašymui (pvz. su Zr [56], V [55], Ge [53] ir Ti [54]), vienas iš šio darbo iššūkių buvo sukurti ir ištirti naują, iki šiol literatūroje neaprašytą medžiagą su Al.

Pirmiausia, polimerai su Ti, V ir Zr buvo susintetinti anksčiau aprašytomis metodikomis [54]–[56]. Polimero su Al paruošimui buvo pasirinktas kelias analogiškas polimerų su Ti ir Zr paruošimui, papildant vienu žingsniu, skirtu ištirpinti aliuminio izopropoksidą toluene, kad šis geriau maišytųsi su kitais komponentais – metakrilo rūgštimi ir MAPTMS. Gautas polimeras su Al yra skaidrus gelsvo atspalvio (dėl pridėto BIS) skystis. Išgarinus tirpiklį, medžiaga pereina į tirštą gelinę būseną. Šis perėjimas sumažina struktūrines deformacijas, kurios gali atsirasti darinių formavimo metu dėl vibracijų, difuzijos ir stalų judėjimo kai kuriose tiesioginio lazerinio rašymo sistemose. Šiame darbe tirti mėginiai buvo miniatiūriniai, todėl buvo labai svarbu užtikrinti tinkamą jų sukibimą su substratu. Siekiant pagerinti borosilikatinių dengiamųjų stiklelių sukibimą su gaminamais mikrodariniais, jų paviršius buvo chemiškai modifikuojamas. Hidrolizuoto MAPTMS Si-OH grupėms sudarius ryšius su stiklo paviršiumi, dvigubieji MAPTMS ryšiai eksponuojami į paviršių, kur gali sudaryti kovalentinius ryšius su polimerinėmis medžiagomis. Siekiant patikrinti ar silanizacijos procedūra pavyko, išmatuoti MAPTMS veiktų ir kontrolinių, etanoliu plautų, stikliukų paviršių kontaktiniai kampai. Rezultatai pateikiami 2 paveiksle. Sėkmingą borosilikatinių stikliukų silanizaciją patvirtina ryškus kontaktinio kampo pasikeitimas po poveikio MAPTMS – nuo maždaug 39 laispnių (etanoliu plauti ir ore džiovinti stikliukai) iki maždaug 53 laispnių (MAPTMS veikti, etanoliu plauti ir ore džiovinti stikliukai). Kitame etape įvertinome susintetintų polimerų kontaktinius kampus.

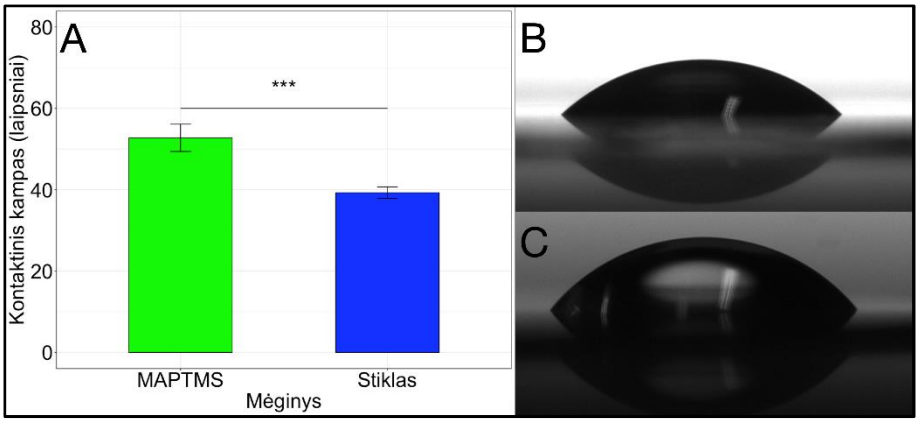

2 paveikslas. A – palyginamųjų ir MAPTMS veiktų borosilikatinių stikliukų kontaktiniai kampai. B – vandens lašelis ant palyginamojo, etanoliu plauto stikliuko. C – vandens lašelis ant MAPTMS veikto stikliuko paviršiaus. Rezultatai pateikiami kaip vidurkis ± standartinis nuokrypis su n = 5. * - $p < 0.05$, ** - $p < 0.01$, *** - $p < 0.001$.

### 2.1.2 Medžiagų charakterizavimas

**Paviršių kontaktiniai kampai**. Vertinant medžiagų biosuderinamumą *in vitro*, vienas pirmųjų procesų yra serumo baltymų adsorbcija ant ląstelių kultūrai naudojamo paviršiaus. Šis procesas tiesiogiai veikia ląstelių adheziją ir viduląstelinius procesus. Paviršiaus kontaktinis kampas yra vienas iš svarbiausių parametrų, nusakančių baltymų-paviršiaus sąveiką, kadangi tai yra tiesioginis medžiagos hidrofobiškumo arba hidrofiliškumo įvertinimas. Dėl šios priežasties, pirmiausiai buvo tiriami skirtingų hibridinių organinių-neorganinių polimerų kontaktiniai kampai.

Kontaktinių kampų matavimas buvo atliekamas ant išsukimo būdu dengtų stikliukų. Visos medžiagos tolygiai padengė stikliukų paviršius ir prie jų prikibo pakankamai stipriai, kad būtų galima pamatuoti kontaktinius kampus. Rezultatai rodo, jog visi hibridiniai organiniai-neorganiniai polimerai turėjo aukštesnius kontakinius kampus (***, $p < 0.001$) nei stiklas – žr. 3 paveikslą.

Al ir Zr hibridai turėjo atitinkamai maždaug 72 ir 71 laipsnio kampus. Ti hibridas buvo hidrofobiškesnis, jo kontaktinis kampas buvo apie 90 laipsnių. V hibridas turėjo didžiausią – vidutiniškai 102 laipsnių kontaktinį kampą.

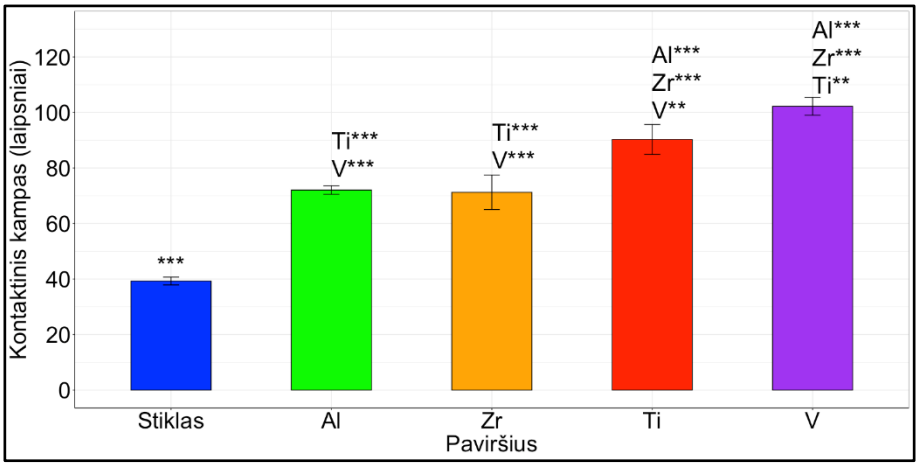


3 paveikslas. Hibridinių organinių-neorganinių polimerų kontaktiniai kampai. Rezultatai pateikiami kaip vidurkiai ± standartiniai nuokrypiai, n = 5. Stiklas buvo naudojamas kaip kontrolė. * - $p < 0.05$, ** - $p < 0.01$, *** - $p < 0.001$.

Kadangi visi gyvi organizmai daugiausiai sudaryti iš vandens, ideali medžiaga audinių inžinerijai turėtų būti kiek įmanoma hidrofiliškesnė. Tačiau ląstelių kultūros metu, ant paviršių adsorbuojasi baltymai ir kitos biomolekulės, kurios gali turėti reikšmingos įtakos jo savybėms. Išmatuoti paviršių kontaktinius kampus, prie kurių adsorbuotos bioaktyvios molekulės, būtų sudėtinga užduotis dėl difuzijos. Todėl be kontaktinio kampo matavimų, turėtų būti taikomos ir kitos metodikos, leidžiančios įvertinti biomolekulių adsorbciją ir ląstelių atsakus.

Parodyta, kad biomolekulės geriausiai adsorbuojasi, esant maždaug 70 laipsnių kontaktiniam kampui [187]. Minimame tyrime naudoti chitosanu dengti titano mėginiai ant kurių buvo vertinta albumino ir fibronektino adsorbcija bei ląstelių prikibimas. Parodyta, kad dengimas chitosanu reikšmingai padidino kontaktinius paviršių kampus nuo maždaug 32 iki 76 laipsnių, bet taip pat pagerino ir tirtų baltymų adsorbciją bei vėlesnę ląstelių adheziją ir proliferaciją.

**Polimerų cheminio integralumo vertinimas**. Kitas polimerų savybių vertinimo žingsnis buvo išsiaiškinti polimerų cheminį integralumą ir sudėtį. Šis žingsnis reikalingas todėl, kad po lazerinės polimerizacijos seka mėginių plovimo etapas, skirtas laisvų monomerų išplovimui. Šio tyrimo esmė - įsitikinti, jog plovimo metu iš polimero neišsiplauna metalų oksidai ir jonai, kurie gali neigiamai veikti ląstelių savybes. Tuo tikslu, hibridinių organinių-neorganinių polimerų su Al, Ti, V ir Zr mėginiai buvo analizuojami EDX spektroskopija.

Analizė buvo atliekama polimerintuose medžiagų lašeliuose, siekiant patvirtinti metalų buvimą juose. Rezultatai pateikiami 4 paveiksle. Polimerų sluoksniai buvo sąlyginai stori (šimtų mikronų eilės), todėl Rentgeno spindulių signalas turėjo būti generuojamas pačiose medžiagose. Toks pats stiklas, kuris buvo naudojamas mėginių paruošimui, naudotas palyginimui. Al hibridas turėjo piką ties 1.5 keV, kuris rodė maždaug 2 kartus aukštesnį Rentgeno fotonų skaičių, nei palyginimui naudotas stiklas, tokiu būdu patvirtinant Al buvimą medžiagoje (būdingas aliuminio Kα = 1.486 keV). V hibrido atveju, pikas ties maždaug 5 keV indikuoja V buvimą (būdingas Kα = 4.949 keV ir Lα = 0.511 keV) – šiuo atveju fotonų skaičius viršijo stiklo kontrolę maždaug 20 kartų prie 4.949 keV. Vanadžio Lαsignalo nebuvo galima atskirti dėl persidengimo su deguonies Kα. Reikšmingai didesni kiekiai Ti buvo pastebėti Ti hibride, lyginant su kontroliniu stiklu, detektuotų Rentgeno fotonų skaičiui prie Kα = 4.508 keV maždaug 2.7 kartus viršijant stiklo. Galiausiai, pikas prie 2 keV indikuoja Zr buvimą (būdingas Lα = 2.042 keV) Zr hibride, kur būdingų fotonų skaičius 10.7 kartus viršijo stiklo. Aukso, kuriuo buvo dengiami visi mėginiai, buvimas patvirtintas visuose tirtuose mėginiuose prie 2.120 keV. Signalai iš K ir Na buvo aptinkami tik stikle, patvirtinant, jog medžiagų sluoksnis ant stikliukų buvo pakankamas, kad Rentgeno spinduliai būtų generuojami medžiagose, o ne po jomis. Taigi, mūsų gauti duomenys parodė, kad metalai po plovimo išlieka medžiagose.

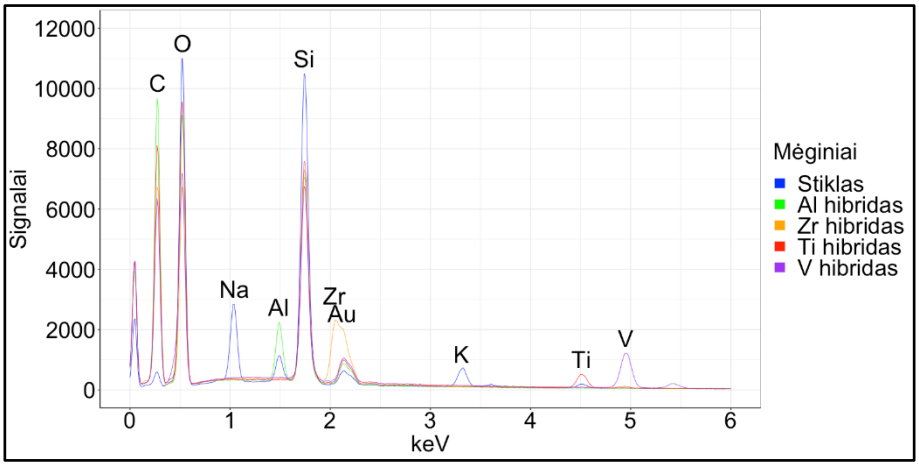


4 paveikslas. Skirtingų hibridinių organinių-neorganinių polimerų EDX spektrai, kuriuose vaizduojami Al, Ti, V ir Zr būdingi pikai. Palyginimui naudotas borosilikatinis stiklas.

### 2.1.3 Darinių formavimas

Tolesniame šio darbo etape tyrėme naujojo polimero su Al struktūrizuojamumą ir lyginome pagamintus darinius su iš analogiškų polimerų (su Ge, Ti, V ir Zr) pagamintais literatūroje aprašytais dariniais. Literatūroje polimerai tiek su Ti, tiek su Zr jau buvo tirti kaip medžiagos, tinkamos karkasų audinių inžinerijai gamybai [58], [65].

Hibridinis polimeras su Al yra permatomas, o jame esantis fotoiniciatorius suteikia fotojautrumą apšvietus lazeriu. Dėl šios priežasties, sąlyčio taško tarp stikliuko ir medžiagos radimas yra toks pat paprastas kaip ir su komerciškai prieinamais fotopolimerais, kaip *OrmoComp*® arba *OrmoClear*®. Pirmiausia ištyrėme hibridinio polimero su Al struktūrizuojamumą, gamindami dvimačius darinius (5 paveikslas). Darinių formavimo procedūra buvo sėkminga, be reikšmingų nukrypimų nuo CAD modelių.

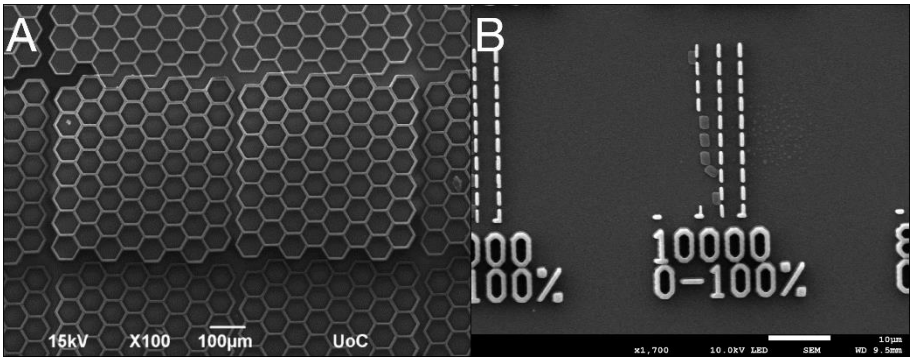


5 paveikslas. Dvimačiai dariniai, pagaminti iš Al turinčio hibridinio polimero. A – koriai, pagaminti Ti:safyro lazerio pagrindu sukonstruota sistema FORTH-IESL, naudojant 40X 0.95 NA objektyvą. B – kalibracinės linijos, pagamintos skirtingais greičiais ir lazerio galiomis, naudojant *Nanoscribe*® sistemą su 63X 1.4 NA imersinu objektyvu.

Toliau buvo tiriama pagamintų darinių paviršiaus topografija. Pagamintos kelių šimtų nanometrų pločio linijos, kurios vėliau stebėtos SEM. Rezultatai pateikiami 6A paveiksle. Nustatyta, jog hibridinio polimero su Al paviršius buvo šiurkštus su nedideliais iškilimais ir grūdeliais. Palyginimui, lašelis nesupolimerizuotos medžiagos buvo išdžiovintas ore ir stebimas analogišku būdu - nustatyta ta pati, granulinė medžiagos struktūra (6B paveikslas).

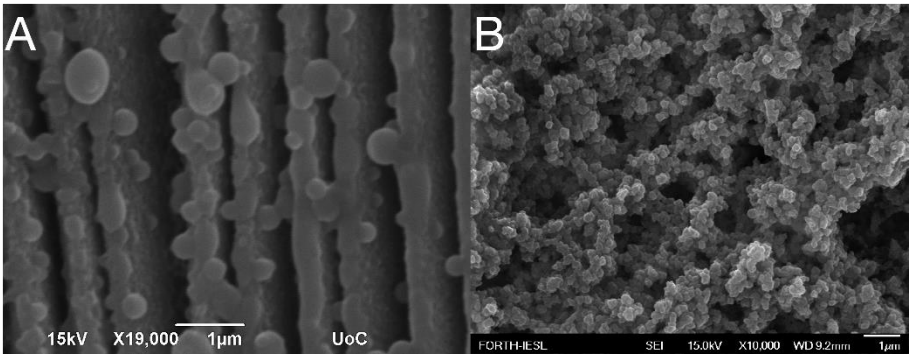

6 paveikslas. Polimerizuoto ir nepolimerizuoto hibridinio polimero su Al paviršiaus topografija. A – linijos, pagamintos 2mm/s greičiu, naudojant 40X 0.8 NA objektyvą. Nanodalelės matomos polimero paviršiuje. B – SEM mikrografija, kurioje pavaizduotas nesupolimerizuotas Al hibridas. Medžiagos tekstūra – nanodalelių pagrindu.

Parodžius, jog iš tiriamosios medžiagos galima formuoti aukštos kokybės darinius su minimaliais erdviniais iškraipymais, buvo sumodeliuotos ir pagamintos suspenduotos linijos tarp laikančių struktūrų. Naudotos skirtingos lazerio galios ir skenavimo greičiai, siekiant nustatyti maksimalią įmanomą iš Al hibrido pagamintų darinių raišką (7 paveikslas). Linijos, kurios išsilaikė plovimo proceso metu, atkartojamai siekė < 200 nm plotį, naudojant 100X 1.4 NA imersinį objektyvą Ti:safyro sistemoje ir < 250 nm, naudojant 63X 1.4 NA imersinį objektyvą *Nanoscribe*® sistemoje.

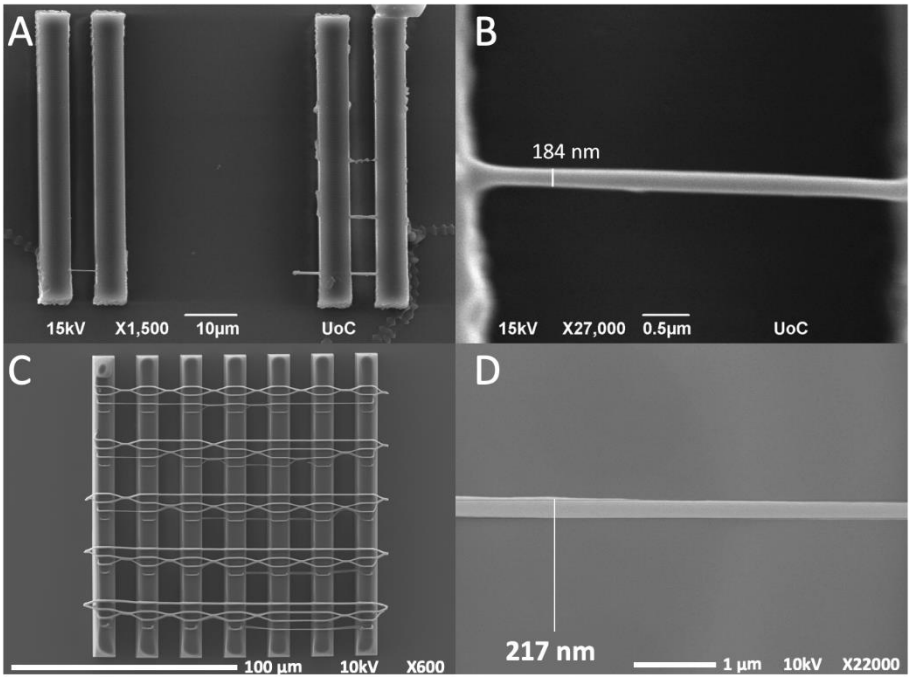


7 paveikslas. Laikančios struktūros ir tarp jų suspenduotos linijos, pagamintos iš Al hibrido. A, B – dariniai suformuoti, naudojant FORTH-IESL tiesioginio lazerinio rašymo sistemą ir 100X 1.4 NA imersinį objektyvą. Vaizdas skirtingais didinimais. C, D – dariniai, pagaminti naudojant *Nanoscribe*® sistemą su 63X 1.4 NA imersiniu objektyvu. Abejomis sistemomis pagamintos linijos, kurių rezoliucijos atkartojamai siekė apie 200 nm.

Gauti rezultatai palyginami su literatūroje aprašytomis hibridinių organininų-neorganinių polimerų skiriamosiomis gebomis. Pavyzdžiui, Sakellari su kolegomis tiesioginio lazerinio rašymo būdu gaminant fotoninius kristalus pavyko pasiekti 100 nm skiriamąją gebą [188].

Galiausiai buvo formuojami trimačiai dariniai (8 paveikslas). Dariniai sėkmingai išsilaikė plovimo procedūros metu su minimaliomis deformacijomis ar susitraukimu. Mikroskopiniame laive ir *Lich King* skulptūrėlėje matomas detalumas palyginamas su CAD modeliais.

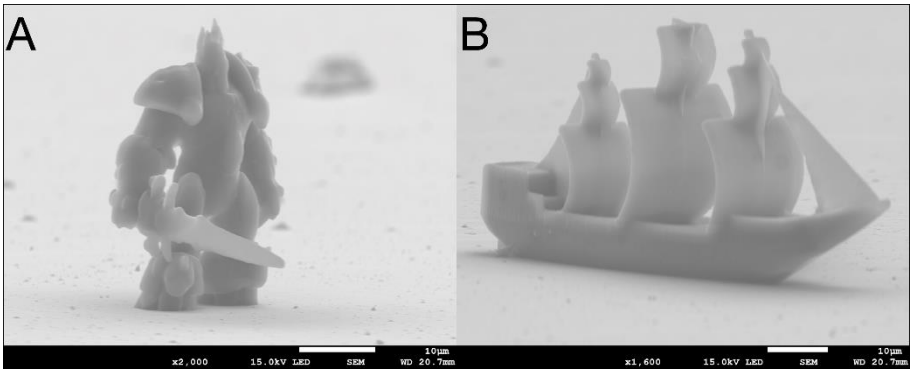

8 paveikslas. 3D dariniai, pagaminti iš Al hibrido, naudojant *Nanoscribe*® sistemą ir 63X 1.4 NA imersinį objektyvą. A – *Lich King*, pagamintas naudojant 40 % (20 mW) lazerio galią ir 10 mm/s skanavimo greitį. B – mikro-laivas, pagamintas analogiškais parametrais. Skalės – po 10 µm.

Taigi, mūsų susintetintas naujasis hibridinis organinis-neorganinis polimeras su Al gali būti naudojamas aukštos raiškos 3D mikro-darinių formavimui ir prilygsta Ge, Ti, V ir Zr hibridams. Rezultatai daug žadantys 3D formavimo prasme, tačiau iki sėkmingo šio polimero panaudojimo audinių inžinerijos taikymams reikalingas išsamus jo biosuderinamumo tyrimas.

### 2.1.4 Baltymų adsorbcijos vertinimas

Biosuderinamumo tyrimus pradėjome įvertindami kaip ekstraląstelinio matrikso baltymai adsorbuojasi prie skirtingų hibridinių organinių-neorganinių polimerų paviršių. I tipo kolagenas buvo pasirinktas kaip modelis šiame eksperimente dėl jo gausos ekstraląsteliniame matrikse. Kolagenas palaiko ląstelių adheziją per RGD sekas, kurios yra specifiškai atpažįstamos integrinų. Šios sąveikos užtikrina stiprų ląstelių susirišimą su ECM, o karkaso gebėjimas išlaikyti tokias biomolekules savo paviršiuje yra svarbus veiksnys konstruojant dirbtinius audinius.

Kolagenas ir pats savaime gali būti naudojamas audinių inžinerijos tikslams, pvz. Ber *et al.* osteoblastų augimą ant dvimačių paviršių reguliavo dengdami juos kolagenu [189], Ramanathan *el al.* darbuose kaip potencialūs antibakteriniai odos pakaitalai buvo tiriamos trimatės hibridinės kolageno matricos [190]. Kolagenas ir jo junginiai yra tinkami minkštųjų audinių inžinerijai, tuo tarpu kietųjų audinių inžinerijai kolagenas gali būti naudojamas paviršių, pagamintų iš kitų medžiagų, padengimui. Daug autorių apžvelgia kolageno panaudojimą tiek jo grynoje, tiek kompozitinėse formose

[191]–[193]. Kolagenas ne tik užtikrina ląstelių adheziją per integrinų aktyvaciją, bet taip pat yra vienas tvirčiausių žinomų baltymų – 1 mm skersmens gija gali išlaikyti maždaug 10 kg masę [194]. Dėl šių priežasčių, galimybė dengti polimerinius darinius kolagenu atrodo patraukli, audinių inžinerijoje naudotina strategija.

Mūsų eksperimentuose baltymų kiekybinio nustatymo metodikos pasirinkimas buvo ribotas dėl tirtose medžiagose esančių fotoiniciatorių, pasižyminčių autofluorescencija. Todėl buvo pasirinkta kolorimetrinė analizė. Kolageno adsorbcija buvo matuojama tiek ant hibridinių polimerų, tiek ant palyginamųjų stiklo paviršių. Nors didžiausias kolageno kiekis buvo rastas ant polimero su Zr paviršiaus, o mažiausias kiekis – ant polimero su Al paviršiaus, rezultatai abiejose šiose grupėse buvo stipriai išsibarstę ir statistiškai reikšmingų skirtumų tarp jų nebuvo rasta – $p = 0.35$ tarp Al ir Zr, $p = 0.72$ tarp stiklo ir Zr, $p = 0.81$ tarp stiklo ir Al. Rezultatai pateikiami 9 paveiksle.

Šioje elektroninėje versijoje 9 paveikslas buvo pakoreguotas.

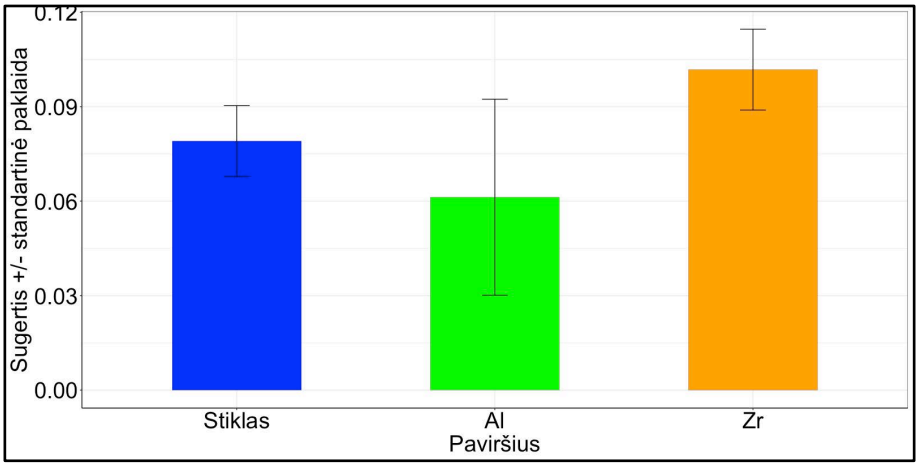


9 paveikslas. Kolageno I adsorbcija prie Al ir Zr hibridų ir stiklo. Rezultatai pateikiami kaip vidutinė *Sirius Red* dažo sugertis ± standarinės paklaidos iš trijų nepriklausomų eksperimentų, kurių kiekviename po n=3 (iš viso n=9 per medžiagą). Statistiškai reikšmingų skirtumų nerasta.

Pagal kalibracinę kreivę (pateikiama disertacijoje anglų kalba, *Supplementary Materials* skyrelyje), parodančią ryšį tarp I tipo kolageno ir *Sirius Red* sugerties, apskaičiuotas ryšys tarp sugerties ir kolageno kiekio polimerų paviršiuose: 5.6 ± 0.55 µg ant stiklo, 4.40 ± 1.76 µg ant Al ir 6.73 ± 0.59 µg ant Zr. Ankstesnėje darbo dalyje parodyti šių paviršių kontaktiniai kampai buvo: stiklo – 39, Al – 72, o Zr – 71 [176]. Nors tarp stiklo ir hibridinių polimerų paviršių yra reikšmingas kontaktinių kampų skirtumas, kolageno

adsorbcijos skirtumai nebuvo pastebimi dėl didžiulio standartinio nuokrypio. Ying *et al.* [195] buvo nustatę, kad paviršiaus kontaktiniam kampui išaugus nuo 40 iki 70 laipsnių, kolageno adsorbcija prie stiklo turėtų padidėti maždaug du kartus. Analogiško rezultato buvo galima tikėtis ant mūsų tirtų paviršių, kadangi baltymų adsorbcija iš esmės priklauso nuo tų pačių veiksnių kaip ir kontaktinis kampas – elektrostatinių ir hidrofobinių sąveikų. Įdomu tai, kad gauti rezultatai ryšio tarp kontaktinio kampo ir kolageno adsorbcijos neparodė.

### 2.1.5 Fibroblastų atsakas į polimerinius paviršius

Įvertinus tiriamų medžiagų struktūrizuojamumą lazeriu bei kolageno adsorbcijos ant jų potencialą, toliau tyrėme kokią įtaką šie paviršiai turi ląstelių gyvybingumui. Biosuderinamumo vertinimui naudojome NIH/3T3 pelės embrionų fibroblastus ir žiurkės raumenų kamienines ląsteles.

Fibroblastai buvo išsėti ant stikliukų, Al, Ti, V ir Zr hibridų ir po 96 valandų auginimo monosluoksniai fotografuoti šviesiniu mikroskopu. Sveiki fibroblastai buvo būdingos verpstės formos, tuo tarpu negyvybingos ląstelės buvo linkusios suapvalėti ir atsikabinti nuo paviršiaus. Po 96 valandų auginimo, verpstės formos ląstelių buvo galima rasti ant visų paviršių, išskyrus V hibridus – žr. 10 paveikslą.

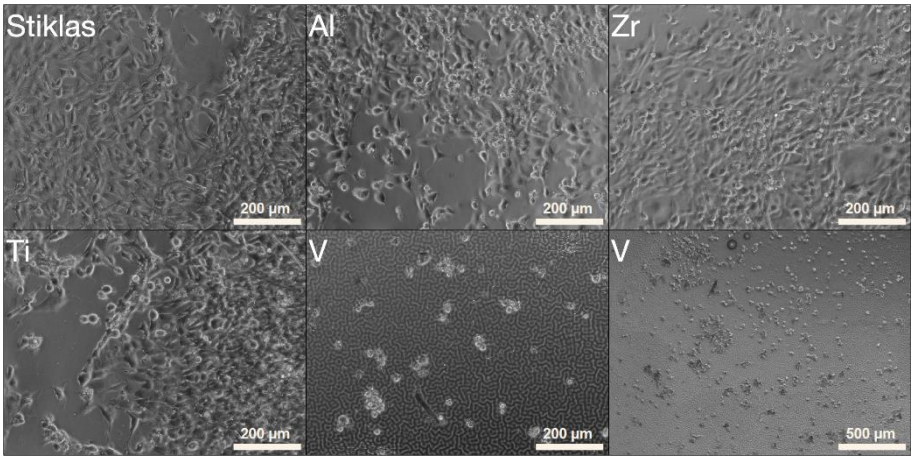


10 paveikslas. NIH/3T3 fibroblastai, auginami ant hibridinių organinių-neorganinių polimerų ir stiklo. Nuotraukos darytos praėjus 96 valandoms nuo ląstelių išsėjimo, naudojant invertuotą šviesinį mikroskopą su 4X arba 10X objektyvu. Sveika ląstelių morfologija stebėta ant stiklo, Al, Zr ir Ti paviršių. Tuo tarpu ant V hibrido nebuvo rasta prikibusių sveikos morfologijos ląstelių.

Siekiant kiekybiškai įvertinti ląstelių gyvybingumą, pasirinktas diferencialinis dažymas AO/EB. Gauti duomenys patvirtino, kad toksiškiausias paviršius ląstelėms buvo polimeras su V (11 paveikslas) – po 24 valandų auginimo didžioji dalis ląstelių ant šio paviršiaus žuvo nekrozės būdu, o po 96 ir 120 val. ant šio paviršiaus praktiškai nebuvo likę nei vienos gyvos ląstelės. Nustatėme, kad visais tirtais atvejais nekrozė buvo vyraujantis ląstelių žūties būdas.

Atlikę statistinę analizę nustatėme, kad ant visų paviršių (išskyrus V hibridus) gyvų ląstelių skaičius buvo tarp 60 ir 80 % visais tirtais laiko momentais (po 24, 96 ir 120 valandų). Patvirtinome anksčiau gautus duomenis – toksiškiausias buvo polimeras su V. Mūsų gauti rezultatai sutampa su literatūros duomenimis – vanadis žinomas kaip toksiška medžiaga tiek elementinėje, tiek oksidų formose [198].

Statistiškai reikšmingų skirtumų tarp apoptozinių ląstelių skaičių ant skirtingų paviršių nenustatėme (9 lentelė).

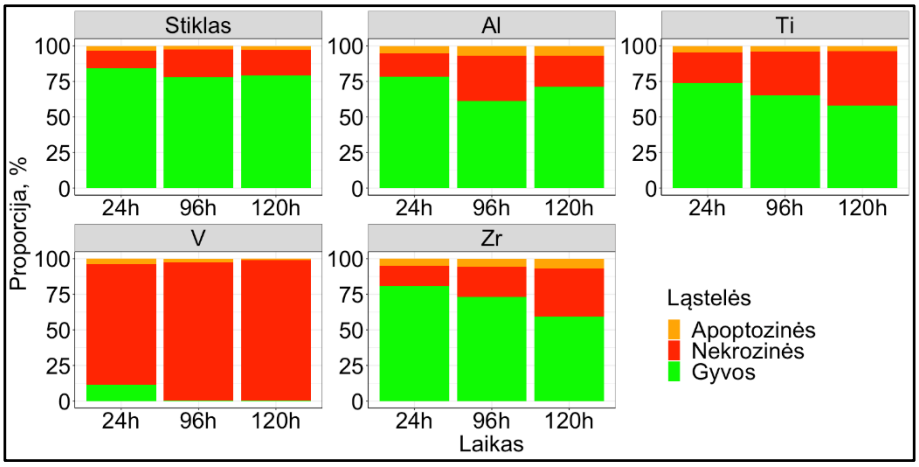


11 paveikslas. Gyvų, apoptozinių ir nekrozinių NIH/3T3 fibroblastų skaičius ant stiklo, Al, Zr, Ti ir V hibridinių organininų-neorganinių medžiagų po 24, 96 ir 120 valandų kultūros, nustatytas dažant AO/EB mišiniu. Tuo tikslu kiekvienai medžiagai ir kiekvienam laiko intervalui naudota po 5 stikliukus ir kiekviename jų suskaičiuota po 100 ląstelių. Rezultatai pateikiami kaip vidurkiai. V hibrido rezultatai reikšmingai skyrėsi nuo visų kitų paviršių su $p < 0.001$ (***). Kiti reikšmingi skirtumai pateikiami 9 lentelėje.

9 lentelė. Statistiškai reikšmingi skirtumai tarp duomenų, pavaizduotų 11 paveiksle. * - $p < 0.05$, ** - $p < 0.01$, *** - $p < 0.001$.

| Palyginimas (Paviršius\|Laikas) | Gyvos | Nekrozinės |
|---|---|---|
| Al96-G24 | ** | * |
| Zr120-G24 | *** | ** |
| Ti96-G24 | * | * |
| Ti120-G24 | *** | *** |
| Zr120-G96 | * | - |
| Ti120-G96 | * | * |
| Zr120-Al24 | * | ** |
| Ti120-Al24 | * | - |
| Zr24-Al96 | * | * |
| Zr120-Zr24 | ** | * |
| Ti120-Zr24 | ** | *** |
| G120-Zr120 | * | - |
| G120-Ti120 | ** | * |

Toliau vertinant NIH/3T3 fibroblastų metabolinį aktyvumą, ląstelės buvo 120 valandas auginamos ant Al, Ti ir Zr paviršių bei kontrolinių stikliukų (12 paveikslas). Gauti rezultatai sutampa su šviesinės mikroskopijos ir AO/EB dažymo rezultatais – NIH/3T3 fibroblastai buvo linkę prisitvirtinti ir proliferuoti ant visų paviršių, išskyrus hibridinį polimerą su V. Aukščiausias metabolinis aktyvumas nustatytas ląstelėse, augintose ant Zr turinčio hibridinio polimero. Gautas rezultatas patvirtina šios medžiagos biosuderinamumą kartu su anksčiau atliktais tyrimais *in vivo*, kurių metu buvo parodyta, jog ši medžiaga palyginama su chirurgine siūle, pagaminta iš glikolido/laktido (*Polysorb™ 4-0*) [63]. Lyginant ląstelių metabolinius aktyvumus ant Al ir Ti hibridų, statistiškai reikšmingų skirtumų nebuvo nustatyta. Zr paviršius palaikė reikšmingai aukštesnį ląstelių metabolinį aktyvumą, nei Al ar Ti paviršiai, tačiau visos medžiagos pasirodė tinkamomis naudoti audinių inžinerijos tikslams.

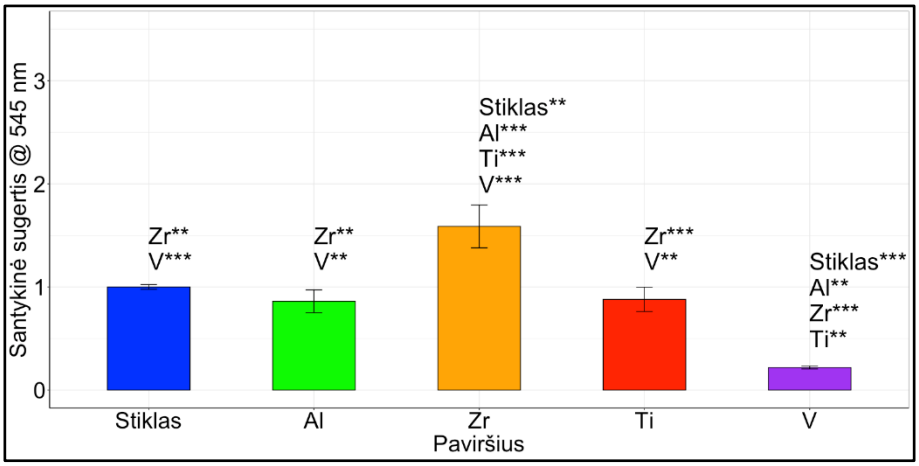


12 paveikslas. Santykinis MTT dažymo optinis tankis, išmatuotas praėjus 120 valandų nuo NIH/3T3 ląstelių išsėjimo. Optinis tankis tiesiogiai proporcingas bendram ląstelių, augančių ant paviršiaus, metaboliniam aktyvumui. Rezultatai pateikiami kaip optinio tankio santykis su ant stiklo augintų ląstelių optiniu tankiu ± standartinė paklaida. ** - $p < 0.01$, *** - $p < 0.001$.

### 2.1.6 Polimerų integralumo vertinimas

Toliau siekėme išsiaiškinti ar polimerų su V paviršių toksiškumas susijęs su medžiagos chemine sudėtimi ir aukštu kontaktiniu kampu ar labiau su toksiškų medžiagos komponentų išsiplovimu į terpę. Tai svarbu įvertinti todėl, kad jei paviršiaus citotoksiškumas pasireiškia dėl aukšto kontaktinio kampo, problema gali būti lengvai išsprendžiama biodekoruojant paviršius hidrofiliškomis medžiagomis, pvz., baltymais ar peptidais. Kita vertus, jei už citotoksiškumą atsakingi polimero skilimo produktai, tokie karkasai po implantacijos gali sukelti ląstelių žūtį, audinio uždegimą ir randėjimą.

Nors aliuminio, vanadžio ir titano jonai žinomi kaip toksiški *in vitro* ir *in vivo* [199], tirtuose junginiuose jie yra oksidų formos ir įjungti į didžiulius makromolekulinius tinklus. Tačiau net ir nedideli šių medžiagų kiekiai gali kauptis ląstelėse bei sukelti nepageidaujamus ilgalaikius padarinius. Dėl tos priežasties buvo svarbu įvertinti polimerų cheminį integralumą.

Rhoads *et al.* pademonstravo, kad ląstelių kultūroje vanadžio oksidai nėra toksiški žmogaus ląstelėms, tačiau toksiški nanovamzdelių pavidalu [200]. Nustatyta, kad nanovamzdelių forma gali turėti įtaką toksiškumo lygiui, t.y. lemti ląstelių pažaidos mechanizmą susijusį arba su adhezijos molekulių inhibicija arba ląstelių membranos pažaidomis. Dėl to būtų galima manyti, kad nanostruktūros pagamintos tiesioginio lazerinio rašymo būdu dėl savo

aštrių formų, galėtų pažeisti ląstelių membranas ir sukelti nekrozę. Tačiau V nano- kristalų susidarymas nėra šio darbo tyrimų objektas ir turėtų būti studijuojamas atskirai, naudojant transmisijos elektronų mikroskopiją.

Sabbioni *et al.* tyrė kaip BALB/3T3 ląstelės veikiamos vanadžio (IV) ir vanadžio (V) [201]. Po poveikio dozėmis nuo $10^{-5}$ to $5x10^{-8}$ M ląstelių kultūroje buvo nustatyta, kad amonio arba natrio metavanadato koncentracijos virš $10^{-5}$ M buvo citotoksiškos (< 3 % ląstelių gyvybingumas). Tuo tarpu tos pačios koncentracijos vanadil sulfato poveikis sumažino gyvybingumą iki <17 %.

Taigi, siekiant įvertinti V išsiplovimą, pirmiausia buvo paruošiami polimerų ekstraktai pilnose augimo terpėse, kuriomis vėliau buvo veikiami ląstelių monosluoksniai. Rezultatai pateikiami 13 paveiksle. Ląstelės, augintos kontrolinėje terpėje, pasižymėjo palyginamu, bet kiek žemesniu metabolizmu, lyginant su Al, Zr ir Ti polimerų ekstraktais. Įdomu tai, kad rastas reikšmingas skirtumas tarp Al ir kontrolinių paviršių su $p < 0.05$. Kaip ir buvo galima spėti, ląstelės augintos su V ekstraktu nebuvo metaboliškai aktyvios. Tai patvirtino, kad iš polimero su V į terpę išsiplovė toksiški komponentai.

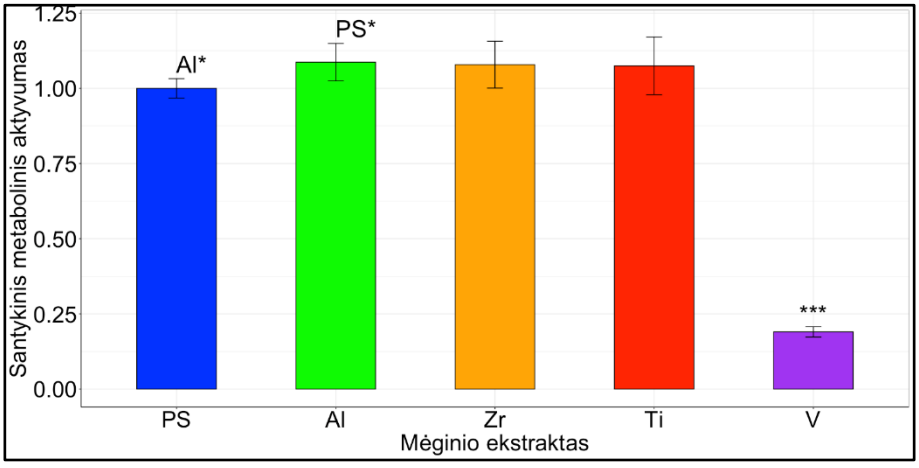


13 paveikslas. NIH/3T3 fibroblastai, auginti terpėse su polimerų ekstraktais. Rezultatai pateikiami kaip sugerties santykis su stiklu ± standartinis nuokrypis. Al ir kontroliniai paviršiai pasižymėjo reikšmingais skirtumais su * - $p < 0.05$, tuo tarpu V reikšmingai skyrėsi nuo visų kitų paviršių su *** - $p < 0.001$. PS – polistirenas.

Taigi, galima daryti prielaidą, kad kitų polimerų citotoksiškumas tyrimo metu nepasireiškė todėl, kad metalų junginiai į terpę neišsiplovė arba jų koncentracijos buvo nepakankamos, kad sukeltų reikšmingą citotoksinį

efektą. Žinoma, kad aliuminio jonai turi pro-oksidantinių ir genotoksinių savybių [202], todėl jų išsiskyrimas į aplinkinius audinius turėtų būti sumažinamas iki minimumo.

Siekiant išsiaiškinti ar polimero su V komponentai ištirpsta terpėje buvo atliktas ICP-OES tyrimas, kuris parodė, kad Al, Ti ir Zr turintys polimerai praktiškai neišskyrė metalų junginių į aplinką. Tuo tarpu, V išsiskyrė iš polimero – PBS druskos kristaluose nustatyta 35000 dalys iš milijono vanadžio jonų (14 paveikslas).

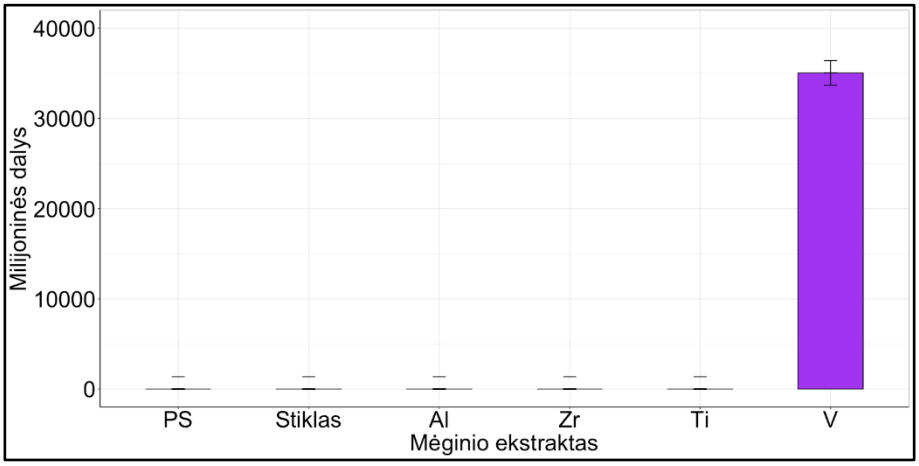


14 paveikslas. ICP-OES ekstraktų duomenys: polistireno (PS), stiklo, Al, Zr, Ti ir V.

Taigi, remiantis gautais rezultatais galime daryti išvadą, kad hibridinis polimeras su V pasižymi žemu cheminu integralumu. Tokio polimero panaudojimas audinių inžinerijoje lemtų reikšmingą V kaupimąsį aplinkinėse ląstelėse, oksiduotų ir modifikuotų ląstelių komponentus, veiktų organeles [201].

### 2.1.7 Biosuderinamumo vertinimas, naudojant raumenų kamienines ląsteles

Biosuderinamumo vertinimui buvo pasirinkta pirminė žiurkės raumens ląstelių linija siekiant kiek įmanoma tiksliau imituoti klinikinį scenarijų. Tokių ląstelių panaudojimas yra daug žadanti strategija dėl didžiulio donorinių audinių šaltinių pasirinkimo, sąlyginai mažos žalos donorinei audinio vietai ir aukšto ląstelių proliferacinio aktyvumo bei multipotentiškumo. Išskirtos žiurkės raumens kamieninės ląstelės turėjo CD34, MYF5 ir c-kit žymenis ir buvo neigiamos CD45 žymens atžvilgiu (15

paveikslas). CD34 yra ląstelių paviršiaus fosfoglikoproteinas, susijęs su ląstelių adhezija ir, nors daugumoje aptinkamas hematopoetinėse ląstelėse, CD34 buvimas parenchiminėse ląstelėse siejamas su progenetorine ar kamienine ląstelių būsena [203]. Myf5 – miogeninis faktorius, randamas ląstelėse, diferencijuojančiose miogenine linkme [204]. Šio faktoriaus buvimas patvirtina raumeninę išskirtų ląstelių kilmę. c-kit (dar žinomas kaip CD117) yra dar vienas hematopoetinėms ir multipotentinėms progenetorinėms ląstelėms būdingas žymuo. Tai – citokinų receptorius tirozino kinazė, atsakingas už signalus, lemiančius ląstelės išgyvenimą, proliferaciją ir diferenciaciją [205]. CD45 – receptorius tirozino fosfatazė, iš esmės atsakingas už citokinų receptorių, pvz. JAK kinazių, signalų slopinimą ir dažniausiai randamas pilnai diferencijavusiose hematopoetinės ir mezenchiminės kilmės ląstelėse. Mūsų gauti rezultatai rodo, kad tiriamos ląstelės yra nepilnos diferenciacijos t.y. kamieninės [206], [207]. Puikus šios kilmės ląstelių pritaikymo pavyzdys buvo aprašytas Nieponice *et al.*, kai iš žiurkės raumens išskirtos kamieninės ląstelės buvo auginamos ant elastomerinių karkasinių medžiagų, konstruojant kraujagyslių gabalėlius [208]. Šis tyrimas pademonstravo, jog ląstelės buvo linkusios migruoti į kraujagyslių gabalėlių vidų, kur ėmė ekspresuoti α-aktiną, kalponiną bei sekretuoti kolageną. Endotelinė diferenciacija, šiuo atveju, buvo patvirtinta *von Willebrand* faktoriaus buvimu.

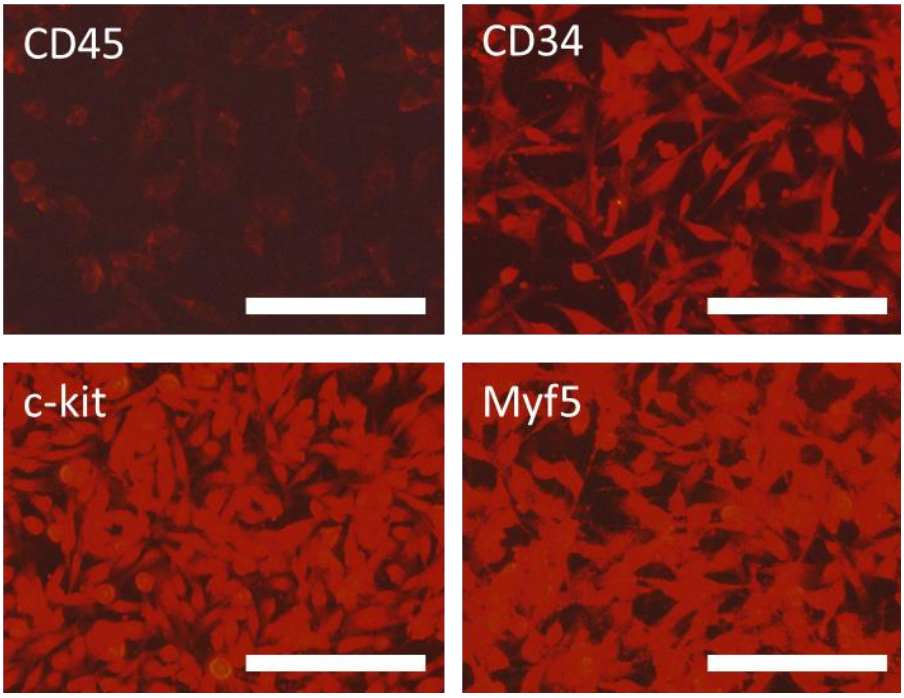


15 paveikslas. Iš žiurkės griaučių raumenų išskirtų ląstelių charakterizavimas. Fluorescencinės mikroskopijos nuotraukos, kuriose ląstelės dažytos fluorescencinėmis žymėmis konjuguotais antikūnais prieš CD45, CD34, c-kit ir MYF5. Skalės - 100 μm.

Tolesniuose tyrimuose buvo vertinami tik trys paviršiai – stiklas, Al ir Zr, nes ankstesniuose tyrimuose nustatėme, jog V yra toksiškas ląstelėms, o Ti ir Zr – panašūs biosuderinamumo prasme. Iš šių dviejų polimerų pasirinktas Zr turintis paviršius, jis plačiau naudojimas tiesioginio lazerinio rašymo taikymuose.

Pirmiausia, skirtingais laiko intervalais įvertinome ląstelių monolsuoksnius šviesinės mikroskopijos pagalba ir nenustatėme reikšmingų skirtumų tarp tiriamų paviršių - žiurkės raumenų kamieninės ląstelės buvo būdingos verpstės morfologijos ir sustojo dalintis suformavusios pilną monosluoksnį (16 paveikslas).

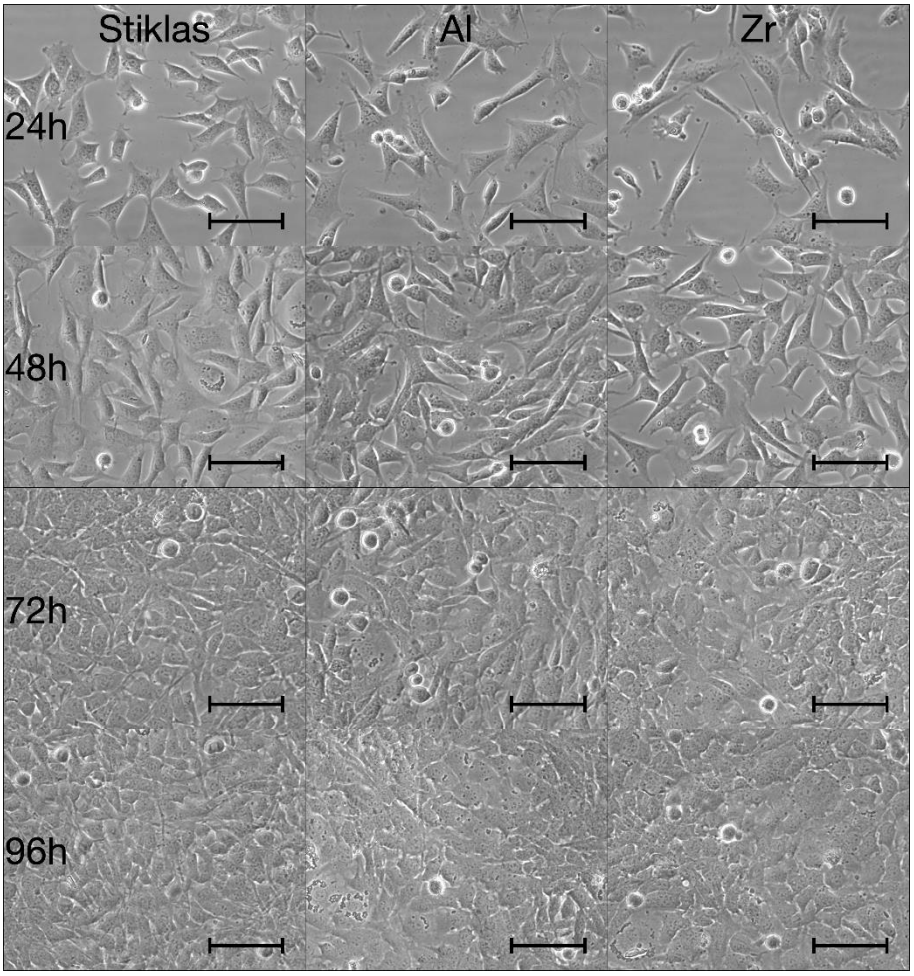


16 paveikslas. Reprezentatyvios ląstelių, augintų ant stiklo, Al ir Zr paviršių, nuotraukos po 24, 48, 72 ir 96 valandų auginimo. 20X didinimas. Skalės atitinka 100 μm.

Sekančiu tyrimu siekėme nustatyti santykius tarp gyvų, apoptozinių bei nekrozinių ląstelių skaičių skirtingais laiko tarpais ant skirtingų paviršių. Tėkmės citometrijos duomenys taip pat neparodė statistiškai reikšmingų skirtumų tarp ląstelių skaičiaus kiekvienoje kategorijoje – didžioji dalis ląstelių visais laiko tarpais buvo gyvybingos (17 paveikslas).

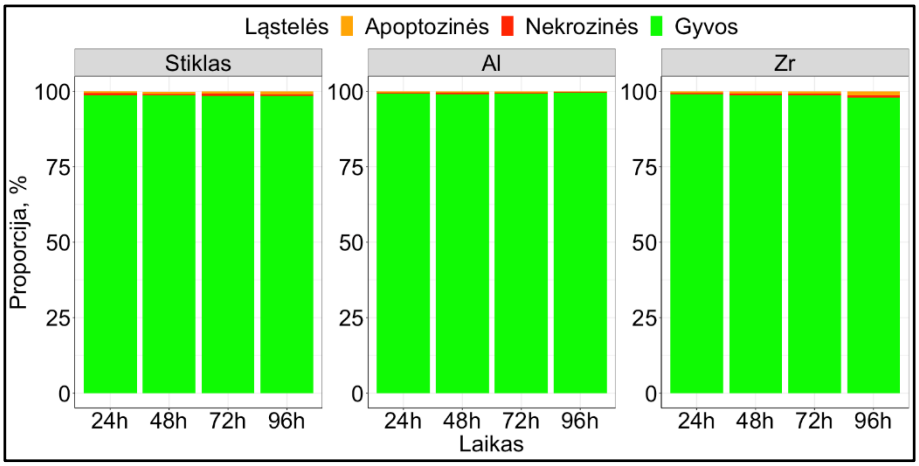


17 paveikslas. Tėkmės citometrijos duomenys, rodantys AO/EB dažytų ląstelių gyvybingumą ant stiklo, Al ir Zr paviršių po 24, 48, 72 ir 96 valandų. Rezultatai pateikti kaip vidutinė sugertis, gauta iš 3 nepriklausomų eksperimentų su n=3 kiekviename eksperimente. Statsitiškai reikšmingų skirtumų tarp paviršių nebuvo rasta.

Gauti rezultatai sutampa su duomenimis, gautais tiriant NIH/3T3 ląsteles. Psycharakis *et al.* [58] savo tyrimuose aptiko palyginamus skaičius gyvybingų NIH/3T3 fibroblastų ant Ti ir Zr hibridų. Su abiem ląstelių tipais gauti rezultatai rodo, jog tiek Al, tiek Zr paviršiai potencialiai gali būti naudojami audinių inžinerijos taikymams.

Ląstelių metabolizmo greičio nukrypimai gali keisti ląstelių savybes – padidėjęs metabolizmo greitis gali būti susijęs su piktybinėmis audinio formacijomis ir ląstelės ciklo išreguliavimu, tuo tarpu žemas metabolizmas gali indikuoti žemą ląstelių gyvybingumą ar perėjimą (difereciacijos ar kitais mechanizmais) į neproliferuojančias ląstelės būsenas. Todėl toliau MTT metodu įvertinome ląstelių, augintų ant tiriamų paviršių metabolinį aktyvumą ir nustatėme, kad stiklo augintų ląstelių jis buvo reikšmingai aukštesnis, nei ant hibridinių organinių-neorganinių polimerų (po 72 ir 96 val. auginimo ($p < 0.001$)) ir taip pat buvo reikšmingai aukštesnis ant Al hibrido (po 48 val. ($p < 0.05$)). Rezultatai pateikiami 18 paveiksle.

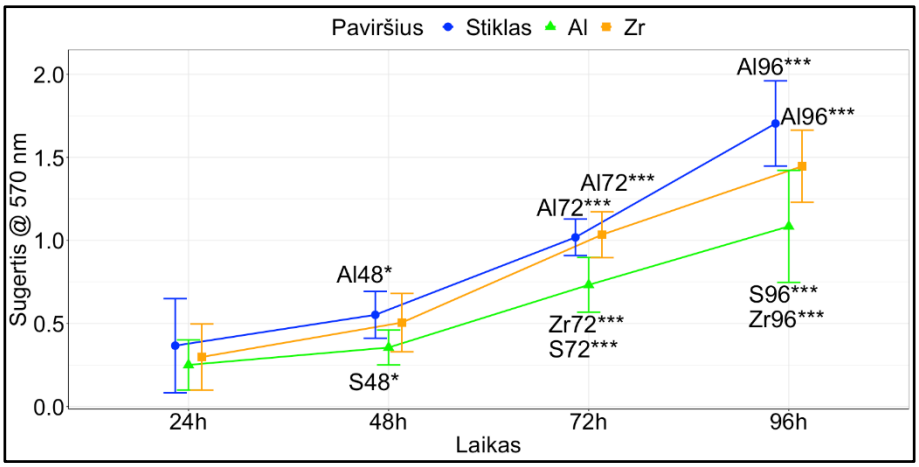


18 paveikslas. Ląstelių proliferacinis aktyvumas, išmatuotas MTT metodu. Rezultatai pateikiami kaip vidurkis ± standartinis nuokrypis. Kiekviename laiko taške kiekviena medžiaga buvo vertinama 9 kartus (3 nepriklausomi eksperimentai su 3 pakartojimais kiekvienu atveju).

Šiame eksperimente gauti rezultatai rodo didžiulį Al ir Zr hibridų panaudojimo potencialą audinių inžinerijos taikymams. Abi tirtos medžiagos palaikė žiurkės miogeninių ląstelių augimą, nepaisant to, kad suminis metabolinis aktyvumas ant jų buvo kiek žemesnis, nei ant kontrolinio stiklo paviršiaus.

### 2.1.8 Adhezijos stiprumo vertinimas

Išsėjus ląsteles ant tiriamųjų paviršių *in vitro,* jos prisitvirtina prie paviršiuje esančių baltymų per integrinus, o tarpusavyje susijungia per kadherinus bei nespecifines sąveikas. Šių procesų visuma lemia ląstelių adhezijos stiprumą. Ląstelių gyvybingumas, proliferacija ir adhezija yra glaudžiai susiję procesai. Pastebėjus, jog gyvybingumas reikšmingai nekinta keičiantis paviršiui, o metabolinis aktyvumas ant Al ir Zr paviršių yra palyginamas, sekančiame eksperimente norėjome įvertinti ar žemesnis metabolinis aktyvumas susijęs su žemesniu adhezijos stiprumu. Siekdami įvertinti, ar mūsų tiriami polimerai užtikrina reikiamą ląstelių adhezijos stiprumą, žiurkės miogenines ląsteles išsėjome ant tiriamųjų paviršių ir po tam tikro auginimo laiko intensyviai papurtėme. Vertinome ant paviršiaus likusių ląstelių skaičių ir apskaičiavome santykį su ant nepurtytų paviršių likusiomis ląstelėmis. Rezultatai pateikiami 19 paveiksle. Pastebėta tendencija (tačiau

statistiškai nereikšminga), kad po 24 valandų ląstelės labiau linkusios atkibti, nei po 4 valandų. Tai reiškia, kad po 4 valandų adhezija buvo stipresnė. Nors buvo nustatyti nemaži skirtumai tarp prikibusių ląstelių skaičiaus po 24 valandų, šie skirtumai nebuvo statistiškai reikšmingi. Pastabėta, kad ant Al paviršiaus likusių ląstelių skaičius buvo mažiausias. Tai atitinka proliferacinio aktyvumo duomenis, kuriuose taip pat parodytas žemiausias aktyvumas ant Al paviršių. Iš gautų duomenų galima daryti išvadą, jog Al paviršius palaiko silpnesnę ląstelių adheziją. To priežastis gali būti žemesnė kolageno adsorbcija prie Al paviršiaus (duomenys pateikiami ankstesniame, 9 paveiksle).

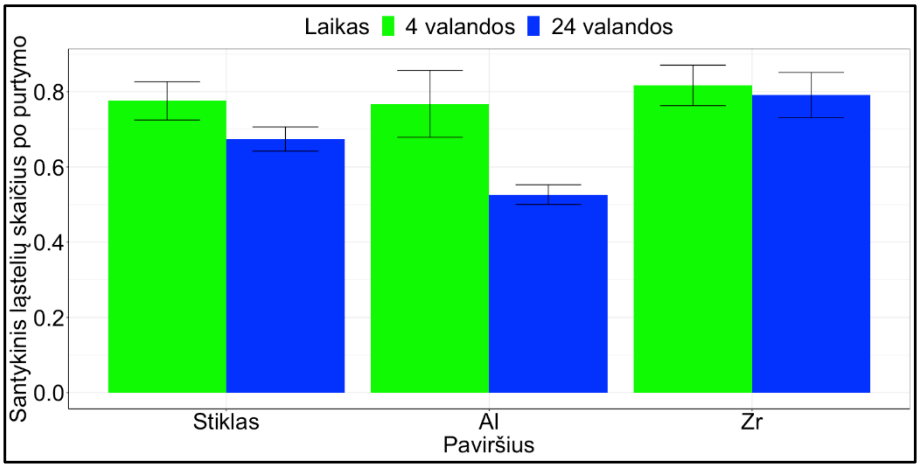


19 paveikslas. Rezultatai pateikti kaip santykis tarp vidutinio ląstelių skaičiaus po purtymo ir skaičiaus prieš purtymą po 4 ir 24 valandų kultūros ± standartinis nuokrypis. Kiekvienos medžiagos atveju buvo atliekama po 9 matavimus (3 nepriklausomi eksperimentai su 3 pakartojimais kiekvienu atveju).

Siekiant giliau suprasti stebimus skirtumus, atliktas tyrimas skirtas nustatyti su adhezija susijusių baltymų raišką.

### 2.1.9 Su adhezija susijusių baltymų raiškos vertinimas

Vykstant nuo integrinų priklausomai ląstelių adhezijai, inicijuojama biocheminių reakcijų kaskada, kuria į ląstelės branduolį perduodamas signalas apie ląstelės sąveiką su užląsteline aplinka. Tai, savo ruožtu, aktyvuoja tam tikrų genų transkripciją ir atitinkamų baltymų transliaciją, reikalingų tolesniam ląstelės atsakui. Ši kaskada aktyvuojama, kai ląstelės paviršiuje esantys integrinai atpažįsta specifines ekstraląstelinio matrikso adhezijos

sekas ir su jomis susijungę dimerizuojasi [209]. Po dimerizacijos, integrinai autofosforilinami ir prie jų prisijungia kiti su adhezija susiję baltymai, kaip FAK (fokalinės adhezijos kinazė), kuri yra vienas iš pirmųjų baltymų, prisijungiančių į naujai besiformuojantį fokalinės adhezijos arba sutelktinio sąlyčio kompleksą. Susiformavus fokalinės adhezijos taškui, gali būti aktyvuojama daugybė signalinių kelių, tarp kurių ir Akt kelias, atsakingas už išgyvenimo ir proliferacijos signalų perdavimą į branduolį per mTOR kelią [210]. Akt gali būti aktyvuojamas fosforilinant Ser473 arba Thr308 – tai priklauso nuo fosforilinančio baltymo. Integrinų medijuojamos adhezijos atveju, aktyvuojama PI3K kinazė, ko pasekoje fosforilinamas Ser473 [211]. Thr308 fosforilinimas vyksta kaip atsakas į mTORC2, kuris susijęs su ląstelės metabolizmu ir citoskeleto reorganizacija [212].

Taigi, toliau *Western Blot* metodu vertinome su adhezija susijusio FAK signalinio kelio baltymų aktyvaciją (20 paveikslas). Gauti duomenys neparodė statistiškai reikšmingų baltymų lygio skirtumų ląstelėse, augintose ant tiriamų paviršių, tačiau buvo stebima fosforilinto Akt baltymo lygio mažėjimo tendencija ant daugumos paviršių (lyginant 4 ir 24 valandų laiko intervalus). To ir buvo galima tikėtis, kadangi Akt kinazės vaidmuo aktyviausias pradinėse ląstelės sąveikos su paviršiais ir kitomis ląstelėmis stadijose.

Šioje elektroninėje versijoje 20 paveikslas buvo pakoreguotas.

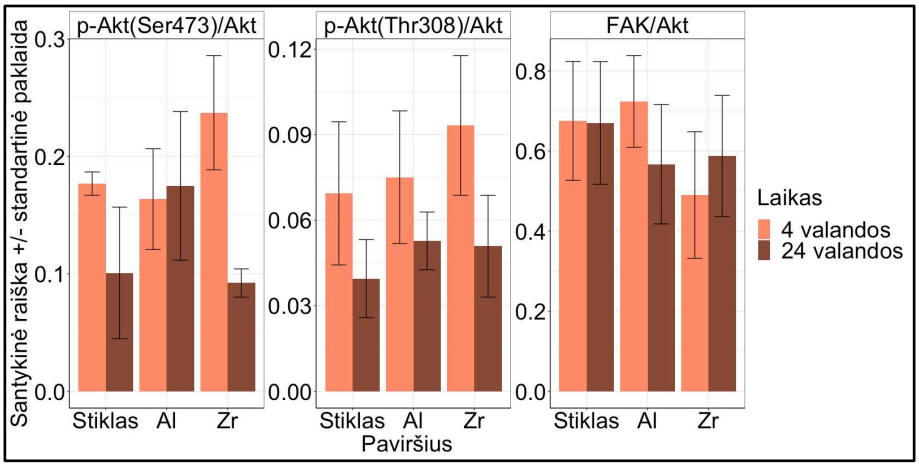


20 paveikslas. *Western blot* duomenys, rodantys FAK bei Akt raišką ir aktyvinimą po 4 ir 24 valandų auginimo ant stiklo, Al ir Zr paviršių. Buvo registruojami p-Akt (Ser 473), p-Akt (Thr308), Akt ir FAK kiekiai. Rezultatai pateikiami kaip santykinė raiška. Atlikti trys nepriklausomi eksperimentai. Statistiškai reikšmingų skirtumų nerasta.

FAK ir Akt kinazių santykis buvo pastovus tarp skirtingų laiko intervalų ir tik nežymiai žemesnis ant Zr paviršių. Tai buvo tikėtina, kadangi bendras

FAK ir Akt kinazių kiekis neturėtų keistis, nebent atsiranda reikšmingų skirtumų fokalinės adhezijos taškų susidaryme.

Ant stiklo paviršiaus, ląstelės buvo linkusios prisikabinti stipriau po 4 valandų – tai sutampa su aukštesne Akt kinazės aktyvacija šiuo laiko momentu. Po 24 valandų stebėtas prisikabinusių ląstelių skaičiaus ir p-Akt (tiek Ser473, tiek Thr308) sumažėjimas, nors ir statistiškai nereikšmingas.

Ant Al paviršiaus, p-Akt (Thr308) prasme, situacija buvo analogiška stiklui – fosforilinto Akt kiekis po 24 valandų buvo sumažėjęs, sufleruojant sumažėjusį signalų, susijusių su citoskeleto persitvarkymu, perdavimą. Tačiau tai nebuvo pastebėta p-Akt (Ser473) tyrimo metu. FAK kiekis taip pat sumažėjo, rodydamas, jog po 24 valandų galimai buvo mažesnis ir fokalinių adhezijų skaičius.

Didžiausias fosforilinimo lygio kritimas buvo pastebėtas ant Zr paviršių. Lyginant 4 ir 24 valandas, p-Akt (Ser473) lygis krito su $p=0.25$, o p-Akt (Thr308) krito su $p=0.67$. Ant Zr paviršių pastebėtas nežymus bendro FAK baltymo lygio padidėjimas. Nors ant Zr buvo stebimas didžiausias fosforilinto Akt baltymo kiekio pasikeitimas, šis rezultatas nesutapo su ant šių paviršių stebėtu ląstelių atkibimu, kuris, šiuo atveju, buvo mažiausias.

Nors galima įžvelgti tam tikras bendras ląstelių adhezijos ir su adhezija susijusių baltymų raiškos tendencijas, reikėtų išsamesnio tyrimo, siekiant susieti šiuos procesus su statistiškai reikšmingu patikimumu.

Stipri ląstelių adhezija yra vienas esminių reikalavimų sėkmingai audinių inžinerijos strategijai, kaip apžvelgta Lee *et al.* [213]. Kaskart kai trūksta su adhezija susijusių signalų, paviršinės ląstelės žūsta anoikio būdu. Dėl šios priežasties, turėtų būti atlikta papildoma ilgalaikė *in vitro* studija, kurios metu būtų įvertinta kaip bėgant laikui kinta su adhezija susijusių baltymų raiška ir kokia jų įtaka ląstelių adhezijai, gyvybingumui ir mataboliniam aktyvumui.

### 2.1.10 Kolageno sintezės vertinimas

Galiausiai siekėme įvertinti, ar tiriami paviršiai turi įtakos I tipo kolageno sintezei. Žiurkės raumenų kamieninės ląstelės buvo auginamos ant hibridinių polimerų ir po 1, 7 arba 14 dienų buvo vertinamas pagaminto kolageno kiekis. Jau anksčiau buvome nustatę, kad kolageno adsorbcija ant Al hibrido buvo silpniausia, tačiau šiuo atveju gavome įdomius rezultatus – kolageno sintezė buvo aukščiausia (21 paveikslas). Kolageno sintezės skirtumai buvo matomi jau po vienos savaitės, tačiau statistiškai reikšmingi tampo tik po 2 tyrimo savaičių. Tokios trukmės buvo galima tikėtis, kadangi ekstraląstelinio

matrikso remodeliavimas yra lėtas procesas. Kiti statistiškai reikšmingi skirtumai buvo aptikti ant Al paviršiaus tarp 1 dienos, 1 savaitės ir 2 savaičių su $p < 0.001$, taip pat ir Zr paviršių po 1 dienos ir 1 savaitės su $p < 0.05$.

Šio tyrimo rezultatai yra daug žadantys audinių inžinerijos taikymams, kadangi parodo reikšmingą kolageno gamybos padidėjimą ląstelėse ant tirtų paviršių.

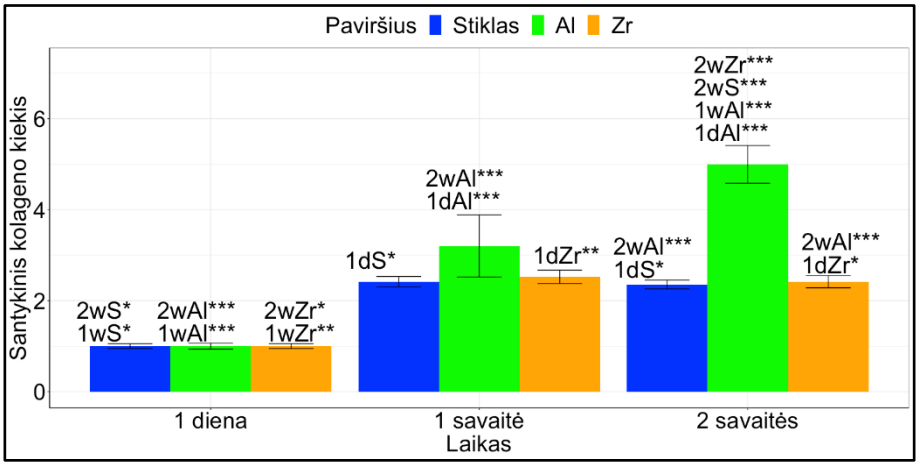


21 paveikslas. Kolageno sintezė. Santykinis kolageno, pagaminto ląstelėse, kiekis ant skirtingų paviršių po 1 dienos (1d), 1 savaitės (1w) ir 2 savaičių (2w).

Šiame tyrime naudota augimo terpė su 10 % fetalinio veršelio serumo, kuris pagrinde sudarytas iš neadhezinių baltymų. Parodyta, jog ląstelės sintetina kolageną, tačiau galimai sintetina ir kitus ekstraląstelinio matrikso baltymus. Taigi, labai tikėtina, jog ECM baltymų sekos, aktyvuojančios integrinus, nedideliais kiekiais randamos terpėje net po ląstelių persėjimo. Koblianski *et al.* [214] parodė, jog neadheziniai baltymai – pvz. jaučio serumo albuminas, kurio yra fetaliniame veršelio serume, reikšmingai padidina integrinų jungimąsį su mažais ECM baltymų kiekiais. Tai patvirtina mūsų gauti rezultatai, pateikti 20 paveiksle – su adhezija susijusios Akt ir FAK kinazės stipriau aktyvuojamos (nors ir statistiškai nereikšmingai) pradinėse ląstelių adhezijos prie paviršių stadijose.

## 2.2 Minkštųjų audinių inžinerija

### 2.2.1 PDMS biodekoracijos įtaka biosuderinamumui

Biodekoracija – tai procesas, kurio metu medžiagos paviršius modifikuojamas papildomu bioaktyvių molekulių sluoksniu. Tai gali būti paprastos biomolekulės (peptidai, oligonukleotidai ar polisacharidai) arba sudėtingesnės (baltymai, antikūnai ar sudėtingi ekstraląstelinį matriksą atkartojantys dariniai). Biodekoracijai pasitelkiamos skirtingos metodikos – kovalentinis biomolekulių pririšimas prie paviršiaus, molekulių nekovalentinis adsorbavimas arba biomolekulių įmaišymas į medžiagos vidų, tokiu būdu gaunant kompozitus, kurių paviršiuje eksponuojamos bioaktyvių molekulių dalys, prie kurių receptoriais gali prisikabinti ląstelės. Visos šios metodikos buvo plačiai aprašytos literatūroje [215], [216].

Biodekoracija taip pat gali būti taikoma nanodalelėms, tokiu būdu suteikiant joms papildomus funkcionalumus, pvz. dekoruojant biomolekulėmis, kurios leistų nanodalelėms nukeliauti tiesiogiai į taikinines ląsteles [217]. Puikus tokios strategijos pavyzdys – Min *et al.* darbas, kuriame PEG-Pt-provaistu padengti aukso nanovamzdeliai buvo sukonstruoti taip, kad specifiškai veiktų vėžines ląsteles [218]. Tokie konstruktai gali būti naudojami vėžio gydyme, kaitinant nanodalelių prikaupusias ląsteles infraraudonaisiais spinduliais.

Literatūroje galima rasti daugybę šio proceso pritaikymo pavyzdžių audinių inžinerijoje. Pavyzdžiui, Ma *et al.* sukonstravo PLA karkasus su kovalentiškai imobilizuotu kolagenu, kuriuos padengė fibroblastų augimo veiksniu [84]. Tai lėmė reikšmingai pagerėjusį chondrocitų išsidėstymą ir augimą ant paviršiaus.

Žinoma, kad PDMS yra biosuderinamas tiek *in vivo*, tiek *in vitro*, tačiau jis taip pat yra hidrofobiškas [219], [220]. Siekiant pagerinti ląstelių adheziją ir augimą, PDMS paviršiai buvo biodekoruojami pasitelkiant keletą skirtingų medžiagų – kolageną, lamininą ir RGD sekas. Palyginimui naudoti PDMS paviršiai buvo inkubuojami FBS, augimo terpėje arba PBS. 22 paveiksle pateikiami triušio raumens ląstelių, auginamų ant skirtingai modifikuotų paviršių, monosluoksnių vaizdai. Matome, kad po 48 tyrimo valandų, ląstelės augusios ant kolagenu dengtų paviršių buvo linkusios suformuoti pilną monosluoksnį. Toks rezultatas buvo tikėtinas, nes kolagenas suteikia ląstelėms aplinką, panašiausią į natyvų ekstraląstelinį matriksą.

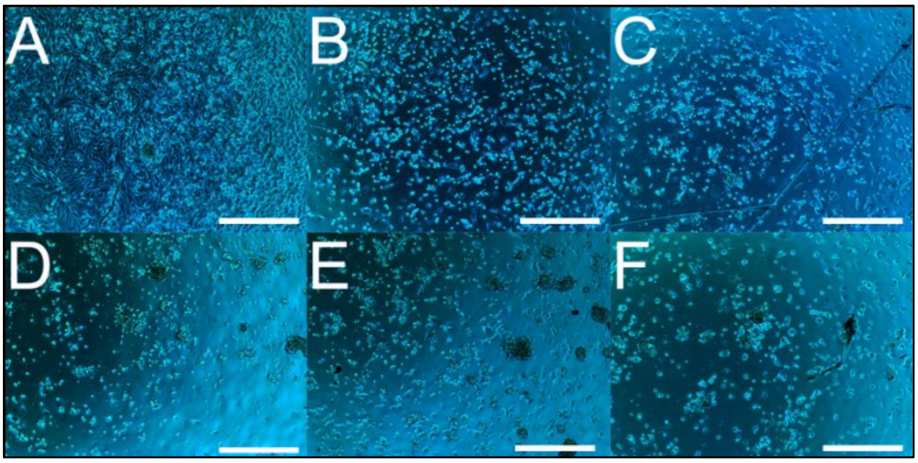

22 paveikslas. Kokybinis triušio raumens ląstelių augimo palyginimas ant skirtingai biodekoruotų PDMS paviršių. Poveikiai: A – kolagenas, B – RGD tripeptidas, C – PBS, D – lamininas, E – FBS, F – IMDM terpė su 10 % FBS ir antibiotikais. Skalės atitinka 400 μm.

RGD seka padengti paviršiai skatino ląstelių augimą geriau už kontrolę, bet kiek prasčiau už kolageną. Šis rezultatas patvirtina prielaidą, kad tik dalis RGD sekų prie paviršiaus prijungiamos reikiama konformacija, kuri reikalinga integrinų aktyvacijai ir nuo FAK priklausomai ląstelių adhezijai [221].

Ant kitų paviršių ląstelių skaičius buvo kiek mažesnis. Įdomu tai, kad poveikis lamininu neparodė reikšmingo ląstelių adhezijos pagerėjimo. Lamininas – tai aukštos molekulinės masės ekstraląstelinio matrikso glikoproteinas, turintis specifišką kryžiaus formos konformaciją. Jis aktyviai dalyvauja ląstelių adhezijoje, migracijoje ir diferenciacijoje [222]. Tačiau jo poveikis daugiausia susijęs su laminino vaidmeniu palaikant kitų ekstraląstelinio matrikso baltymų struktūrą. Lamininas neturi RGD sekų, tai paaiškintų reikšmingai silpnesnę ląstelių adheziją. Kitas rezultatų paaiškinimas galėtų būti žemesnė laminino adsorbcija prie PDMS, taip pat galimai nepalanki konformacija ląstelių prisirišimui. Tik tam tikros ląstelių rūšys pasižymi stipria sąveika su lamininu – iš esmės tik tos, kurios randamos pamatinėse membranose [223]. Tačiau tai nereiškia, kad lamininas negali būti naudojamas audinių inžinerijos taikymams. Pavyzdžiui, Junka *et al.* panaudojo lamininą, kad padengti PCL-chitosano nano-siūlų matricas ir tai lėmė reikšmingą Švano ląstelių adhezijos ir proliferacijos pagerėjimą [224].

Toliau buvo vertinama kaip skirtingi paviršiai veikia ląstelių metabolizmą. Rezultatai, gauti MTT metodu, pateikiami 23 paveiksle.

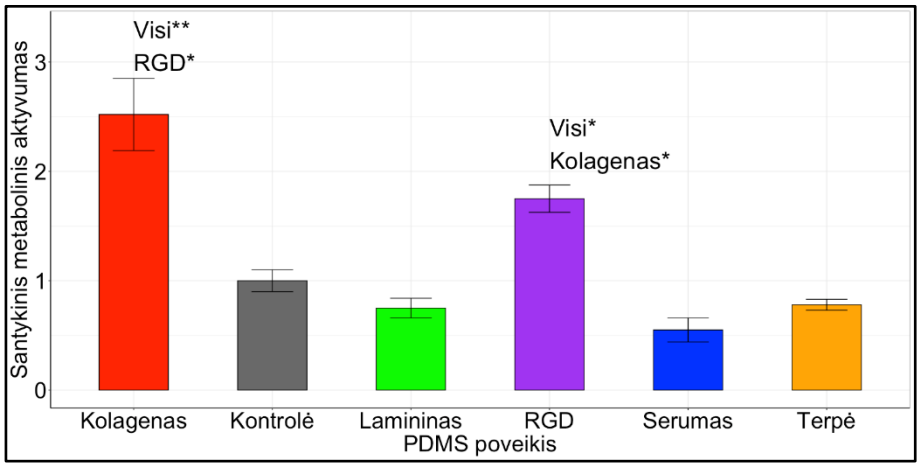


23 paveikslas. PDMS paviršiaus biodekoravimo įtaka triušio raumens ląstelių proliferacijai po 48 valandų. Grafike atvaizduotas suminis ląstelių metabolinis aktyvumas ant skirtingai biodekoruotų PDMS paviršių. Rezultatai pateikiami lyginant su kontroliniais (PBS-inkubuotais) PDMS paviršiais.

Gauti rezultatai sutampa su prieš tai atlikto eksperimento duomenimis. Triušio raumens ląstelės buvo gerokai metaboliškai aktyvesnės ant kolagenu dengtų mėginių, nei ant daugumos kitų paviršių ($p<0.01$). RGD dengti paviršiai palaikė kiek mažesnį ląstelių metabolinį aktyvumą, nei kolagenu dengti paviršiai ($p <0.05$), tačiau jis vis tiek buvo aukštesnis, nei ant kitų paviršių ($p <0.05$).

### 2.2.2 PDMS blokinių kopolimerų tyrimas

Nors PDMS turi patrauklias mechanines ir fizikines savybes bei gerą darinių formavimo potencialą, jo ląstelių adhezijos ir integracijos palaikymas gali būti patobulintas. Vienas būdų, kaip tai padaryti, yra PDMS blokinių kopolimerų su kitais junginiais kūrimas. Literatūroje tokių darbų apstu. Pavyzdžiui, dar 1999 Sugiyama su kolegomis sukūrė PDMS kopolimerus su poli(2-metakriloksi)etilfosforilcholino segmentais ir parodė, kad jie ne tik turėjo hidrogelinių savybių, bet taip pat pagerino kraujo baltymų adsorbciją prie paviršių [225].

Kai *et al.* sukūrė poli(ε-PCL)-PDMS kopolimerus ir iš jų išliejo gijas su formos atmintimi (angl. *shape memory*), kuriuos galima pritaikyti kaulinio

audinio inžinerijai [76]. Tam buvo pasitelkta elektrospiningo technologija. Keičiant proporcijas tarp PCL ir PDMS, tyrėjams pavyko išgauti įvairių skersmenų, terminio elgesio ir mechaninių savybių gijas. Pagaminti karkasai galėjo sugrįžti į savo buvusią formą iki 7 kartų po mechaninio ištempimo ir vėlesnio pakaitinimo. Šie kompozitai taip pat pasižymėjo puikiu biosuderinamumu su žmogaus fetaliniais osteoblastais, o kai kurios kompozito variacijos pagerino osteogeninę diferenciaciją.

Blokiniai kopolimerai PDMS pagrindu, tirti šiame darbe, turėjo skirtingus brinkimo vandenyje lygius – kai kurios medžiagos, pamerktos į vandeninį tirpalą, buvo linkusios išsiplėsti iki penkių kartų savo pradinio tūrio. Šios hidrogelių savybės gali pasitarnauti pakraunant karkasus vaistais ar kitomis biologinį aktyvumą turinčiomis molekulėmis. Taigi, pirmiausia buvo matuojami susintetintų medžiagų kontaktiniai kampai su vandeniu. Rezultatai pateikiami 24 paveiksle.

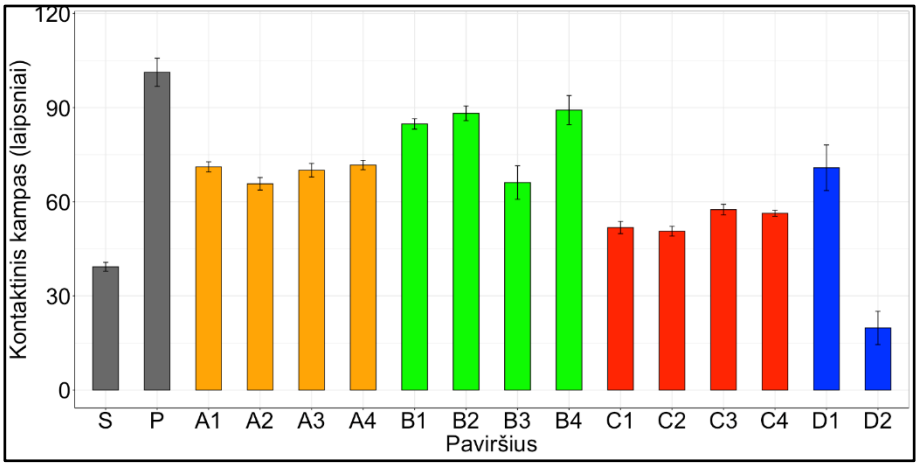


24 paveikslas. Tirtų PDMS blokinių kopolimerų kontaktiniai kampai. Rezultatai pateikiami kaip vidurkis ± standartinis nuokrypis su n = 5. S – stiklas, P – PDMS.

Grynas PDMS turėjo aukščiausią vandens kontaktinį kampą iš visų mėginių, viršijusį 100 laipsnių. A grupės blokiniai kopolimerai turėjo palyginamus kontaktinius kampus, siekiančius apie 70 laipsnių. B3 pasižymėjo žemiausiu kontaktiniu kampu grupėje, siekiančiu vos daugiau nei 60 laipsnių, tuo tarpu kiti grupės nariai turėjo maždaug 85 laipsnių kontaktinus kampus. C grupė pasižymėjo žemiausiais kontaktiniais kampais, kurie buvo maždaug 50 laipsnių. D grupė pasižymėjo didžiuliais skirtumais, kur D2

polimeras turėjo žemiausią kontaktinį kampą, siekiantį maždaug 20 laipsnių, o D1 – maždaug 70 laipsnių.

Medžiagų kontaktiniai kampai ne visada koreliuoja su biosuderinamumu. Pavyzdžiui, Seo su kolegomis modifikavo PDMS paviršius, naudodami ABA tipo blokinius kopolimerus su fosfolipidinėmis grupėmis [226]. Gauti polimerai turėjo reikšmingai žemesnius kontaktinius kampus lyginant su grynu PDMS. Įdomu tai, kad į paviršių eksponuotos fosfolipidinės grupės sumažino baltymų rišimąsį su paviršiumi ir tokiu būdu susilpnino ląstelių adheziją. Tai parodo, jog kontaktinis kampas nėra vienintelis veiksnys, lemiantis baltymų adsorbciją ir ląstelių adheziją. Todėl kitame mūsų darbo etape tyrėme polimerų ekstraktų citotoksiškumą. Rezultatai pateikiami 25 paveiksle.

| Polimero ekstraktas | A1 | A2 | A3 | A4 | B1 | B2 | B3 | B4 | C1 | C2 | C3 | C4 | D1 | D2 |
|---|---|---|---|---|---|---|---|---|---|---|---|---|---|---|
| Lyginant su PDMS po 24h | + | ± | + | + | + | + | ± | ± | + | - | ± | ± | ± | ± |
| Lyginant su PDMS po 48h | - | - | - | - | - | - | + | + | - | ± | - | - | ± | ± |

25 paveikslas. Polimerų ekstraktų toksiškumas *in vitro*. Žiurkės miogeninės kamieninės ląstelės buvo veikiamos augimo terpe, papildyta skirtingų blokinių kopolimerų ekstraktais, o po kurio laiko buvo matuojamas jų metabolinis aktyvumas ir lyginamas su kontrolinės terpės, inkubuotos su PDMS, poveikiu. Rezultatai interpretuojami kaip „+“ – geriau už PDMS, „±“ – palyginama su PDMS ir „-“ – prasčiau už PDMS.

Kai kurie medžiagų ekstraktai nežymiai pagerino žiurkės miogeninių kamieninių ląstelių proliferaciją, kiti pablogino, tuo tarpu beveik pusė jų neturėjo ženklios įtakos, lyginant su natyviu PDMS. Sprendžiant iš gautų rezultatų būtų galima manyti, kad kai kurios medžiagos skleidžia junginius, kurie toksiški ląstelėms, tuo tarpu kiti junginiai pagerina ląstelių proliferaciją. Įdomu tai, kad junginiai, pasižymėję teigiamu poveikiu po 24 valandų, turėjo neigiamą poveikį po 48 valandų.

Kaip ir manyta, tiek cheminė struktūra, tiek polimerizacijos sąlygos turėjo stiprią įtaką ląstelių metabolizmui. Visgi, dalis šių kopolimerų potencialiai gali būti naudojami audinių inžinerijoje.

Nustačius ląstelių, augančių ant skirtingų PDMS blokinių kopolimerų, metabolinius aktyvumus, toliau siekėme išsiaiškinti ar stebimi skirtumai susiję su žiurkės miogeninių kamieninių ląstelių gyvybingumu. Tuo tikslu, po 24

valandų auginimo, ląstelės buvo dažomos AO/EB mišiniu. Rezultatai pateikiami 26 paveiksle.

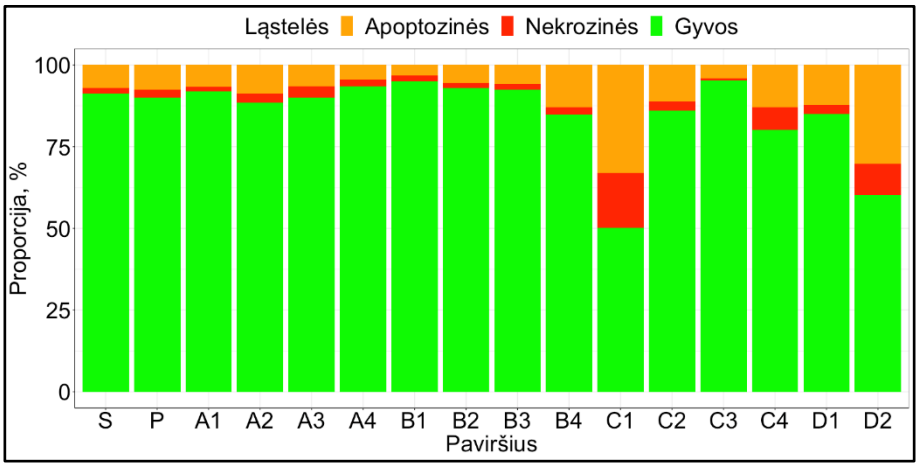


26 paveikslas. Ląstelių, dažytų AO/EB, fluorescencija po 24 valandų auginimo. Rezultatai pateikti kaip santykis su ant palyginimui naudoto polisitireno paviršiaus augintomis ląstelėmis. S – stiklas, P – PDMS.

Dažniausiai, gyvybingų ląstelių skaičius buvo aukštesnis ant blokinių kopolimerų, nei ant PDMS. B1 ir C3 palaikė aukščiausius ląstelių gyvybingumo lygius po 24 valandų, kurie siekė apie 90 %. C1 ir D2 pasižymėjo žemiausiais gyvybingumo lygiais, kur 50-60 % ląstelių žuvo po pirmų 24 valandų.

### 2.2.3 Šilku sutvirtinto PDMS mechaninės savybės

Pastebėjome, kad šilku sutvirtinti PDMS mėginiai viduje turėjo susiformavusius oro burbuliukus. Tai iš dalies galėjo paveikti mechanines mėginių savybes. Šilkas mėginiuose pasiskirstė nehomogeniškai – žr. 27 paveikslą.

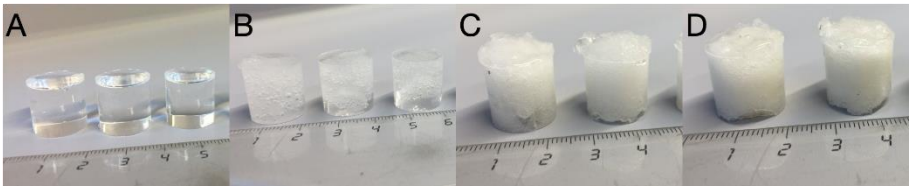


27 paveikslas. PDMS mėginiai su skirtingais šilko kiekiais. A – grynas PDMS, B – su 1 % šilko, C – su 5 % šilko, D – su 10 % šilko.

Atlikome keletą suspaudimo testų, siekdami įvertinti kaip skirtingi kompozitai elgiasi. Pirmiausia, buvo sugeneruotos gryno PDMS deformacijos-apkrovos kreivės, siekiant įvertinti mėginių mechaninių savybių atkartojamumą – žr. 28 paveikslą. Deformacijos-apkrovos kreivės buvo pamatuotos 5 mėginiuose ir vėliau suvidurkintos. Suspaudimo-atpalaidavimo cikluose stebėta histerezė – t. y. pavėluotas mėginio grįžimas į buvusią padėtį. Rezultatai pateikiami kaip taškinės diagramos, rodančios, kad tirtos medžiagos pasižymi netiesinėmis elastinėmis savybėmis viso eksperimento metu. Apkrova prie didžiausios (4 mm) deformacijos buvo 145 N. Variacija tarp mėginių buvo minimali.

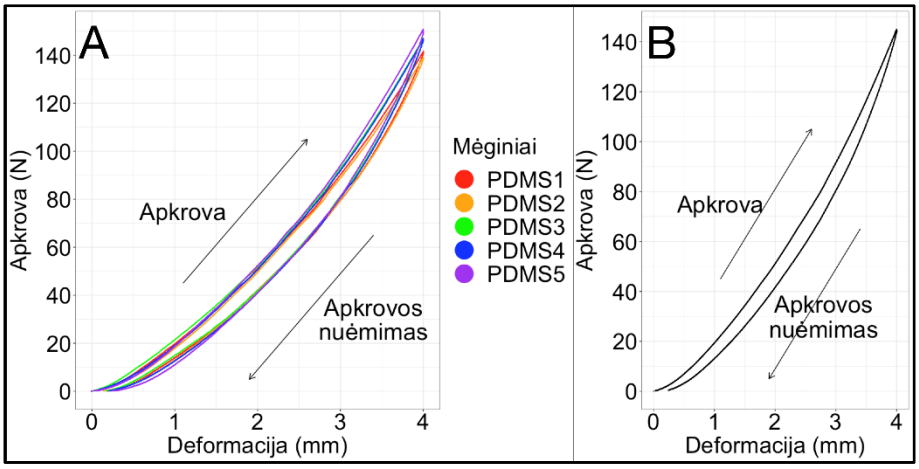


28 paveikslas. Gryno PDMS deformacijos-apkrovos kreivės. Suspaudimo ir atpalaidavimo žingsniai grafike atitinkamai pažymėti strėlytėmis. A – 5 nepriklausomų testų duomenys. B – suvidurkinta 5 eksperimentų poslinkio-apkrovos kreivė.

Toliau, šilku sutvirtinti mėginiai buvo tiriami analogiškai ir pateikiamos jų deformacijos-apkrovos kreivės, įvertinant mėginių paviršiaus plotą – žr. 29 paveikslą.

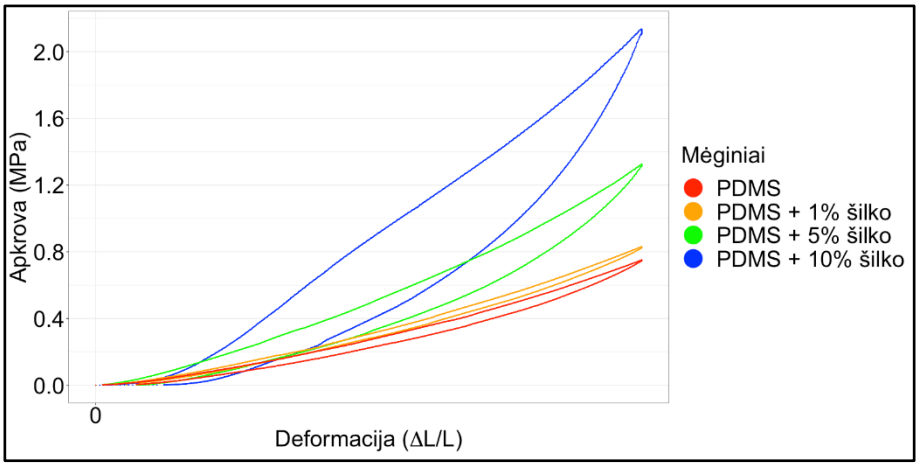


29 paveikslas. Šilku sutvirtintų PDMS mėginių deformacijos-apkrovos kreivės. Rezultatai pateikti suvidurkinus 5 eksperimentų duomenis kiekvienai medžiagai.

Rezultatai rodo, kad gryno PDMS mėginiai buvo minkščiausi ir norint juos maksimaliai deformuoti 0.27 karto (4 mm suspaudimas), reikėjo 752 kPa. Didėjant šilko koncentracijai nuo 1 % iki 5 % ir 10 %, atitinkamai augo ir reikalingas slėgis (bei tamprumo moduliai) nuo 820 kPa (3.04 MPa) iki 1324 kPa (4.90 MPa) iki 2144 kPa (7.94 MPa). Tai reiškia, kad didėjant šilko koncentracijai, reikalinga didesnė jėga, norint pasiekti tą pačią mėginio deformaciją. Šie rezultatai – priešingi nei manyta, kadangi tikėjomės, jog oro burbuliukai, susidarę mėginiuose, sumažins mėginių kietumą. Ryšys tarp šilko kiekio mėginiuose ir tamprumo modulio pavaizduotas 30 paveiksle.

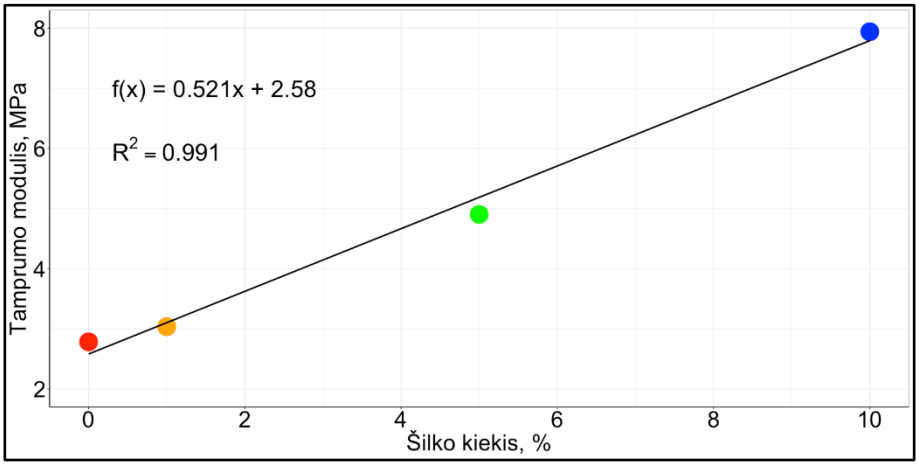


30 paveikslas. Ryšys tarp šilko kiekio mėginyje ir šilku sutvirtinto PDMS tamprumo modulio.

Sutvirtinimas šilku gali būti naudingas ne tik moduliuojant mechanines mėginių savybes, bet ir keičiant paviršių savybes, siekiant išgauti geresnę ląstelių adheziją ir proliferaciją. Pavyzdžiui, Lawrence *et al.* naudojo medžiagas šilko pagrindu siekdami sukonstruoti karkasus, skirtus ragenos rekonstrukcijai, auginant žmogaus ir triušio ragenos fibroblastus [227]. Tyrėjai nustatė, kad ląstelių citoskeletai buvo linkę išsidėstyti išilgai šilko gijų, o tai parodo patrauklią sąveiką su aplinka. Ląstelės išliko gyvybingos 10 dienų.

# IŠVADOS

1. Susintetintas naujas hibridinis organinis-neorganinis polimeras su aliuminiu ir charakterizuotos jo fizikocheminės savybės. Nustatyta, jog jo vandens kontaktinis kampas – apie 72 laipsniai. Medžiaga nepasižymėjo statistiškai reikšmingais kolageno adsorbcijos skirtumais, lyginant su stiklo ar Zr turinčio hibridinio polimero paviršiais. Nustatyta, kad aliuminis išlieka medžiagos cheminėje struktūroje po polimerizacijos, o vandeninėje terpėje medžiaga reikšmingai neskyla.

2. Pasitelkiant tiesioginį lazerinį rašymą, iš Al turinčio hibridinio polimero buvo sukonstruoti aukšto preciziškumo dariniai, kurių raiška siekė 200 nm. Sudėtingi trimačiai dariniai su kabančiais motyvais sėkmingai išsilaikė mėginių gamybos ir plovimo procedūrų metu ir puikiai atitiko CAD modelius.

3. Al, Ti ir Zr turintys hibridiniai polimerai biosuderinami *in vitro* su NIH/3T3 fibroblastais ir žiurkės miogeninėmis kamieninėmis ląstelėmis.

4. Al ir Zr turintys hibridiniai polimerai demonstravo su stiklu palyginamą adhezijos palaikymą, auginant žiurkės miogenines kamienines ląsteles.

5. Al turintis hibridinis polimeras indukavo aukščiausią kolageno sekrecijos lygį žiurkės miogeninėse kamieninėse ląstelėse, lyginant su Zr turinčio hibridinio polimero ar stiklo paviršiais.

6. Įvertinus žiurkės miogeninių kamieninių ląstelių dauginimosi intensyvumą nustatyta, kad keletas naujai susintetintų PDMS blokinių kopolimerų su BMA-HEMA-VP, AzA-DEG-MAA ir GMA-PVA yra biosuderinami hidrogeliai *in vitro*.

7. PDMS biodekoravimas kolagenu ir RGD reikšmingai pagerina triušio miogeninių kamieninių ląstelių adheziją.

8. Šilko įmaišymas į PDMS mėginius reikšmingai keičia tamprumo modulį. Didinant šilko koncentraciją, tamprumo modulis didėja.

# ACKNOWLEDGEMENTS

I would like to acknowledge and express my gratitude to all colleagues and associates with whom we have collaborated over the years. The following list highlights the most significant academic interactions that led to this thesis being written:

1. Vilnius University, Life Sciences Center. Dr. Nadežda Dreižė, Dr. Milda Alksnė and Monika Grubliauskaitė for meticulous hands-on support in performing multitudes of laborious experiments.
2. Foundation for Research and Technology-Hellas, Institute of Electronic Structure and Laser. Dr. Maria Farsari and Dr. Anthi Ranella for access to laser two-photon polymerisation and cell culture facilities, Ms. Aleka Manousaki for SEM imaging.
3. Lancaster University, Department of Chemistry and Materials Science Institute. Dr John G. Hardy and Dr. Sara J. Baldock for access to chemical synthesis, laser two-photon polymerisation and SEM facilities.
4. Vilnius Gediminas Technical University, Faculty of Mechanics. Prof. Rimantas Kačianauskas and others for testing the mechanical properties of silk-reinforced PDMS.
5. Vilnius University, Faculty of Physics, Laser Research Center. Prof. Roaldas Gadonas and Dr. Mangirdas Malinauskas for training and access to laser two-photon polymerisation and SEM facilities.
6. Vilnius University, Faculty of Chemistry and Geosciences. Prof. Saulutė Budrienė, Dr. Tatjana Kochanė and their students. For synthesising PDMS block copolymers investigated in this work.
7. Kratos Analytical Ltd. Dr. Sarah Coultas and Dr. David L. Rochester for performing the ICP-OES experiments.
8. Prof. Juozas Kulys and Prof. Evaldas Liutkevičius for valuable discussions and career guidance.

A great big thanks also goes to everyone else who was involved – professors, colleages and coworkers, who are too numerous to mention here, but contributed their thoughts, ideas and insights via countless discussions.

My family and friends deserve an honorable mention here for all of their support and endurance in dealing with my lack of time and attention.

Most of all, I would like to thank Daiva Baltriukienė and Virginija Bukelskienė for all of their warm support and guidance throughout the years.

Ačiū!

# LIST OF PUBLICATIONS

1. **Balčiūnas E**, Dreižė N, Grubliauskaitė M, Urnikytė S, Šimoliūnas E, Bukelskienė V, Valius M, Baldock SJ, Hardy JG, Baltriukienė D. Biocompatibility investigation of hybrid organometallic polymers for sub-micron 3D printing via laser two-photon polymerisation. Materials. 2019; 12(23):3932.
2. **Balčiūnas E**, Baldock SJ, Dreižė N, Grubliauskaitė M, Coultas S, Rochester DL, Valius M, Hardy JG, Baltriukienė D. 3D printing hybrid organometallic polymer-based biomaterials via laser two-photon polymerisation. Polymer International. 2019; 68(11):1928-1940.
3. Kilikevičius A, **Balčiūnas E**, Kilikevičienė K, Maknickas A, Bukelskienė V, Baltriukienė D, Kačianauskas R. Modelling of silk-reinforced PDMS properties for soft tissue engineering applications. Technology and Health Care. 2018; 26(S2):679-688.

## OTHER PUBLICATIONS AND CONFERENCES

### List of other peer-reviewed publications

1. Nazir R, Thorsted B, **Balčiūnas E,** Mazur L, Deperasińska I, Samoć M, Brewer J, Farsari M, Gryko, DT. Π-expanded 1,3-diketones – synthesis, optical properties and application in two-photon polymerization. Journal of Materials Chemistry C. 2016; 4(1):167-177.
2. Nazir R, **Balčiūnas E,** Buczynska D, Bourquard F, Kowalska D, Gray D, Mackowski S, Farsari M, Gryko DT. Donor-acceptor type thioxanthones: synthesis, optical properties and two-photon induced polymerization. Macromolecules. 2015; 48(8):2466-2472.
3. Rutkūnas V, Bukelskienė V, Sabaliauskas V, **Balčiūnas E**, Malinauskas M, Baltriukienė D. Assesment of human gingival fibroblast interaction with dental implant abutment materials. Journal of Materials Science: Materials in Medicine. 2015; 26:169.
4. Rekštytė S, Kaziulionytė E, **Balčiūnas E**, Kaškelytė D, Malinauskas M. Direct laser fabrication of composite material 3D microstructured scaffolds. Journal of Laser Micro Nanoenigneering. 2014; 9(1):25-30.
5. Nazir R, Bourquard F, **Balciunas E**, Smolen S, Gray D, Tkachenko NV, Farsari M, Gryko DT. Π-expanded α,β-unsaturated ketones: synthesis, optical properties and two-photon induced polymerization. Journal of Chemical Physics and Physical Chemistry. 2014; 16(3):682-690.
6. Malinauskas M, Rekštytė S, Lukoševičius L, Butkus S, **Balčiūnas E,** Pečiukaitytė M, Baltriukienė D, Bukelskienė V, Butkevičius A, Kucevičius P, Rutkūnas V, Juodkazis S. 3D microporous scaffolds manufactured via combination of fused filament fabrication and direct laser writing ablation. Micromachines. 2014; 5(4):839-858.
7. Danilevičius P, Rekštytė S, **Balčiūnas E**, Kraniauskas A, Širmenis R, Baltriukienė D, Bukelskienė V, Gadonas R, Sirvydis V, Piskarskas A, Malinauskas M. Laser 3D micro/nanofabrication of polymers for tissue engineering applications. Optics and Laser Technology. 2013; 45:518-524.
8. Baltriukienė D, Sabaliauskas V, **Balčiūnas E,** Melninkaitis A, Liutkevičius E, Bukelskienė V, Rutkūnas V. The effect of laser-treated titanium surface on human gingival fibroblast behavior. Journal of Biomedical Materials Research Part A. 2013; 102(3):713-720.
9. Danilevičius P, Rekštytė S, **Balčiūnas E,** Kraniauskas A, Širmenis R, Baltriukienė D, Malinauskas M, Bukelskienė V, Gadonas R, Sirvydis V, Piskarskas A. Direct laser fabrication of polymeric implants for cardiovascular surgery. Materials Science. 2012; 18(2):145-149.

10. Danilevičius P, Rekštytė S, **Balčiūnas E**, Kraniauskas A, Jarašienė R, Širmenis R, Baltriukienė D, Bukelskienė V, Gadonas R, Malinauskas M. Micro-structured polymer scaffolds fabricated by direct laser writing for tissue engineering. Journal of Biomedical Optics. 2012; 17(8):0814051-0814057.
11. Danilevičius P, Rekštytė S, **Balčiūnas E**, Kraniauskas A, Širmenis R, Baltriukienė D, Malinauskas M, Bukelskienė V, Gadonas R, Sirvydis V, Piskarskas A. Direct laser fabrication of polymeric implants for cardiovascular surgery. Materials Science. 2012; 18(2):145-149.
12. Malinauskas M, Baltriukienė D, Kraniauskas A, Danilevičius P, Jarašienė R, Širmenis R, Žukauskas A, **Balčiūnas E,** Purlys V, Gadonas R, Bukelskienė V, Sirvydis V, Piskarskas A. *In vitro* and *in vivo* biocompatibility study on laser 3D microstructurable polymers. Applied Physics A. 2012; 108(3):751-759.

**List of other, non-peer-reviewed publications**

1. Bukelskienė V, **Balčiūnas E**, Pečiukaitytė M, Burinskij J, Jarašienė R, Malinauskas M, Baltriukienė D. Poly (dimethylsiloxane) scaffolds for tissue engineering: an *in vitro* study. Journal of Tissue Engineering and Regenerative Medicine, 2014; 8:322.
2. Pečiukaitytė M, **Balčiūnas E,** Burinskij J, Jarašienė R, Malinauskas M, Bukelskienė V, Baltriukienė D. Investigation of progenitor cell interactions with 3D printed PLA scaffolds for tissue engineering applications. Journal of Tissue Engineering and Regenerative Medicine, 2014; 8:337.
3. Malinauskas M, Lukoševičius L, Mackevičiūtė D, **Balčiūnas E**, Rekštytė S, Paipulas D. Multiscale 3D manufacturing: combining thermal extrusion printing with additive and subtractive direct laser writing. Proceedings of SPIE, 2014; 9135.
4. **Balčiūnas E**, Lukoševičius L, Mackevičiūtė D, Rekštytė S, Rutkūnas V, Paipulas D, Stankevičiūtė K, Baltriukienė D, Bukelskienė V, Piskarskas AP, Malinauskas M. Combination of thermal extrusion printing and ultrafast laser fabrication for the manufacturing of 3D composite scaffolds. Proceedings of SPIE, 2014; 8972.
5. Rekštytė S, Kaziulionytė E, **Balčiūnas E**, Kaškelytė D, Malinauskas M. Direct laser fabrication of composite material 3D microstructured scaffoldings. The 6th International Congress on Laser Advanced Materials Processing, 2013 Proceedings.
6. Rekštytė S, **Balčiūnas E**, Baltriukienė D, Rutkūnas V, Bukelskienė V, Gadonas R, Malinauskas M. Direct laser fabrication of composite material 3D microstructured scaffolds. Lasers and Electro-Optics Europe (CLEO EUROPE/IQEC) 2013 Proceedings.
7. Stankevičius E, **Balčiūnas E**, Baltriukienė D, Bukelskienė V, Malinauskas M, Račiukaitis G. Scaffolds fabricated by the interference lithography technique and evaluation of their suitability for biomedical applications. Radiation Interaction with Material and Its Use in Technologies 2012 Proceedings. 185-188.

8. **Balčiūnas E**, Jonušauskas L, Baltriukienė D, Malinauskas M. Lithographic microfabrication of polymer structures for tissue engineering applications. Radiation Interaction with Material and Its Use in Technologies 2012 Proceedings. 413-416.
9. **Balčiūnas E,** Jonušauskas L, Valuckas V, Baltriukienė D, Bukelskienė V, Gadonas R, Malinauskas M. Lithographic microfabrication of biocompatible polymers for tissue engineering and lab-on-a-chip applications. Biophotonics: Photonics Solutions for Better Healthcare III. Proceedings of SPIE, 2012; 8427.
10. Stankevičius E, **Balčiūnas E**, Malinauskas M, Račiukaitis G, Baltriukienė D, Bukelskienė V. Holographic lithography for biomedical applications. Laser Sources and Applications. Proceedings of SPIE, 2012; 8433.
11. Malinauskas M, Danilevičius P, **Balčiūnas E**, Rekštytė S, Stankevičius E, Baltriukienė D, Bukelskienė V, Račiukaitis G, Gadonas R. Applications of nonlinear laser nano/micro-lithography: fabrication from nanophotonic to biomedical components. Smart Nano-Micro Materials and Devices. Proceedings of SPIE, 2011; 8204.
12. Malinauskas M, Baltriukienė D, Kraniauskas A, Danilevičius P, **Balčiūnas E**, Žukauskas A, Purlys V, Širmenis R, Bukelskienė V, Gadonas R, Sirvydis V, Piskarskas A. Laser microstructured 3D polymeric biocompatible implants. Lasers and Electro-Optics Europe (CLEO EUROPE/EQEC) 2011 Proceedings.

**List of conference presentations (Presenter)**

1. **Balčiūnas E**, Kochanė T, Bukelskienė V, Budrienė S, Baltriukienė D. PDMS-based block copolymers for soft tissue engineering applications. European Chapter Meeting of the Tissue Engineering and Regenerative Medicine International Society (TERMIS), Davos (Switzerland), 2017 June 26-30. Poster presentation.
2. **Balčiūnas E**, Baldock S, Baltriukienė D, Hardy JG. Production of organometallic polymer-based biomaterials by laser two-photon polymerisation. Rapid Design, Prototyping and Manufacturing, Newcastle (United Kingdom), 2017 April 27-28. Podium presentation.
3. **Balčiūnas E**, Baldock S, Hardy JG, Baltriukienė D. Biocompatibility testing of aluminium and zirconium based hybrid organic-inorganic materials. Laboratory Animals in Research, Vilnius (Lithuania), 2016. Poster presentation.
4. **Balčiūnas E**, Kochanė T, Budrienė S, Bukelskienė V, Baltriukienė D. PDMS-based block copolymer biocompatibility testing for tissue engineering applications. Laboratory Animals in Research, Vilnius (Lithuania), 2016. Poster presentation.
5. **Balčiūnas E,** Baltriukienė D, Hardy JG. An aluminium-based hybrid organic-inorganic material for laser multiphoton polymerisation. Life Sciences Baltics, Vilnius (Lithuania), 2016 November 24-25. Poster presentation.

6. **Balčiūnas E**, Ranella A, Baltriukienė D, Farsari M. A novel material for tissue engineering via direct laser writing. Advanced Functional Polymers for Medicine, Galway (Ireland), 2015 March 23-25. Poster presentation.
7. **Balčiūnas E,** Nazir R, Gryko DT, Ranella A, Farsari M. Novel materials for tissue engineering via direct laser writing. New Year's Physics Student Conference, Vilnius (Lithuania), 2015 January 2-3. Podium presentation.
8. **Balčiūnas E**, Selimis A, Ranella A, Baltriukienė D, Farsari M. Direct laser writing and replica molding of cellular differentiation-inducing polymer scaffolds for tissue engineering applications. The 15th International Symposium on Laser Precision Microfabrication, Vilnius (Lithuania), 2014 June 17-20. Poster presentation.
9. **Balčiūnas E**, Jonušauskas L, Baltriukienė D, Malinauskas M. Replication of microstructured polymer scaffolds and their biocompatibility tests for tissue engineering. Open Readings, Vilnius (Lithuania), 2012 March 28-31. Poster presentation.
10. **Balčiūnas E**, Jonušauskas L, Baltriukienė D, Malinauskas M. Lithographic microfabrication of polymer structures for tissue engineering applications. Radiation Interaction with Material and Its Use in Technology, Kaunas (Lithuania), 2012 May 14-17. Poster presentation.
11. **Balčiūnas E**, Jonušauskas L, Rekštytė S, Žukauskas A, Malinauskas M, Gadonas R. Lazeriu pagamintų darinių replikavimas minkštosios litografijos metodu. 39th Lithuanian National Physics Conference, Vilnius (Lithuania), 2011 October 6-8. Poster presentation.
12. **Balčiūnas E**, Rekštytė S, Danilevičius P, Malinauskas M. Replication of laser written micro/nanostructures using soft lithography. Developments in Optics and Communications, Riga (Latvia), 2011 April 28-30. Poster presentation.
13. **Balčiūnas E**, Rekštytė S, Jonušauskas L, Malinauskas M. Replication of micro/nanostructures using polydimethylsiloxane soft lithography. Open Readings, Vilnius (Lithuania), 2011 March 17-19. Poster presentation.

**List of conference presentations (coauthor)**

1. Baltriukienė D, **Balčiūnas E**, Kochanė T, Budrienė S, Bružaitė I, Liutkevičius E, Bukelskienė V, Vaineikytė R, Jasmontaitė D. Co-culture of endothelial and myogenic stem cells: strategies and applications for tissue engineering. European Chapter Meeting of the Tissue Engineering and Regenerative Medicine International Society (TERMIS), Davos (Switzerland), 2017 June 26-30.
2. Grigalevičiūtė G, **Balčiūnas E,** Jonušauskas L, Rekštytė S, Baltriukienė D, Bukelskienė V, Malinauskas M. Fabrication of flexible microporous 3D scaffolds via tabletop-stereolithography. Open Readings, Vilnius (Lithuania), 2017 March 14-17.
3. Barasa P, Pečiukaitytė M, **Balčiūnas E**, Šimoliūnas E, Baltriukienė D, Bukelskienė V. Influence of surface topography on the vital processes of myogenic cells *in vitro*. XIV International Conference of the Lithuanian Biochemical Society, Druskininkai (Lithuania), 2016 June 28-30.
4. Vaineikytė R, **Balčiūnas E**, Baltriukienė D, Bukelskienė V. Effect of nanoparticles on endothelial and myogenic origin stem cells and their co-culture. XIV International Conference of the Lithuanian Biochemical Society, Druskininkai (Lithuania), 2016 June 28-30.
5. Lukoševičius L, Mackevičiūtė D, **Balčiūnas E**, Rekštytė S, Malinauskas M. 3D micromanufacturing: combining thermal extrusion printing with additive and subtractive direct laser writing. The 15th International Symposium on Laser Precision Microfabrication, Vilnius (Lithuania), 2014 June 17-20.
6. Rekštytė S, **Balčiūnas E**, Baltriukienė D, Rutkūnas V, Bukelskienė V, Gadonas R, Malinauskas M. Direct laser fabrication of composite material 3D microstructured scaffolds. The European Conference on Lasers and Electro-Optics, Munich (Germany), 2013 May 12-16.
7. Bukelskienė V, Baltriukienė D, Kraniauskas A, Širmenis R, Jarašienė R, **Balčiūnas E**, Malinauskas M. Heart tissue reconstruction applying microstructured polymer scaffolds and autologous cells in a rabbit model. The European Chapter Meeting of the Tissue Engineering and Regenerative Medicine International Society (TERMIS), Istanbul (Turkey), 2013 June 17-20.
8. Stankevičius E, **Balčiūnas E,** Baltriukienė D, Bukelskienė V, Malinauskas M, Račiukaitis G. Interference lithography for tissue engineering. Fundamentals of Laser Assisted Micro- & Nanotechnologies, St. Petersburg (Russia), 2013 June 24-28.
9. Jonušauskas L, **Balčiūnas E**, Rekštytė S, Malinauskas M. Trimačių darinių lazerinis formavimas iš polimero be fotoiniciatoriaus. 40th Lithuanian National Physics Conference, Vilnius (Lithuania), 2013 June 10-12.
10. Stankevičius E, **Balčiūnas E**, Baltriukienė D, Bukelskienė V, Malinauskas M, Račiukaitis G. PEGDA scaffolds fabricated by holographic lithography. 5th Vienna Biomaterials Symposium, Vienna (Austria), 2012 November 19-21.

11. Stankevičius E, **Balčiūnas E**, Baltriukienė D, Bukelskienė V, Malinauskas M, Račiukaitis G. Scaffolds fabricated by the interference lithography technique and evaluation of their suitability for biomedical applications. Radiation Interaction with Material and Its Use in Technology, Kaunas (Lithuania), 2012 May 14-17.
12. Baltriukienė D, Malinauskas M, Kraniauskas A, Danilevičius P, **Balčiūnas E**, Širmenis R, Bukelskienė V, Gadonas R, Sirvydis V, Piskarskas A. Biocompatibility of laser microstructured 3D polymeric scaffolds. World Conference on Regenerative Medicine, Leipzig (Germany), 2011 November 2-4.
13. Danilevičius P, **Balčiūnas E**, Malinauskas M. Direct laser writing of microstructured polymer scaffolds for tissue engineering applications. Open Readings, Vilnius (Lithuania), 2011 March 17-19.
14. Danilevičius P, **Balčiūnas E**, Malinauskas M. Laser multi-photon polymerization for tissue engineering applications. Developments in Optics and Communications, Riga (Latvia), 2011 April 28-30.
15. Rekštytė S, **Balčiūnas E**, Žukauskas A, Malinauskas M. Direct laser writing of microstructures on metal and silicon surfaces. Developments in Optics and Communications, Riga (Latvia), 2011 April 28-30.
16. Danilevičius P, **Balčiūnas E**, Malinauskas M. Laser 3D fabrication of polymeric micro/nanostructures for biomedical applications. The 8th International Conference of Young Scientists on Energy Issues, Kaunas (Lithuania), 2011 May 26-27.
17. Rekštytė S, **Balčiūnas E**, Žukauskas A, Malinauskas M. Direct laser writing of microstructures on opaque surfaces. The 13th International Conference – School Advanced Materials and Technologies, Palanga (Lithuania), 2011 August 27-31.
18. Gadonas R, Danilevičius P, **Balčiūnas E,** Rekštytė S, Malinauskas M. Laser fabrication of polymeric implants for cardiovascular surgery. The 13th International Conference – School Advanced Materials and Technologies, Palanga (Lithuania), 2011 August 27-31.
19. Malinauskas M, Baltriukienė D, Kraniauskas A, Danilevičius P, **Balčiūnas E**, Tikuišis K, Rekštytė S, Žukauskas A, Širmenis R, Bukelskienė V, Gadonas R, Sirvydis V, Piskarskas A. Laser microstructured 3D polymer scaffolds as biocompatible implants. SPIE Microtechnologies, Prague (Czech Republic), 2011 April 18-20.
20. Malinauskas M, Baltriukienė D, Kraniauskas A, Danilevičius P, **Balčiūnas E**, Žukauskas A, Purlys V, Širmenis R, Bukelskienė V, Gadonas R, Sirvydis V, Piskarskas A. Laser microstructured 3D polymeric biocompatible implants. The European Conference on Lasers and Electro-Optics, Munich (Germany), 2011 May 22-26.

COPIES OF PUBLICATIONS

# 1

# Biocompatibility Investigation of Hybrid Organometallic Polymers for Sub-Micron 3D Printing via Laser Two-Photon Polymerisation

Evaldas Balčiūnas, Nadežda Dreižė, Monika Grubliauskaitė, Silvija Urnikytė, Egidijus Šimoliūnas, Virginija Bukelskienė, Mindaugas Valius, Sara J. Baldock, John G. Hardy and Daiva Baltriukienė

Materials, 2019, Vol. 12

doi:10.3390/ma12233932

*materials*

MDPI

*Article*

# Biocompatibility Investigation of Hybrid Organometallic Polymers for Sub-Micron 3D Printing via Laser Two-Photon Polymerisation

**Evaldas Balčiūnas [1], Nadežda Dreižė [1], Monika Grubliauskaitė [1], Silvija Urnikytė [1], Egidijus Šimoliūnas [1], Virginija Bukelskienė [1], Mindaugas Valius [1], Sara J. Baldock [2,3], John G. Hardy [2,3,*] and Daiva Baltriukienė [1,*]**

1 Institute of Biochemistry, Life Sciences Centre, Vilnius University, 10257 Vilnius, Lithuania; ev.balciunas@gmail.com (E.B.); nadezda.dreize@gmail.com (N.D.); monika.grub@gmail.com (M.G.); urniksi@gmail.com (S.U.); egidijus.simoliunas@gmail.com (E.Š.); virginija.bukelskiene@bchi.vu.lt (V.B.); mindaugas.valius@bchi.vu.lt (M.V.)

2 Department of Chemistry, Lancaster University, Lancaster LA1 4YB, UK; s.baldock@lancaster.ac.uk

3 Materials Science Institute, Lancaster University, Lancaster LA1 4YB, UK

* Correspondence: j.g.hardy@lancaster.ac.uk (J.G.H.); daiva.baltriukiene@bchi.vu.lt (D.B.); Tel.: +370-5223-4379 (D.B.)

Received: 29 October 2019; Accepted: 24 November 2019; Published: 27 November 2019


**Abstract:** Hybrid organometallic polymers are a class of functional materials which can be used to produce structures with sub-micron features via laser two-photon polymerisation. Previous studies demonstrated the relative biocompatibility of Al and Zr containing hybrid organometallic polymers in vitro. However, a deeper understanding of their effects on intracellular processes is needed if a tissue engineering strategy based on these materials is to be envisioned. Herein, primary rat myogenic cells were cultured on spin-coated Al and Zr containing polymer surfaces to investigate how each material affects the viability, adhesion strength, adhesion-associated protein expression, rate of cellular metabolism and collagen secretion. We found that the investigated surfaces supported cellular growth to full confluency. A subsequent MTT assay showed that glass and Zr surfaces led to higher rates of metabolism than did the Al surfaces. A viability assay revealed that all surfaces supported comparable levels of cell viability. Cellular adhesion strength assessment showed an insignificantly stronger relative adhesion after 4 h of culture than after 24 h. The largest amount of collagen was secreted by cells grown on the Al-containing surface. In conclusion, the materials were found to be biocompatible in vitro and have potential for bioengineering applications.

**Keywords:** bioactive surfaces; biomaterials; hybrid organometallic polymers; laser two-photon polymerisation; tissue engineering

## 1. Introduction

The concept of growing human replacement parts in the lab has been around for several decades [1,2]. Researchers have used different approaches for the engineering of artificial tissues—from allogeneic or xenogeneic tissue decellularisation [3] to approaches based on additive manufacturing [4], the latter of which offers a route to the generation of an optimal scaffold for a specific tissue type and patient which has significant potential for economic/health/societal impacts.

Laser two-photon polymerisation (LTPP) is a 3D fabrication technique capable of producing materials with fine details in their structures at sub-micron resolutions [5,6]. Various materials can be used to make 3D structures using this technique including derivatives of natural polymers

(e.g., hyaluronic acid [7], gelatin [8]) and synthetic ones (e.g., derivative of polyethylene glycol [9] and SU-8 [10]).

The LTPP technique is highly versatile and allows several materials to be used in the same sample [11,12]. Compared to other fabrication techniques like stereo-lithography [13], fused deposition modelling [14,15] and selective laser sintering [16], LTPP is the only technique that allows for resolutions below the diffraction limit of light to be fabricated [17]. In addition, LTPP allows for fine-tuning of structural motifs as opposed to randomised porous structures obtained by other means, like template-casting [18] or particulate-leaching [19]. A group of interesting materials for LTPP are hybrid organometallic polymers [20]. To date, materials based on Al [21], Ge [22], Ti [23], V [24] and Zr [25] have been shown to be structurable using LTPP systems. An in vitro biocompatibility screening study showed that Al and Ti hybrids supported a comparable number of cells to glass, while the Zr-based hybrid exceeded the biocompatibility of all the other surfaces [21]. An in vivo study of our Zr-based hybrids showed them to be relatively biocompatible when implanted in rabbit muscle and that they did not cause inflammation or foreign body reaction as demonstrated by hematoxylin and eosin staining [26].

Cell-extracellular matrix interactions are among the most important processes to attenuate in attempting to recreate structurally and functionally viable tissue constructs analogous to natural tissues (where the resident cells adhere to the ECM and take part in remodelling it over time). For many applications, it is important to have materials that support a native-like cellular response and integration. To understand the influence of the metals contained in the organometallic hybrids on cellular behaviour, we have investigated the process of adhesion and adhesion-associated kinase expression, as well as collagen secretion of primary rat myogenic cells grown on these surfaces. We believe that this work will prove useful for tissue engineering researchers focusing on artificial scaffold-based tissue remodelling techniques in that the materials investigated in this work are highly biocompatible, precisely structurable at sub-micron resolutions and simple to prepare.

## 2. Materials and Methods

### *2.1. Material Synthesis*

The hybrid organometallic polymers were synthesised according to published protocols [21,25] Briefly, the Al-based material was prepared by dissolution of aluminium isopropoxide (AIP, ≥98%, Merck, Kenilworth, NJ, USA) in toluene (ACS, ISO, Reag. Ph Eur, Merck, Kenilworth, NJ, USA). In parallel, 3-(trimethoxysilyl)propyl methacrylate (MAPTMS, 98%, Sigma-Aldrich, St. Louis, MO, USA) was hydrolysed using HCl (0.1 M, Applichem, Darmstadt, Germany). Methacrylic acid (MAA, 99%, Sigma-Aldrich, USA) was then added to the solution of aluminium isopropoxide in toluene at a 1:1 molar ratio and subsequently, hydrolysed MAPTMS was added to the mixture at a 1:1:4 AIP:MAA:MAPTMS molar ratio. Finally, 1% of photoinitiator (4,4'-bis(diethylamino)benzophenone, Sigma-Aldrich, St. Louis, MO, USA) was added to the weight of AIP, MAA and 3-(trihydroxysilyl)propyl methacrylate (the product of MAPTMS hydrolysis) and stirred, while shielding from ambient light to prevent undesired crosslinking.

The Zr-based material was prepared in an analogous manner, with molar ratios of zirconium (IV) propoxide, MAA and MAPTHS being 1:1:4 with 1% of photoinitiator by weight (excluding solvents).

### *2.2. 2D Sample Preparation*

To secure polymer bonding to glass, MAPTMS-treated glass slides were prepared according to a protocol adopted from Kapyla et al. [27]. Briefly, circular 12 mm diameter borosilicate glass slides (Thermo Fisher Scientific, Waltham, MA, USA) were washed in ethanol, then immersed in a mixture of MAPTMS/ethanol/acetic acid/water overnight and finally washed in ethanol in an ultrasonic bath (EMAG, Mörfelden-Walldorf, Germany).

The hybrid materials were then spin-coated @ 3000 rpm for 30 s per sample and left at room temperature in the dark overnight for the solvents to evaporate. The samples were then polymerised using a UV lamp (UV-C, G15W T8, Sylvania, London, UK) for at least 5 h at around 20 cm distance, corresponding to about 1.8 mW/cm$^2$. The samples were sterilised under UV for at least one hour on each side, subsequently washed in sterile PBS to remove residual initiator and low molecular weight components. They were then immersed in sterile growth medium prior to cell culture.

### *2.3. 3D Sample Fabrication via Laser Two-Photon Polymerisation*

For laser two-photon polymerisation, a droplet of a hybrid material was placed on a glass slide and then left in a fume hood to evaporate overnight while covered from ambient light. After 24 h such samples were used for structure fabrication on a commercially available Nanoscribe® Photonic Professional GT system (Nanoscribe GmbH, Eggenstein-Leopoldshafen, Germany) that is based at the Department of Chemistry at Lancaster University. A 63X 1.4 NA oil immersion lens was used to focus the laser beam into the polymer. Stereolithography (STL) flies were downloaded from the internet [28] and sliced using proprietary Nanoscribe software (DeScribe 2.3.3). Hatching and slicing distances in X, Y and Z coordinates were set to 100 nm. The laser scanning speed was set to 10 mm/s and the laser power was in the range of 20% to 100% (corresponding to 10–50 mW). After polymerization, the Al based hybrid material was developed in toluene for at least 15 min, followed by air-drying. The structures were then sputter-coated at a thickness of 10 nm using a Q150 RS coater (Quorum Technologies, Lewes, UK) and subsequently observed using a SEM (JSM 7800F, JEOL, Tokyo, Japan) operating at 10–15 kV at the Department of Chemistry at Lancaster University.

### *2.4. Collagen Adsorption and Secretion Assays*

A protocol for assessing the concentration of collagen was adapted from Tullberg-Reinert and Jundt [29] with slight modifications. The protocol used is based on in situ staining of cell monolayers using Sirius Red. This dye has strong interactions with collagen types I and III, but weak interaction with collagen type IV.

First, a solution of collagen type I (1 mg/mL in 0.1 N acetic acid, Sigma-Aldrich, St. Louis, MO, USA) was added to the sample and incubated for 1 h at 37 °C. Then, the collagen solution was gently replaced with fixating Bouin's solution (15 mL saturated aqueous picric acid (Sigma-Aldrich, St. Louis, MO, USA) with 5 mL 35% formaldehyde (Sigma-Aldrich, St. Louis, MO, USA) and 1 mL glacial acetic acid (Sigma-Aldrich, St. Louis, MO, USA), incubated for 1 h and then washed using PBS. The samples were then transferred to new wells with a solution of Sirius Red (1 mg/mL in picric acid) for 1 h under mild rocking conditions (30 rpm). Afterwards, the samples were washed with 0.01 N hydrochloric acid to remove unbound dye. The dye was then dissolved in 0.2–0.3 mL of 0.1 N sodium hydroxide by shaking at room temperature for 30 min. Non-coated samples were stained and measured in the same way and their signals were subtracted from collagen-coated sample signals prior to analysis.

The optical density of the solution was measured using a Varioskan Flash microplate reader (Thermo Fisher Scientific, Waltham, MA, USA) at 550 nm. For reference, a calibration curve was prepared by using known concentrations of collagen type I in order to link them to the absorbance of Sirius Red at 550 nm (Figure S1 in Supplementary Materials). A total of 3 independent experiments were carried out and the results are presented as averages +/- standard errors.

Collagen synthesis was assessed in an analogous way to adsorption. The cells were seeded on the test surfaces at a density of 20,000 cells/mL/sample in 24 well tissue culture plates. After 1, 7 and 14 days of incubation, the samples were fixated using Bouin's solution, then dyed using a solution of Sirius Red (Sigma-Aldrich, St. Louis, MO, USA) and subsequently washed with a solution of HCl (Sigma-Aldrich, St. Louis, MO, USA). Finally, the dye was dissolved in a solution of NaOH (Merck, Kenilworth, NJ, USA) and measured spectrophotometrically against pure NaOH, and the amount of collagen was determined from the calibration curve. 3 independent experiments were performed with 3 repetitions per material within each experiment.

### *2.5. Cell Isolation, Culture and Characterisation*

A Wistar rat was euthanised and a small piece of skeletal muscle tissue was removed. The experiments were approved by License of Animal Research Ethics Committee (Lithuania) No. G2-39, 03/08/2016. Large blood vessels were separated, then skeletal muscle tissue was minced and incubated in a solution of EDTA-trypsin (Gibco, Thermo Fisher Scientific, Waltham, MA, USA) with collagenase and hyaluronidase (0.5% and 0.3%, respectively, Sigma-Aldrich, St. Louis, MO, USA) for 30 min at 37 °C under mild shaking conditions. The resulting cell suspension was centrifuged, mixed with growth medium and seeded to tissue culture plates. The growth medium was replaced every 3–4 days and after 5 passages the cells were cloned by serial dilution. A highly proliferative colony forming unit was selected as a cell source, multiplied in vitro and banked in liquid nitrogen for further use.

The cells were cultured in Iscove's modified Dulbecco's medium (IMDM), supplemented with 10% Foetal bovine serum (Gibco, Thermo Fisher Scientific, Waltham, MA, USA) and Penicillin-Streptomycin (100 U/mL and 100 µg/mL, Gibco, Thermo Fisher Scientific, Waltham, MA, USA). They were subcultured every 3–4 days, by detaching with EDTA-trypsin and resuspending in fresh medium. The cells were grown in an incubator (Thermo Fisher Scientific, Waltham, MA, USA) at 37 °C with 5% $CO_2$.

For characterization, cells were grown in 30 mm diameter Petri dishes with glass slides on the bottom, fixed with 4% paraformaldehyde for 15 min. Then the cells were washed with PBS and incubated with 0.2% Triton X-100 in PBS for 15 min to permeabilise the membranes. After blocking in 1% BSA in PBS, the cells were incubated with primary antibodies against CD34, C45 (both from Abcam, Cambridge, UK), Myf5 and c-kit (both from Thermo Fisher Scientific, Waltham, MA, USA) overnight according to manufacturer's instructions at 4 °C. The samples were then rinsed with 1% BSA in PBS and incubated with Cy3-conjugated secondary antibodies (Merck, Kenilworth, NJ, USA). Analysis was performed using an Olympus IX71 (Olympus, Tokyo, Japan) fluorescence microscope.

### *2.6. Analysis of Cell Viability*

AO/EB staining distinguishes cells into four categories: live (bright green, intact nucleus), early apoptotic (bright green, but fragmented nucleus), late apoptotic (orange, fragmented nucleus) and necrotic (bright orange, intact nucleus). Cells were cultured on the hybrid polymer and glass surfaces for 24, 48, 72 and 96 h. Then, the growth medium with any unattached cells was collected and the monolayer of cells were treated with EDTA-trypsin and then collected as well. All of them were subsequently stained by acridine orange and ethidium bromide (Sigma-Aldrich, St. Louis, MO, USA) as described in [30]. The cells were analysed using a BD FACSCanto™ II (BD Biosciences, San Jose, CA, USA) flow cytometer, registering 10,000 events per sample and time point. Green fluorescence of acridine orange was detected using FITC channel and red fluoresce of ethidium bromide was detected using PE channel. A total of 3 independent experiments were performed with 3 repetitions per material within each experiment. The cells were split into four categories based on their fluorescence profile.

### *2.7. MTT Assay*

MTT assay is based on cellular mitochondrial reductase activity. The absorption measured using this technique is directly proportional to the amount of active enzyme, which gives an idea on the number of viable cells and their metabolic activity.

The cells were seeded at a density of 20,000 cells/mL/sample in 24 well tissue culture plates on the hybrid material and glass surfaces and cultured for 24, 48, 72 and 96 h at 37 °C. The samples were then gently transferred to new tissue culture plates containing a solution of MTT (0.2 mg/mL in PBS) and incubated for 2 h at 37 °C. The solution was subsequently removed and the formazan crystals dissolved in ethanol (96%, Vilniaus degtinė, Vilnius, Lithuania). The absorption was measured using a Varioskan Flash microplate reader (Thermo Fisher Scientific, Waltham, MA, USA) at 570 nm with ethanol as a reference. A total of 3 independent experiments were performed with 3 repetitions per material within each experiment.

### *2.8. Adhesion Strength*

The cells were seeded at a density of 100 000 cells/mL/sample in 24 well tissue culture plates and cultured for either 4 or 24 h at 37 °C with 5% $CO_2$. At those time points, samples were transferred to new tissue culture plates, and half of the plates were subjected to shaking at 500 rpm for 5 min using a tissue culture plate shaker (Thermomixer Comfort, Eppendorf, Hamburg, Germany). The reference samples (unshaken) were incubated at 37 °C. The number of cells remaining adhered to the surface was measured by replacing the growth medium with 0.1% crystal violet solution in 20% ethanol for 30 min. Then cells were washed with tap water. Before the measurement of absorption, dye was solubilised with 0,1% acetic acid solution in 50% ethanol. Optical density proportional to cell number was measured using a Varioskan Flash microplate reader (Thermo Fisher Scientific, Waltham, MA, USA) at 570 nm and comparing it to analogously dyed, unshaken cell monolayers. A total of 3 independent experiments were performed with 3 repeats per material within each experiment.

### *2.9. Signalling Protein Expression and Phosphorylation*

The cells were seeded on the samples at a density of 100,000 cells/mL/sample and cultured for either 4 or 24 h. At these timepoints, the samples were transferred to new tissue culture plates and gently washed with PBS. The PBS was then replaced with a lysis buffer consisting of 8 M urea, 2 M thiourea and 50 mM DTT. Cells were collected from 5 samples for each timepoint by pipetting 5–10 times. The lysates were then centrifuged for 10 min at 20,000 × G at RT. The supernatants of each vial were then transferred to new vials and frozen at −20 °C until further use. A total of 3 independent experiments was carried out.

Protein concentrations were normalised by running an SDS-PAGE gel, staining with Coomassie brilliant blue, taking images using a transilluminator (UVP, Upland, CA, USA) using analysing by ImageJ software. After diluting the highest concentration samples using lysis buffer, the concentration-equalised samples were subjected to gel electrophoresis again at 200 V for 45 min using a BioRad (Hercules, CA, USA) electrophoresis apparatus. The proteins were then transferred to a PVDF membrane (Carl Roth, Karlsruhe, Germany) using a Biometra Fastblot transfer device (Biometra GmbH, Göttingen, Germany) at 25 V and 300 mA. The membranes were blocked using 1% BSA (Sigma-Aldrich, St. Louis, MO, USA) in TBS with 0.1% Tween 20 (Sigma-Aldrich, St. Louis, MO, USA).

The membranes were subsequently treated with primary antibodies against p-Akt (Ser473 and Thr308, Cell Signalling technology, Danvers, MA, USA), Akt (Molecular Probes, Eugene, OR, USA), FAK (BD Biosciences, San Jose, CA, USA) and fluorescently-labelled anti-α-tubulin (Sigma-Aldrich, St. Louis, MO, USA) overnight according to manufacturer's instructions at 4 °C.

Next day, the membranes were washed three times using wash buffer and incubated with secondary antibodies. FAK and Akt were treated with HRP-conjugated goat anti-mouse (Invitrogen, Carlsbad, CA, USA) and HRP-conjugated anti-rabbit (Invitrogen, Carlsbad, CA, USA) according to manufacturer's instructions for 1 h. Finally, the membranes were washed again three times using wash buffer. FAK and Akt were detected using by treating with ECL reagent, which upon catalysis by HRP yields chemiluminescence that was detected using a transilluminator (UVP, Upland, CA, USA).

P-Akt (Ser473) and p-Akt (Thr308) were treated with secondary goat-anti-rabbit antibodies conjugated to a fluorescent infrared dye (IRDye 800CW, LI-COR, Lincoln, NE, USA) and detected using an infrared imaging system (Odyssey, LI-COR, Lincoln, NE, USA).

Membrane image analysis was performed using ImageJ software (National Institutes of Health, USA).

### *2.10. Statistical Analysis*

All experiments were repeated at least 3 times independently with 3 repetitions within each experiment. The results are presented as averages +/− standard deviations ($n$ = 0–5) or errors

($n$ = 6+). Statistical significance was assessed using one-way or two-way ANOVA and Tukey's HSD post-hoc tests using RStudio (RStudio Inc., Boston, MA, USA) and plotted using the ggplot2 package. Statistical significance was considered to be achieved with $p < 0.05$.

## 3. Results and Discussion

### *3.1. Laser Two-Photon Polymerisation*

As mentioned in the introduction and methods, the possibility of structuring the Al-based hybrid material has already been described previously [21]. However, we wanted to further demonstrate our ability to fabricate complex 3D shapes and thus have fabricated a micro-structure reminiscent of Zerg (StarCraft, Blizzard Entertainment©, Irvine, CA, USA)—see Figure 1. High volume suspended features were reproducibly fabricated, like the claws of the Zerg hydralisk. Literature shows that by precisely controlling the 3D cell microenvironments, one can achieve complex cellular responses, like stem cell homing towards artificially designed niches [31]. Another important group of factors in designing artificial cell niches are associated to the material chemistry and properties [32]. Integration of several materials in a single structure will hopefully one day help to guide stem cell differentiation towards different lineages on the same sample.

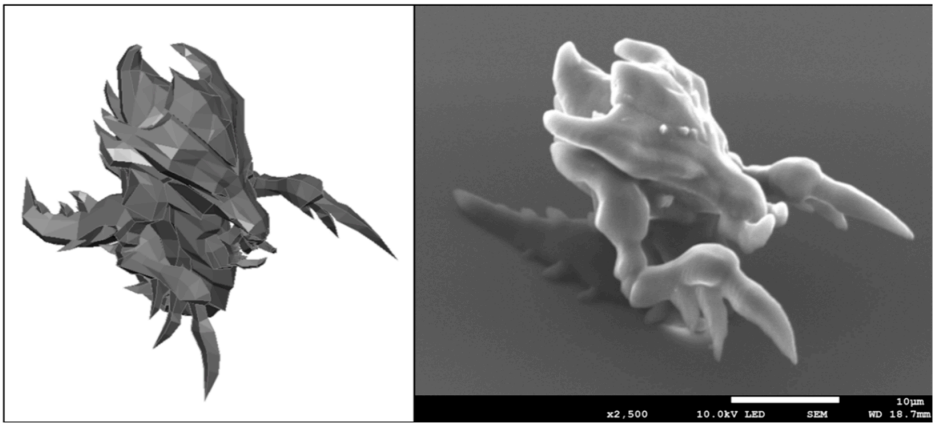


**Figure 1.** Right, A 3D micro-structure reminiscent of Zerg fabricated using a commercially available Nanoscribe Photonic Professional GT system. The scale bar corresponds to 10 microns. Left, A CAD model of the structure.

Multiple materials can be structured with laser two-photon polymerisation and the Al-based hybrid organometallic polymer presented in this work expands the selection of possible cellular niche materials even further. To date, a number of reports have been made of multiple-material structure fabrication using laser two-photon polymerization—including some of our own, in which PDMS, hybrid organometallic polymer based on Zr, PEG-DA and commercially-available OrmoComp have been integrated together [12]. Lamont et al. have developed a technique to exchange the material that is being used to fabricate structures on-the-go, allowing up to five different materials to be incorporated within the same structure with increased fabrication speed and potentially, multiple functionalities for applications like drug delivery, advanced optics, meta-materials and microrobotics [33]. Additionally, two or even more disparate fabrication techniques can be employed within the same structure as demonstrated with fused filament fabrication 3D-printed structure modification using laser ablation [34].

The addition of yet another 3D-printable material with new properties to the engineer's menu will allow for a wider variety of new structures and applications to be envisaged, particularly in fields that require high precision micro-fabrication, like tissue engineering scaffolds and drug delivery devices.

### *3.2. Protein Adsorption Assay*

Extracellular matrix protein adhesion to the different surfaces may affect the subsequent adhesion of cells to the surfaces. Collagen type I was chosen as a model system for this experiment—its adsorption to simple spin-coated samples was assessed due to collagen type I abundance in the extracellular matrix. Collagen supports cellular adhesion via RGD sequences, which are specifically recognised by cellular adhesion proteins integrins. These interactions facilitate strong integration between a tissue engineered scaffold and the surrounding tissues, so it is important to have a material that supports collagen adsorption to its surface well for applications where cell adhesion is beneficial.

Collagen itself has been used as a tissue engineering building block in various studies, for example that of Ber et al., where osteoblast growth was guided on 2D surfaces of collagen [35] or work by Ramanathan et al., who have investigated 3D hybrid collagen matrixes as antibacterial dermal substitutes [36]. Collagen and its derivatives are a widely investigated group of materials for soft tissue engineering, while for hard tissue, like bone, collagen coating is a highly desirable approach that can be used in conjunction with other materials. Multiple reviews have focused on the use of collagen as a tissue engineering material either in a pure or composite form [37–39]. Consequently, a possibility of coating hybrid polymer structures with collagen seems like a good approach for improving cellular integration and therefore chosen in this study.

In our experiments, the choice of protein quantification technique was limited by residual photo-initiators within the materials which rendered them fluorescent. Thus, the signal of fluorescence-based techniques for protein visualisation would have been hindered by sample autofluorescence. To overcome this issue, a colorimetric assay was employed.

Collagen adsorption was measured on both the hybrid polymers and reference glass slides by immersion in a solution of collagen, then dying the bound collagen and measuring the optical absorption of the dye. We found that even though the largest amount of collagen was found on the Zr surface and the smallest amount on Al surface, the results in each group were highly disperse, and no statistically significant differences were determined with $p = 0.35$ between Al and Zr, $p = 0.72$ between Glass and Zr and $p = 0.81$ between Glass and Al. The results are presented in Figure 2.

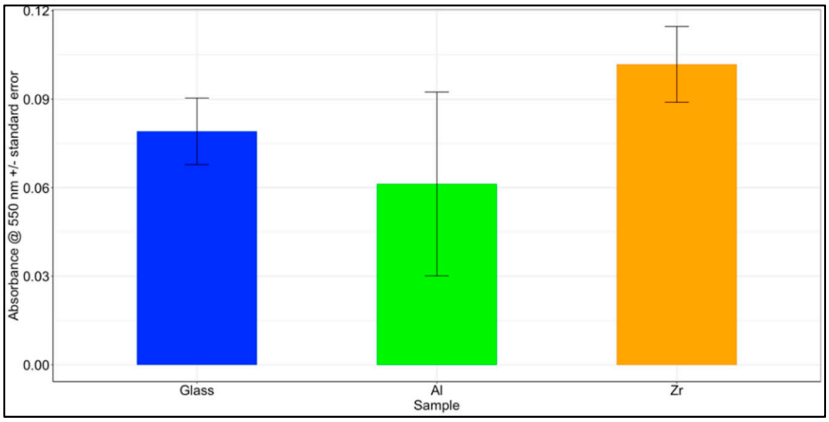


**Figure 2.** Collagen I adsorption to Al and Zr based hybrid organometallic polymers and glass. The results are presented as average Sirius Red absorbances + standard errors for three independent experiments with n = 3 per each experiment (a total of n = 9 per material).

A calibration curve between the total amount of collagen I and Sirius Red absorption was prepared and is presented in Supplementary Materials Figure S1. A highly linear relation was found in the range of 0–100 μg with an $R^2$ value of 0.994. The amounts of collagen adsorbed to the samples were calculated according to the linear model and were found to be 5.59 μg for Glass, 4.40 μg for Al and 6.73 μg for Zr on average per sample.

In our previous work [21], we investigated the contact angles of these materials and found them to be 39° for Glass, 72° for Al-based hybrid materials and 71° for Zr-based hybrid materials. The collagen adsorption data does not seem to correlate with the surface contact angles. Even though there is a significant difference between the contact angle of glass to Al or Zr surfaces, the difference in collagen I adsorption could not be distinguished due to a high deviation from the mean. A paper by Ying et al. [40] indicates that around a two-fold increase in the adsorption of collagen I to the glass surface is expected with an increase of the surface contact angle from 40° to 70°. An analogous result would be expected on other surfaces, since protein adsorption is governed by the same forces as surface contact angle—electrostatic and hydrophobic interactions.

### *3.3. Cell Viability*

Having established the structurability of the materials as well as their collagen adsorption capacity, we investigated how their surfaces influence cellular viability. In this particular study, a primary rat muscle cell line was used to model a situation that would be as close as possible to a clinical one. Using primary muscle-derived stem cells is a safe choice in designing a possible future tissue engineering strategy due to the abundance of donor tissue sites, relatively mild donor site morbidity and high proliferative capacity as well as multipotency of the cells. A great example by Nieponice et al. demonstrates how rat muscle-derived stem cells could be used together with elastomeric scaffold-building materials in constructing vascular grafts [41]. The study successfully showed that the cells tended to home to the lumen of the vascular grafts and started to express α-actin, calponin as well as secrete collagen. Endothelial differentiation was supported via the presence of von Willebrand factor. Our isolated rat muscle-derived progenitor cells were positive for CD34, Myf5 and c-kit and negative for CD45 (Figure S2).

This experiment aimed to find the ratios between the numbers of viable, early apoptotic, necrotic and late apoptotic cells at different timepoints and on different surfaces. Flow cytometry data shows that no statistically significant differences between the numbers of cells in each category can be observed, since the majority of cells at each time point was viable (Figure 3). Additional data is presented in the Supplementary Materials, providing light microscopy images of cell culture at different time points as well as statistical analysis (Figure S3 and Figure S4 in the Supplementary Materials).

The results are in accord with our previous work on these materials with NIH/3T3 cells, which showed that the cells remain viable in culture for extended periods of time [21]. Data obtained in this experiment open the way for the future applications of both Al and Zr based hybrid materials. Long-term viability support of the cells is the first step towards engineering adequate implants for patients.

### *3.4. Cell Proliferation and Metabolism*

As a subsequent step after viability assessment, the rate of cellular metabolism was measured using MTT assay. This test is a direct indicator of mitochondrial activity, since the dye is being digested by mitochondrial reductase to yield a colorimetric signal. This can be used as an indicator for overall cellular metabolism. It is important to know if cellular metabolism rates are different among the various surfaces, since significant deviations in cellular metabolism rates could potentially yield new properties of the cell population on that particular surface. Increased rates of metabolism could be associated with malignant formations and dysregulation of the cell cycle, while down-regulated rates of metabolism could indicate low cellular viability or transfer into a more quiescent state via differentiation or other mechanisms [42].

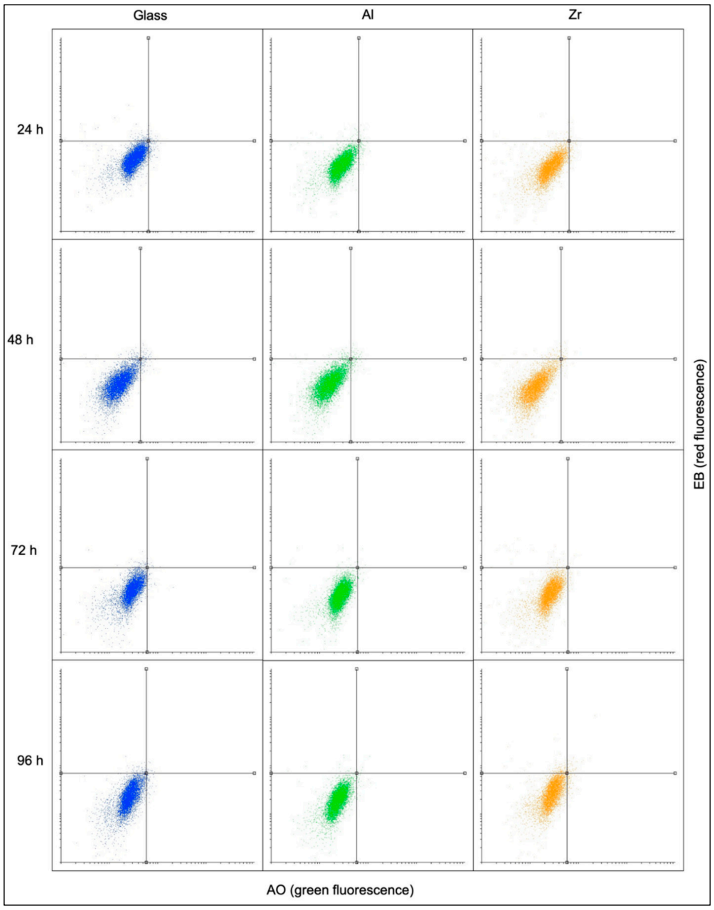


**Figure 3.** Flow cytometry data on cellular viability on Glass, Al and Zr surfaces after 24, 48, 72 and 96 h. The four quadrants in each case show the following: lower left—viable cells, upper left—necrotic cells, upper right—late apoptotic cells, lower right—early apoptotic cells. The lower left quadrant corresponds to 95% of all signals in all cases.

Light microscopy images show cells grown on both the hybrid polymer and glass surfaces to have formed confluent monolayers after 48 to 72 h (Supplementary Materials, Figure S3). No significant differences were observed neither in daily culture check-ups nor in the images taken of those cells. The cells had healthy spindle-shaped morphologies and stopped dividing after having reached confluency.

The assessment of total metabolic activity revealed that the metabolic rate of cells grown on glass was significantly higher than on the hybrid organometallic polymers after 96 h of culture ($p < 0.001$) and significantly higher than on the Al-based hybrid starting from 48 h ($p < 0.05$). These results are presented in Figure 4. Our previous study [21] investigated the proliferation rate of NIH/3T3 fibroblasts on analogous surfaces after 120 h and showed the Zr surface to support the highest rate, while no statistically significant differences were observed between Glass and Al.

The results obtained in this experiment show promise in using both the Al and Zr hybrid polymers in tissue engineering applications. Both materials supported cell growth, even though the total rate of metabolism was lower than on reference glass surfaces.

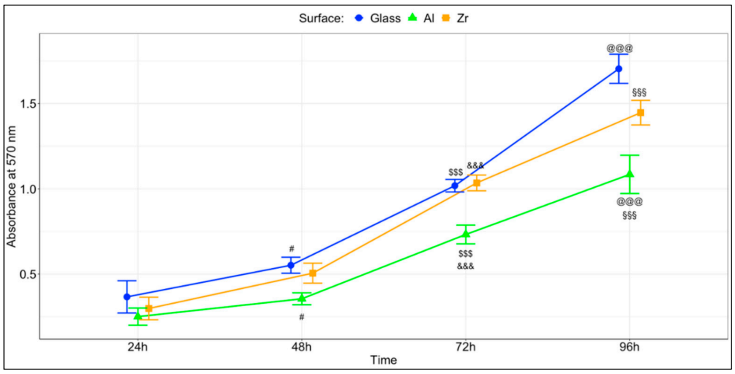


**Figure 4.** Cell proliferation as measured by MTT. The results are presented as average +/- standard error. A total of 9 measurements were performed per material per time point (3 independent experiments with 3 repetitions in each). #—significant difference between glass and Al with $p < 0.05$; $$$—significant difference between glass and Al with $p < 0.001$; &&&—significant difference between Al and Zr with $p < 0.001$; @@@—significant difference between glass and Al with $p < 0.001$; §§§—significant difference between Al and Zr with $p < 0.001$.

### *3.5. Cell Adhesion Strength*

Cellular viability, proliferation and adhesion are highly intertwined processes. Knowing that the viability does not change with surface and that the rate of cellular metabolism grown on the Al hybrid is lower, we sought to understand if the reduced metabolic activity was associated with weaker adhesion. The cells were seeded on the samples and then shaken vigorously at two timepoints. The number of remaining cells was counted and calculated against the number of cells on reference surfaces without shaking. The results are presented in Figure 5. There was a clear trend that showed a decrease in the number of adhered cells after 24 h, suggesting that the initial stage of attachment after 4 h was stronger. Even though there were substantial differences between the number of adhered cells after 24 h, the differences were not statistically significant. However, in spite of a lack of statistical significance, the number of cells that remained attached to the Al surface was the lowest and thus in accord with the proliferation data, that showed the lowest rate of MTT metabolism on the Al- based hybrid. Overall, the Al surface seems to be slightly less supportive of cell adhesion, though insignificantly. The reason for that could potentially be the lowest adsorption of collagen to the Al surface, as presented in Figure 2. To further investigate this difference, an experiment was devised to assess the expression of adhesion-associated proteins.

### *3.6. FAK/Akt Expression and Activation*

When integrin-mediated cell adhesion takes place, a cascade of biochemical reactions is activated that delivers a signal about cellular attachment to the cell nucleus, which in turn activates the transcription and translation of certain proteins that are required for these processes. The cascade is activated when cell surface integrins dimerise after binding to a specific adhesion sequence in the ECM [43]. To initiate intracellular signalling integrin dimer induces conformational changes in focal adhesion kinase (FAK), which is one of the first proteins to join the newly forming focal adhesion. Subsequently, this leads to the recruitment of multiple other adhesion-associated proteins to the focal adhesion site. Upon formation of a focal adhesions, multiple pathways can be activated, one of which is the Akt pathway. This pathway is responsible for transferring a survival and proliferation signal to the nucleus via the mTOR pathway [44]. Akt can be activated by either phosphorylation on Ser473 or Thr308—this depends on the phosphorylating protein. In the case of integrin-mediated adhesion,

PI3K is being activated and thus, only Ser473 is phosphorylated [45]. Phosphorylation on the Thr308 occurs from mTORC2, which is associated with cellular metabolism and cytoskeletal reorganisation.

To assess the expression and activation of adhesion-associated FAK pathway proteins, a Western blot analysis was performed on cells grown on the investigated Glass, Al and Zr surfaces. The results are presented in Figure 6 with membrane images presented in Supplementary Materials Figure S5. Even though no statistically significant results were observed on the investigated surfaces, a tendency for reduced phosphorylation of Akt kinase can be seen in most of the cases when comparing 4 and 24 h. This is to be expected as the adhesion-associated Akt kinase's role is mostly pronounced during the initial cell-to-surface and cell-cell interactions that take place upon cell seeding.

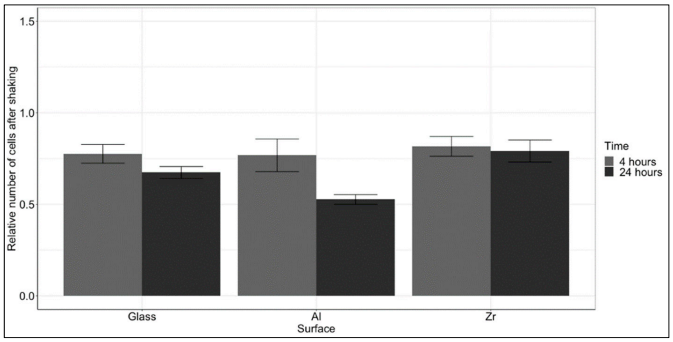


**Figure 5.** Evaluation of cell adhesion strength on the tested surfaces. The results are presented as a ratio between the average number of cells after shaking to that of cells before shaking after 4 and 24 h of culture + standard errors. A total of 9 measurements per material were performed (3 independent experiments with 3 repetitions each). No statistically significant differences were observed between the different time points on each surface.

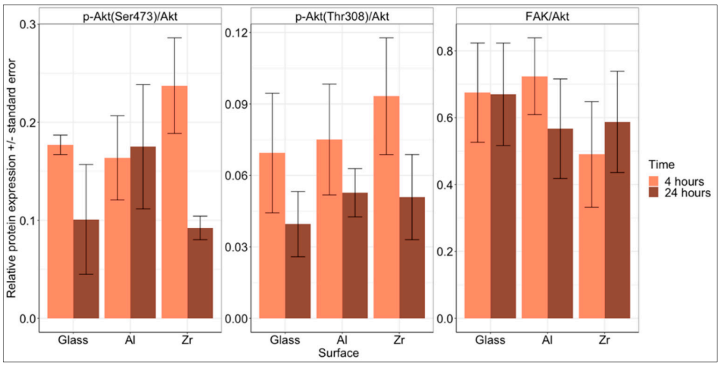


**Figure 6.** Western blot data, showing the expression of FAK and the expression and activation of Akt kinase after 4 and 24 h of culture on glass, Al and Zr surfaces. The amount of p-Akt (Ser 473), p-Akt (Thr308), Akt and FAK were observed. The results are presented as relative expression +/- standard error. Three independent experiments were performed. No statistically significant differences were observed.

The ratio between FAK and Akt kinases was mostly unchanged between time points and only slightly and insignificantly lower on Zr surfaces. This is again to be expected as the total amount of FAK and Akt kinases should remain unchanged.

On the glass surface, the cells tended to attach stronger during the initial 4 h—this is in accord with a higher level of Akt kinase activation in this time point. After 24 h the drop in the number of adhered cells and p-Akt (both Ser473 and Thr308) is clearly visible, though insignificant.

On the Al surface, the situation is similar in terms of p-Akt (Thr308), where the amount of phosphorylated Akt drops after 24 h in accord with a decreased number of cells. However, this was not observed in the p-Akt (Ser473) test. The level of FAK decreased as well, suggesting that the number of focal adhesions had been reduced as well.

The highest drop in terms of level of phosphorylation was observed on the Zr surface. From 4 to 24 h, the level of p-Akt (Ser473) dropped with a $p = 0.25$ and the level of p-Akt (Thr308) dropped with a $p = 0.67$. A slight, but insignificant increase was observed in the level of total FAK. Even though the changes in phosphorylation of Akt on Zr surfaces was the highest, the change in observed cell detachment was lowest in this case.

Even though some tendencies in cell attachment and adhesion-associated protein expression can be seen, these are not statistically significant.

Strong cellular adhesion is an essential prerequisite for successful tissue engineering techniques as discussed in a review by Lee et al. [46]. Whenever adhesion-associated signalling is insufficient, anchorage-dependent cells undergo anoikis, a form of programmed cell death that occurs in anchorage-dependent cells when they detach from the surrounding ECM.

### *3.7. Collagen Synthesis*

Finally, we wanted to investigate whether the surface had any effect on the synthesis of collagen type I. Collagen is one of the main components of the extracellular matrix. Healthy tissues constantly undergo remodelling of their protein structures with the creation and digestion of new proteins by parenchymal cells, like fibroblasts. In tissue engineering, it is essential to have cells be able to model their environments by secreting ECM proteins, like collagen I.

Even though the adsorption was weakest to the Al-based hybrid and so was the cellular adhesion and proliferation, the synthesis of collagen in cells grown on the Al hybrid was the highest. The results are presented in Figure 7. The difference is already visible after one week, but it becomes significant after 2 weeks. This is to be expected as the process of extracellular matrix remodelling takes a substantial amount of time.

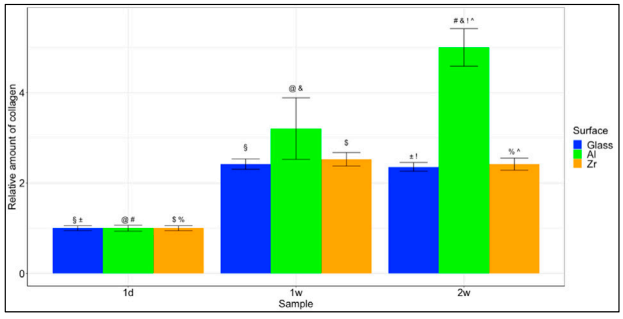


**Figure 7.** Collagen synthesis. Relative amount of collagen produced by cells grown on the different surfaces after 1 day, 1 week and 2 weeks. The results are presented as averages +/- standard errors. Statistically significant differences are indicated using different symbols. §—$p < 0.05$ between 1 day and 1 week glass; ±—$p < 0.05$ between 1 day and 2 week glass; @@@—$p < 0.001$ between 1 day and 1 week Al; ###—$p < 0.001$ between 1 day and 2 week Al; $$—$p < 0.01$ between 1 day and 1 week Zr; %—$p < 0.05$ between 1 day and 2 week Zr; &&&—$p < 0.001$ between 1 week and 2 week Al; !!!—$p < 0.001$ between 2 week glass and 2 week Al; ^^^—$p < 0.001$ between 2 week Al and 2 week Zr. Other statistically significant differences (those between both different materials and different timepoints) are not presented.

Other statistically significant differences were observed between Al surfaces after 1 day, 1 week and 2 weeks with $p < 0.001$ between all periods. As well as Zr surfaces after 1 day and 1 week with a $p < 0.05$.

The results show promise for tissue engineering applications, because they show a significant increase in the collagen produced in the cells grown on these surfaces. This means that the cells had not only attached to the surfaces, but they are comfortable and viable enough to start remodelling their environment via collagen synthesis.

## 4. Conclusions

We believe that the materials investigated in this work may be useful in constructing tissue engineered grafts of the future. This study provides a direct comparison between two materials that can be structured for laser two-photon polymerisation, assessing their support of primary rat myogenic cell growth. The differences between Zr and Al surfaces could potentially be attributed to a difference in adsorption of collagen, which in turn affects cellular adhesion strength, proliferation and the rate of extracellular matrix remodelling, but the results to support this are insignificant, suggesting a more thorough investigation into this process should be carried out.

An additional in vitro study should be performed in the future in order to evaluate how the adhesion-associated protein expression and activation changes over longer periods of time (several days or a couple of weeks) and whether that impacts cellular adhesion, viability and metabolism in a significant way.

Future studies in tissue engineering are likely to focus on integrating several materials with different properties in order to precisely guide cellular behaviour as well as investigating the role that artificial 3D niches with different geometries might play in affecting cellular differentiation and tissue maturation. As such, an extra option in the form of Al-containing hybrid organometallic polymer, presented in this work, is a choice, judging by its biocompatibility demonstrated in this study. In conjunction with its other advantages, like great 3D structuring capabilities, we believe the materials described in this work have potential to add value for the field of biomedical engineering.

**Supplementary Materials:** The following are available online at http://www.mdpi.com/1996-1944/12/23/3932/s1, Figure S1: A curve of collagen I content vs Sirius Red absorbance at 550 nm. An average of three independent experiments with n = 3 in each is presented ± standard deviation. Regression analysis was performed, showing that the dependence is linear in the measurement range (0–100 μg) with $R^2 = 0.994$ and f(x) = 0.0199x−0.0322, Figure S2: Characterization of rat skeletal muscle-derived progenitor cells. Fluorescent microscope images of cells immunostained for CD45, CD34, c-kit and Myf5. The scale bars correspond to 100 microns, Figure S3: Representative images of cells grown on glass, Al and Zr surfaces after 24, 48, 72 and 96 h. The scale bars correspond to 100 microns, Figure S4: Flow cytometry data on cellular viability on Glass, Al and Zr surfaces after 24, 48, 72 and 96 h. The results are presented as average absorbance +/- standard deviation, derived from 3 independent experiments with n = 3 per experiment. No statistically significant differences were found between the surfaces, Figure S5: Images of the Western blot membranes, showing the expression levels of p-Akt (Ser473), p-Akt (Thr308), Akt and FAK proteins. Tubulin was used as a reference. From left to right: 1st membrane: ladder, Al(4 h), Al(24 h), Zr(4 h), Zr(24 h), Glass(4 h), Glass(24 h), Al(4 h), Al(24 h), Zr(4 h); 2nd membrane: ladder, Zr(24 h), Glass(4 h), Glass(24 h), Al(4 h), Al(24h), Zr(4 h), Zr(24 h), Glass(4 h), Glass(24 h).

**Author Contributions:** Conceptualization, E.B. and D.B.; methodology, E.B., S.J.B., J.G.H., D.B.; formal analysis, all authors; investigation, all authors; resources, J.G.H. and D.B.; data curation, D.B.; writing—original draft preparation, all authors; writing—review and editing, E.B., J.G.H. and D.B.; supervision, J.G.H. and D.B.; project administration, D.B.; funding acquisition, J.G.H. and D.B.

**Funding:** This research was funded by INFOBALT Lithuania and the World Federation of Scientists. The work was supported by the European Commission via the Marie Skłodowska-Curie research fellowship programme AngioMatTrain (Grant agreement 317304), and a Lancaster University Faculty of Science and Technology Early Career Internal Grant, a Royal Society Research Grant (RG160449), an EPSRC First Grant (EP/R003823/1), and the Research Council of Lithuania (Grant No. SEN-13/2015).

**Conflicts of Interest:** The authors declare no conflict of interest.

## References


1. Cima, L.G.; Vacanti, J.P.; Vacanti, C.; Ingber, D.; Mooney, D.; Langer, R. Tissue Engineering by Cell Transplantation Using Degradable Polymer Substrates. *J. Biomech. Eng.* **1991**, *113*, 143–151. [CrossRef] [PubMed]
2. Langer, R.; Vacanti, J. Advances in tissue engineering. *J. Pediatr. Surg.* **2016**, *51*, 8–12. [CrossRef] [PubMed]
3. Crapo, P.M.; Gilbert, T.W.; Badylak, S.F. An overview of tissue and whole organ decellularization processes. *Biomaterials* **2011**, *32*, 3233–3243. [CrossRef] [PubMed]
4. Melchels, F.P.W.; Domingos, M.A.N.; Klein, T.J.; Malda, J.; Bartolo, P.J.; Hutmacher, D.W. Additive manufacturing of tissues and organs. *Prog. Polym. Sci.* **2012**, *37*, 1079–1104. [CrossRef]
5. Raimondi, M.T.; Eaton, S.M.; Nava, M.M.; Laganà, M.; Cerullo, G.; Osellame, R. Two-photon laser polymerization: From fundamentals to biomedical application in tissue engineering and regenerative medicine. *J. Appl. Biomater. Funct. Mater.* **2012**, *10*, 55–65. [CrossRef]
6. Selimis, A.; Mironov, V.; Farsari, M. Direct laser writing: Principles and materials for scaffold 3D printing. *Microelectron. Eng.* **2014**, *132*, 83–89. [CrossRef]
7. Kufelt, O.; El-Tamer, A.; Sehring, C.; Schlie-Wolter, S.; Chichkov, B.N. Hyaluronic acid based materials for scaffolding via two-photon polymerization. *Biomacromolecules* **2014**, *15*, 650–659. [CrossRef]
8. Ovsianikov, A.; Deiwick, A.; Van Vlierberghe, S.; Dubruel, P.; Möller, L.; Drager, G.; Chichkov, B. Laser fabrication of three-dimensional CAD scaffolds from photosensitive gelatin for applications in tissue engineering. *Biomacromolecules* **2011**, *12*, 851–858. [CrossRef]
9. Ovsianikov, A.; Malinauskas, M.; Schlie, S.; Chichkov, B.; Gittard, S.; Narayan, R.; Löbler, M.; Sternberg, K.; Schmitz, K.P.; Haverich, A. Three-dimensional laser micro- and nano-structuring of acrylated poly(ethylene glycol) materials and evaluation of their cytoxicity for tissue engineering applications. *Acta Biomater.* **2011**, *7*, 967–974. [CrossRef]
10. Thiel, M.; Fischer, J.; Von Freymann, G.; Wegener, M. Direct laser writing of three-dimensional submicron structures using a continuous-wave laser at 532 nm. *Appl. Phys. Lett.* **2010**, *97*, 221102. [CrossRef]
11. Rekštyte, S.; Jonavičius, T.; Malinauskas, M. Direct laser writing of microstructures on optically opaque and reflective surfaces. *Optics Laser Eng.* **2014**, *53*, 90–97. [CrossRef]
12. Rekštytė, S.; Kaziulionytė, E.; Balčiūnas, E.; Kaškelytė, D.; Malinauskas, M. Direct laser fabrication of composite material 3D microstructured scaffolds. *J. Laser Micro Nanoeng.* **2014**, *9*, 25–30. [CrossRef]
13. Liu, X.; Miller, A.L.; Park, S.; George, M.N.; Waletzki, B.E.; Xu, H.; Terzic, A.; Lu, L. Two-Dimensional Black Phosphorus and Graphene Oxide Nanosheets Synergistically Enhance Cell Proliferation and Osteogenesis on 3D Printed Scaffolds. *ACS Appl. Mater. Interfaces* **2019**, *11*, 23558–23572. [CrossRef] [PubMed]
14. Zein, I.; Hutmacher, D.W.; Tan, K.C.; Teoh, S.H. Fused deposition modeling of novel scaffold architectures for tissue engineering applications. *Biomaterials* **2002**, *23*, 1169–1185. [CrossRef]
15. Lin, M.; Firoozi, N.; Tsai, C.T.; Wallace, M.B.; Kang, Y. 3D-printed flexible polymer stents for potential applications in inoperable esophageal malignancies. *Acta Biomater.* **2019**, *83*, 119–129. [CrossRef] [PubMed]
16. Olakanmi, E.O.; Cochrane, R.F.; Dalgarno, K.W. A review on selective laser sintering/melting (SLS/SLM) of aluminium alloy powders: Processing, microstructure, and properties. *Prog. Mater. Sci.* **2015**, *74*, 401–477. [CrossRef]
17. Farsari, M.; Chichkov, B.N. Materials processing: Two-photon fabrication. *Nat. Photonics* **2009**, *3*, 450–452.
18. Wang, X.; Lin, M.; Kang, Y. Engineering Porous β-Tricalcium Phosphate (β-TCP) Scaffolds with Multiple Channels to Promote Cell Migration, Proliferation, and Angiogenesis. *ACS Appl. Mater. Interfaces* **2019**, *11*, 9223–9232. [CrossRef]
19. Reignier, J.; Huneault, M.A. Preparation of interconnected poly(ε{lunate}-caprolactone) porous scaffolds by a combination of polymer and salt particulate leaching. *Polymer (Guildf.)* **2006**, *47*, 4703–4717.
20. Farsari, M.; Vamvakaki, M.; Chichkov, B.N. Multiphoton polymerization of hybrid materials. *J. Opt.* **2010**, *12*, 124001. [CrossRef]
21. Balčiūnas, E.; Baldock, S.J.; Dreižė, N.; Grubliauskaitė, M.; Coultas, S.; Rochester, D.L.; Valius, M.; Hardy, J.G.; Baltriukienė, D. 3D printing hybrid organometallic polymer-based biomaterials via laser two-photon polymerization. *Polym. Int.* **2019**, *68*, 1928–1940. [CrossRef]

22. Malinauskas, M.; Gaidukevičiute, A.; Purlys, V.; Žukauskas, A.; Sakellari, I.; Kabouraki, E.; Candiani, A.; Gray, D.; Pissadakis, S.; Gadonas, R.; et al. Direct laser writing of microoptical structures using a Ge-containing hybrid material. *Metamaterials* **2011**, *5*, 135–140. [CrossRef]
23. Sakellari, I.; Gaidukeviciute, A.; Giakoumaki, A.; Gray, D.; Fotakis, C.; Farsari, M.; Vamvakaki, M.; Reinhardt, C.; Ovsianikov, A.; Chichkov, B.N. Two-photon polymerization of titanium-containing sol-gel composites for three-dimensional structure fabrication. *Appl. Phys. A Mater. Sci. Process.* **2010**, *100*, 359–364. [CrossRef]
24. Kabouraki, E.; Giakoumaki, A.N.; Danilevicius, P.; Gray, D.; Vamvakaki, M.; Farsari, M. Redox multiphoton polymerization for 3D nanofabrication. *Nano Lett.* **2013**, *13*, 3831–3835. [CrossRef] [PubMed]
25. Ovsianikov, A.; Viertl, J.; Chichkov, B.; Oubaha, M.; MacCraith, B.; Sakellari, I.; Giakoumaki, A.; Gray, D.; Vamvakaki, M.; Farsari, M.; et al. Ultra-low shrinkage hybrid photosensitive material for two-photon polymerization microfabrication. *ACS Nano* **2008**, *2*, 2257–2262. [CrossRef] [PubMed]
26. Malinauskas, M.; Baltriukiene, D.; Kraniauskas, A.; Danilevicius, P.; Jarasiene, R.; Sirmenis, R.; Zukauskas, A.; Balciunas, E.; Purlys, V.; Gadonas, R.; et al. In vitro and in vivo biocompatibility study on laser 3D microstructurable polymers. *Appl. Phys. A Mater. Sci. Process.* **2012**, *108*, 751–759. [CrossRef]
27. Käpylä, E.; Sorkio, A.; Teymouri, S.; Lahtonen, K.; Vuori, L.; Valden, M.; Skottman, H.; Kellomäki, M.; Juuti-Uusitalo, K. Ormocomp-Modified glass increases collagen binding and promotes the adherence and maturation of human embryonic stem cell-derived retinal pigment epithelial cells. *Langmuir* **2014**, *30*, 14555–14565. [CrossRef]
28. Thingiverse. Available online: https://www.thingiverse.com (accessed on 24 October 2019).
29. Tullberg-Reinert, H.; Jundt, G. In situ measurement of collagen synthesis by human bone cells with a sirius red-based colorimetric microassay: Effects of transforming growth factor beta2 and ascorbic acid 2-phosphate. *Histochem. Cell Biol.* **1999**, *112*, 271–276. [CrossRef]
30. Mercille, S.; Massie, B. Induction of apoptosis in nutrient-deprived cultures of hybridoma and myeloma cells. *Biotechnol. Bioeng.* **1994**, *44*, 1140–1154. [CrossRef]
31. Raimondi, M.T.; Eaton, S.M.; Laganà, M.; Aprile, V.; Nava, M.M.; Cerullo, G.; Osellame, R. Three-dimensional structural niches engineered via two-photon laser polymerization promote stem cell homing. *Acta Biomater.* **2013**, *9*, 4579–4584. [CrossRef]
32. Murphy, W.L.; McDevitt, T.C.; Engler, A.J. Materials as stem cell regulators. *Nat. Mater.* **2014**, *13*, 547–557. [CrossRef] [PubMed]
33. Lamont, A.C.; Restaino, M.A.; Kim, M.J.; Sochol, R.D. A facile multi-material direct laser writing strategy. *Lab Chip* **2019**, *19*, 2340–2345. [CrossRef] [PubMed]
34. Malinauskas, M.; Rekštyte, S.; Lukoševičius, L.; Butkus, S.; Balčiunas, E.; Pečiukaityte, M.; Baltriukiene, D.; Bukelskiene, V.; Butkevičius, A.; Kucevičius, P.; et al. 3D microporous scaffolds manufactured via combination of fused filament fabrication and direct laser writing ablation. *Micromachines* **2014**, *5*, 839–858. [CrossRef]
35. Ber, S.; Torun Köse, G.; Hasirci, V. Bone tissue engineering on patterned collagen films: An in vitro study. *Biomaterials* **2005**, *26*, 1977–1986. [CrossRef]
36. Ramanathan, G.; Singaravelu, S.; Muthukumar, T.; Thyagarajan, S.; Perumal, P.T.; Sivagnanam, U.T. Design and characterization of 3D hybrid collagen matrixes as a dermal substitute in skin tissue engineering. *Mater. Sci. Eng. C* **2017**, *72*, 359–370. [CrossRef]
37. Antoine, E.E.; Vlachos, P.P.; Rylander, M.N. Review of Collagen I Hydrogels for Bioengineered Tissue Microenvironments: Characterization of Mechanics, Structure, and Transport. *Tissue Eng. Part B Rev.* **2014**, *20*, 683–696. [CrossRef]
38. Sarker, B.; Hum, J.; Nazhat, S.N.; Boccaccini, A.R. Combining collagen and bioactive glasses for bone tissue engineering: A review. *Adv. Healthc. Mater.* **2015**, *4*, 176–194. [CrossRef]
39. Dong, C.; Lv, Y. Application of collagen scaffold in tissue engineering: Recent advances and new perspectives. *Polymers (Basel).* **2016**, *8*, 42. [CrossRef]
40. Ying, P.; Jin, G.; Tao, Z. Competitive adsorption of collagen and bovine serum albumin - Effect of the surface wettability. *Colloids Surfaces B Biointerfaces* **2004**, *33*, 259–263. [CrossRef]
41. Nieponice, A.; Soletti, L.; Guan, J.; Hong, Y.; Gharaibeh, B.; Maul, T.M.; Huard, J.; Wagner, W.R.; Vorp, D.A. In Vivo Assessment of a Tissue-Engineered Vascular Graft Combining a Biodegradable Elastomeric Scaffold and Muscle-Derived Stem Cells in a Rat Model. *Tissue Eng. Part A* **2010**, *16*, 1215–1223. [CrossRef]

42. Shi, N.; Chen, S.Y. Mechanisms simultaneously regulate smooth muscle proliferation and differentiation. *J. Biomed. Res.* **2014**, *28*, 40–46. [PubMed]
43. Reddig, P.J.; Juliano, R.L. Clinging to life: Cell to matrix adhesion and cell survival. *Cancer Metastasis Rev.* **2005**, *24*, 425–439. [CrossRef] [PubMed]
44. Lee, D.Y.; Li, Y.S.J.; Chang, S.F.; Zhou, J.; Ho, H.M.; Chiu, J.J.; Chien, S. Oscillatory flow-induced proliferation of osteoblast-like cells is mediated by αvβ3 and β1 integrins through synergistic interactions of focal adhesion kinase and Shc with phosphatidylinositol 3-kinase and the Akt/mTOR/p70S6K pathway. *J. Biol. Chem.* **2010**, *285*, 30–42. [CrossRef] [PubMed]
45. Martini, M.; De Santis, M.C.; Braccini, L.; Gulluni, F.; Hirsch, E. PI3K/AKT signaling pathway and cancer: An updated review. *Ann. Med.* **2014**, *46*, 372–383. [CrossRef]
46. Lee, S.; Choi, E.; Cha, M.J.; Hwang, K.C. Cell adhesion and long-term survival of transplanted mesenchymal stem cells: A prerequisite for cell therapy. *Oxid. Med. Cell. Longev.* **2015**, *2015*, 1–9. [CrossRef] [PubMed]


# 2

# Modelling of Silk-Reinforced PDMS Properties for Soft Tissue Engineering Applications

Artūras Kilikevičius, Evaldas Balčiūnas, Kristina Kilikevičienė, Algirdas Maknickas, Virginija Bukelskienė, Daiva Baltriukienė and Rimantas Kačianauskas

Technology and Health Care, 2018, Vol. 26

doi:10.3233/thc-182515

Technology and Health Care 26 (2018) S679–S688
DOI 10.3233/THC-182515
IOS Press



# Modelling of silk-reinforced PDMS properties for soft tissue engineering applications

Artūras Kilikevičius[a], Evaldas Balčiūnas[b], Kristina Kilikevičienė[a], Algirdas Maknickas[a,*], Virginija Bukelskienė[b], Daiva Baltriukienė[b] and Rimantas Kačianauskas[a]
[a]*Institute of Mechanical Science, Faculty of Mechanics, Vilnius Gediminas Technical University, Vilnius, Lithuania*
[b]*Institute of Biochemistry, Life Sciences Center, Vilnius University, Vilnius, Lithuania*

**Abstract.**
**BACKGROUND:** Polydimethylsiloxane (PDMS) is widely used in biomedical research and technology, but its mechanical properties should be tuned according to the desired product specifications. Mixing ratio of base polymer to curing agent or additives enables its mechanical properties to be manipulated and fit to mechanical properties of biological tissues.
**OBJECTIVE:** In this paper, we analysed the effect of mechanical load on silk-reinforced PDMS depending on silk concentration.
**METHODS:** We prepared cylinder-type PDMS samples with different silk concentrations and performed cyclic uniaxial compression tests with a fixed magnitude of applied strain. Next, we analysed the mechanical charascteristics of PDMS using computational modelling.
**RESULTS:** The stress-strain data within the large-strain region of different PDMS cylinders without silk and with 1%, 5% and 10% silk concentrations was fitted to non-linear second order Mooney-Rivlin, and third-order Ogden models. The results show the equivalence of both models for investigated strain region of PDMS. On the other hand, PDMS cylinders with 10% silk concentration allowed the successful fitting of experimental data just for the second-order Mooney-Rivlin model, while all numerical probes to find an appropriate fitting parameters for third-order Ogden models were unsuccessful.
**CONCLUSIONS:** The second-order Mooney-Rivlin model is preferable for analysing the properties of silk-reinforced PDMS over the entire measurement range.

Keywords: Biomaterials, tissue engineering, PDMS, silk, nonlinear materials

## 1. Introduction

Polydimethylsiloxane (PDMS) is a silicone elastomer that is highly biocompatible, biostable and supports extracellular matrix deposition. Its suitability for microporous scaffold fabrication has been demonstrated [1,2]. These characteristics together with its gas permeability, good optical transparency and low autofluorescence make PDMS an attractive candidate for tissue engineering applications as a scaffold material. However, tissues in the organism depending on their location are exposed to various mechanical

*Corresponding author: Algirdas Maknickas, Institute of Mechanical Science, Faculty of Mechanics, Vilnius Gediminas Technical University, Basanavičiaus str. 28, 03224 Vilnius, Lithuania. E-mail: algirdas.maknickas@vgtu.lt.

forces such as compression, fluid shear stress, hydrostatic pressure, and stretching [3]. Numerous studies have demonstrated how scaffold mechanical properties affect cell adhesion, cytoskeletal arrangement, motility [4], proliferation [5], and differentiation [6].

PDMS resistance to mechanical loading such as pressure or external force is limited. On the other hand, mechanical properties of the elastomer can be optimised by varying curing temperature and mixing ratio or adding other materials. Young's modulus, ultimate tensile strength, compressive modulus, ultimate compressive strength and hardness dependency on curing temperature were characterized by Johnston et al. [7]. To modulate PDMS properties, Quake and his colleagues proposed the structural bonding of relatively flexible vinyl PDMS and rigid Si-H PDMS [8]. Kim et al. used this method to demonstrate the possibility of fabricating many devices [9]. As a composite component to stabilize PDMS, silk fibroin, a natural biomaterial produced by silkworms and spiders, can be used. Because of its unique mechanical properties, biocompatibility and the ability to support cell differentiation, silk is favourable for a numerous tissue engineering applications, especially in bone tissue engineering [10–12]. Moreover, silk may be combined synergistically with other biomaterials to form composites of desired physical and biological features.

It is widely agreed that it is very difficult to predict and evaluate the nearly incompressible mechanical behaviour of PDMS structures [9]. Therefore, computational modelling is needed in order to understand and choose optimal mechanical properties for bioapplications [13–20]. In this paper, we analyse the effect of mechanical load on silk-reinforced PDMS depending on silk concentration. The nonlinear material properties of PDMS were modelled using both the second-order Mooney-Rivlin and the third-order Ogden models.

## 2. Experimental methods

### *2.1. Silk-reinforced PDMS sample fabrication*

The silk preparation procedure was adopted from the protocol developed by Rockwood et al. [21]. Silkworm (Bombyx mori) cocoons were fragmented using scissors and subsequently boiled for 1 h in a 0.02 M solution of $\mathrm{Na_2CO_3}$ that was gently stirred. Cocoon leftovers were removed from the solution, and the remaining silk was washed three times with deionised water for 1 h each. The silk fibers were then pressed to remove excess water and left to dry overnight.

PDMS (Sylgard 184, Dow Corning) was thoroughly mixed with the proprietary thermoinitiator at a mass-to-mass ratio of 10:1. Silk was subsequently added to the mixture at 1%, 5%, or 10% mass ratio, and a pure PDMS-thermoinitiator mixture was used as the reference. The mixtures were poured into wells of 24-well polystyrene tissue culture plates (cylinders with diameters of 15.6 mm, heights of 17.8 mm, and volumes of approximately 3.4 mL) and left in a refrigerator (4°C) for 1 hour for the air bubbles to evaporate. The plate with PDMS-silk mixtures was then heated for 1 h at 100°C. Finally, the polystyrene plate was mechanically crushed to remove the samples.

### *2.2. Experimental setup*

The compression tests were performed using a Mecmesin MultiTest 2,5-i micro-compression machine (Mecmesin Limited., Slinfold, UK) in a Mecmesin AFG25 load cell with controlled load of measured accuracy $\pm$ 0.01 mm, compression force in range 2–2500 N and accuracy $\pm$ 0.1% where croohead speed accuracy of indicated speed was $\pm$ 0.1%. After installing a sample, cyclic loading was applied (Fig. 1

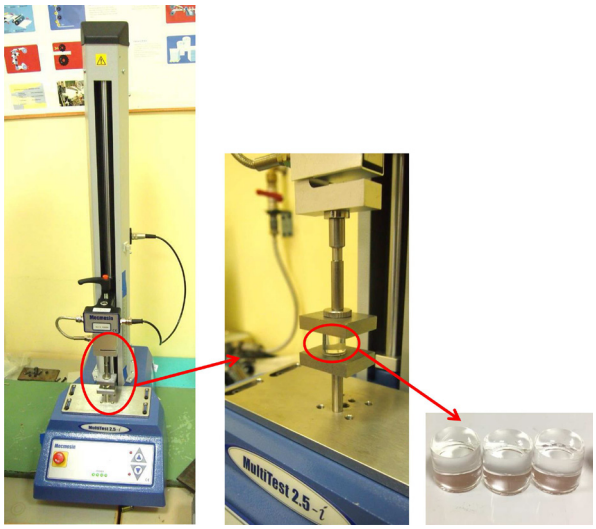


Fig. 1. PDMS sample during the cyclic compression test.

shows photographs of the system and PDMS sample during cyclic compression). The displacement and applied force during the test were recorded automatically. The measurements were performed at room temperature.

The loading was controlled by measured the displacement until the maximum displacement value of $\Delta L = 4$ mm for all specimens (Fig. 2) within a compression speed value of 0.167 mm/s.

## 3. Modelling approach of material properties

### *3.1. Different models of hyperelasticity*

Each hyperelastic model defines its own energy deformation function with material constants that should be obtained by fitting experimental data with model curves. In essence, these are phenomenological models that treat the problem from the perspective of mechanical continuity and stress-deformation behaviour, ignoring the microscopic properties of the structure. However, if appropriate, the revised physics models should consider the characteristics of the microscopic properties. The following section presents a brief overview of hyperelastic models used in this study and an explanation of the algorithm that performs a nonlinear fit of the constants in the models.

### *3.2. Full polynomial model*

The polynomial model for isotropic and compressible rubber is described as follows [22]:

$$U = \sum_{i,j=0}^{N} C_{ij}(\bar{I}_1 - 3)^i(\bar{I}_2 - 3)^j + \sum_{i=1}^{N} D_i(J_{el} - 1)^{2i} \tag{1}$$

Here, $N$ represents the number of terms in strain energy function, $C_{ij}$ represent the material constants that control the shear behaviour and can be determined from uniaxial, biaxial and planar tests and $\bar{I}_i$ for $i = 1, 2$ represent the first and second strain invariants divided by $J_{el}^{-2/3}$ and $J_{el}^{-4/3}$, respectively. $D_i$ represents a material constant that controls bulk compressibility and is equal to zero for fully incompressible rubber. It is non-zero in volumetric tests. Finally, $J_{el}$ represents the elastic volume ratio.

### *3.3. Ogden model*

This model was proposed in 1972 by Ogden [23] as a phenomenological model that was based on the use of principal stretches instead of invariants. The model can describe upturn (stiffening) of stress-strain curve and is accurate in models of rubber for large ranges of deformation. However, the use of this model is limited. (e.g. only when the tension is uniaxial).

$$U = \sum_{i=1}^{N} \frac{2\mu_i}{\alpha_i^2}(\lambda_1^{\alpha_i} + \lambda_2^{\alpha_i} + \lambda_3^{\alpha_i} - 3) + \sum_{i=1}^{N} D_i(J_{el} - 1)^{2i} \tag{2}$$

where $\lambda_i$ represents the deviatoric principal stretch and $\mu_i$ and $\alpha_i$ represent temperature-dependent material properties, as presented in the full polynomial model.

### *3.4. Nonlinear curve fitting*

The nonlinear curve fitting is based on finding one or more parameters of a model equation $\sigma(\lambda, C)$ so that the residual of experimental curve $\sigma_M(\lambda)$ and model equation is as small as possible. In this study, the stress-strain curves for compression tests must be approximated. The stress-strain curve in compression is used to explain the regression analysis process. The final goal is creating a fitting model equation resulting from regression analysis so that the equation yields the same stress values as the curve obtained using measured data:

$$|\sigma(\lambda, C) - \sigma_M(\lambda)| < \varepsilon \tag{3}$$

where $\sigma(\lambda, C)$ represents the model function, which depends on stretch parameters, and $\sigma_M(\lambda)$ denotes the measured stress-stretch curve and $\varepsilon$ represents the maximum fitting residuals, which should be as much as possible. The model equation for compression can be written in the following form:

$$\sigma = f(\lambda, C_{10}, C_{01}, C_{20}, C_{02}, C_{11}) \tag{4}$$

The material constants $C_ij$ must be determined through regression analysis by solving equations of equality to zero of partial derivatives of each constant in the regression equation, which linearly appears in the compression model equation. Finally, an overdetermined system of linear equations should be solved [24] in such a way that would yield a satisfactory level of fit.

## 4. Results

### *4.1. Preparation of silk-reinforced PDMS samples*

Three samples were fabricated in each of the following categories: control PDMS samples without silk, samples with 1% silk, samples with 5% silk and samples with 10% silk (Fig. 2). The samples with silk tended to have air bubbles formed within the materials due to insufficient degassing as compared to pure PDMS, and this might have influenced the mechanical properties of the samples. In addition, the silk dispersed throughout the samples randomly, possibly yielding varying degrees of stiffness within and between the samples.

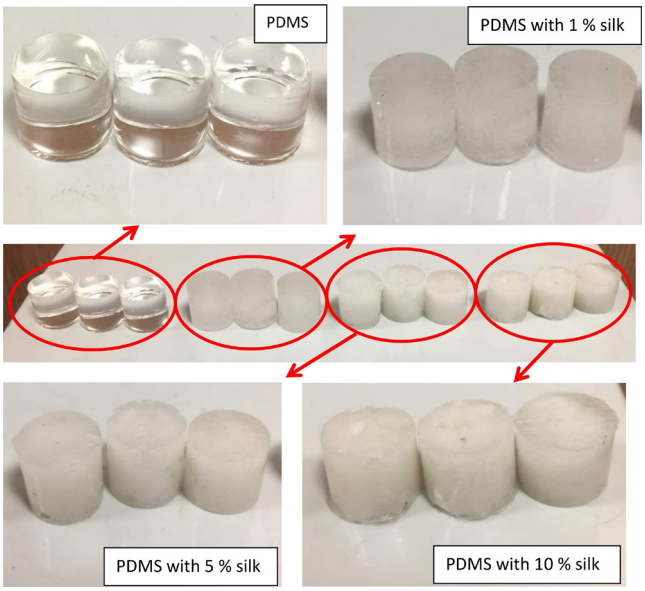


Fig. 2. Pictures of PDMS samples with varying concentrations of silk.

### *4.2. Experimental results of compression tests*

Compression tests were performed on all samples. The stress-strain curves averaged from measured displacement-load curves of different PDMS samples are shown in Fig. 3A–D. Hysteresis was observed during the cyclic loading and relaxing paths of the stress-strain curves. The results retain initial series measured within the limits of accuracy; therefore, fully nonlinear elasticity behaviour was observed during the experiment.

The results presented in Fig. 3 show that for PDMS with 10% silk, the maximum stress was 2144 MPa; for PDMS with 5% silk, the maximum stress was 1324 MPa; for PDMS with 1% silk, the maximum stress was 832 MPa; and in pure PDMS, the maximum stress was the smallest and equal to 752 MPa. The changes in $\Delta L/L$ in the hysteresis loops to determine the widest areas for each material were $-0.009$ (PDMS with 1% silk), 0.0201 (pure PDMS), 0.0299 (PDMS with 5% silk), and 0.0637 (PDMS with 10% silk). The hysteresis loops show that the $\Delta L/L$ (when PDMS samples were loaded and unloaded) was the smallest in PDMS samples with 1% silk and the largest in PDMS samples with 10% silk.

These results show that the mechanical properties of silk-reinforced PDMS can be controlled. The hysteresis can be reduced by changing the proportions of the composite components. These results provide a qualitative understanding of silk-reinforced PDMS.

### *4.3. Uncertainties measurement of material properties*

The experimental data for the cyclic compression tests of PDMS with different silk concentrations were modelled (Fig. 3). Two different material models, Ogden and Polynomial, were examined. The

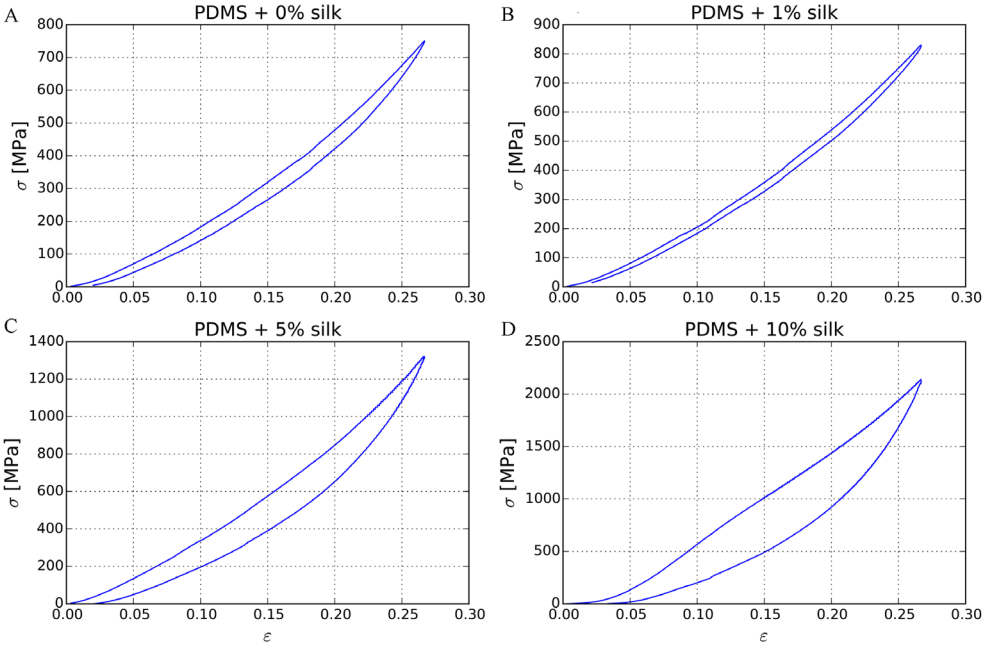


Fig. 3. Experimental stress-strain relations. A – PDMS, B – PDMS + 1% silk, C – PDMS + 5% silk, D – PDMS + 10% silk.

quality of nonlinear fitting was measured by calculating the mean absolute percentage error (MAPE) as follows:

$$\text{MAPE} = \frac{100}{n}\sum_{i=1}^{n}\left|\frac{A_i - F_i}{A_i}\right| \tag{5}$$

where $A_i$ represent the experimental values and $F_i$ represent the model values. Obtained MAPE values are summarized in Fig. 4. The y-axis of the chart presents MAPE values in percentages, and $x$ axis denotes the percentage concentrations of silk in the PDMS test specimens. The material constants of each model for silk-reinforced PDMS samples are summarized in Table 1.

As shown in Fig. 4, MAPE ranges from 1.36% to 1.58% for the polynomial $N = 2$ coefficient fitting and ranges from 5.36% to 6.35% for PDMS with 0%, 1%, and 5% silk. In contrast, MAPE increases until 8.35% for Polynomial material, and the fitting with Ogden $N = 3$ model results in failure. Similar results were obtained for root mean squired error (RMSE). RMSE values are in range from 0.92% to 1.12% for the polynomial $N = 2$ coefficient fitting and ranges from 3.95% to 4.87% for PDMS with 0%, 1%, and 5% silk for Ogden $N = 3$ model.

Combined uncertainties of measured material properties in compression tests is expressed as follow

$$u_c = \sqrt{u_E^2 + u_{CoMa}^2 + u_\sigma^2 + u_{Califer}^2 + V_i} \tag{6}$$

where $u_E$ is uncertainty of tangent curve value of nonlinear stress-strain relations, $u_{CoMa}$ is uncertainty measurement of compression machine, $u_\sigma$ uncertainty of of tangent curve value of non linear stress-strain relations due to stress variation, $u_{Califer}$ is uncertainty of micrometer and $V_i$ is mean squared error

Table 1
Material models of silk-reinforced PDMS samples and their corresponding material constants obtained from experiments

| Material model | Material constants | PDMS + 0% silk [MPa] | PDMS + 1% silk [MPa] | PDMS + 5% silk [MPa] | PDMS + 10% silk [MPa] |
|---|---|---|---|---|---|
| Poly, $N = 2$ | $C_{10}$ | 2.239 | −1.554 | −3.202 | −11.96 |
| | $C_{01}$ | −1.864 | 1.868 | 3.844 | 14.39 |
| | $C_{20}$ | 0.06726 | 0.05517 | 0.1167 | 0.4030 |
| | $C_{11}$ | −0.3478 | −0.2859 | −0.6030 | −2.113 |
| | $C_{02}$ | 1.006 | 0.8344 | 1.736 | 6.326 |
| Ogden, $N = 3$ | $\mu_1$ | −0.01457 | −0.01486 | −0.02185 | – |
| | $\mu_2$ | 0.00277 | 0.00280 | 0.00413 | – |
| | $\mu_3$ | 0.01761 | 0.01769 | 0.02569 | – |
| | $\alpha_1$ | 2.078e-9 | 2.045e-6 | 2.028e-6 | – |
| | $\alpha_2$ | 3.967e-9 | 3.974e-6 | 3.978e-6 | – |
| | $\alpha_3$ | −2.356e-9 | −2.229e-6 | −2.166e-6 | – |

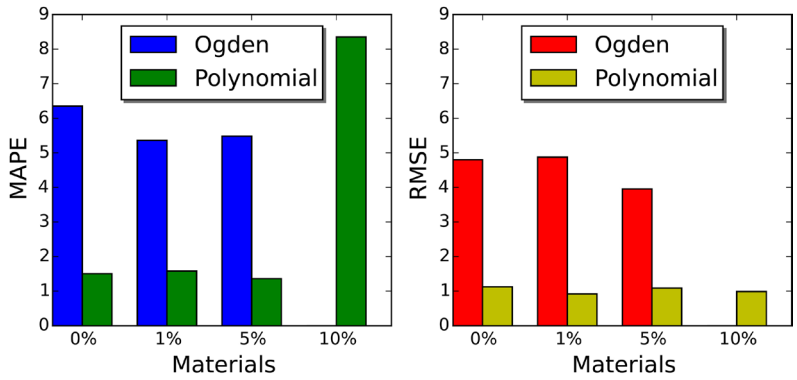


Fig. 4. MAPE and RMSE for different materials.

of stress-strain(stretch) curve fitting. Analysis shows that $V_i$ term is much more bigger than other terms, so expanded uncertainty $U_E$ on measured parameters of PDMS with and without silk inclusions can be expressed as follow

$$U_E = k \cdot \sqrt{V_i} \tag{7}$$

where $k$ is depending on the desired level of confidence ($k = 2$ for 95% confidence).

Figure 5 represents the nonlinear fitting results for silk-reinforced PDMS samples. Two material models, second-order Mooney and second-order Ogden models, were evaluated. Considering the number of coefficients (presented in Table 1) and calculation time required in finite element method simulations, both models are suitable for describing the small strain region of silk-reinforced PDMS. In the nonlinear and large strain region, the second-order Mooney-Rivlin model defined the mechanical behaviour of the silk-reinforced PDMS elastomer better than the second-order Ogden model. The silk-reinforced PDMS samples were too stiff or flexible in the measurement range for the second-order Ogden model. In particular, the nonlinear model of the second-order Mooney-Rivlin model matched the measured strain-stress curves for load regime in Fig. 3 well. Consequently, the second-order Mooney-Rivlin model is preferable to analyse silk-reinforced PDMS structures over the entire measurement range.

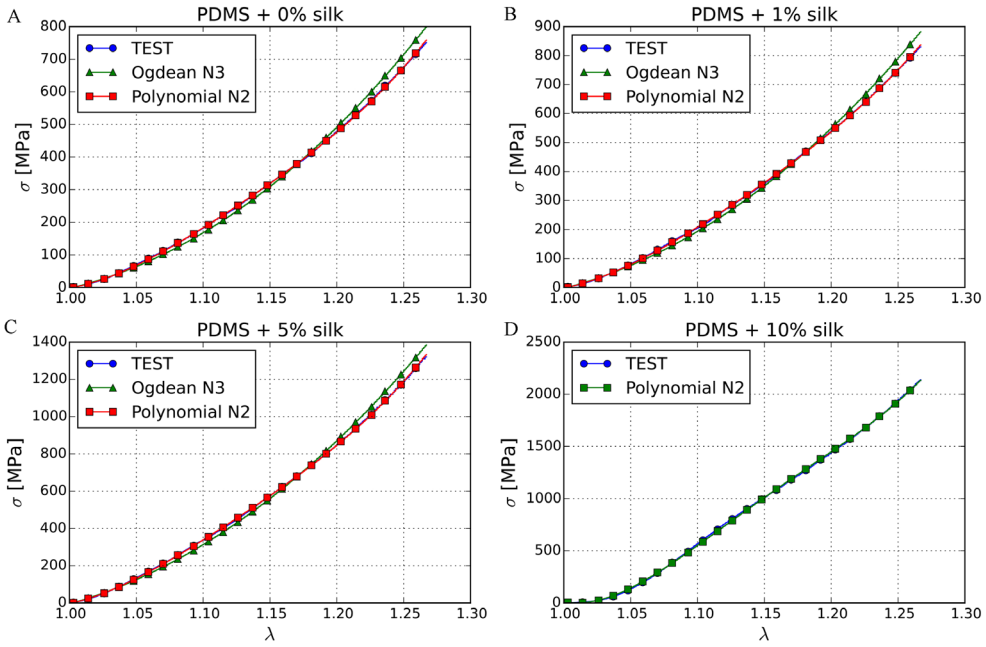


Fig. 5. Comparison of Ogden and polynomial curves with experimental data. A – PDMS, B – PDMS + 1% silk, C – PDMS + 5% silk, D – PDMS + 10% silk.

## 5. Discussion

The nonlinear mechanical properties of silk-reinforced PDMS were obtained from a nonlinear fit of the experimental stress-strain curves of the silk-reinforced PDMS samples. The modelling results show that both the second-order Mooney-Rivlin model and the third-order Ogden model were suitable for the small strain region of silk-reinforced PDMS. However, in the nonlinear and large strain regions, only the second-order Mooney-Rivlin model characterized the mechanical behaviour of silk-reinforced PDMS. Because of stiffness and flexibility in the measurement range, the third-order Odgen model was not functional enough. Hence we may conclude that the second-order Mooney Rivlin model is preferable for modelling the nonlinear behaviour of silk-reinforced PDMS over the entire measurement range.

The results obtained in this work can serve as a basis in constructing silk-reinforced PDMS scaffolds for soft tissue engineering applications, where it is essential to finely tune the mechanical properties of the artificial cell niches to both integrate with the surrounding tissues and to guide cellular differentiation towards the desired lineages. Future work should be focussed on the investigation of cellular responses to such silk-reinforced materials.

## 6. Conclusions

PDMS-silk composites were prepared, and cyclic compression tests were performed. The materials

showed varying degrees of hysteresis, with $\Delta L/L$ ranging from 0.009 (PDMS with 1% silk), 0.0201 (PDMS), 0.0299 (PDMS with 5% silk) to 0.0637 (PDMS with 10% silk). The maximum obtained values of stress in silk-reinforced PDMS increased with increasing silk reinforcement (752 MPa in the case of pure PDMS and 2144 MPa in the case of PDMS with 10% silk).

## Acknowledgments

This research was funded by a grant (No. SEN-13/2015) from the Research Council of Lithuania. E. B. would also like to acknowledge Dr. John G. Hardy from Lancaster University (Lancaster, United Kingdom) for generously providing the silk used in these experiments.

## Conflict of interest

None to report.

## References

[1] Ozbolat V, Dey M, Ayan B, Povilianskas A, Demirel MC, Ozbolat IT. 3D printing of PDMS improves its mechanical and cell adhesion properties. ACS Biomaterials Science & Engineering 2018; 4: 682-693.
[2] Chuah YJ, Koh YT, Lim K, Menon NV, Wu Y, Kang Y. Simple surface engineering of polydimethylsiloxane with polydopamine for stabilized mesenchymal stem cell adhesion and multipotency. Scientific Reports 2015; 5: 18162.
[3] Stoltz JF, Dumas D, Wang X, Payan E, Mainard D, Paulus F, Maurice G, Netter P, Muller S. Influence of mechanical forces on cells and tissues. Biorheology. 2000; 37(1-2): 3-14.
[4] Yeung T, Georges PC, Flanagan LA, Marg B, Ortiz M, Funaki M, Zahir N, Ming W, Weaver V, Janmey PA. Effects of substrate stiffness on cell morphology, cytoskeletal structure, and adhesion. Cell Motility and the Cytoskeleton 2005; 60: 24-34.
[5] Hadjipanayi E, Mudera V, Brown RA. Close dependence of fibroblast proliferation on collagen scaffold matrix stiffness. Journal of Tissue Engineering and Regenerative Medicine 2009; 3: 77-84.
[6] Engler AJ, Sen S, Sweeney HL, Discher DE. Matrix elasticity directs stem cell lineage specification. Cell 2006; 126: 677-689.
[7] Johnston ID, McCluskey DK, Tan CKL, Tracey MC. Mechanical characterization of bulk Sylgard 184 for microfluidics and microengineering. Journal of Micromechanics and Microengineering 2014; 24: 035017.
[8] Unger MA, Chou HP, Thorsen T, Scherer A, Quake SR. Monolithic microfabricated valves and pumps by multilayer soft lithography. Science 2000; 288: 113-116.
[9] Kim TK, Kim JK, Jeong OC. Measurement of nonlinear mechanical properties of PDMS elastomer. Microelectronic Engineering 2011; 88(8): 1982-1985.
[10] Yang Z, Xu LS, Yin F, Shi YQ, Han Y, Zhang L, Jin HF, Nie YZ, Wang JB, Hao X, Fan DM, Zhou XM. In vitro and in vivo characterization of silk fibroin/gelatin composite scaffolds for liver tissue engineering. Journal of Digestive Diseases 2012; 13: 168-178.
[11] Bhattacharjeea P, Kundu B, Naskar D, Kim H-W, Maiti TK, Bhattacharya D, Kunduc SC. Silk scaffolds in bone tissue engineering: An overview. Acta Biomaterialia 2017; 63: 1-17.
[12] Melke J, Midhac S, Ghosh S, Ito K, Hofmanna S. Silk fibroin as biomaterial for bone tissue engineering. Acta Biomaterialia 2016; 31: 1-16.
[13] Belanger MC, Marois Y. Hemocompatibility, biocompatibility, inflammatory and in vivo studies of primary reference materials low-density polyethylene and polydimethylsiloxane: a review. Journal of Biomedical Materials Research 2001; 58: 467-77.
[14] Piruska A, Nikcevic I, Lee SH, Ahn C, Heineman WR, Limbach PA, Seliskar CJ. The autofluorescence of plastic materials and chips measured under laser irradiation. Lab on a Chip 2005; 5: 1348-54.
[15] Hua F, Sun Y, Gaur A, Meitl MA, Bilhaut L, Rotkina L, Wang J, Geil P, Shim M, Rogers JA. Polymer Imprint Lithography with Molecular-Scale Resolution. Nano Letters 2004; 4: 2467-2471.

[16] du Roure O, Saez A, Buguin A, Austin RH, Chavrier P, Silberzan P, Ladoux B. Force mapping in epithelial cell migration. PNAS 2005; 102: 2390-2395.
[17] Charati SG, Stern SA. Diffusion of Gases in Silicone Polymers: Molecular Dynamics Simulations. Macromolecules 1998; 31: 5529-5535.
[18] Leclerc E, Sakai Y, Fujii T. Cell Culture in 3-Dimensional Microfluidic Structure of PDMS (polydimethylsiloxane). Biomedical Microdevices 2003; 5: 109-114.
[19] Paguirigan AL, Beebe DJ. From the cellular perspective: exploring differences in the cellular baseline in macroscale and microfluidic cultures. Integrative Biology 2009; 1: 182-195.
[20] Mukhopadhyay R. When PDMS isn't the best. Analytical Chemistry 2007; 79: 3248-3253.
[21] Rockwood DN, Preda RC, Yucel T, Wang X, Lovett ML, Kaplan DL. Materials fabrication from Bombyx mori silk fibroin. Nature Protocols 2011; 6: 1612-1631.
[22] Rivlin RS, Saunders DW. Large elastic deformations of isotropic materials VII. Experiments on the deformation of rubber. Philosophical Transactions of the Royal Society of London A 1951; 243(865): 251-288.
[23] Ogden RW. Large Deformation Isotropic Elasticity – On the Correlation of Theory and Experiment for Incompressible Rubberlike Solids. Proceedings of the Royal Society of London A: Mathematical, Physical and Engineering Sciences 1972; 326: 565-584.
[24] Hartmann S. Numerical studies on the identification of the material parameters of Rivlin's hyperelasticity using tension-torsion tests. Acta Mechanica 2001; 148: 129-155.

# 3

# 3D Printing Hybrid Organometallic Polymer-Based Biomaterials via Laser Two-Photon Polymerization

Evaldas Balčiūnas, Sara J. Baldock, Nadežda Dreižė, Monika Grubliauskaitė, Sarah Coultas, David L. Rochester, Mindaugas Valius, John G. Hardy and Daiva Baltriukienė

Polymer International, 2019, Vol. 68

doi:10.1002/pi.5909

Research Article

Received: 22 June 2019 Revised: 10 August 2019 Accepted article published: 16 August 2019 Published online in Wiley Online Library: 10 September 2019

(wileyonlinelibrary.com) DOI 10.1002/pi.5909

# 3D printing hybrid organometallic polymer-based biomaterials via laser two-photon polymerization

**Evaldas Balčiūnas,[a] Sara J Baldock,[b,c] Nadežda Dreižė,[a] Monika Grubliauskaitė,[a] Sarah Coultas,[d] David L Rochester,[b] Mindaugas Valius,[a] John G Hardy[b,c*] and Daiva Baltriukienė[a*]**

## Abstract

**Materials with microscale structures are gaining increasing interest due to their range of technical and medical applications. Additive manufacturing approaches to such objects via laser two-photon polymerization, also known as multiphoton fabrication, enable the creation of new materials with diverse and tunable properties. Here, we investigate the properties of 3D structures composed of organometallic polymers incorporating aluminium, titanium, vanadium and zirconium. The organometallic polymer-based materials were analysed using a variety of techniques including SEM, energy-dispersive X-ray spectroscopy, X-ray photoelectron spectroscopy analysis and contact angle measurements and their biocompatibility was tested *in vitro*. Cell viability and mode of death were determined by 3-(4,5-dimethyl-2-thiazolyl)-2,5-diphenyl-2H-tetrazolium bromide (MTT) assay and acridine orange/ethidium bromide staining. Polymers incorporating Al, Ti and Zr supported cell adhesion and proliferation, and showed low toxicity *in vitro*, whereas the organometallic polymer incorporating V was shown to be cytotoxic. Inductively coupled plasma optical emission spectrometry suggested that leaching of the V from the organometallic polymer is the likely cause of this. The preparation of the organometallic polymers is straightforward and both simple 2D and complex 3D structures can be fabricated with ease. Resolution tests of the newly developed organometallic polymer incorporating Al show that suspended lines with widths down to 200 nm can be fabricated. We believe that the materials described in this work show promising properties for the development of objects with sub-micron features for biomedical applications (e.g. biosensors, drug delivery devices, tissue scaffolds etc.).**



*Supporting information may be found in the online version of this article.*

**Keywords:** 3D printing; laser two-photon polymerization; photopolymers; organometallic polymers; tissue engineering

## INTRODUCTION

Laser two-photon polymerization (LTPP) is a very promising technique for 3D microstructure fabrication. It has been used to make structures for a variety of applications, ranging from photonic crystals,[1] metamaterials,[2] micromachines,[3] waveguides,[4] microoptical components,[5] microelectromechanical systems[6] and scaffolds for tissue engineering.[7] Some excellent reviews regarding the use of LTPP for biological applications have been written.[8–10] Various materials can be polymerized using LTPP systems, including polyethylene glycol-diacrylate,[11] epoxy-based glycidyl ether of bisphenol A (SU-8),[12] gelatine methacrylate[13] and many others. The materials can incorporate drugs, quantum dots or even living cells. Gittard *et al.* have reported the fabrication of microneedles doped with gentamicin sulfate.[14] Jia *et al.* have fabricated quantum dot doped structures with nonlinear optical properties.[15] Marino *et al.* have functionalized commercially available Ormocomp® photopolymer with barium titanate nanoparticles, endowing it with piezoelectric properties.[16] Ovsianikov *et al.* have demonstrated the possibility of encapsulating living cells inside photopolymerizable materials and keeping them viable after structure formation.[17]

The chemical, mechanical and topographical properties of materials can influence cellular processes. It has been shown that cellular differentiation can be affected by matrix stiffness[18] or topography.[19] Cellular proliferation rate can be tuned by treating

* *Correspondence to: JG Hardy, Department of Chemistry, Lancaster University, Lancaster, UK, E-mail: j.g.hardy@lancaster.ac.uk; or D Baltriukienė, Institute of Biochemistry, Life Sciences Centre, Vilnius University, Vilnius, Lithuania. E-mail: daiva.baltriukiene@bchi.vu.lt*

a *Institute of Biochemistry, Life Sciences Centre, Vilnius University, Vilnius, Lithuania*

b *Department of Chemistry, Lancaster University, Lancaster, UK*

c *Materials Science Institute, Lancaster University, Lancaster, UK*

d *Kratos Analytical Ltd, Manchester, UK*

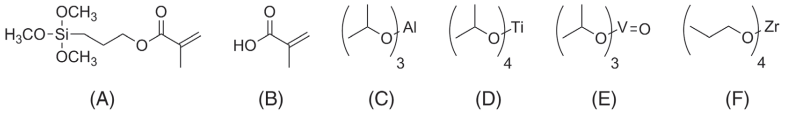


**Figure 1.** Components used in the organometallic polymers studied here: (A) 3-(trimethoxysilyl)propyl methacrylate; (B) methacrylic acid; (C) aluminium isopropoxide; (D) titanium(IV) isopropoxide; (E) vanadium(V) oxytriisopropoxide; (F) zirconium(IV) propoxide.

the substrate in various ways. Hamid *et al.* showed that modifying the chemical properties of materials by plasma treatment can significantly improve the biocompatibility of SU-8 microfluidic chips,[20] and a study by Thrivikraman *et al.* demonstrated the effects of electrical conductivity on cellular proliferation and differentiation.[21]

LTPP-fabricated structures have been investigated for their potential as scaffolds for tissue engineering applications.[7,22–24] 3D structures capable of supporting embryonic stem cells in an undifferentiated state without the use of feeder cells have been demonstrated before.[25]

A widely investigated class of materials for LTPP are hybrid organic–inorganic materials, some of which are based on organometallic polymers.[26] These materials are composed of metal alkoxides and acrylates that often contain silicon oxide. In most cases, the hybrid materials are rendered photosensitive by adding photoinitiators with high two-photon absorption cross-sections, either commercially available ones (e.g. Irgacure 2959, Irgacure 369 and Michler's ketone) or custom-synthesized ones.[27–31] Hybrid organic–inorganic materials such as those based on organometallic polymers are highly promising due to their versatility of applications and properties. To date, organometallic materials incorporating Ge,[32] Ti,[33] V[34] and Zr[35] have been produced by LTPP. Hybrid materials incorporating Zr have been most widely used in the production of various 3D structures, from elements of microoptics,[36] photonics,[37] metamaterials,[2] to scaffolds for tissue engineering.[38,39] Tissue scaffolds fabricated out of this material have been shown to improve the proliferative potential, clonogenic capacity and differentiation potential of human mesenchymal stem cells.[40] The post-fabrication shrinkage of this material can be tuned by changing the duration of laser irradiation.[41] The polymer poly(2-(dimethylamino)ethyl methacrylate) can be used to further tune the mechanical properties of this material.[42] The *in vivo* biocompatibility of one of the iterations of the Zr-based hybrid material[35] was shown to be comparable to that of Polysorb™ 4-0 glycolide/lactide copolymer surgical sutures.[43] LTPP-produced Ti-based hybrid organic–inorganic materials have been less frequently described in the literature but have been used in the production of tissue scaffolds[44] and photonic crystals.[33] Ge-based hybrids have been used to fabricate photonic structures and microoptical elements such as photonic crystals, prisms and spatial polarization plates on either flat substrates or fibre tips.[32] V-based hybrids generated from pentavalent vanadium in vanadium triisopropoxide oxide (VOTIP) do not necessarily require photoinitiators to be added, since they absorb light and generate radicals which induce polymerization. Over the course of the polymerization V is reduced to its tetravalent form, while photonic crystal structures have been fabricated from this material as described earlier.[34]

Aluminium is another metal with great potential for biomedical applications. Its benefits include low cost, lightness and good biocompatibility. Poinern *et al.* have demonstrated the *in vitro* biocompatibility of anodic aluminium oxide membranes in culture with RK-13 rabbit kidney epithelial cells.[45] Furthermore, work by Kolekar *et al.* showed that Al doped hydroxyapatite was biocompatible with L929 mouse fibroblast cells *in vitro*.[46]

The development of complex tissue engineering products may require the integration of materials with different properties, yielding site-specific cellular adhesion, proliferation and differentiation, which motivates the creation of new polymers for precise microfabrication via LTPP. To the best of our knowledge, no LTPP-produced hybrid materials incorporating Al have yet been reported. Here, we report the use of LTPP to fabricate 3D structures based on a novel organometallic polymer containing Al. We then compare its spectroscopic and surface properties to those of Ti-, V- and Zr-incorporating organometallic polymers (the monomers used are displayed in Fig. 1) and relate them to their *in vitro* biocompatibilities.

## EXPERIMENTAL

### Materials

HCl (37% ultrapure) was purchased from AppliChem GmbH., Darmstadt, Germany. Aluminium isopropoxide (AIP) (≥98%) and toluene (ACS, ISO, Reag. Ph Eur) were purchased from Merck, Watford, UK. 3-(trimethoxysilyl)propyl methacrylate (MAPTMS) (98%), 4,4′-bis(diethylamino) benzophenone (DEABP) (≥99%), methacrylic acid (MAA) (99%), titanium(IV) isopropoxide (97%), VOTIP (Cat. #404926) and zirconium(IV) propoxide (70% in isopropanol) were purchased from Sigma-Aldrich, Gillingham, UK. Circular borosilicate cover glass slides 13 mm in diameter were purchased from Thermo Scientific, Warrington, UK. NIH/3T3 mouse embryo fibroblasts were purchased from ATCC, Kielpin, Poland. Dulbecco's phosphate buffered saline (DPBS), (ethylenediaminetetraacetic acid)–trypsin, foetal bovine serum, Iscove's modified Dulbecco's medium (IMDM) and penicillin–streptomycin mixture were purchased from Gibco, Thermo Scientific, Vilnius, Lithuania. 3-(4,5-dimethyl-2-thiazolyl)-2,5-diphenyl-2H-tetrazolium bromide (MTT) (98.9%) was purchased from Merck, Vilnius, Lithuania. Acridine orange (AO), ethidium bromide (EB) and dimethyl sulfoxide (DMSO) (≥99.5%) were purchased from Sigma-Aldrich, Gillingham, UK.

### Synthesis

The Al-containing hybrid was synthesized by hydrolysis of MAPTMS using 0.1 mol $L^{-1}$ HCl (10:1 v/v ratio) to 3-(trihydroxysilyl)propyl methacrylate (MAPTHS), stirring for 15 min. In parallel, AIP was dissolved in toluene in an ultrasonic bath for 15 min. MAA was then added to the AIP solution at a 1:1 AIP:MAA molar ratio. The two solutions of MAPTHS and MAA-AIP/toluene were mixed together at 1:1:4 AIP:MAA:MAPTHS molar ratio and stirred for *ca* 15 min. DEABP was used as a photoinitiator (1% by weight to the sum of AIP, MAA and MAPTHS) and stirred for 15 min.

Other hybrid materials were prepared in accordance with the literature. Zr-based hybrid materials were prepared with a molar



  
*Polymer International* published by John Wiley & Sons Ltd on behalf of Society of Chemical Industry.

ratio of 1:1:4 between zirconium propoxide, MAA and MAPTHS with 1% DEABP.[35] Ti-based hybrid materials were prepared with a 1:1:4 molar ratio between Ti isopropoxide:MAA:MAPTHS with 1% DEABP.[33] V-based hybrid materials were prepared with a 1:1 molar ratio between VOTIP and MAPTHS.[34]

### Sample preparation

Cover glass slides were washed and silanized using MAPTMS according to a protocol adapted from Käpylä *et al.*[47] to ensure polymer bonding to the slides. Finally, the slides were washed again in ethanol to remove any uncrosslinked MAPTMS. Films were prepared by drop-casting a small volume of a precursor material on a slide and leaving the sample overnight in a fume hood in order for the solvent to evaporate. Samples were shielded from ambient light at all steps prior to photopolymerization to avoid unintentional crosslinking.

For energy dispersive X-ray (EDX) spectroscopy measurements, the slides were prepared in an analogous manner to those for structure fabrication. However, after solvent evaporation in a fume hood, the samples were polymerized using a UV lamp (UV-C, 40 W, Phillips, Amazon, Manchester, UK) for at least 2 h and then washed in a solvent for 15 min: Al hybrids were washed in toluene, Ti hybrids and Zr hybrids were washed in 4-methyl-2-pentanone and V hybrids were washed in isopropanol. Subsequently, all materials and reference glass slides were rinsed with ethanol and air-dried.

For biocompatibility testing, thin polymer films were prepared by spin-coating at 1500 rpm for 30 s on 13 mm circular glass slides and subsequently leaving them in a fume hood overnight for evaporation of the solvents. The films were polymerized using a 248 nm KrF excimer laser (30 ns pulse duration operating at 21 kV, 5 Hz repetition rate) for 2 min per sample or a UV lamp (UV-C, 40 W, Phillips, Amazon, Manchester, UK) for at least 2 h.

Prior to cell culture, the samples were washed in DPBS (three times for at least an hour each). The samples were disinfected under UV light in a laminar flow hood for at least 1 h per side to allow *in vitro* cell culture and were placed in sterile 24-well tissue culture plates.

### Laser two-photon polymerization (multiphoton fabrication)

Two LTPP systems were used in structure fabrication. One is a commercially available Nanoscribe Photonic Professional GT (Nanoscribe GmbH/Eggenstein-Leopoldshafen, Baden-Wurttemberg/Germany) and based in the Department of Chemistry at Lancaster University. The system is based on a Topica FemtoFiber pro 100 fs pulsed 780 nm wavelength laser with a maximum power of 50 mW. A 63× 1.4 NA oil immersion Zeiss objective lens was used for fabrication. Structures were imported or programmed in DeScribe scripting software for controlling the fabrication process.

The other system was custom-built (described previously)[48] and based at FORTH-IESL. A schematic representation is given in Fig. 2. A Ti:sapphire laser (Femtolasers Fusion) was used as a light source, operating at 780 nm central wavelength with 20 fs pulse duration and 75 MHz repetition rate. The average laser power was set between 10 and 100 mW using an attenuator (Altechna). The sample was positioned on piezoelectric stages and the laser beam was guided using a galvanometric mirror scanner (Scanlabs Hurryscan II) through a 40× 0.95 NA (Zeiss, Plan-Apochromat) or an oil immersion 100× 1.4 NA (Zeiss, Plan-Apochromat) objective lens. The process of fabrication was controlled by SAMLight (SCAPS) software. Writing speeds between 0.1 and 1 mm $s^{-1}$ were found to be suitable for this purpose.

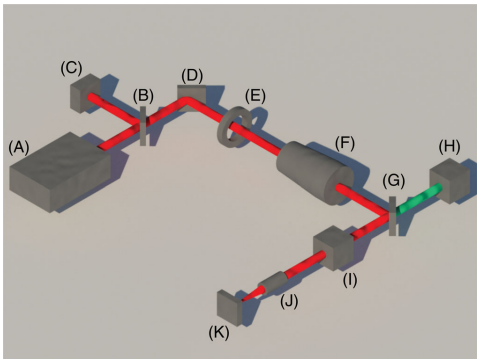


**Figure 2.** A schematic representation of the LTPP system used at FORTH-IESL: (A) the laser; (B) a beam splitter; (C) spectrum analyser; (D) mirror; (E) an attenuator; (F) a telescope; (G) a dichroic mirror; (H) a CCD camera for real-time observation of the fabrication process; (I) a galvo-scanner; (J) an objective lens; (K) the sample stage with light-emitting diode illumination for the CCD camera.

### Scanning electron microscopy (SEM)

Samples were washed in toluene for 15 min and then rinsed with isopropanol and air-dried. Prior to imaging the samples were sputter coated with a 10 nm layer of gold. The structures were observed using either a JEOL JSM−6390L V operating at 15 kV or a JEOL JSM 7800F scanning electron microscope (JEOL, Welwyn Garden City, UK) operating at 10–15 kV.

### EDX analysis

For qualitative EDX analysis, the samples were sputter coated with a layer of gold (60 s, 20 mA, $8 \times 10^{-2}$ mBar, *ca* 5 nm) using a Quorum Q150RES sputter coater (Quorum Technologies Ltd) and then investigated using a field-emission SEM JEOL JSM 7800F with an EDX system (X-Max50, Oxford Instruments, Abingdon, UK) at 10 mm working distance and 10 kV voltage mounted on a brass JEOL holder with 25 mm carbon tables (G3348N, Agar Scientific, Stansted, UK). Three measurements were performed per sample and average results are presented.

### X-ray photoelectron spectroscopy (XPS) analysis

The XPS analyses were carried out with a Kratos Axis Supra spectrometer (Kratos Analytical, Manchester, UK) using a monochromatic Al K$\alpha$ source (20 mA, 15 kV). XPS can detect all elements except hydrogen and helium, probes the surface of the sample to a depth of 5–7 nm and has detection limits ranging from 0.001 to 0.5 at% depending on the element. The instrument work function was calibrated to give a binding energy of 83.96 eV for the Au 4f7/2 line for metallic gold and the spectrometer dispersion was adjusted to give a binding energy of 932.62 eV for the Cu 2p3/2 line of metallic copper. The Kratos charge neutralizer system was used on all specimens. Survey scan analyses were carried out with an analysis area of 300 × 700 μm and a pass energy of 160 eV. High resolution analyses were carried out with an analysis area of 300 × 700 μm and a pass energy of 20 eV. Spectra have been charge corrected to the main line of the carbon 1s spectrum (adventitious carbon) set to 285.0 eV.



  
*Polymer International* published by John Wiley & Sons Ltd on behalf of Society of Chemical Industry.

### Contact angle measurements

Two microlitre droplets were placed on spin-coated sample slides or ethanol-washed reference glass slides and pictures were taken using a Krüss EasyDrop contact angle measurement system (KRÜSS GmbH Wissenschaftliche Laborgeräte, Hamburg, Germany) and analysed using proprietary software. The sample chamber temperature was kept constant at 21 °C using a LabTech H50-500 water chiller (Thermo Scientific, Vilnius, Lithuania). A total of five measurements per material were performed. Results are presented as mean ± standard deviation.

### Polymer extracts

Polymer samples were spin-coated and polymerized under UV as in the case with biocompatibility testing. The samples were then incubated in DPBS on a plate shaker at 40 rpm for 24 h at room temperature. The PBS containing spin-coated polymer extracts was subsequently aspirated to new tissue culture plate wells and heated for 5 h at 80 °C until the water had evaporated.

### Polymer extract metal content analysis via inductively coupled plasma optical emission spectrometry (ICP-OES)

Measurements were performed using an Agilent 5100 VDV inductively coupled plasma optical emission spectrometer (Agilent Technologies UK Limited, Cheadle, UK) in axial mode. The sample introduction system consisted of a glass concentric nebuliser, a glass cyclonic double pass spray chamber and a demountable dual view quartz 1.8 mm torch. The solid samples were dissolved directly from the well-plate locations in dilute nitric acid (2% w/v) with several washings and made up to the final volume (10 mL) with dilute nitric acid (2% w/v). Calibration curves of the target elements Al, Ti, V, Zr, Na and P were prepared between 1 and 100 ppm using single element standards (Sigma-Aldrich, TraceCERT, 2% $HNO_3$), with the exception of P (Alfa Aesar, SpecPure, 5% $HNO_3$). All blanks were prepared from the original stock of dilute nitric acid (2% w/v) used to prepare standards and samples. All blanks, standards and samples were prepared with yttrium internal standard (1 ppm, Sigma-Aldrich, TraceCERT, 2% $HNO_3$).

### Cell culture and maintenance

All biocompatibility tests were performed on NIH/3T3 mouse embryo fibroblasts from American Type Culture Collection (ATCC, Manassas, USA). The cells were cultured in IMDM supplemented with 10% foetal bovine albumin, 100 U mL$^{-1}$ penicillin and 100 μg mL$^{-1}$ streptomycin. The cells were maintained at 37 °C with 5% $CO_2$ and passaged every 3–4 days. The passage procedure started with washing the monolayer of cells once with DPBS followed by 0.25% (ethylenediaminetetraacetic acid)–trypsin treatment for 1 min. Detached cells would later be collected in full medium and passaged in a new flask.

### Polymer extract toxicity

Polymer samples were spin-coated and polymerized under UV as described for the biocompatibility testing. The samples were then incubated in a full cell growth medium (containing serum and antibiotics) for 24 h at room temperature. The medium containing spin-coated polymer extracts was subsequently aspirated and used on NIH/3T3 fibroblasts grown in a monolayer for 24 h. They were cultured for another 24 h with normal medium as a reference point at 37 °C with 5% $CO_2$ atmosphere. An MTT assay was then performed on the cells grown in extract-containing media.

### MTT assay and light microscopy

NIH/3T3 mouse embryo fibroblasts were seeded on spin-coated samples at a density of 20 000 cells mL$^{-1}$ per sample, using glass slides as control. The samples were incubated at 37 °C with 5% $CO_2$ atmosphere. Light microscopy images were taken after 96 h of culture on each surface and cellular morphology was qualitatively assessed. After 120 h of culture, the samples were transferred to new tissue culture plates, where they were treated with 0.2 mg mL$^{-1}$ and incubated for 1 h at 37 °C. The MTT solution was then carefully replaced with 200 μL of DMSO to solubilize the formazan. The optical density at 545 nm was measured by using an automatic microplate reader. Results were calculated as the ratio between cells grown on hybrid materials and glass. A total of 40 samples per material were prepared and split into eight independent experiments with $n = 5$ per experiment. Results are presented as averages ± standard error.

### Analysis of cell death

NIH/3T3 mouse embryo fibroblasts were seeded and cultured as described in the previous section. The type of cell death was determined microscopically by using two fluorescent dyes, AO/EB, as described by Mercille and Massie.[49] Briefly, cells from the different samples and glass slides were individually collected, centrifuged and suspended in 20 μL of fresh IMDM supplemented with foetal bovine serum and antibiotics and stained with 4 μL of AO (100 μg mL$^{-1}$)/EB (100 μg mL$^{-1}$) solution for 5 min. Then, the cells were observed using an Olympus IX51 inverted fluorescence microscope with an X-Cite 120PC Q UV lamp (Lumen Dynamics) and photographed using an ExiBlue camera (QImaging) with proprietary imaging software. 100 cells were counted per sample and split into three categories based on their nuclear and membrane integrity: live (cells with uniform green nucleus), apoptotic (cells with fragmented nuclei that fluoresce green (early apoptosis) or orange (late apoptosis)) and necrotic (intact, bright orange stained nuclei). Five independent experiments were carried out and averages ± standard deviations are presented.

### Statistical analysis

Statistical analysis was performed using RStudio® (version 1.1.383 for Mac running on R 3.4.2) and plotted using the ggplot2 package. The data are presented as either mean ± standard error or standard deviation. Statistical significance was assessed using one-way ANOVA and Tukey's honestly significant difference (HSD) *post hoc* test. Differences between groups were considered to be significant for $P < 0.05$ (*), $P < 0.01$ (**) and $P < 0.001$ (***).

## RESULTS AND DISCUSSION

### Material preparation

The Ti, V and Zr formulations were adapted from the literature.[33–35] The preparation procedure of the Al hybrid is analogous to those of other hybrid materials that have been used for LTPP except that the metal propoxide comes in a powder form, so it has to be dissolved first. Several solvents were tested for this purpose, including ethanol, isopropanol, hexane, cyclohexane and benzene, but the best solubility was obtained using toluene. The resulting material is a clear liquid with a yellow hue because of the presence of DEABP. After evaporation of the solvent, the material transitions to a viscous gel-like state. Gelation reduces structural distortions that would arise during fabrication in a liquid due to vibrations, diffusion and stage movement in some LTPP systems.



  
*Polymer International* published by John Wiley & Sons Ltd on behalf of Society of Chemical Industry.

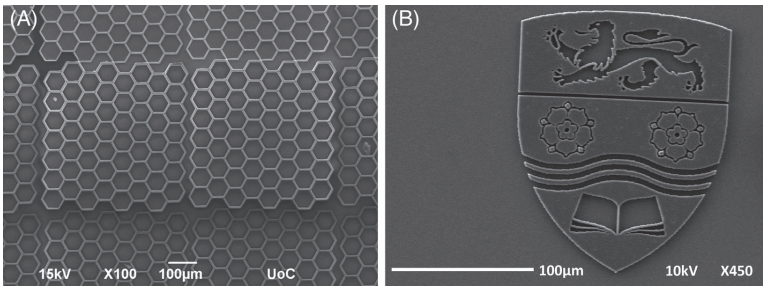


**Figure 3.** 2D structures fabricated out of the Al hybrid material: (A) honeycomb patterns fabricated using the custom-built LTPP system with a 40× 0.95 NA objective lens; (B) the coat of arms of Lancaster University fabricated using the Nanoscribe® system with a 63× 1.4 NA oil immersion lens.

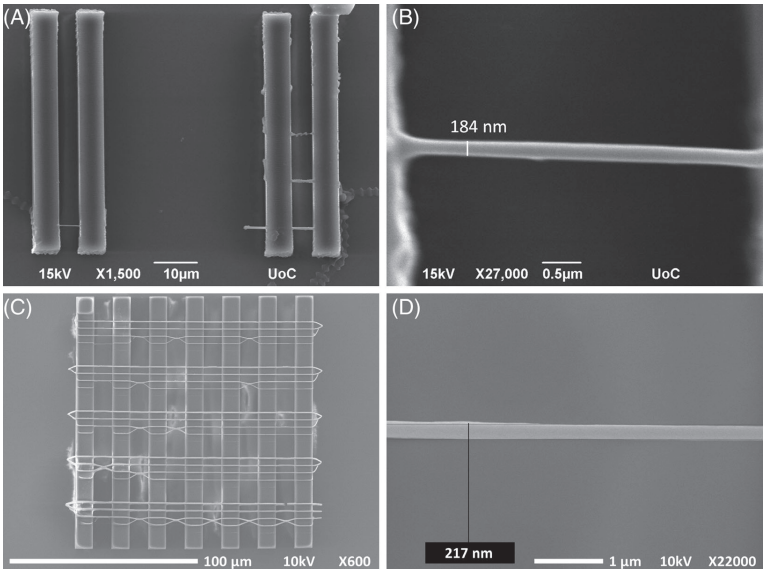


**Figure 4.** Support structures with suspended lines between them fabricated out of the Al hybrid material: (A), (B) structures fabricated using the custom-built LTPP system with a 100× 1.4 NA oil immersion lens at different magnifications; (C), (D) structures fabricated using the Nanoscribe® system with the 63× 1.4 NA oil immersion lens. Lines with resolutions down to around 200 nm were reproducibly fabricated using both systems.

Material iterations with different proportions between the components were tested with the AIP:MAA molar ratio remaining constant at 1:1 and AIP:MAPTHS being 1:1, 1:4 or 1:9. All the combinations were shown to be polymerizable in 3D, but 1:4 AIP:MAPTHS was chosen to be the same as in Ti and Zr hybrid materials.

**Laser two-photon polymerization (multiphoton fabrication)**

LTPP of hybrid organometallic polymers based on Ti,[33] V[34] and Zr[35] have been described in the literature. Both Ti and Zr hybrid materials have been used to produce scaffolds for tissue engineering.[24,44] Consequently, in this work we focused on investigating the properties and structurability of the novel Al hybrid material. The Al hybrid material is transparent, while the intrinsic photoinitiator renders it fluorescent upon irradiation with a laser. This makes finding the interface between the material and the glass slide as straightforward as with commercially available photoresists such as OrmoComp® or OrmoClear®. We first tested the Al hybrid organometallic polymer on both the Nanoscribe® and the custom-built LTPP systems in an attempt to fabricate 2D structures (Fig. 3). The printing of each of these structures took no more than 10 min.

Having shown that it is possible to fabricate high quality structures with minimal spatial distortions (Fig. 3), we modelled and fabricated suspended lines with varying laser power and scanning speed between bulky support structures to assess maximum resolution of the Al hybrid (Fig. 4). Lines that survived the development process reproducibly reached <200 nm in width



  

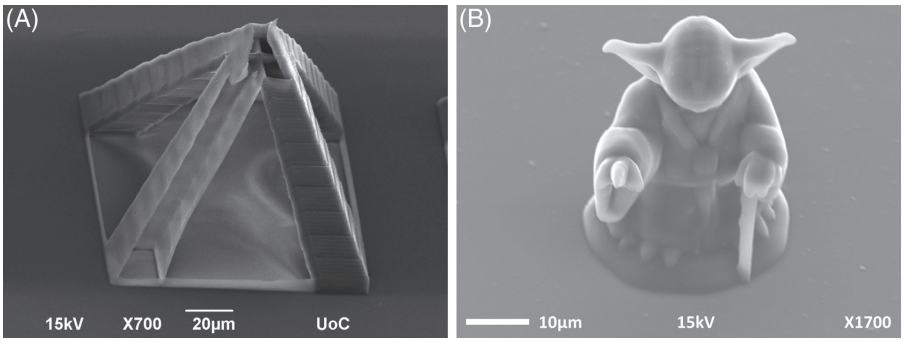


**Figure 5.** 3D structures fabricated out of the Al hybrid material: (A) a hollow pyramid shell fabricated using the custom-built LTPP system with a 100× 1.4 NA oil immersion lens; (B) a micro-Yoda fabricated using the Nanoscribe® system with a 63× 1.4 NA oil immersion lens.

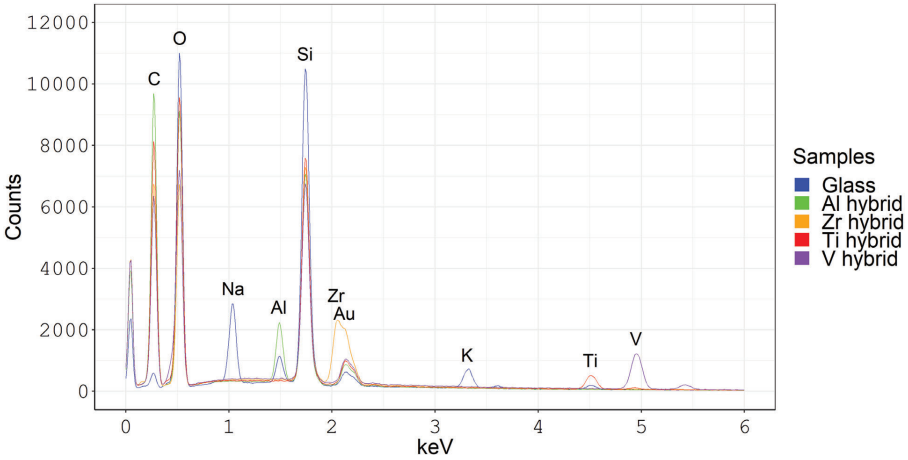


**Figure 6.** EDX spectra of the different organometallic hybrid polymers containing Al, Ti, V and Zr, and the borosilicate glass control.

using the 100× 1.4 NA oil immersion lens on the custom-built LTPP system and <250 nm using a 63× 1.4 NA oil immersion lens on the Nanoscribe® system. The result is comparable to resolutions reached using other hybrid organic–inorganic materials via LTPP. 3D structures were fabricated on both systems (Figs 4 and 5), taking no more than 30 min each. The structures survived the development and washing processes with minimal shrinkage or deformation. The hollow pyramid and Yoda structures (Fig. 5) demonstrate the relative rigidity of the material.

### EDX analysis

EDX spectroscopy was performed on all the tested materials based on Al, Ti, V and Zr in order to compare their chemical constituents. The analysis was performed on drop-cast films and confirmed the presence of metals in the organometallic materials (Fig. 6). The films were relatively thick (of the order of hundreds of microns), so the X-ray signals were most likely being generated by the materials. The same type of glass slides on which the materials were drop-cast were used as references. The Al hybrid showed a peak at around 1.5 keV that had 1.96 times greater X-ray photon count than that measured in glass, indicating the presence of Al (characteristic K$\alpha$ = 1.486 keV). In the case of the V hybrid, a peak at around 5 keV indicates the presence of V (characteristic K$\alpha$ = 4.949 keV and L$\alpha$ = 0.511 keV) with X-ray photon count differing around 20 times from that of glass at 4.949 keV. The L$\alpha$ of V was not visible due to overlap with the K$\alpha$ of O. Significantly larger amounts of Ti were found in Ti hybrid material compared to control glass slides, with X-ray photon count at K$\alpha$ = 4.508 keV being around 2.7 times greater than in reference glass. Finally, a peak at 2 keV indicates the presence of Zr (characteristic L$\alpha$ = 2.042 keV) in the Zr hybrid with X-ray photon counts differing from glass by 10.7 times. The presence of gold due to the coating method was confirmed in all samples at 2.120 keV. Signals from K and Na were only detectable in the glass, confirming that the resin thickness was high enough for the X-rays to be generated within the resins.



  
*Polymer International* published by John Wiley & Sons Ltd on behalf of Society of Chemical Industry.

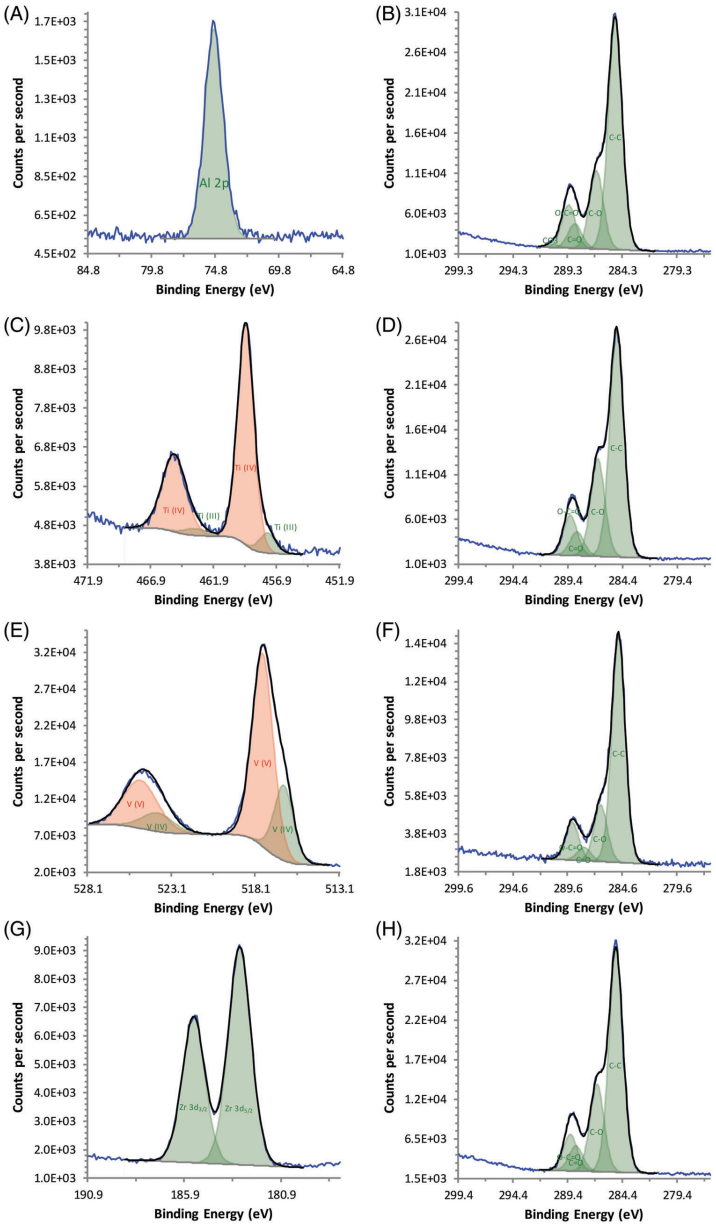


**Figure 7.** XPS spectra of the different organometallic hybrid polymers containing Al (A), (B), Ti (C), (D), V (E), (F) and Zr (G), (H). (A), (C), (E) and (G) show the oxidation state of the metals in the polymers and relative proportions thereof. (B), (D), (F), (H) show the compositions of carbonaceous species in the polymers and relative proportions thereof.



  

**Table 1.** A summary of the surface compositions (%) of the metal-based species from the representative large area survey XPS spectrum of the various samples

| | Substrate | | | |
|---|---|---|---|---|
| Metal | Al | Ti | V | Zr |
| Binding energy (eV) | 74.90 | 457.65 and 459.37 | 516.31 and 517.63 | 183.07 |
| Possible species | $Al(OH)_3$ or AlO(OH) | Ti(III) or Ti(IV) | V(IV) or V(V) | Zr(IV) |

**Table 2.** A summary of the surface compositions (%) of the C-based species from the representative large area survey XPS spectrum of the various samples

| | Substrate | | | |
|---|---|---|---|---|
| C 1s | Al | Ti | V | Zr |
| C–C | 60.63 | 58.31 | 67.75 | 59.78 |
| C–O | 20.67 | 25.22 | 16.89 | 23.57 |
| C=O | 6.46 | 6.18 | 4.02 | 6.82 |
| O–C=O | 11.37 | 10.30 | 11.33 | 9.83 |
| $(C–O)_3$ | 0.87 | 0.00 | 0.00 | 0.00 |

### XPS analysis

Akin to EDX analysis, XPS analysis (Fig. 7, Tables 1 and 2, Figs S1–S12 and Tables S1–S3) confirms the presence of the metals in the polymer films. XPS also offers insight into the oxidation state of the metals (and relative proportions thereof, Fig. 7 and Table 1) and carbonaceous species (and relative proportions thereof, Fig. 7 and Table 2). Interestingly, XPS shows that the polymers for Al-, Ti- and Zr-containing polymers have similar compositions of carbonaceous species. By comparison, the V-containing polymer compositions had lower C=O content which is related to their content of MAA which would bind the metal cation through interaction with the anionic carboxylates from MAA moieties (i.e. weaker metal ion binding than the other polymers).

### Contact angle measurements

The results show that the hybrid organic–inorganic materials had higher contact angles than those of glass slides (Fig. 8). We found that the average contact angle of glass slides prior to washing was 64° and 39° after ethanol washing and air-drying. The Al and Zr hybrid materials had contact angles of *ca* 72° and 71°, respectively. The Ti hybrid material was more hydrophobic, with a contact angle of around 90°. The V hybrid material had the highest contact angle of *ca* 102°.

### Biocompatibility assessment

NIH/3T3 fibroblasts were seeded on the surfaces to investigate their biocompatibility. Light microscopy images were taken after 96 h of culture. Healthy fibroblasts tend to be spindle-shaped, while non-viable cells tend to become rounded and detach from the surface. We observed that after 96 h spindle-shaped cells can be found on all surfaces except for the V hybrids (Fig. 9).

All surfaces supported cell adhesion and proliferation (probably via protein-adsorption-mediated adhesion in line with other biomaterials) with the exception of the V-containing hybrid which is likely to be because vanadium oxides are more toxic than vanadium in its elemental form. To quantify the biocompatibility results, MTT assays were performed after 120 h of culture. The data obtained are presented as a ratio of optical density of cells grown on the hybrid materials to that of cells grown on glass (Fig. 10). The total cellular metabolic activity is proportional to the optical density. NIH/3T3 mouse fibroblasts tended to attach and proliferate on all surfaces except the V hybrid material. We observed that the cells tended to have the highest metabolic activity on the Zr-based hybrid material. These findings support the biocompatibility notion of this material together with *in vivo* studies that have previously shown the material to be of comparable biocompatibility to that of a surgical suture composed of glycolide/lactide (Polysorb™ 4–0).[43] There were no significant differences between the rates of total cellular metabolism on the

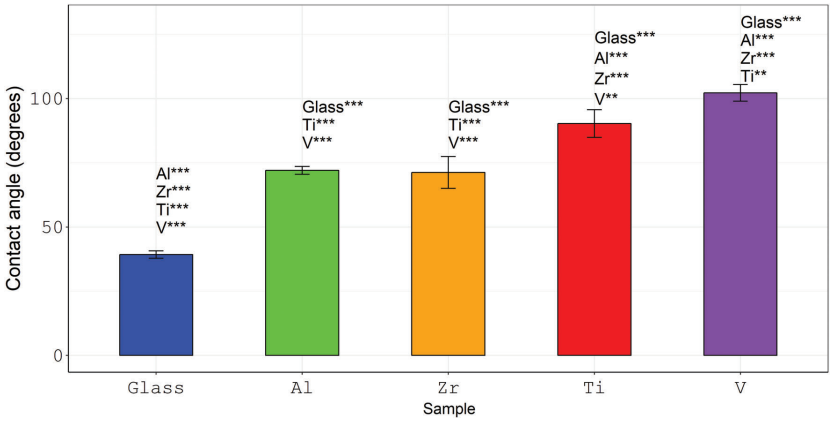


**Figure 8.** Water contact angles ± standard deviation. Al, Ti, V and Zr correspond to Al, Ti, V and Zr hybrid materials; glass was used as a control. $^{**}P < 0.01$, $^{***}P < 0.001$, glass was significantly different from all other surfaces with $P < 0.001$.




*Polymer International* published by John Wiley & Sons Ltd on behalf of Society of Chemical Industry.

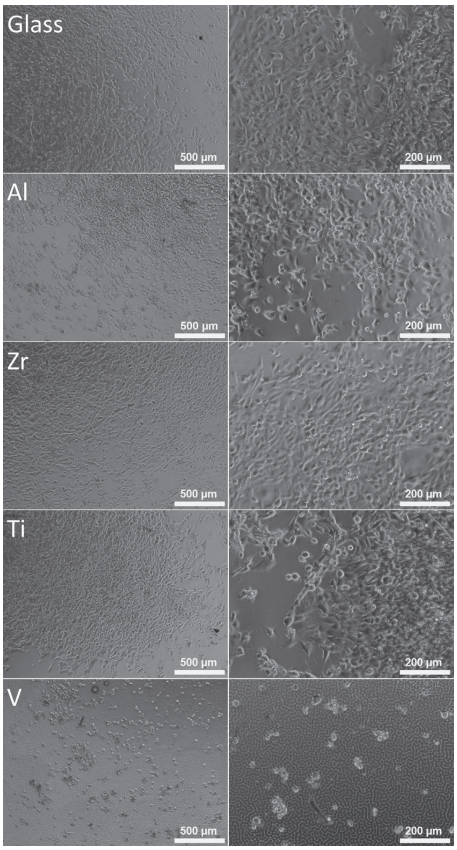


**Figure 9.** NIH/3T3 fibroblasts grown on the organometallic polymer materials and control glass surfaces. Pictures were taken 96 h after cell seeding using both 4× and 10× objective lenses on an inverted light microscope. Cellular morphology is healthy in glass and Al-, Zr- and Ti-containing polymers. However, none of the cells was attached to the V-containing polymers after 96 h (probably due to leaching of V from the films).

Al and Ti hybrids. The Zr hybrid was significantly more supportive of cell growth than Al- and Ti-based hybrids. The preliminary studies de-risk a more extensive (and costly) investigation into the cell–surface interactions and surface protein adsorption that would underpin the use of the materials in tissue engineering or other biological applications.

To investigate whether the toxicity of the V-containing polymers is due to their surface properties or to some components being washed out into the medium, we used sample extracts to treat cells grown in a monolayer. The results are presented in Fig. 11 showing that the Al extract was significantly ($P < 0.05$) beneficial to the cell culture, while control, Ti and Zr sample extracts did not have significantly different effects on cellular viability. The V sample extract was highly toxic to the cell monolayer with $P < 0.001$ compared to all other sample extracts. This suggests non-crosslinked metal ions are washed out into the medium, thus contributing to the toxicity towards cells grown *in vitro* (which correlates with the ICP-OES data).

To assess the mechanism of cell death, differential staining with AO/EB was applied and the numbers of live, apoptotic and necrotic cells were calculated. Results confirm that the most cytotoxic surface for cell culture was the V hybrid (Fig. 12). The majority of cells had undergone necrosis after 24 h of culture, while after 96 h and 120 h there were virtually no living cells remaining on these surfaces. Necrosis was a much more prevalent type of cell death on all of the surfaces compared to apoptosis. We investigated whether there were any significant differences between the numbers of live cells on the surfaces. We observed that the number of live cells on all samples (except for the V hybrids) was between 60% and 80% at all time points (24, 96 and 120 h).

The V hybrid materials displayed the highest cytotoxicity with the majority of cells dying via necrosis. Statistically significant ($P < 0.001$) differences were found between all samples compared to the V hybrid material in terms of the number of live and necrotic cells (Fig. 12), consistent with very low optical density in the MTT assay and ICP-OES confirmed leaching of the V (Fig. 13). This is in accordance with previously reported work showing the toxicity of V both in its elemental and oxide forms.[50] No statistically significant differences were observed between the numbers of apoptotic cells (Fig. 12). Other statistically significant differences between the numbers of live and necrotic cells on the surfaces are summarized in Table 3.

Al-, Ti- and Zr-based hybrid organometallic polymers showed good biocompatibility *in vitro*. The numbers of live, apoptotic and necrotic cells on all these surfaces were comparable at every time point (after 24, 96 and 120 h). However, the highest metabolic rate according to the MTT assay was found on the Zr hybrid.

Increased surface hydrophobicity improves irreversible protein adsorption with albumin being one of the first proteins to reach the surface[51] which does not have cell adhesion motifs, possibly having a negative impact on material biocompatibility.

Ti is attractive due to its mechanical strength and biological inertness as its alloys are widely used in dental[52] and orthopaedic[53] applications. Zr-based biomaterials are also widely used in the clinic, and zirconia ceramics are a class of biocompatible materials with comparable properties to those of Ti.[54] Since both Ti and Zr are being widely used for biomedical applications, hybrid organometallic polymers containing these metals are worthy of investigation.

Good *in vitro* biocompatibility has been demonstrated in many 3D printing materials ranging from hydroxyapatites[55] to organic polymers, such as polyvinyl alcohol reinforced with cellulose nanofibrils.[56] However, a limited number of the existing biocompatible materials offer the possibility of reproducible sub-micron structure fabrication in 3D.

Al is not used for implant fabrication due to its solubility under acidic conditions as well as limited mechanical strength. $Al^{3+}$ has also been linked to Alzheimer's disease and other types of neurodegeneration.[57] However, in chemically stable and inert structures, the presence of Al is not considered to be dangerous, and it is noteworthy that Al is a part of many Ti alloys used in biomedical applications.[58] While the toxicity of $Al^{3+}$ is known, compounds of Al such as oxides and hydroxides are widely used as food additives, pharmaceuticals and personal care products and are considered safe.[59] Our data presented in this work confirm that Al-containing polymers have potential to be used in biomedical applications.



  
*Polymer International* published by John Wiley & Sons Ltd on behalf of Society of Chemical Industry.

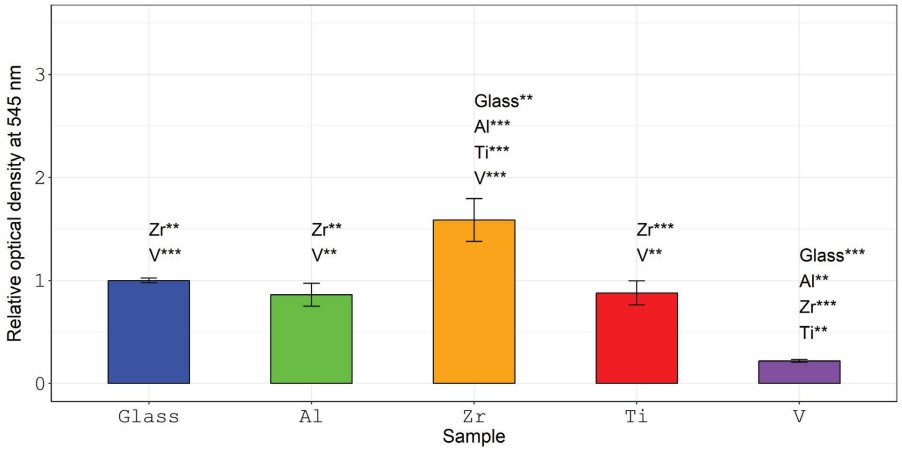


**Figure 10.** Relative optical density as measured via MTT after 120 h of cell culture. The optical density is directly proportional to the total metabolic activity of cells on each surface. Results are presented as absorption ratio to that of glass ± standard error. $^{**}P < 0.01$, $^{***}P < 0.001$.

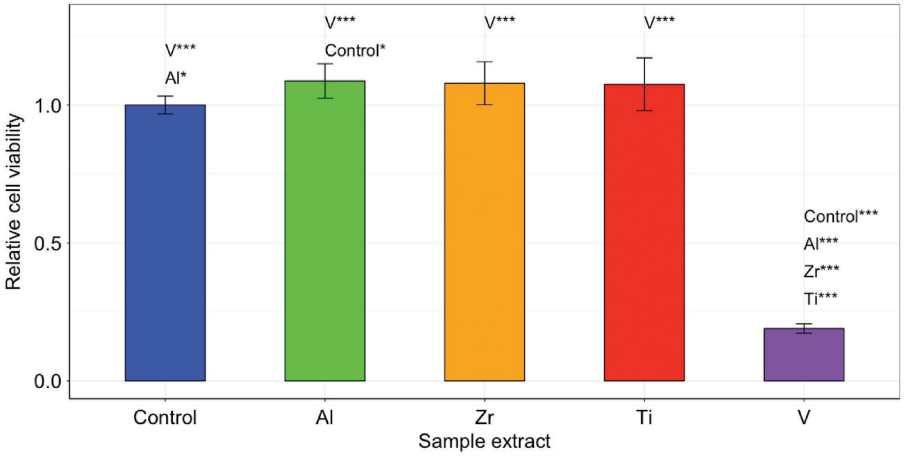


**Figure 11.** Cells cultured in media containing the polymer sample extracts. Results are presented as absorption ratio to that of glass ± standard deviation. Al and control surfaces had a significant difference with $^{*}P < 0.05$, while V was significantly different from all other surfaces with $^{***}P < 0.001$.

The use of hybrid organometallic polymer-based materials as implants is a relatively new concept and is being more thoroughly investigated due to the possibility of 3D microstructure fabrication. Good *in vitro* biocompatibility has been demonstrated in many 3D printing materials, ranging from hydroxyapatites[55] to organic polymers, such as polyvinyl alcohol reinforced with cellulose nanofibrils.[56] However, a limited number of the existing biocompatible materials offer the possibility of reproducible sub-micron structure fabrication in 3D. Moreover, integration of several different materials with varying properties will allow bioengineers to finely tune both the mechanical and biological properties of this next generation of implants.

## CONCLUSIONS

A hybrid organic–inorganic material based on Al has been developed for laser 3D fabrication purposes. LTPP experiments show that the organometallic polymer-based materials can be used to easily fabricate 2D and 3D structures. Low shrinkage of the material allows high resolution (down to 200 nm) structures to be made, which is on a comparable scale to other hybrid organic–inorganic materials.

Biocompatibility testing shows that Al-, Ti- and Zr-containing organometallic polymers support NIH/3T3 fibroblast growth. Cell viability on these surfaces was comparable to that of control glass surfaces. We observed that the rate of metabolism on Al-



  

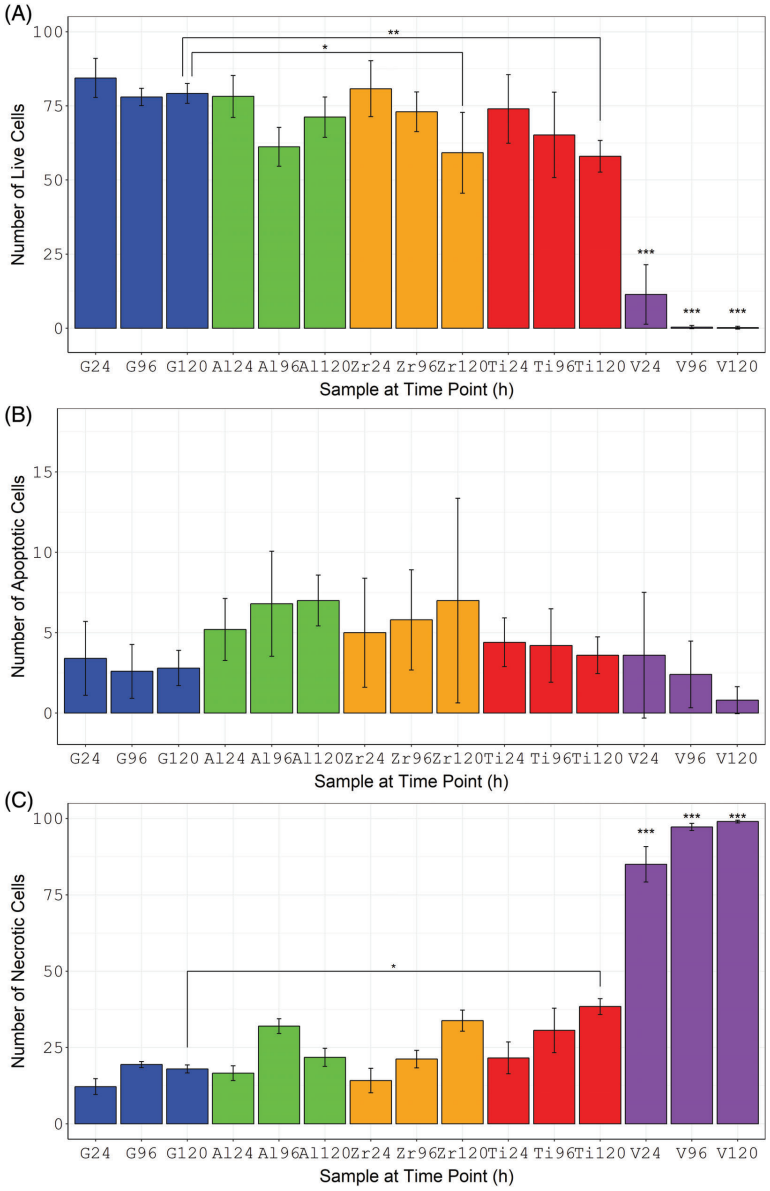


**Figure 12.** Number of live, apoptotic and necrotic cells on glass, Al, Zr, Ti and V organometallic hybrid materials after 24, 96 and 120 h of culture determined via acridine orange/ethidium bromide staining. Five samples per material per time point were used to calculate 100 cells on each. The results are presented as averages ± standard deviation. Statistical analysis was performed between all groups; however, only differences between corresponding time points are presented. In both live and necrotic cell cases, the results for V hybrids were significantly different from all other surfaces with a $P$ value of <0.001 (***). *$P < 0.05$, **$P < 0.01$, ***$P < 0.001$.






*Polymer International* published by John Wiley & Sons Ltd on behalf of Society of Chemical Industry.

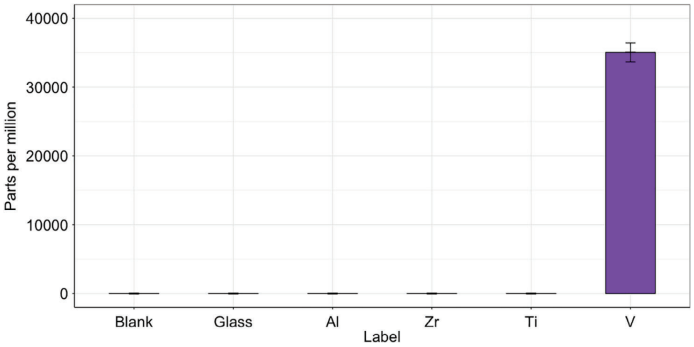


**Figure 13.** ICP-OES data of extracts from Al, Zr, Ti and V organometallic hybrid materials.

**Table 3.** A summary of statistically significant differences not presented in Fig. 10

| Comparison | Live | Necrotic |
|---|---|---|
| Al96-G24 | ** | * |
| Zr120-G24 | *** | ** |
| Ti96-G24 | * | * |
| Ti120-G24 | *** | *** |
| Zr120-G96 | * | – |
| Ti120-G96 | * | * |
| Zr120-Al24 | * | ** |
| Ti120-Al24 | * | – |
| Zr24-Al96 | * | * |
| Zr120-Zr24 | ** | * |
| Ti120-Zr24 | ** | *** |

*$P < 0.05$.
**$P < 0.01$.
***$P < 0.001$.

and Ti-containing materials was comparable to that of glass, while Zr supported a significantly higher proliferation rate of NIH/3T3 fibroblasts. Cellular morphology was normal on Al-, Zr- and Ti-containing materials. The V-containing organometallic polymer was shown to be toxic to cells and induced necrosis. The Al-, Zr- and Ti- containing organometallic polymers have been shown to be promising candidates for tissue engineering applications. However, an extensive investigation of cell topography responses, taking into account the expression of adhesion proteins, long-term viability and biodegradability studies of the materials are needed if they are to be used for tissue engineering or other *in vivo* applications, and the specific tissue niches in which they may be applicable based on the conditions to which the materials would be exposed *in vivo* (fluid flow, mechanical stress, tissue mechanics etc.).

## ACKNOWLEDGEMENTS

We thank Dr Maria Farsari and Dr Anthi Ranella from the Institute of Electronic Structure and Laser, Foundation for Research and Technology – Hellas (FORTH-IESL) for providing E. B. with access to the laser two-photon polymerization and cell culture facilities, and Ms Aleka Manousaki from the University of Crete for SEM imaging. We thank Dr Gintaras Valinčius and Dr Tadas Ragaliauskas for access to spin-coating and contact angle measurement equipment, and Dr Virginija Bukelskienė for insightful discussions.

The work was supported by the European Commission via the Marie Skłodowska-Curie research fellowship programme AngioMatTrain (Grant agreement 317304) and a Lancaster University Faculty of Science and Technology Early Career Internal Grant, a Royal Society Research Grant (RG160449) and an EPSRC First Grant (EP/R003823/1).

## SUPPORTING INFORMATION

Supporting information may be found in the online version of this article.

## REFERENCES

1 Deubel M, von Freymann G, Wegener M, Pereira S, Busch K and Soukoulis CM, *Nat Mater* **3**:444–447 (2004). https://doi.org/10.1038/nmat1155.
2 Kenanakis G, Xomalis A, Selimis A, Vamvakaki M, Farsari M, Kafesaki M *et al.*, *ACS Photon* **2**:287–294 (2015). https://doi.org/10.1021/ph5003818.
3 Galajda P and Ormos P, *Appl Phys Lett* **78**:249–251 (2001). https://doi.org/10.1063/1.1339258.
4 Lee W, Pruzinsky SA and Braun PV, *Adv Mater* **14**:271–274 (2002). https://doi.org/10.1002/1521-4095.
5 Guo R, Xiao S, Zhai X, Li J, Xia A and Huang W, *Opt Express* **14**:810–816 (2006). https://doi.org/10.1364/OPEX.14.000810.
6 Maruo S, Ikuta K and Hayato K, Technical Digest. MEMS 2001. 14th IEEE International Conference on Micro Electro Mechanical Systems (Cat. No.01CH37090), pp. 594–597 (2001). https://doi.org/10.1109/MEMSYS.2001.906611
7 Danilevicius P, Rekstyte S, Balciunas E, Kraniauskas A, Jarasiene R, Sirmenis R *et al.*, *J Biomed Opt* **17**:081405 (2012). https://doi.org/10.1117/1.JBO.17.8.081405.
8 Marino A, Filippeschi C, Mattoli V, Mazzolai B and Ciofani G, *Nanoscale* **7**:2841–2850 (2015). https://doi.org/10.1039/c4nr06500j.
9 Xing J-F, Zheng M-L and Duan X-M, *Chem Soc Rev* **44**:5031–5039 (2015). https://doi.org/10.1039/c5cs00278h.
10 Kasko AM and Wong DY, *Future Med Chem* **2**:1669–1680 (2010). https://doi.org/10.4155/fmc.10.253.
11 Ovsianikov A, Malinauskas M, Schlie S, Chichkov B, Gittard S, Narayan R *et al.*, *Acta Biomater* **7**:967–974 (2011). https://doi.org/10.1016/j.actbio.2010.10.023.
12 Ovsianikov A, Schlie S, Ngezahayo A, Haverich A and Chichkov BN, *J Tissue Eng Regen Med* **1**:443–449 (2007). https://doi.org/10.1002/term.57.



  

13 Ovsianikov A, Deiwick A, Van Vlierberghe S, Dubruel P, Möller L, Drager G *et al.*, *Biomacromolecules* **12**:851–858 (2011). https://doi.org/10.1021/bm1015305.
14 Gittard SD, Ovsianikov A, Akar H, Chichkov B, Monteiro-Riviere NA, Stafslien S *et al.*, *Adv Eng Mater* **12**:B77–B82 (2010). https://doi.org/10.1002/adem.200980012.
15 Jia B, Buso D, Van Embden J, Li J and Gu M, *Adv Mater* **22**:2463–2467 (2010). https://doi.org/10.1002/adma.201000513.
16 Marino A, Barsotti J, De Vito G, Filippeschi C, Mazzolai B, Piazza V *et al.*, *ACS Appl Mater Interfaces* **7**:25574–25579 (2015). https://doi.org/10.1021/acsami.5b08764.
17 Ovsianikov A, Mühleder S, Torgersen J, Li Z, Qin XH, Van Vlierberghe S *et al.*, *Langmuir* **30**:3787–3794 (2014). https://doi.org/10.1021/la402346z.
18 Evans ND, Minelli C, Gentleman E, LaPointe V, Patankar SN, Kallivretaki M *et al.*, *Eur Cell Mater* **18**:1–13 (2009). https://doi.org/10.22203/eCM.v018a01.
19 Yin Z, Chen X, xin Song H, jie Hu J, mei Tang Q, Zhu T *et al.*, *Biomaterials* **44**:173–185 (2015). https://doi.org/10.1016/j.biomaterials.2014.12.027.
20 Hamid Q, Wang C, Snyder J and Sun W, *J Biomed Mater Res B* **103**:473–484 (2015). https://doi.org/10.1002/jbm.b.33223.
21 Thrivikraman G, Mallik PK and Basu B, *Biomaterials* **34**:7073–7085 (2013). https://doi.org/10.1016/j.biomaterials.2013.05.076.
22 Weiss T, Hildebrand G, Schade R and Liefeith K, *Eng Life Sci* **9**:384–390 (2009). https://doi.org/10.1002/elsc.200900002.
23 Basu S, Gomi K, Campagnola PJ, Kanazashi M, Lickorish D, Arai T *et al.*, *J Biomed Mater Res A* **71**:359–368 (2004). https://doi.org/10.1002/jbm.a.30174.
24 Mačiulaitis J, Deveikytė M, Rekštytė S, Bratchikov M, Darinskas A, Šimbelytė A *et al.*, *Biofabrication* **7**:015015 (2015). https://doi.org/10.1088/1758-5090/7/1/015015.
25 Nava MM, Piuma A, Figliuzzi M, Cattaneo I, Bonandrini B, Zandrini T *et al.*, *Stem Cell Res Ther* **7**:132 (2016). https://doi.org/10.1186/s13287-016-0387-z.
26 Farsari M, Vamvakaki M and Chichkov BN, *J Opt* **12**:124001 (2010). https://doi.org/10.1088/2040-8978/12/12/124001.
27 Nazir R, Bourquard F, Balčiūnas E, Smoleń S, Gray D, Tkachenko NV *et al.*, *ChemPhysChem* **16**:682–690 (2015). https://doi.org/10.1002/cphc.201402646.
28 Nazir R, Balčiunas E, Buczyńska D, Bourquard F, Kowalska D, Gray D *et al.*, *Macromolecules* **48**:2466–2472 (2015). https://doi.org/10.1021/acs.macromol.5b00336.
29 Nazir R, Thorsted B, Balčiunas E, Mazur L, Deperasińska I, Samoć M *et al.*, *J Mater Chem C* **4**:167–177 (2015). https://doi.org/10.1039/c5tc03334a.
30 Nazir R, Danilevicius P, Gray D, Farsari M and Gryko DT, *Macromolecules* **46**:7239–7244 (2013). https://doi.org/10.1021/ma4010988.
31 Nazir R, Danilevicius P, Ciuciu AI, Chatzinikolaidou M, Gray D, Flamigni L *et al.*, *Chem Mater* **26**:3175–3184 (2014). https://doi.org/10.1021/cm500612w.
32 Malinauskas M, Gaidukevičiute A, Purlys V, Žukauskas A, Sakellari I, Kabouraki E *et al.*, *Metamaterials* **5**:135–140 (2011). https://doi.org/10.1016/j.metmat.2011.04.002.
33 Sakellari I, Gaidukeviciute A, Giakoumaki A, Gray D, Fotakis C, Farsari M *et al.*, *Appl Phys A* **100**:359–364 (2010). https://doi.org/10.1007/s00339-010-5864-0.
34 Kabouraki E, Giakoumaki AN, Danilevicius P, Gray D, Vamvakaki M and Farsari M, *Nano Lett* **13**:3831–3835 (2013). https://doi.org/10.1021/nl401853k.
35 Ovsianikov A, Viertl J, Chichkov B, Oubaha M, MacCraith B, Sakellari I *et al.*, *ACS Nano* **2**:2257–2262 (2008). https://doi.org/10.1021/nn800451w.
36 Malinauskas M, Žukauskas A, Purlys V, Belazaras K, Momot A, Paipulas D *et al.*, *J Opt* **12**:124010 (2010). https://doi.org/10.1088/2040-8978/12/12/124010.
37 Vasilantonakis N, Terzaki K, Sakellari I, Purlys V, Gray D, Soukoulis CM *et al.*, *Adv Mater* **24**:1101–1105 (2012). https://doi.org/10.1002/adma.201104778.
38 Raimondi MT, Eaton SM, Laganà M, Aprile V, Nava MM, Cerullo G *et al.*, *Acta Biomater* **9**:4579–4584 (2013). https://doi.org/10.1016/j.actbio.2012.08.022.
39 Rezende RA, Pereira FDAS, Kasyanov V, Ovsianikov A, Torgensen J, Gruber P *et al.*, *Virtual Phys Prototyping* **7**:287–301 (2012). https://doi.org/10.1080/17452759.2012.740877.
40 Nava MM, Di Maggio N, Zandrini T, Cerullo G, Osellame R, Martin I *et al.*, *J Tissue Eng Regen Med* **11**:2836–2845 (2016). https://doi.org/10.1002/term.2187.
41 Ovsianikov A, Shizhou X, Farsari M, Vamvakaki M, Fotakis C and Chichkov BN, *Opt Express* **17**:2143–2148 (2009). https://doi.org/10.1364/OE.17.002143.
42 Terzaki K, Kissamitaki M, Skarmoutsou A, Fotakis C, Charitidis CA, Farsari M *et al.*, *J Biomed Mater Res A* **101**:2283–2294 (2013). https://doi.org/10.1002/jbm.a.34516.
43 Malinauskas M, Baltriukiene D, Kraniauskas A, Danilevicius P, Jarasiene R, Sirmenis R *et al.*, *Appl Phys A* **108**:751–759 (2012). https://doi.org/10.1007/s00339-012-6965-8.
44 Psycharakis S, Tosca A, Melissinaki V, Giakoumaki A and Ranella A, *Biomed Mater* **6**:045008 (2011). https://doi.org/10.1088/1748-6041/6/4/045008.
45 Poinern GEJ, Le XT, O'Dea M, Becker T and Fawcett D, *Biomed Res Int* **2014**:238762 (2014). https://doi.org/10.1155/2014/238762.
46 Kolekar TV, Thorat ND, Yadav HM, Magalad VT, Shinde MA, Bandgar SS *et al.*, *Ceram Int* **42**:5304–5311 (2016). https://doi.org/10.1016/j.ceramint.2015.12.060.
47 Käpylä E, Sorkio A, Teymouri S, Lahtonen K, Vuori L, Valden M *et al.*, *Langmuir* **30**:14555–14565 (2014). https://doi.org/10.1021/la5023642.
48 Claeyssens F, Hasan EA, Gaidukeviciute A, Achilleos DS, Ranella A, Reinhardt C *et al.*, *Langmuir* **25**:3219–3223 (2009). https://doi.org/10.1021/la803803m.
49 Mercille S and Massie B, *Biotechnol Bioeng* **44**:1140–1154 (1994). https://doi.org/10.1002/bit.260440916.
50 Eisenbarth E, Velten D, Müller M, Thull R and Breme J, *Biomaterials* **25**:5705–5713 (2004). https://doi.org/10.1016/j.biomaterials.2004.01.021.
51 Elbert DL and Hubbell JA, *Annu Rev Mater Sci* **26**:365–394 (1996). https://doi.org/10.1146/annurev.ms.26.080196.002053.
52 Liu X, Chen S, Tsoi JKH and Matinlinna JP, *Regen Biomater* **4**:315–323 (2017). https://doi.org/10.1093/rb/rbx027.
53 Geetha M, Singh AK, Asokamani R and Gogia AK, *Prog Mater Sci* **54**:397–425 (2009). https://doi.org/10.1016/j.pmatsci.2008.06.004.
54 Hisbergues M, Vendeville S and Vendeville P, *J Biomed Mater Res B* **88**:519–529 (2009). https://doi.org/10.1002/jbm.b.31147.
55 Zeng Y, Yan Y, Yan H, Liu C, Li P, Dong P *et al.*, *J Mater Sci* **53**:6291–6301 (2018). https://doi.org/10.1007/s10853-018-1992-2.
56 Chen X, Chen C, Zhang H, Huang Y, Yang J and Sun D, *Carbohydr Polym* **173**:547–555 (2017). https://doi.org/10.1016/j.carbpol.2017.06.036.
57 Bondy SC, *Neurotoxicology* **31**:575–581 (2010). https://doi.org/10.1016/j.neuro.2010.05.009.
58 Abdel-Hady Gepreel M and Niinomi M, *J Mech Behav Biomed Mater* **20**:407–415 (2013). https://doi.org/10.1016/j.jmbbm.2012.11.014.
59 Krewski D, Yokel RA, Nieboer E, Borchelt D, Cohen J, Harry J *et al.*, *J Toxicol Environ Health B* **10**:1–269 (2007). https://doi.org/10.1080/10937400701597766.




  

Vilniaus universiteto leidykla
Saulėtekio al. 9, III rūmai, LT-10222 Vilnius
El. p. info@leidykla.vu.lt, www.leidykla.vu.lt
Tiražas 15 egz.